UNIVERSITY OF SOUTHAMPTON

FACULTY OF ENGINEERING AND THE ENVIRONMENT

Airbus Noise Technology Centre

Modelling Counter Rotating Open Rotor Installation Noise Sources

by

Ravish Karve

Thesis for the degree of Doctor of Philosophy

Supervisors: David Angland, Xin Zhang

April 25, 2019

UNIVERSITY OF SOUTHAMPTON

ABSTRACT

FACULTY OF ENGINEERING AND THE ENVIRONMENT
Aeronautics and Astronautics

Doctor of Philosophy

MODELLING COUNTER ROTATING OPEN ROTOR INSTALLATION NOISE SOURCES

by Ravish Karve

Open rotors are an engine technology that could bring a step change in propulsive efficiency for the next generation of aircraft. As such, there is a large research effort that aims to accurately predict the noise radiated by open rotors. This thesis focuses on the noise radiated by an installed open rotor. In this configuration one of the major noise sources could be the ingestion of a turbulent boundary layer that has developed on the fuselage of the aircraft.

This thesis presents an analytical model that predicts this noise source. The analytical model is based on the simplified rotor noise model of Amiet with blade-to-blade correlation modelled. The model is extended in three ways to include the boundary layer ingestion noise source. The first extension is to include a numerical switch to model the partial loading of a rotor ingesting a boundary-layer. The second extension is to include wall-effects using the method of images. The assumptions that are made in the method of images are tested by examining the simpler case of a two-dimensional aerofoil ingesting turbulence in proximity to a hard-wall. This is done by extending Amiet's two-dimensional leading-edge noise model and comparing the predictions from this model to two Computational Aeroacoustic (CAA) simulations. The first CAA simulation uses the method of images to model the wall and the second uses a physically representative hard-wall boundary condition to model the wall. By comparing the differences between the analytical predictions and the CAA simulations, it is shown that the method of images accurately predicts wall-effects except for a small range of observers that are in the shadow-zone of the aerofoil. The method of images is then implemented in the rotor noise model to predict wall-effects for a rotor. Finally, an axisymmetric anisotropic turbulence model is used to approximate boundary layer turbulence. The extended rotor noise model is validated by comparing it to experimental measurements and to a time-domain rotor noise model that does not model boundary layer turbulence.

Contents

Declaration of Authorship xvii

Acknowledgements xix

Nomenclature xxv

Acronyms xxix

1 Introduction 1
- 1.1 Aims of the current work . . . 2
- 1.2 Original contributions . . . 5
- 1.3 Thesis structure . . . 5

2 Literature Review 7
- 2.1 Boundary layer turbulence . . . 8
- 2.2 Analytical modelling of leading-edge/turbulence interaction noise . . . 12
  - 2.2.1 Analytical modelling of leading-edge noise due to translating aerofoils interacting with turbulence . . . 12
  - 2.2.2 Analytical modelling of rotor noise . . . 15
- 2.3 Experimental studies of open rotor noise . . . 18
  - 2.3.1 Experimental investigations of leading-edge noise from translating aerofoils . . . 19
  - 2.3.2 Experimental investigations of open rotor noise . . . 20
  - 2.3.3 Experimental investigations of boundary layer ingestion noise . . . 22
- 2.4 Computational modelling of leading-edge noise . . . 23
  - 2.4.1 Simulations of leading-edge noise using hybrid methods . . . 24
  - 2.4.2 CAA simulations of leading-edge noise . . . 25
  - 2.4.3 Simulations of leading-edge noise using Lattice Boltzman solvers . 27
- 2.5 Conclusions . . . 27

3 Amiet's rotor noise formulation 29
- 3.1 Rotor noise model . . . 30
  - 3.1.1 Coordinate systems . . . 30
  - 3.1.2 Formulation for the power spectral density for the rotor . . . 32
  - 3.1.3 Numerical switch to account for the presence of the boundary layer 40
- 3.2 Results . . . 41
  - 3.2.1 Comparison with experimental results . . . 41

3.2.2 Parameter study of the integral length scale using an isotropic velocity spectrum . . . 45
3.2.2.1 Results without blade-to-blade correlation . . . 45
3.2.2.2 Results with blade-to-blade correlation . . . 47
3.3 Conclusions . . . 48

4 The noise radiated by a flat plate ingesting turbulence near a hard-wall 51
4.1 Analytical formulation . . . 52
4.1.1 Coordinate system . . . 52
4.1.2 Formulation of the power spectral density . . . 53
4.1.3 Formulation for the radiated power of the flat plate . . . 59
4.2 Computational method . . . 62
4.2.1 Investigating the errors introduced due to the grid . . . 64
4.2.2 Computational setup for verification tests . . . 66
4.2.3 Computational setup for the quantification of the assumptions made in the analytical solution . . . 67
4.3 Results . . . 68
4.3.1 Verification of the analytical method using CAA . . . 68
4.3.2 Quantification of the assumptions made in the analytical model using CAA . . . 72
4.3.3 The effect of changing the distance of the aerofoil to the wall. . . . 77
4.4 Conclusions . . . 79

5 Modelling wall-effects in Amiet's rotor noise model 83
5.1 Formulation for the power spectral density of the rotor . . . 84
5.1.1 Coordinate systems . . . 84
5.1.2 Formulation for the power spectral density of a rotor near a hard-wall 85
5.1.3 Formulation for the radiated power in the low-frequency low Mach number limit . . . 90
5.2 Results . . . 96
5.2.1 Comparison with experimental results . . . 96
5.2.2 The effect of the hard-wall . . . 97
5.2.2.1 Without blade-to-blade correlation . . . 97
5.2.2.2 With blade-to-blade correlation . . . 99
5.3 Conclusions . . . 105

6 Modelling anisotropy 107
6.1 Formulation of the 3D axisymmetric anisotropic velocity spectrum . . . 108
6.2 Investigating the effects of anisotropy in a translating aerofoil ingesting anisotropic turbulence . . . 110
6.2.1 The PSD of the sound radiated by a translating aerofoil ingesting turbulence . . . 110
6.2.2 The effect of changing the transverse and axial length scales . . . 111
6.3 Investigating the effect of anisotropy in a rotor ingesting anisotropic turbulence . . . 114
6.3.1 Comparison with experimental measurements . . . 114
6.3.1.1 Comparison of the axisymmetric model spectrum with boundary layer turbulence . . . 115

6.3.2 Coupling the Kerschen and Gliebe turbulence model to Amiet's simplified rotor noise model . . . 120
6.3.2.1 Comparison of the PSD of the acoustic pressure with experimental measurements . . . 120
6.3.3 The effect of anisotropy on the noise radiated by a rotor ingesting anisotropic turbulence . . . 123
6.3.4 Investigating the parameters that affect the blade-to-blade correlation for a rotor ingesting anisotropic turbulence . . . 127
6.4 Conclusions . . . 130

7 Validation of the rotor noise model 131
7.1 Results . . . 132
7.2 Sensitivity study . . . 138
7.3 Conclusions . . . 139

8 Conclusions and future work 141
8.1 Future work . . . 145

Appendix A Derivation of the emission distance and the Doppler factor used in the rotor noise model 147
A.1 Derivation of the emission distance . . . 147
A.2 Derivation of the Doppler factor . . . 148

Appendix B Description of the benchmark case 149
B.1 Extraction of turbulence data from the test case to input into the rotor noise model . . . 149

Appendix C The power factor of a two-dimensional vertical dipole 153

Appendix D Glegg's time-domain formulation for the noise radiated by a rotor ingesting a turbulent boundary layer 155
D.1 Formulation of the PSD of the acoustic pressure . . . 155
D.2 Greens functions terms . . . 157
D.3 Computation of the unsteady loading . . . 158
D.4 The blade loading correlation function . . . 161

Bibliography and references 162

List of Figures

1.1 Various turbo-props with counter rotating propellers. 3

2.1 Potential sources of noise due to the installation of a Counter Rotating Open Rotor (CROR) on an aircraft fuselage. 8
2.2 The various regions of the boundary layer. 9
2.3 The various coherent motions in a boundary layer. 10
2.4 The von Kármán and Liepmann isotropic model spectra. The model spectra are computed using an integral length scale (L) of 0.1 m and a turbulence velocity (u) of $1\,\mathrm{m\,s^{-1}}$. 12
2.5 An example measurement of the Power Spectral Density (PSD) of the noise for a scaled Sevik rotor operating at 2734 RPM in a mean flow of 30 $\mathrm{m.s^{-1}}$ for three different axial angles. The observer is located at a radius of 3.01 m. The arrows depict the Blade Passing Frequencies of the rotor . 23
2.6 The increasing number of cells used in the Computational Fluid Dynamics (CFD) computations of CRORs. 25

3.1 The coordinate systems used in the rotor noise model. 31
3.2 Velocity triangle for the source velocity in the engine-fixed frame. 32
3.3 An eddy moving through the rotor disk. 36
3.4 Contours of the Doppler correction factor ω/ω_ϕ that needs to be applied to account for the rotation of the aerofoil. The Doppler factor is computed for $M_\phi = M_x = 0.1$. 39
3.5 Schematic showing the relative positions of the observer and the rotor blade. 39
3.6 Schematic showing the region where a rotor blade is partially immersed in a turbulent boundary layer. d_{wall} is the distance from the centre of the hub to the wall, R is the distance from the hub centre to blade tip and δ is the height of the boundary layer. 41
3.7 Comparison of the noise spectrum produced using the frequency-domain method with results from experiments. 43
3.8 Contours of the Sound Pressure Level (SPL) for varying observer angles (0° points downstream) and varying frequencies. The dashed lines represent the BPFs of the rotor. 44
3.9 The decay of the SPL for the rotor at $f = 450$ Hz. 44
3.10 The energy spectra for different integral length scales. 46
3.11 Power spectral density of the acoustic pressure at various integral length scale. The arrows are at multiples of the BPF. 47

3.12 Power spectral density of the acoustic pressure at various integral length scales with the correlation between the blades modelled. The arrows are at multiples of the BPF. 48

4.1 A schematic of an aerofoil (modelled as a flat plate) near a wall and its image source. The flat plate has a chord c and is at a height d_{wall} from the wall. The observer is located at (r_0, θ) from the flat plate and at $(r_0^{\#}, \theta^{\#})$ from the image source. 53
4.2 A schematic of an aerofoil (modelled as a flat plate) ingesting turbulence near a hard-wall. 53
4.3 The real and imaginary parts of the second and third terms of the PSD in Equation (4.20). The observer is at 45° and in a free-stream at Mach number 0.1. 57
4.4 Example spectrum for a flat plate ingesting turbulence near a hard-wall. The observer is at 45° and in a free-stream at Mach number 0.1. The red lines represent the peak locations predicted using Equation (4.21). 58
4.5 The directivity of the PSD of the noise and the power ratio in the low frequency low Mach number limit. 61
4.6 The power factor computed using Eqn. (4.31). 62
4.7 The upwash velocity spectra computed at a location $0.02c$ upstream of the aerofoil compared with the analytical upwash velocity spectra. $L_{ref} = 1\,\mathrm{m}$ and $U_{ref} = 1\,\mathrm{ms}^{-1}$. 64
4.8 Details of the grid that was used for the Computational AeroAcoustic (CAA) simulations. 65
4.9 The PSD of the acoustic pressure computed using Amiet's (first term of Eqn. (4.20)) formulation with the velocity spectrum determined analytically (black), determined from the Advanced Digital Filter method and the PSD of the acoustic pressure determined directly from a CAA simulation (green). 66
4.10 The schematic of the CAA simulation used to validate the analytical model. S1 and S2 represent the data collection surfaces for the real and image aerofoils. Using this data collection strategy one can model the analytical solution without using a hard slip-wall boundary condition. . . 67
4.11 The schematic of the physically representative CAA simulation used to test the assumptions made in the analytical model for an aerofoil ingesting turbulence near a hard slip-wall. 68
4.12 Contours of sound pressure level (SPL) as a function of reduced frequency $K = fc/U$ and observer angle θ for analytical (Equation 4.20) (top) and CAA (bottom) predictions. 69
4.13 Spectral plots of SPL and sound PoWer Level (PWL). The wall is located at $d_{wall} = 2c$ and is simulated using the Method of Images (MOI). 71
4.14 Directivity plots of sound pressure level for analytical and CAA simulations at two different reduced frequencies. The wall is located at $d_{wall} = 2c$ and is simulated using the MOI. 72
4.15 Contours of instantaneous non-dimensional pressure $p/(\rho_0 c_0^2)$ for CAA simulations with (right) and without (left) the hard-wall boundary condition. 72

4.16 Contours of sound pressure level as a function of reduced frequency $K = fc/U$ and observer angle θ for analytical (Equation 4.20) (bottom) and CAA (top) predictions. 75
4.17 Spectral plots of SPL and PWL. The wall is located at $d_{wall} = 2c$ and is simulated in the CAA simulation using both the MOI and the hard-wall boundary condition. 76
4.18 Directivity plots of sound pressure level for analytical and CAA simulations at two different reduced frequencies. The green lines indicate the extent of the shadow zone. 78

5.1 The engine-fixed coordinate system for a rotor and its mirror image. . . . 85
5.2 A schematic of one rotor blade at azimuthal angle $(\phi) = 90°$. Setting the stagger angle (α) to $0°$ results in a vertical dipole and setting the stagger angle (α) to $0°$ results in a horizontal dipole. 92
5.3 The low frequency low Mach number power ratio and directivity functions for a vertical and a horizontal dipole. The observer is at a radius $r_0 = 1$ m. 94
5.4 The azimuthally averaged directivity and power ratio. 95
5.5 Comparison of the noise spectrum, for a rotor in the free-field and in the presence of a hard-wall, produced using the frequency-domain method with results from experiments and an analytical time-domain method. . . 96
5.6 SPL directivity computed for a rotor in the presence of a hard-wall and in the free-field. The rotor is operation at 2734 RPM in a mean flow of $30\,\mathrm{m\,s^{-1}}$. The wall is at $d_{wall} = 0.2486$ m and the observer is at $r_0 = 3.01$ m. 98
5.7 The PWL spectra and OASPL for the rotor with and without a hard-wall. The rotor is operation at 2734 RPM in a mean flow of $30\,\mathrm{m\,s^{-1}}$. The wall is at $d_{wall} = 0.2486$ m and the observer is at $r_0 = 3.01$ m. 100
5.8 Individual components of Eqn. (5.11) for PSD of the acoustic pressure with a hard-wall. The observer is at (r_0, θ)=(3.01 m, 45°). 101
5.9 SPL directivity computed for a rotor with blade-to-blade correlation modelled in the presence of a hard-wall and in the free-field. The rotor is operation at 2734 RPM in a mean flow of $30\,\mathrm{m\,s^{-1}}$. The wall is at $d_{wall} = 0.2486$ m and the observer is at $r_0 = 3.01$ m. 102
5.10 SPL directivity computed for a rotor with blade-to-blade correlation modelled in the presence of a hard-wall and in the free-field. The rotor is operation at 2734 RPM in a mean flow of $30\,\mathrm{m\,s^{-1}}$. The wall is at $d_{wall} = 0.2486$ m and the observer is at $r_0 = 3.01$ m. 103
5.11 The PWL spectra and OASPL for the rotor with blade-to-blade correlation modelled with and without a hard-wall. The rotor is operation at 2734 RPM in a mean flow of $30\,\mathrm{m\,s^{-1}}$. The wall is at $d_{wall} = 0.2486$ m and the observer is at $r_0 = 3.01$ m. 104
5.12 PWL spectra for a rotor at varying distances to the hard-wall. The observer is at $r_0 = 3.01$ m. 104

6.1 A schematic of a flat plate ingesting turbulence. 111
6.2 The PSD of the transverse velocity perturbations for varying axial and transverse length scales with $L_{ref} = 1$ m and $U_{ref} = 10^{-6}\,\mathrm{m\,s^{-1}}$ and the PWL spectra for varying axial and transverse length scales. The white lines on the contours of the PSD shows the frequency at which the PSD is a maximum. 112

6.3 The maximum power at various axial and transverse length scales. 113
6.4 The Lumley triangle. The dots represent boundary layer turbulence data obtained from the Fundamental Case 3 (FC3) dataset at zero spanwise separation and zero time lag. The larger dots represent values obtained farther from the wall. 115
6.5 RMS velocities. 117
6.6 One dimensional energy spectra at varying wall-normal locations. Experimental data is extracted from the FC3 dataset. The theoretical 1D spectra are computed using Eqn. (6.23). $L_{ref} = 1\,\text{m}$ and $U_{ref} = 1\,\text{ms}^{-1}$. 118
6.7 The integral length scales computed from experimental data by integrating the normalized correlation curves and using Eqn. (6.31). 119
6.8 The PSD of the acoustic pressure for a rotor operating at the zero thrust operating condition. Predictions are made using the transverse integral length scale obtained from experimental data. The arrows represent the BPFs of the rotor. The observer is located at $r_0 = 3.01$ m and $\theta = 127.3°$ (upstream). 121
6.9 The PSD of the acoustic pressure for a rotor operating at the zero thrust operating condition. The transverse integral length scale is chosen to be $l_t = 0.3$ m. All other variables are extracted from experimental data. The arrows represent the BPFs of the rotor. The observer is located at $r_0 = 3.01$ m and $\theta = 127.3°$ (upstream). 122
6.10 The PSD of the acoustic pressure for a rotor operating at the zero thrust advance ratio. Predictions are computed using the anisotropic velocity spectrum and the isotropic von Kármán spectrum with the eddy speed artificially slowed down. The arrows represent the BPFs of the rotor. The observer is located at $r_0 = 3.01$ m and $\theta = 127.3°$ (upstream). 123
6.11 The PWL spectra for varying length scales and frequencies. The dashed lines indicate the BPFs of the rotor. 124
6.12 The maximum PWL for varying axial and transverse length scales. 125
6.13 A schematic showing the definition of the bandwidth. 125
6.14 The width of the first haystack for varying axial and transverse length scales. The bandwidth is computed at 3 dB below the peak value of the 1^{st} haystack. 126
6.15 The directivity of the rotor for varying axial and transverse length scales. The directivity plots are obtained at a frequency of 455 Hz. 126
6.16 The PWL spectra for varying length scales and frequencies. The dashed lines indicate the BPFs of the rotor. 128

7.1 Schematic of the different microphone locations. 133
7.2 Predictions using Amiet's extended frequency domain rotor noise model and Glegg's time-domain model compared to experimental measurements for the rotor operating at 2734 RPM with a mean-flow speed of $30\,\text{m}\,\text{s}^{-1}$ (OpA). 135
7.3 Predictions using Amiet's extended frequency domain rotor noise model and Glegg's time-domain model compared to experimental measurements for the rotor operating at 2500 RPM with a mean-flow speed of $20\,\text{m}\,\text{s}^{-1}$ (OpB). 137

7.4 Predictions using Amiet's extended frequency domain rotor noise model and Glegg's time-domain model compared to experimental measurements for the rotor operating at 4500 RPM with a mean-flow speed of $30\,\mathrm{m\,s^{-1}}$ (OpC). 138
7.5 The variation of the PSD of the acoustic pressure at one observer location ($r_0 = 3.01$ m, $\theta = 127.3°$). 139

B.1 Configuration of fundamental case three. 150
B.2 The integral length scales, RMS velocities, and normalised correlation functions. The points show the least square fits for each of the variables computed using Eqns. (B.3) and (B.4). The normalised correlation functions are computed at $r/R_{tip} = 0.825$. 152

C.1 A schematic of a point source (S), its image (I), and an observer (O). . . 153

D.1 Coordinate system for the rotor. 156
D.2 The approximate Sears, Kussener, and Amiet response functions at $M = 0.19$. 160

List of Tables

2.1 Timeline showing the various developments of flat-plate response functions and noise propagation theories 14

4.1 Computational parameters used to validate the analytical method. 63
4.2 Parameters for the Gaussian superposition used in the advanced digital filter method. 63
4.3 Computational parameters. 67

7.1 The different advance ratios of the Fundamental Case 3 (FC3). 132
7.2 Microphone positions at which experimental measurements were taken. . 133
7.3 The OverAll Sound Pressure Level (OASPL) from the experimental measurements and Amiet's extended frequency-domain rotor noise model. . . 136
7.4 The OASPL from the experimental measurements and Glegg's time-domain rotor noise model. 136

Declaration of Authorship

I , Ravish Karve , declare that the thesis entitled *Modelling Counter Rotating Open Rotor Installation Noise Sources* and the work presented in the thesis are both my own, and have been generated by me as the result of my own original research. I confirm that:

- this work was done wholly or mainly while in candidature for a research degree at this University;
- where any part of this thesis has previously been submitted for a degree or any other qualification at this University or any other institution, this has been clearly stated;
- where I have consulted the published work of others, this is always clearly attributed;
- where I have quoted from the work of others, the source is always given. With the exception of such quotations, this thesis is entirely my own work;
- I have acknowledged all main sources of help;
- where the thesis is based on work done by myself jointly with others, I have made clear exactly what was done by others and what I have contributed myself;
- parts of this work have been published as:

  1. R. Karve, D. Angland, and J. Gill, An analytical model for predicting rotor broadband noise due to turbulent boundary layer ingestion, in Applied Aerodynamics Conference, Bristol, Jul 2016.
  2. R. Karve, J. R. Gill, F. Gea Aguilera, D. Angland, and T. Node-Langlois, Including Wall Effects in Analytical Leading Edge Noise Predictions, in 23rd AIAA/CEAS Aeroacoustics Conference, AIAA 2017-3198. Denver. American Institute of Aeronautics and Astronautics, Jun 2017.
  3. R. Karve, D. Angland, and T. Node-Langlois, "An analytical model for predicting rotor broadband noise due to turbulent boundary layer ingestion". Submitted to the Journal of Sound and Vibration
  4. R. Karve, D. Angland, and T. Node-Langlois, "Investigating the Effect of Anisotropy in Amiet's Analytical Leading-Edge Noise Model". Submitted to the 24th AIAA/CEAS Aeroacoustics Conference. Atlanta. American Institute of Aeronautics and Astronautics, Jun 2018.
  5. R. Karve, D. Angland, and T. Node-Langlois, Including Wall Effects in Analytical Leading Edge Noise Predictions. Submitted to the International Journal of Aeroacoustics.

.....

Date.....

Acknowledgements

I would like to begin by thanking my supervisor Dr. David Angland. His support and advice during the course of this thesis has been invaluable and is greatly appreciated. I would also like to thank Professor Phil Joseph, Thomas Nodé-Langlois, Dr. James Gill, and Dr. Fernando Gea-Aguilera for their patient discussions and many fruitful ideas. Dr. Fernando Gea-Aguilera also provided the grids that were used for the CAA studies in this thesis.

I would like to next thank the colleagues in our office for the enjoyable lunch sessions that instigated many thought provoking discussions but ultimately failed to solve world peace. I would also like to thank Laura, Hernan, and Vasileos for being excellent friends and making my time during the PhD much more enjoyable.

Finally, I would like to thank my family without whose support this thesis would not be possible. They have provided me with unconditional love, encouragement, and support and I owe them a debt of gratitude that no amount of words will convey. I have written this thesis with Apuma in my heart, and I so wish she could see it.

For Apuma.

Nomenclature

A	Term used to define interference term.	
B	Number of blades.	
b	Blade semi-chord.	m
b_w	Wake half-width	m
$\mathcal{C}$	Correlation distance.	m
c	Blade chord.	m
c_0	Speed of sound.	m
$\mathcal{D}$	Low Mach number low frequency directivity function.	
d	Blade semi-span.	m
d_{wall}	Distance to the wall.	m
E^*	Fresnel integral.	
$\mathbb{E}$	Expected value operator	
$\mathcal{F}$	Function used to specify the axisymmetric anisotropic turbulence model.	
$\mathcal{G}$	Function used to specify the axisymmetric anisotropic turbulence model.	
g	Leading-edge response function.	
G	Green's function.	
H	Hankel function.	
K_i	Vortical wave-number specified by the sifting property of the Dirac delta function.	m^{-1}
k_i	Vortical wave-number.	m^{-1}
k_e	Constant used to specify the von Kármán spectrum.	
k_0	Acoustic wave-number.	m^{-1}
L	Integral length scale.	m
l_a	Axial length scale.	m
$L_{ij}^{(k)}$	Length scale over which the fluctuations in the i and j directions are correlated in the k direction.	m
$\mathcal{L}$	Non-dimensional acoustic lift.	
$\mathcal{L}_{high}$	High-frequency limit of the non-dimensional acoustic lift.	
$\mathcal{L}_{low}$	Low-frequency limit of the non-dimensional acoustic lift.	

l_t	Transverse length scale.	m
$\mathbf{M}_\phi^F$	The Mach number of the source with respect to the fluid.	
$\mathbf{M}_\phi^O$	The Mach number of the source with respect to the observer.	
$\mathbf{n}$	Normal vector	
$\mathbf{O}$	The location of the observer in the engine-fixed frame.	m
p	Acoustic pressure.	Pa
$\mathcal{P}$	Power.	W
$\mathcal{P}_0$	Free-field power.	W
$\mathcal{P}_{ref}$	Reference power.	W
p_{ref}	Reference pressure.	Pa
r_e	Retarded distance to the observer.	m
r_0	Distance to the observer.	m
R_{pp}	Cross-correlation of the acoustic pressure.	m^{-1}
$\mathbf{S}$	The location of the source in the engine-fixed frame.	m
S_{pp}	PSD of the acoustic pressure.	$\mathrm{Pa}^2/\mathrm{Hz}$
S	Sears function	
t	Time.	s
T_0	Blade passage time.	s
T_1	Time between two blades chopping an eddy.	s
$T^\#$	Time between two blades of the image rotor chopping an eddy as heard by the observer.	s
T^{P1}	Time between a blade of the image rotor chopping an eddy and a blade of the real rotor chopping an eddy as heard by the observer.	s
T^{P2}	Time between a blade of the real rotor chopping an eddy and a blade of the image rotor chopping an eddy as heard by the observer.	s
(u, v, w)	Turbulent fluctuating velocity.	$\mathrm{m\,s}^{-1}$
U_X	Chordwise component of the flow speed.	$\mathrm{m\,s}^{-1}$
v_g	Gust upwash velocity.	$\mathrm{m\,s}^{-1}$
v_r	Spatial Fourier transform of the Gust upwash velocity.	$\mathrm{m\,s}^{-1}$
$(\tilde{x}, \tilde{y}, \tilde{z})$	Coordinate system fixed to the blade aligned with the engine.	m
(X, Y, Z)	Coordinate system fixed to the blade aligned with the blade chord.	m
(x, y, z)	Coordinate system fixed to the engine-hub aligned with the engine axis.	m

Greek

α	Blade stagger angle.	deg
β	Compressibility factor.	
δ	Height of the boundary layer.	m
δ_{rj}	Strip width.	m

Γ	Gamma function.	
Ψ	Interference term.	
κ	Acoustic coupling wavenumber.	m^{-1}
μ	Acoustic reduced frequency.	
μ_h	Hydrodynamic reduced frequency.	
Ω	Rotational speed of the rotor.	RPM
ϕ	Azimuthal angle of the blade.	deg
Φ_{vv}	3D Power spectral density of the transverse velocity perturbations.	$\mathrm{m}^5\,\mathrm{s}^{-2}$
$\Phi_{vv}^{(2D)}$	2D velocity spectrum.	$\mathrm{m}^3\,\mathrm{s}^{-2}$
ρ_0	Mean density.	$\mathrm{kg}\,\mathrm{m}^{-3}$
σ	Flow corrected distance to the observer.	m
θ	Axial angle of the observer.	deg
Θ_1	Term used to describe the acoustic lift.	
Θ_2	Term used to describe the acoustic lift.	
Θ_3	Term used to describe the acoustic lift.	
θ_s	Shadow-zone extent.	deg
ω	Angular frequency.	$\mathrm{rad}\,\mathrm{s}^{-1}$
ξ	Non-dimensional wavenumber.	

Subscripts

$(.)_0$	Mean quantity.
$(.)_\phi$	Quantity computed with the source frequency.
$(.)_X$	Value aligned to the X-axis in the blade-fixed frame aligned with the blade chord.
$(.)_x$	Value aligned to the x-axis in the engine-fixed frame.

Superscripts

$()^{\#}$	Quantity corresponding to the mirror source.
$\tilde{(.)}$	Variable non-dimensionalised by the semi-chord.
$(.)^*$	Complex conjugate.
$\hat{(.)}$	Fourier transformed variable.

Acronyms

ACARE	Advisory Council for Aeronautics Research in Europe
AIAA	American Institute of Aeronautics and Astronautics
BPF	Blade Passing Frequency
CAA	Computational AeroAcoustic
CFD	Computational Fluid Dynamics
CROR	Counter Rotating Open Rotor
DES	Detached Eddy Simulations
DNS	Direct Numerical Simulations
FBN	Fan Broadband Noise
FC3	Fundamental Case 3
FWH	Ffowcs Williams and Hawkings
LE	Leading-edge
LEE	Linearised Euler Equations
LES	Large Eddy Simulations
MOI	Method of Images
NASA	National Aeronautics and Space Administration
OASPL	OverAll Sound Pressure Level
PIV	Particle Image Velocimetry
PPW	Points Per Wavelength
PSD	Power Spectral Density
PWL	sound PoWer Level
SPL	Sound Pressure Level
URANS	Unsteady Reynolds Averaged Navier-Stokes Equations

Chapter 1

Introduction

Aviation plays a vital role in today's globalised economy. In 2016, 3.7 billion passengers were transported by airlines across the world. This represents a 175% increase in the number of passengers transported since 2006. This growth is forecast to continue over the coming years driven by a global increase of the gross domestic product [1].

To keep up with this growth in an economically viable and environmentally sustainable manner, Europe is making a concerted and cohesive research effort. In 2001 the Advisory Council for Aeronautics Research in Europe (ACARE) outlined a set of ambitious goals for aircraft companies to target in the Strategic Research Agenda (SRA) [2]. These goals have been subsequently updated in 2011. These updated goals are outlined in Flightpath 2050, Europe's Vision for Aviation [3]. This document targets a 75% reduction in carbon dioxide emissions per passenger kilometre, a 90% reduction in nitrous oxide emissions and a 65% reduction in noise by 2050 [3].

This thesis focuses on the noise produced by aircraft engines. A number of evolutionary engine technologies (for high bypass turbofans) are being investigated in order to meet the Flightpath 2050 goals. These include increasing the overall pressure ratio, turbine entry temperature, and increasing the engines bypass ratio.

Along with the evolutionary changes, radical engine architectures that could lead to a step change in the efficiency and environmental footprint of aircraft engines are being investigated. The introduction of Counter Rotating Open Rotors (CRORs) is one such step change. An open rotor is a gas turbine engine in which the fan is not within the nacelle. When the fan is not enclosed within the nacelle, there can either be a single rotor, i.e. a turboprop, or two contra-rotating propellers.

The CROR is not a new design and has been of interest to aircraft engineers for over 60 years. Early examples of aircraft with counter rotating propellers include the American Chance Vought F4U, Convair R3Y-1, Northrop XB-35, the British Avro Shackleton and the Russian TU-114 as shown in Fig. 1.1. However, most of these early designs were not as efficient as they were expected to be. One reason is evident from the shape of the blades which represented more conventional propeller blades. Current generation prop-fans have a heavily optimised blade shape with high sweep that allows faster more optimal flight speeds. Another reason for the inefficiency of the early generation open rotors was that the gearboxes required for a CROR were considerably more complicated than the ones prevalent at that time. This resulted in significant increases in weight and complexity. This coupled with the wide adoption of jet engines during the second world war meant that CROR technology was not developed further [4; 5; 6]. There was a resurgence in the interest of CRORs in the 1970s due to a sharp rise in oil prices. However, a fall in oil prices in the 1980s combined with the introduction of more stringent noise regulations and the introduction of much quieter high-bypass turbofans lead once again to the loss of interest in the development of CRORs [7].

Due to recent advancements in the fields of aerodynamics and aeroacoustics, CRORs have once again become relevant today. Recent turboprop aircraft include the Antonov An70 and a number of experimental prop-fans from Airbus, Rolls-Royce, Snecma (now called Safran Aircraft Engines), and General Electric.

CRORs offer a significant advantage over a turbofan as they increase the bypass ratio significantly. This is a consequence of the fans not being enclosed within a nacelle. As the diameter of the fans is relatively small compared to a conventional turbofan engine, the rotor imparts significant swirl to the flow. A CROR minimises the performance loss because the second contra-rotating propeller corrects the swirl that is imparted to the propeller wake [8]. This implies a larger propulsive efficiency and also allows for a smaller diameter fan that can be operated at higher rotational speeds. Additional benefits of open rotors include optimal matching of turbine and propeller speeds and the fact that a duct or thrust reverser is not required. Disadvantages of a CROR include additional weight, increased complexity in the gearbox design and a significant increase in noise. Due to the mentioned advantages, fuel consumption can be decreased by up to 35% with the introduction of open rotors [9].

1.1 Aims of the current work

The current project aims to further understand and predict open rotor noise due to the installation of open rotors. There have been a number of semi-empirical analytical models proposed to predict various uninstalled CROR noise sources (for example see Blandeau

(a) Vought F4-U Corsair.

(b) Convair R3Y1.

(c) Tupolev 114.

(d) Northrop YB-25.

Figure 1.1: Various turbo-props with counter rotating propellers [10; 11; 12; 13].

et al. [14; 15], these are discussed in detail in Chapter 2). Installation noise sources have not been investigated as thoroughly.

Installation noise sources are an important contributor to the overall noise produced by an open rotor as the exposed rotor blades can interact with various flow features from the aircraft fuselage or installation pylons, leading to a significant increase in the noise [16]. The current work specifically focuses on one source of installation noise; this source of noise is the noise produced by the leading-edge of the rotor blades due to the ingestion of a turbulent boundary layer. A typical CROR aircraft configuration has the open rotor engine mounted at the rear of the fuselage [16]. In this configuration, the engine is mounted close to the fuselage and can thus ingest large boundary layers that have formed on the fuselage. This is also true for the more unconventional blended wing-body configurations. Additionally, in both of these configurations, the acoustic waves produced by the rotor can reflect off the fuselage and interfere with the acoustic field of the rotor. This could significantly alter the sound radiation characteristics of the open

rotor and increase the Sound Pressure Level (SPL) by up to 6 dB due to the constructive interference of coherent acoustic waves [17].

The goal of this thesis is to develop a semi-empirical rotor noise model that predicts the noise radiated by a rotor ingesting a turbulent boundary layer in proximity to a hard-wall. The semi-empirical rotor noise model that will be used for this study is the simplified rotor noise model of Amiet [18] with blade-to-blade correlation modelled. This model is fast to run and has been shown to produce representative results when used to model the noise produced by subsonic rotors ingesting turbulence. This model will be extended in order to model the turbulent boundary layer ingestion noise source.

The first extension that will be made to the model is the addition of a hard-wall. To model the effect of acoustic waves reflecting off a hard-wall, the Method of Images (MOI) will be used. The MOI is an analytical method in which a reflecting surface is modelled by adding a mirror source. The first aim of this thesis is to test the accuracy of the MOI when used for a translating aerofoil in proximity to a hard-wall. This will be accomplished by running two Computational AeroAcoustic (CAA) simulations. Once the efficacy of the MOI to simulate a hard-wall has been established, it will be implemented in Amiet's [18] rotor noise model to simulate a rotor ingesting turbulence in proximity to a hard-wall.

The second extension that needs to be made is that an anisotropic velocity spectrum must be used to accurately model the turbulence in the boundary layer. The incoming turbulent boundary layer will have elongated turbulent structures in the axial direction. A key characteristic of the noise spectrum of a rotor ingesting a turbulent boundary layer is the appearance of prominent peaks at the Blade Passing Frequency (BPF) of the rotor. This is because multiple blades chop the same coherent structures in the boundary layer. The anisotropy also significantly affects the distribution of energy in the noise spectrum [19]. This thesis will introduce the modified Liepmann spectrum of Kerschen *et al.* [20] in the rotor noise model to characterize the anisotropy. A final extension that needs to be made is that a numerical switch must be introduced in order to model the partial loading of the rotor.

The rotor noise model will be validated using two different datasets. The first is a set of experimental measurements from a test campaign of a model rotor at the Virginia Institute of Technology's stability wind tunnel. The second validation data set will be from predictions of a time-domain rotor noise model. The time-domain rotor noise model is very accurate because it takes as input a 4D time and space varying velocity correlation tensor. Thus, it does not need to model the turbulence in the boundary layer.

1.2 Original contributions

1. Amiet's [21] 2-dimensional leading edge noise model is extended using the MOI to account for a wall using the MOI.

2. The accuracy of the MOI is determined using CAA simulations. This is done by running two CAA simulations. One that models the wall using the MOI and one that models the wall using a hard-wall boundary condition. By comparing the differences between these two simulations and the analytical model, the accuracy of the MOI for predicting broadband noise is ascertained.

3. Amiet's [18] simplified rotational model is extended to model a hard-wall using the MOI. Blade-to-blade correlation is modelled by computing the cross Power Spectral Density (PSD) and accounting for the time difference between two blades of the real/image rotor chopping an eddy.

4. Amiet's [18] simplified rotational model is extended to model anisotropy by introducing an axisymmetric anisotropic turbulence model. The axisymmetric turbulence model is compared to boundary layer turbulence. Additionally, the effect of changing the axial and transverse length scale on the resultant noise spectrum is determined.

A conference paper presenting a re-derivation of Amiet's [18] rotor noise model and a parameter study of the integral length scales has been published at the 2016 Applied Aerodynamics Conference [22]. Items 1 and 2 have been presented at the 23$^{\text{rd}}$ AIAA/CEAS Aeroacoustics Conference [23] and have also been submitted to International Journal of Aeroacoustics. Item 3 has been submitted to the Journal of Sound and Vibration and Item 4 will be presented at the 24$^{\text{th}}$ AIAA/CEAS Aeroacoustics Conference.

1.3 Thesis structure

This thesis presents a frequency-domain rotor noise model that models blade-to-blade correlation, anisotropy and the effect of a hard-wall. The work done in developing this model is presented in the following manner,

- Chapter 2 presents a review of the literature that exists on leading-edge noise. An overview of analytical, experimental, and numerical methods is presented.

- Chapter 3 presents a frequency-domain rotor noise model based on Amiet's [18] simplified rotational model. The frequency-domain rotor noise model is re-derived and a numerical switch is introduced to model the partial loading of a rotor ingesting

a boundary layer. The predictions from this rotor noise model are compared with experimental measurements and it is shown that there are several discrepancies. A parameter study of the integral length scale with and without blade-to-blade correlation is presented to demonstrate how blade-to-blade correlation affects the distribution of energy in the noise spectra.

- Chapter 4 extends Amiet's [21] 2D leading-edge noise theory to include the effect of a wall using the MOI. The accuracy of the MOI is tested using 2 CAA simulations. The first CAA simulation models the wall using the MOI and the second CAA simulation models the wall using a hard-wall boundary condition. The accuracy of the MOI is examined by comparing these two CAA simulations with predictions from the analytical model.

- Chapter 5 uses the MOI to extend Amiet's [18] frequency-domain rotor noise model presented in Chapter 3 to model a hard-wall. Blade-to-blade correlation is also modelled by computing the appropriate cross PSDs.

- Chapter 6 presents the axisymmetric turbulence model of Kerschen and Gliebe [24]. This turbulence model is then used to extend the rotor noise model presented in Chapter 3 to account for anisotropy.

- Chapter 7 presents a comparison of the predictions made using the developed rotor noise model with experimental measurements and predictions from the time-domain model of Glegg [25].

- Chapter 8 presents the conclusions.

Chapter 2

Literature Review

This chapter will provide a literature review of open rotor noise, with a specific focus on leading-edge noise. The main sources of tonal noise in uninstalled open rotor engines are the tonal noise produced by each rotor and the tonal noise that is a result of interactions between the two rotors. These interactions are due to the impingement of the front rotor wakes on the rear rotor and due to the interaction of the tip vortices of the front rotor with the rear rotor [26]. These noise sources are well understood and a number of solutions have been put forward to ameliorate this noise source. These methods include the clipping of the rear rotor to avoid the tip vortex of the front rotor hitting the tip of the rear rotor, a mismatched number of blades for the front and rear rotors to reduce wake impingement, and more recently trailing-edge blowing from the rear rotor in order to manage the front rotor wakes [27]. The main sources of broadband noise in uninstalled open rotor engines are [28],

- The interaction of the front rotor wakes with the blade of the rear rotor.
- The scattering of the boundary layer of each of the rotor blades at the trailing edge.
- Ingestion of atmospheric turbulence by the front rotor.
- Interaction of the tip vortex of the front rotor with the rear rotor.

Installation noise of open rotors is of particular concern as the blades of an open rotor are not enclosed within a nacelle. Because of this various flow features generated by the fuselage of the aircraft or the pylons connecting the engine to the fuselage can interact with the rotor blades. Installed CROR broadband noise can arise due to a variety of sources as shown in Fig. 2.1. The main sources of installation noise that have been identified are,

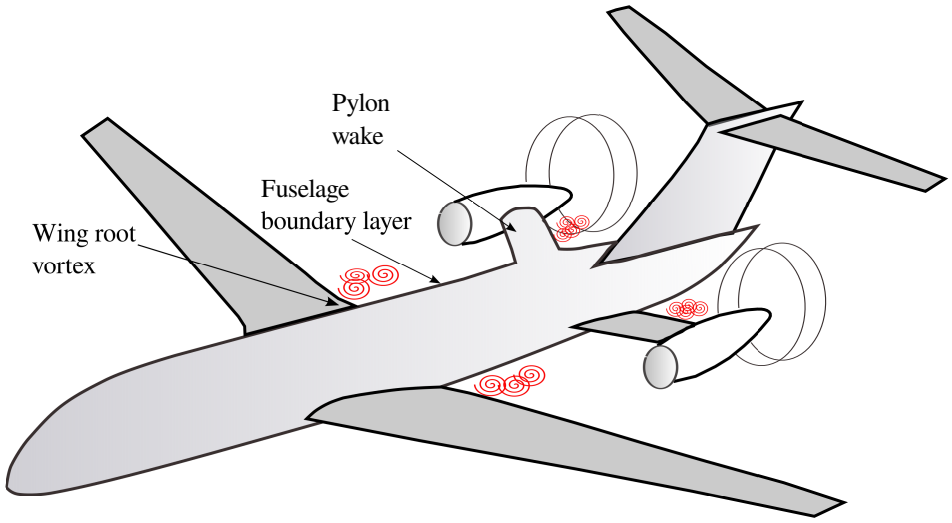

Figure 2.1: Potential sources of noise due to the installation of a Counter Rotating Open Rotor (CROR) on an aircraft fuselage.

- Pylon wake interaction noise: The wake generated by the pylon is ingested by the open rotor.
- Fuselage vortex ingestion noise: Large vortices that form at the wing root could potentially be ingested by the rotor.
- Boundary layer ingestion noise: A large boundary layer develops over the fuselage of an aircraft.

As has been mentioned, the main purpose of this thesis is to study the third source of installation noise, i.e., the ingestion of a boundary layer by an open rotor. The following sections will first detail boundary layer turbulence and various turbulence models. Next, an overview of analytical methods that predict leading-edge noise will be presented. Finally, experimental measurements and numerical simulations of open rotor noise will be detailed.

2.1 Boundary layer turbulence

In this section, an overview of boundary layer turbulence is presented. First, the various regions in the boundary layer are described. Next, a brief description of the various coherent structures present in the boundary layer are described. Finally, various turbulence models are described.

Fully-developed turbulent boundary layers have been extensively studied. Boundary layers are self similar and the mean statistics collapse when appropriately normalised

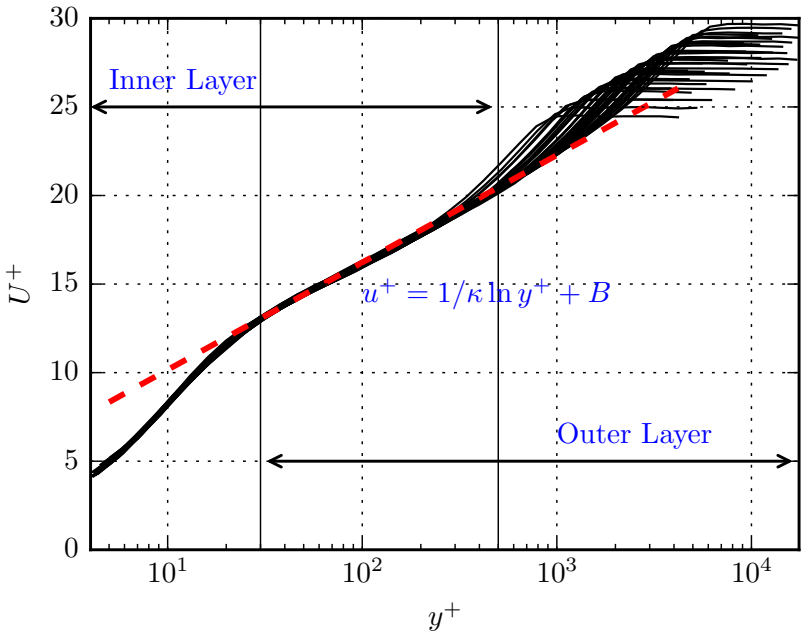

Figure 2.2: Mean velocities normalised by the skin friction velocity ($U^+ = U/u_\tau$) plotted against the wall-normal distance normalised by the skin friction velocity and viscosity ($y^+ = yu_\tau/\nu$). Data taken from experimental measurements of Österlund [30].

as shown in Fig. 2.2. However, due to the complexity of the problem involved many questions regarding the generation of turbulence and its self-similarity at high Reynolds numbers remain [29]. Recent studies at very high Reynolds numbers have found an additional peak in the turbulent kinetic energy and questions have been raised regarding the self similarity of boundary layer turbulence at these Reynolds numbers [29].

Turbulent boundary layers have three distinct regions as shown in Fig. 2.2. The first region is the inner layer and in this region the viscosity (ν) is significant. In the inner layer flow variables can be scaled by the inner variables; the skin friction velocity (u_τ) and the viscosity. The region in which the viscosity plays an important role extends up to $y^+ = 30$ and can be further divided into the viscous sub-layer and the buffer layer. The viscous sub-layer is a region very close to the wall ($y^+ < 5$). In this region very close to the wall only the viscous stresses are important. Slightly further from the wall, in the buffer layer, both the viscous stresses and the shear stresses are important. The second region is the outer layer. In the outer layer the viscosity is no longer an important parameter and the mean velocity determines the physics of the flow. This region is not universal and changes based on the mean velocity of the experiment. The third region is where the inner layer and the outer layer overlap. In this region, both the viscosity and mean flow variables influence the physics of the flow. In the overlap region the mean velocity normalised by the skin friction velocity (U^+) can be determined as a function

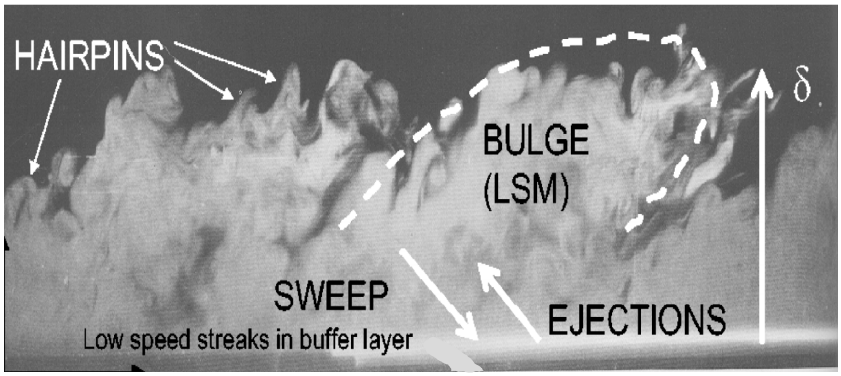

Figure 2.3: The various coherent motions in a boundary layer from Adrian [31].

of the wall normal distance (y) non-dimnesionalised by the wall units (ν/u_τ),

$$U^+ = \frac{1}{\kappa}\ln y^+ + B, \tag{2.1}$$

where κ and B are universal constants.

The characteristics of turbulence that are most significant for acoustic computations are the integral length scales and turbulence intensities. In order to gain a better understanding of the integral length scales of the eddies in the boundary layer a brief overview of the different structures that are present in a boundary layer will now be presented. The main coherent motions that are found in a boundary layer are categorized by Robinson *et al.* [32] as,

- Low-speed streaks in the viscous sub-layer.
- Ejections of low-speed fluid outward from the wall that include the lifting of the low-speed streaks.
- Sweeps of high-speed fluid towards the wall.
- Vortical structures such as horse-shoe vortices that are inclined to the wall [33; 34].
- Sloping near-wall shear layers with locations of high spanwise (parallel to the wall and perpendicular to the flow) vorticity.
- Near wall locations of fluid that are swept away. These regions are referred to as 'pockets'.
- Large-scale outer motions (LSM).

Some of these coherent motions are shown in Fig. 2.3. Of these coherent motions, the structures that are important to understand are the structures in the log layer and the outer layer. This is because the blades of a rotor ingesting a boundary layer are most

likely to pass through these regions of the boundary layer. One of the first studies of the structures was by Head and Bandyopadhyay [33]. They performed flow visualization studies of a zero pressure gradient turbulent boundary layer (using a boundary layer filled with light-oil vapour and illuminating it by an intense plain of light) to show that a majority of the boundary layer was filled with hairpin vortices inclined at 40° to 50° to the wall. A more recent study by Hutchins *et al.* [34] repeated this experiment using stereoscopic Particle Image Velocimetry (PIV) at Reynolds numbers based on the skin friction velocity ranging from 690 to 2800 to visualise the flow. They performed a PIV study using two image planes at 45° and 135° to the streamwise axis. Both studies confirm the existence of hairpin vortices inclined at approximately 45° to the streamwise axis. Hutchins *et al.* [34] have also shown that the spanwise length scales of the boundary layer scale with the height of the boundary layer in the log and outer layer.

From the studies presented above, the eddies that are likely to be chopped by a blade of a rotor ingesting a turbulent boundary layer are hairpin vortices that are inclined to the wall. In a simplified sense these can be considered to be long cylindrical eddies (whose axis is aligned with the mean flow direction) that are being chopped by multiple blades of the rotor. Modelling the inclination of these cylindrical structures is not possible using a simple turbulence model and this could have consequences if strip theory is used to determine the noise radiated by the rotor as the strips will no longer be uncorrelated.

The most common turbulence models that are used for acoustic computations are the isotropic turbulence model of von Kármán and Liepmann. The von Kármán turbulence spectrum models the energy spectrum as [35],

$$E(k) = \frac{55}{9\sqrt{\pi}} \frac{\Gamma(5/6)}{\Gamma(1/3)} \frac{u^2}{k_e^5} \frac{k^4}{\left[1 + \hat{k}^2\right]^{17/6}}, \tag{2.2}$$

where $k_e = \frac{\sqrt{\pi}}{L} \frac{\Gamma(5/6)}{\Gamma(1/3)}$ and $\hat{k}_i = k_i/k_e$, Γ is the Gamma function, u is the turbulence velocity, L is the integral length scale and k is the wavenumber vector. The Liepmann spectrum models the energy spectrum as [36],

$$E(k) = \frac{8}{\pi} u^2 L^5 \frac{k^4}{\left[1 + L^2 k^2\right]^3}. \tag{2.3}$$

Both these model spectra reproduce the Kolmogrov 5/3 decay [37] in the inertial subrange as shown in Fig. 2.4. One of the main differences in the model spectra is that the Liepmann spectrum produces a faster decay at high wavenumbers.

From this discussion of boundary layer turbulence presented above, it is evident that boundary layer turbulence can be significantly anisotropic. Therefore, isotropic model spectra are not suitable to model boundary layer turbulence. A turbulence model that

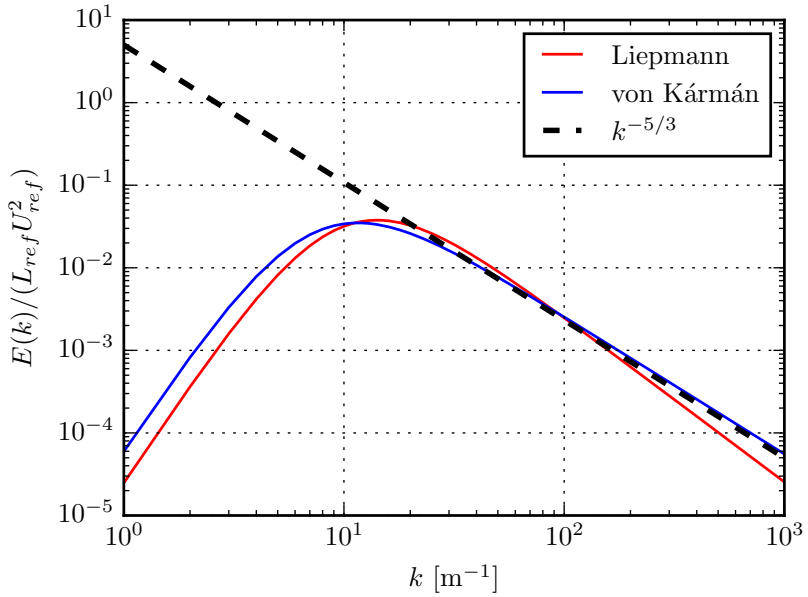

Figure 2.4: The von Kármán and Liepmann isotropic model spectra. The model spectra are computed using an integral length scale (L) of 0.1 m and a turbulence velocity (u) of 1 m s^{-1}.

has been used to model anisotropy for turbulence/leading-edge interactions is the axisymmetric turbulence model of Kerschen and Gliebe [20]. This model is a modified Liepmann spectrum and the model is based on the works of Chandrashekar [38] and Batchelor [39] who determined the appropriate form for the axisymmetric velocity tensor. Further details of this turbulence model are provided in Chapter 6.

2.2 Analytical modelling of leading-edge/turbulence interaction noise

In this section, an overview of the various analytical methods that predict the broadband noise produced due to turbulence leading-edge interactions will be presented. First, an overview of the noise produced due to the interaction of a turbulent gust with the leading-edge of a translating aerofoil will be provided. Then, an overview of analytical models that predict rotor noise due to the ingestion of turbulence will be discussed.

2.2.1 Analytical modelling of leading-edge noise due to translating aerofoils interacting with turbulence

The problem of determining the flat-plate response function for a flat-plate interacting with a two-dimensional sinusoidal gust was first investigated by Sears [40; 41]. Sears

determined the lift force produced by an aerofoil as a result of a sinusoidal gust impacting the leading-edge of the aerofoil. The lift computed analytically by Sears [41] in this thesis is referred to as the Sears function and it appears frequently as the basis of other methods to compute the lift force produced by an aerofoil due to the ingestion of a sinusoidal gust. It was shown that the total lift acts at the quarter chord point and there appears to be no critical frequency that produces a significant increase in the lift force. The formulation of Sears [41] was generalised for the case of finite wings by Liepmann [42]. The formulation of Sears [41] was then extended analytically by Filotas [43] and numerically by Graham [44] to account for oblique gusts. Thus the one-wavenumber analysis of Sears [41] was extended to account for two wavenumbers.

The problem of an aerofoil interacting with a skewed gust is an inherently three-dimensional one. This makes the analysis of the problem complicated. To simplify this Graham [45] developed similarity rules for thin aerofoils. These similarity rules showed that if an incoming oblique gust sweeps the leading-edge of a two-dimensional wing supersonically then the appropriate flat-plate response function to use is the two-dimensional compressible response function. On the other hand, if the gust sweeps the leading-edge of the wing sub-sonically then the appropriate response function to use is the three-dimensional incompressible solution. For aeroacoustic problems, the most efficient radiators of acoustic waves are compressible gusts. It is therefore sufficient to consider only the gusts that sweep the leading-edge of the aerofoil supersonically.

The lift produced by an aerofoil interacting with a skewed gust was developed for an incompressible flow. Amiet [46; 47] extended this method to account for a compressible sinusoidal gust. Amiet's flat-plate response function for a two-dimensional compressible gust is widely used in leading-edge noise models.

With regards to the problem of far-field propagation of sound, one of the first theories that was proposed was the theory of aerodynamic sound of Lighthill [48]. Lighthill [48] reorganised the Navier-Stokes equations into an inhomogeneous wave equation and ignored all source terms except the contributions of the velocity fluctuations which manifest themselves in the sound-field as 'quadrupole' sources. This theory was extended by Curle [49] to account for the presence of solid bodies and subsequently by Ffowcs-Williams and Hawkings [50] to account for solid bodies in arbitrary motion. The reduced form of the Ffowcs Williams and Hawkings (FWH) equation is given by,

$$\left(\frac{1}{c_0^2}\frac{\partial^2}{\partial t^2} - \nabla^2\right) p = \frac{\partial}{\partial t}\Big[\rho_0 \mathbf{U}\cdot\mathbf{n}|\nabla f|\delta(f)\Big] - \nabla\cdot\Big[p\mathbf{n}|\nabla f|\delta(f)\Big], \tag{2.4}$$

where p is the pressure, $f = 0$ represents the surface of a solid body that is moving at velocity U, $\mathbf{n}$ is the surface normal, δ is the Dirac delta function, c_0 is the mean speed of sound and ρ_0 is the mean density. The first term on the right hand side of Eqn. (2.4) is called the thickness noise and is a result of the solid body displacing fluid. The second

TABLE 2.1 Timeline showing the various developments of flat-plate response functions and noise propagation theories

1941	Sears [41] determines an analytical formulation for the pressure jump on a flat-plate due to the impingement of a 2D incompressible sinusoidal gust
1951	Lighthill [48] presents his theory of aerodynamic sound
1955	Curle [49] extends Lighthill's theory of aerodynamic sound to account for the presence of solid surfaces
1965	Lowson [51] determines the sound field of a point force in arbitrary motion
1968	Ffowcs-Williams and Hawkings [50] extend Lighthill's [48] and Curle's [49] theory of aerodynamic sound to account for bodies in arbitrary motion
1969	Ffowcs-Williams and Hawkings [52] determine the sound for rotating dipoles
1969	Filotas [43] determines an analytical formulation for the pressure jump on a flat-plate due to the impingement of a 2D incompressible skewed sinusoidal gust
1970	Graham [44] determines a numerical formulation for the pressure jump on a flat-plate due to the impingement of a 2D incompressible skewed sinusoidal gust
1970	Graham [45] develops similarity rules to link the 3D and 2D pressure jumps depending on the speed at which the gusts sweep the leading-edge
1974	Amiet [46] determines the pressure jump across a flat-plate in the low-frequency limit for 2D compressible flows
1975	Amiet [47] determines the pressure jump across a flat-plate in the high-frequency limit for 2D compressible flows
1989	Amiet [18] determines an approximate method to account for aerofoil rotation

term on the right hand side is called the loading noise and is a result of normal surface stresses due to the pressure distribution. This is the result of the force distribution of the body. The above form is the reduced form as the quadrupole sources consisting of Lighthill's stress tensor and the shear stresses have been neglected as these are usually negligible on the surface of a body.

Most leading-edge noise models thus combine Amiet's [46; 47] response functions with with either Curle's [49] or Ffowcs-Williams *et al.* [50] theories for far-field propagations to determine the noise spectrum.

2.2.2 Analytical modelling of rotor noise

Analytical models of fan noise can broadly be classified into models that take into account potential effects between blades (cascade effects) and models that don't. One of the first rotor noise models was a harmonic model formulated by Gutin [53] for propellers. This was a frequency-domain harmonic method that predicted the tonal noise of propellers. This model was subsequently extended by Hanson to include the effects of thickness, forward flight, and blade sweep [54; 55; 5]. More recently Carazo *et al.* [27] have developed a model to predict CROR tonal noise. They model the rotor blade as a rotating dipole and use an extended version of Amiet's [21] theory that accounts for blade sweep and chord variation with span to determine the unsteady loading of the blade. While they find a good agreement with experimental measurements, the analytical predictions over-predict the sound levels for most of the cases considered.

Recent years have seen turbofan engines with ever increasing bypass ratios accompanied by a reduction in the jet exhaust velocity to maximize efficiency [56]. This has made fan wake/stator interaction noise a dominant source of noise in turbofan engines [57]. As a result of this, a large research undertaking was carried out to understand this noise source. As stators in a turbofan engine have a high solidity, cascade effects can be important. Glegg [58] used a Wiener-Hopf technique to determine an analytical expression for the sound power radiated by a three-dimensional cascade of blades with finite chords when a three dimensional vortical gust impacts their leading-edge.

Posson *et al.* [59; 60; 61] extended this model by providing a closed form expression for the acoustic field in the inter-blade channels as well as the pressure jump on the blades in subsonic flows. Using their extended model Posson *et al.* [59; 60; 61] have shown that cascade effects are of importance only when the blades overlap significantly. Posson *et al.* [61] have used their cascade model to study the noise produced by fan-wakes impinging on the outlet guide vanes of a turbofan engine. They use a strip theory approach with the three-dimensional cascade formulation to compute the pressure jump on the cascade blades. This pressure jump is then fed into a acoustic analogy in an annular duct. They have also investigated the effect of anisotropy in this model and it is found that anisotropy can have a significant effect on the radiated noise. Hanson *et al.* [62] have also modified the cascade solution of Glegg [58] to include the effects of non-homogeneous inflow and have also modelled the lean and sweep of the cascade blade by using appropriate coordinate transformations.

One of the first studies of CROR broadband noise due to rotor wake interaction was by Blandeau *et al.* [14]. They used a Gaussian self-preserving wake based on the models by Wygnanski *et al.* [63] and Jurdic *et al.* [64] to model the wake shed by the front rotor.

The turbulent velocity normal to the blade (v) was modelled as,

$$v\left(\mathbf{X},t\right)=f_w\left(\mathbf{X},t\right)v_w\left(\mathbf{X},t\right), \tag{2.5}$$

where $\mathbf{X}$ is the vector of the spatial coordinates, v_w is a random function that has the same statistics as the wake turbulence and f_w is the wake profile function given by,

$$f_w\left(\mathbf{X},t\right)=\sum_{k=-\infty}^{+\infty}\exp\left\{-\frac{a}{b_w^2}\left(y+kd\right)^2\right\}, \tag{2.6}$$

where a is the empirical wake parameter [1], b_w is the wake half-width, y is the distance normal to the blade in the rotating frame and d is the inter-blade spacing. Eqn. (2.6) therefore represents an infinite train of Gaussian wakes. These wakes are then used in Amiet's [46] formulation to determine the pressure jump on the flat-plate. The noise radiated to the far-field is then computed using the loading term of the Ffowcs-Williams *et al.* [50] equation in the frequency domain.

Another formulation of wake interaction noise was by Kingan [65]. Their formulation predicted uninstalled CROR noise due to rotor/wake interaction and the noise of a CROR due to the ingestion of the wake emanating from an upstream pylon. They used the rotor-wake turbulence interaction of Blandeau *et al.* [15] with the number of blades of the front rotor set to 1 and its rotational seed set to 0. This pylon-wake interaction noise model was subsequently studied by Nodé-Langlois *et al.* [66]. They, however, used Amiet's [18] simplified rotational model to determine the noise. They found good agreement with the predictions of Kingan *et al.* [65] with the added benefit that Amiet's [18] simplified model was considerably faster to run.

Amiet's [18] simplified rotational model uses Lowson's [51] theory of rotating dipoles to determine the noise produced by a rotor ingesting turbulence. The far-field sound pressure (p) of a rotating dipole is [51],

$$p=\frac{1}{4\pi c_0 r^2\left(1-M_n\right)^2}\mathbf{X}\cdot\left(\dot{\mathbf{F}}+\frac{\mathbf{F}\dot{M}_n}{1-M_n}\right), \tag{2.7}$$

where M_n is the component of the Mach number in the direction of the observer, c_0 is the speed of sound, r is the distance to the observer, $\mathbf{X}$ is the position vector, $\mathbf{F}$ is the force vector and variables with a dot above them indicate differentiation with respect to time. Additionally, all terms in Eqn. (2.7) must be evaluated at the retarded time. The main simplifying assumption that is made in the formulation is that the acceleration of the dipole is neglected. This implies that in Eqn. (2.7), $\dot{M}_n$ is negligible. This assumption is based on the fact that for most cases of interest the frequency of the forces generated by the turbulent fluctuations is much larger than the rotational frequency of the rotor.

[1] It is given as 0.637 by Wygnanski *et al.* [63]

The advantage of making this assumption is that the formulation for the noise spectrum of a translating aerofoil can be extended to determine the noise spectrum of a rotating aerofoil by applying an appropriate Doppler correction and averaging the noise spectrum over the azimuth. Various authors [67; 68] have found that this simplification is valid except at very low frequencies.

Amiet's [18] simplified rotational model has been used to study both leading-edge and trailing-edge noise. Sinayoko *et al.* [67], Blandeau [68], and Rozenberg *et al.* [69], have used this method to study trailing-edge noise. Glegg *et al.* [70] and Pagano *et al.* [71] have used it to study leading-edge and trailing-edge noise of wind turbines and open propellers respectively. Blandeau [68] also shows that the directivity function of the simplified rotational model is exactly the same as that of the full rotational model.

Amiet's [18] rotor noise model has also been used by Kucukcoskun *et al.* [72; 73] to model the noise radiated by a rotor in proximity to a hard-wall. Amiet's [18] rotor noise model was extended to account for wall reflections using the Method of Images (MOI). They used the MOI with an extended version of Amiet's [18] simplified rotor noise model, in which near-field effects and the effects of lean and sweep were added, to model the noise radiated by a fan in the presence of a scattering surface. The solutions compared favourably with results from boundary element simulations and from experimental measurements. While including near-field effects makes the model more general it also increases the complexity of the rotor noise model considerably. This, in turn, implies that it is not easy to determine the physics of the noise source by examining the analytical solution. Additionally, the effects of blade-to-blade correlation are neglected.

Paterson and Amiet [74] have also used Amiet's simplified rotor noise model to study the noise radiated by a scale helicopter (having a diameter of 0.76 m) ingesting grid generated and atmospheric turbulence. Amiet's theory was modified to account for anisotropic turbulence. This was accomplished by multiplying the von Kármán velocity spectrum by a constant factor. Additionally, the wave-number in the direction of thrust of the rotor was also multiplied by a constant. This is equivalent to a stretching in the rotor thrust direction and this is approximately equivalent to having the elliptical eddies moving at a slower speed through the rotor disk plane. It was found that this modification is essential to make, as using an isotropic spectrum to predict the radiated noise showed severe discrepancies. The theoretical model with the anisotropic modification predicted sound levels to within 5 dB for a majority of the cases. Using an isotropic model produced discrepancies of up to 25 dB. It should be noted that the turbulence in this experiment was highly anisotropic with $18 < L_{11}^{(1)}/L_{22}^{(1)} < 59$ (this value should be 2 for isotropic turbulence) [2].

[2]The integral length scale is defined as $L_{ij}^{(k)} = \int_0^\infty \frac{\langle u_i(\mathbf{r}) u_j(\mathbf{r}+\mathbf{x}_k)\rangle}{\langle u_i(\mathbf{r}) u_i(\mathbf{r})\rangle} \mathrm{d}\mathbf{x}_k$

To determine the effects of the installation of open rotors one also needs to take into account any scattering geometries that may be present when propagating the pressure jump on a flat-plate to the far-field. As the scattering of sound fields is typically very involved due to the complicated scattering geometries involved, it is usually studied using computational tools such as a boundary element method [72]. However, for simple scattering geometries, the hard-wall can be modelled by modifying the propagation terms using the method of images [17] or by using a tailored Green's function [75]. While the method of images has not been thoroughly investigated for complex non-compact broadband sound fields, there exist studies that have investigated the tonal scattering of fuselage centre bodies. One of the first such studies was by Glegg *et al.* [76]. Glegg's [76] solution was then extended by Kingan *et al.* [75] to include a distributed rotating source.

All of the rotational models that have been discussed until now have been semi-empirical models that require one to model the turbulence using a velocity spectrum. Glegg *et al.* [25] have developed a time-domain rotor noise model to determine the noise produced by a rotor ingesting a turbulent boundary layer that does not require one to model the turbulence. The model convolves a time-varying velocity correlation tensor obtained from experiments with Amiet's [77] time-domain response function to determine the response of a flat-plate. This is used with a Ffowcs-Williams and Hawkings (FWH) *et al.* [50] formulation to determine the far-field noise. This model has the advantage that it does not need to model the complicated physics of the turbulence in the turbulent boundary layer and thus is accurate. However, the velocity correlation data that is required for this model has to be obtained from an experimental study or a time-resolved numerical simulation that is very expensive. Further details of this model are presented in Appendix D. Another model that relies on knowing the turbulent field in advance is the model of Stephens *et al.* [78]. This model uses the same approach as the time-domain model of Glegg *et al.* [25]. However, instead of directly obtaining the velocity correlation data from an experimental data set, polynomial curve fits to experimental data are used.

Most semi-empirical analytical models require a statistical description of the turbulence that is interacting with the aerofoil in order to predict the far-field sound. The two most commonly used model spectra are the turbulence model of von Kármán [37] and Liepmann *et al.* [36] for isotropic turbulence.

2.3 Experimental studies of open rotor noise

In this section, an overview of the experimental studies of open rotors will be presented. This section will explore experimental investigations of leading-edge noise, open rotor noise, and boundary layer ingestion noise.

2.3.1 Experimental investigations of leading-edge noise from translating aerofoils

The first experiments of the noise radiated by an aerofoil due to turbulence interacting with the leading-edge of an aerofoil were by Patterson and Amiet [79; 80]. The authors measured the far-field noise radiated by a NACA 0012 aerofoil in an open-jet anechoic wind tunnel. The tests were conducted at five different velocities ranging from 40-165 $\mathrm{m\,s^{-1}}$ and at 0° and 8° angles of attack. The experimental measurements were compared with the theoretical predictions of Amiet [21]. The experimental measurements showed that this noise mechanism was approximately an order of magnitude higher than the noise produced by the aerofoil alone (trailing-edge noise). It was observed that a majority of the noise is produced from the leading-edge of the aerofoil. While the experimental measurements compared well to the theoretical predictions, an under-prediction at high frequencies was observed at most observer angles. This is attributed to the effect of aerofoil thickness. The under-prediction occurs when the gust wavelength is comparable to the aerofoil thickness in the vicinity of the aerofoil leading-edge. The authors also tested the effect of angle of attack on the noise produced and have found it to have a negligible impact on the radiated noise of the aerofoil.

Recent experimental work on turbulence interaction noise has focused on quantifying the effects of aerofoil thickness, geometry, and angle of attack on the radiated noise. Moreau *et al.* [81] have conducted tests with a 3 % flat-plate, an industrial aerofoil, and a NACA 0012 aerofoil in an anechoic open-jet wind tunnel. The tests were conducted at three velocities ranging from 20.5 to 40 $\mathrm{m\,s^{-1}}$ and five angles of attack ranging from 0° to 15°. They confirmed the findings of Paterson and Amiet [79] and showed that as the aerofoil thickness is increased a larger reduction in noise is observed at higher frequencies. The tests conducted by Moreau *et al.* [81] also showed that the angle of attack had a minor effect on the noise spectrum. They presented three semi-empirical corrections to Amiet's [21] theoretical formulation to account for the effect of angle of attack, thickness and camber. These semi-empirical corrections are yet to be verified for a larger experimental data set.

The negligible angle of attack effects reported by Paterson and Amiet [80] and Moreau *et al.* [81] should be viewed with caution as the experiments were conducted in an open-jet wind tunnel. Measuring angle of attack effects in open-jet wind tunnels is difficult as large angle of attack corrections are required. Moreau *et al.* [81] discuss that this in turn implies a substantial deflection of the jet and distortion of the incoming turbulence thus making it hard to discern angle of attack effects in open-jet wind tunnels.

Davenport *et al.* [82] have conducted experimental measurements of three different aerofoils of varying camber and thickness. They find that while the radiated noise spectrum is not affected by a change in angle of attack of the aerofoil, the aerofoil response function

varies significantly with the angle of attack. These variations are lost when the pressure perturbations are radiated to the far-field due to the averaging of the response function with the turbulence velocity spectrum. From this, it is inferred that changing the velocity spectrum or aerofoil shape could significantly alter the far-field radiated sound. This is verified using the panel method code of Glegg *et al.* [83]. Using this code it is demonstrated that using the anisotropic velocity spectrum of Kerschen and Gliebe [20] a noise increase of 10 dB is observed when the aerofoils angle of attack is changed from 0° to 12°.

However, work done by Gea-Aguilera [84] shows a negligible effect of angle of attack on the radiated noise of an aerofoil ingesting anisotropic turbulence. This could be due to the fact that the method of Gea-Aguilera [84] uses a compressible LEE solver that allows the resolution of higher frequencies (8160 Hz compared to the panel method of Glegg *et al.* which is limited to frequencies below 1000 Hz). The effect of angle of attack was also measured in a closed test section wind-tunnel by Staubs [85]. Their experiments confirmed that the angle of attack has a negligible effect on the noise-radiated to the far-field for isotropic homogeneous turbulence.

PIV flow-field measurements of Chaitanya *et al.* [86] have investigated the behaviour of the mean flow in the vicinity of the aerofoil leading-edge in order to understand the reason for the reduction of noise due to aerofoil thickness. It is found that thin aerofoils have a sharper distortion of the transverse velocity perturbations, which are the main contributors of leading-edge noise [21], around the leading-edge when compared to thick aerofoils. This additional distortion causes a larger suction peak and subsequently a higher radiated noise level.

There have been very few experimental studies that have investigated the effect of the noise radiated by a translating aerofoil in proximity to a hard-wall or an anisotropic/inhomogeneous turbulent flow field. While the experiments listed above had nearly isotropic turbulence generated by grids, they did include a small amount of anisotropy. The experiments listed in this section show that the noise produced due to the interaction of turbulence with an aerofoil is a significant source of noise. While the flat-plate theory of Amiet [21] predicts the radiated noise for thin aerofoils, it significantly over-predicts the noise of thick aerofoils, especially at high frequencies. Aerofoil angle of attack and camber have been shown to have only a minor effect on the radiated noise.

2.3.2 Experimental investigations of open rotor noise

Examples of experimental studies of open rotors focused on determining the noise of rotors due to steady loading, for examples see Hubbard [87] and Succi *et al.* [88]. Insight

into rotor noise was also obtained through experiments that investigated helicopter rotor noise.

Paterson and Amiet [74] studied the noise radiated by a scale helicopter rotor ingesting turbulence of varying intensities. The experimental measurements were compared with theoretical predictions obtained from Amiet's [18] simplified rotor noise model. The experiments of Paterson and Amiet [74] highlight the importance of modelling anisotropy as has already been discussed.

Experiments conducted by Block *et al.* in the 1980s [89; 90; 91; 92] studied the noise produced by single rotors and CRORs with unsteady loading. All of the experiments showed an increase in noise levels for the unsteadily loaded propellers. Block *et al.* [90] compared noise directivity patterns of single and CRORs and found a large increase in noise levels in the axial directions of the CRORs when compared to the single rotor. They also investigated the effect of a pylon wake on the noise produced by a propeller [91]. In this study, they investigated the noise penalties due to pusher versus tractor configurations and have reported a sharp decrease in pusher noise at ninety degrees to the pylon.

Recent investigations by the National Aeronautics and Space Administration (NASA) of open rotors by Horváth *et al.* [93; 94] have used beamforming to study open rotor tonal and broadband noise. In these studies, the dominant tonal and broadband noise sources are localised. It is found that the location of certain tonal noise sources could be off the blade. With regards to broadband noise sources, the location and extent of the leading-edge and trailing-edge noise on the aft rotor is determined for various frequencies.

Experimental campaigns have also recently been carried out by Kingan *et al.* [26] and Parry *et al.* [95] on open rotors designed by Rolls-Royce. Kingan *et al.* [26] studied the relative importance of tonal noise versus broadband noise for three engine designs, one from the 1980s (RIG 140), one from 2008 (RIG 145 build 1) and one design from 2010 (RIG 145 build 2). In all of these engines, it is concluded that broadband noise can be a significant contributor of noise in open rotor engines. Parry *et al.* [95] conducted experiments on the uninstalled configuration of RIG 145 build 1 and RIG 145 build 2. They showed that the aerodynamically optimized blades of RIG 145 build 2 can provide a reduction in noise levels.

Further to the earlier studies of Block *et al.* [91] there have been recent investigations of the installation noise of open rotors. Ricouard *et al.* [96] performed an extensive study of pylon-interaction noise. They tested the pylon at various locations and also tested the effect of pylon trailing-edge blowing on the radiated noise. They show that the pylon significantly affects the harmonics of the front rotor but has a negligible effect on the

interaction noise of the rotors or on the noise of the rear rotor. The pylon trailing-edge blowing is shown to significantly reduce the noise radiated by the front rotor.

A more holistic study of open rotor installation noise was performed by Czech *et al.* [16]. They studied the effect of various aircraft configurations on the installation noise of open rotors. These configurations included the rotors placed in front of the wing, on top of the wing, behind the wing, in a U-tail, and on top of the wing in a blended wing-body configuration. They found that when the open rotor is placed on top of the wing (for both the conventional and blended wing-body configurations) and within a U-tail there was a significant reduction in noise levels.

2.3.3 Experimental investigations of boundary layer ingestion noise

This section will highlight experimental work that has been done to determine the noise radiated by a rotor ingesting a boundary layer.

For the case of a rotor ingesting a turbulent boundary layer a recent comprehensive test campaign at the Virginia Institute of Technology has been undertaken by Alexander *et al.* [97; 19] and Wisda *et al.* [98]. These experiments were run with a 2.25 scale Sevik rotor placed in close proximity to a wall. The incoming boundary layer was measured without the presence of the rotor, i.e., without any distortion. From these measurements a four-dimensional time and space varying velocity correlation matrix was obtained [99]. Alexander *et al.* [97] showed that the broadband noise spectra from these experiments show prominent peaks at the Blade Passing Frequencies, as shown in Fig. 2.5, because multiple rotor blades pass through the same turbulent structures and thus their noise signatures are highly correlated. These frequency peaks that appear in the broadband noise spectrum due to blade-to-blade correlation are referred to as haystacks for the remainder of this literature review. It is also observed that directivity of the rotor is not a simple dipole but has a more complex shape due to the blade twist and due to the presence of the hard-wall underneath the rotor.

A subsequent paper by Wisda *et al.* [98] expanded the previous analysis of Alexander *et al.* [97] by investigating a broader range of rotor operating conditions (13 different advance ratios). The streamwise length scales in this study were determined directly from the eddy passage signature by investigating the pressure data received at a single microphone. The lateral length scales were obtained by integrating under the autocorrelation curve of the pressure. The normalised streamwise length scale was found to have an approximately constant value of $TU_\infty/\delta = 2.5$ for all operating points. The lateral length scales obtained by analysing the autocorrelation of the pressure was found to be $TU_{R=95\%}/\delta = 0.375$. This value was also found to be constant with varying operating points.

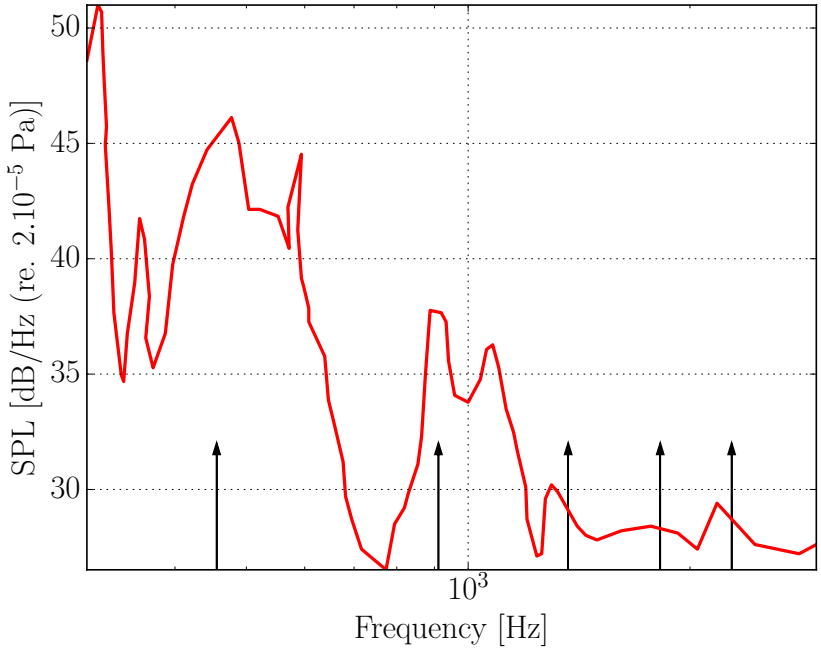

Figure 2.5: An example measurement of the Power Spectral Density (PSD) of the noise for a scaled Sevik rotor operating at 2734 RPM in a mean flow of 30 m.s^{-1} for three different axial angles. The observer is located at a radius of 3.01 m. The arrows depict the BPFs of the rotor [97].

Alexander *et al.* [19] studied the turbulence distortion of a rotor in a rotating reference frame by attaching probes to the blades of the rotor. Four cross-wire probes were attached at different spanwise locations of the leading blade and two cross-wire probes were attached at two different spanwise locations of the trailing blade. The largest blade-blade correlations are found between the cross-wire probes at 95 % of the span of the leading blade and 98.5 % of the span of the trailing-edge blade. This indicates that the eddies in the boundary layer are inclined slightly as has been previously mentioned. While the spanwise coherence is also found to be high, it is seen to start decaying near the BPF. This paper also compares the upwash coherence computed from an undistorted boundary layer using the rapid distortion theory of Glegg *et al.* [100] with the ones computed using the probes on the blade. It is observed that the predictions compare well at low thrust advance ratios and become worse as the advance ratio is decreased (thrust increased).

2.4 Computational modelling of leading-edge noise

While analytical models have been the tool of choice for modelling leading-edge noise, the increase in computing power and simulation technology in the recent decades has seen computational tools become increasingly prevalent. In this section, a brief overview of leading-edge noise and open rotor noise studies using computational tools will be provided.

The main challenge of using computational methods for aero-acoustic problems is the wide ranges of scales that are involved in the problem. The acoustic spectra are generally of interest in the far-field whereas the length scale of the sources that generate the acoustic disturbances are very small. The matter is further complicated due to the fact that only a very small proportion of the energy in the flow gets converted to acoustic disturbances [101]. The two main methods that have been used to simulate leading-edge noise are hybrid methods and Computational AeroAcoustic (CAA) methods that solve the Linearised Euler Equationss (LEEs). More recently solvers that simulate the Lattice Boltzman equations have shown promise. In the following sections each of these three methods will be detailed further.

2.4.1 Simulations of leading-edge noise using hybrid methods

Hybrid methods are the most common methods to predict the noise from large-scale CROR geometries [102]. Hybrid methods use a Computational Fluid Dynamics (CFD) solver to determine the acoustics sources. These source perturbations are then propagated to the far-field using an integral method. The predominant CFD methods that have been used to study open rotors are Unsteady Reynolds Averaged Navier-Stokes Equations (URANS) methods. While URANS methods coupled with the advances in computer technologies can solve large-scale problems they still cannot resolve the smallest scales that are required to predict broadband noise. The CFD techniques that resolve the smaller scales such as Detached Eddy Simulations (DES), Large Eddy Simulations (LES) or Direct Numerical Simulations (DNS) are still too expensive to solve for large-scale problems. Hybrid methods based on URANS simulations are, therefore, limited to predicting tonal noise [103].

The increase in computational resources in recent years has seen the uses of ever-increasing computational domains and resolution as shown in Fig. 2.6. Examples of hybrid methods include studies by Stuermer *et al.* [104] (using the TAU CFD code from DLR), Spalart *et al.* [105] (using the NTS code [113]), Deconinck *et al.* [106] (using the FINE code of NUMECA), and Akkermans *et al.* [114]. Most of these studies have established efficient computational procedures for simulations of large-scale open rotors. These studies have also performed parameter studies of the open rotor blades that show that clipping the rear rotor blades [107] and adjusting the blade counts [105] of the open rotors significantly reduces the tonal noise of the rotors. One study by Akkermans *et al.* [110] has also studied the effectiveness of front rotor trailing-edge blowing on the emitted noise. They used the TAU CFD code of DLR to perform URANS simulation of open rotors. They show that using front rotor trailing-edge blowing reduces all interaction tones except the first interaction tone. This first interaction tone was shown to radiate more strongly due to the front rotor trailing-edge blowing.

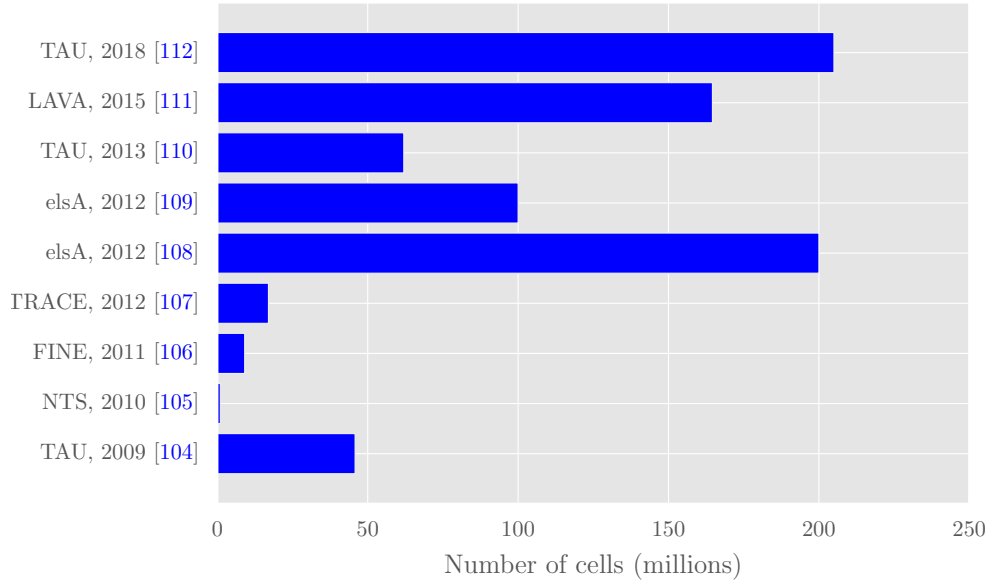

Figure 2.6: The increasing number of cells used in the CFD computations of CRORs. The vertical axis shows the code that was used to run the numerical computation along with the year that the computation was carried out in.

2.4.2 CAA simulations of leading-edge noise

While hybrid methods are the tool of choice for large-scale problems, smaller-scale problems can be solved by computationally solving the LEEs [101]. To accurately solve the LEEs for the human hearing range (20 Hz to 20 kHz), very high fidelity finite-difference solvers are required. High order finite-difference schemes with low dissipation and low dispersion time-stepping are used to ensure that the acoustic perturbations are captured accurately with minimal loss of acoustic energy. Over the years numerous authors have provided increasingly accurate spatial schemes that are highly optimised for parallel computing. Example finite difference schemes that are commonly used in CAA solvers are schemes by Hixon [115], Ashcroft *et al.* [116], and Kim [117; 118].

CAA methods that solve the LEEs must also provide careful treatment at the boundaries of the domain. This is done to ensure that no spurious acoustic reflections from the boundaries re-enter the domain. Non-reflective boundary conditions can be categorized as those that use asymptotic far-field solutions, those that use characteristic methods, and those that use buffer zones. Some CAA codes combine more than one of these methods to provide accurate and effective damping of the acoustic waves [119].

Using the LEEs to model leading-edge noise also requires synthesising turbulence. As no viscosity is included in the LEEs synthetic turbulence must be injected into the domain to model the leading-edge interaction noise. There are a variety of methods that can be used to synthesize turbulence. These methods can be broadly categorised into methods

based on the summation of Fourier modes and methods based on synthetic eddies/digital filters [120].

Fourier mode summations rely on adding harmonic gusts that have the same energy as the turbulence that is to be modelled. It has been shown that as the transverse velocity perturbations are the major contributors to leading-edge noise, Fourier mode methods can accurately predict leading-edge noise by modelling 1-component of the velocity perturbations as shown by Gill *et al.* [121]. Thus the summation of a few Fourier mode components can provide reasonably accurate results at a low computational cost. The Fourier mode technique has been used by Clair *et al.* [122] and Gill *et al.* [123] to study leading-edge noise.

One of the first uses of the digital filter method to solve aeroacoustic problems was by Ewert [124]. The turbulence is synthesized using a random particle mesh (RPM) method that spatially filters white noise to generate a stream function that models a Gaussian turbulence spectrum. This results in a divergence free velocity field that produces no pressure perturbations. The RPM method was used to generate a Gaussian noise spectrum to study slat and trailing-edge noise. The synthetic turbulence method of Ewert [124] was extended by Dieste *et al.* [125] to synthesize turbulence spectra modelled by the Liepmann and von Kármán isotropic energy spectra. Gea-Aguilera *et al.* [126; 84] have used the mathematical background of the RPM method with the numerical implementation of synthetic eddy methods to develop an efficient synthetic turbulence method that is termed the advanced digital filter method. This method does not require the filtering of random white noise and is therefore computationally efficient. The advanced digital filter method is capable of generating isotropic and anisotropic 2- and 3-dimensional velocity spectra. The advanced digital filter method was compared to Fourier mode methods by Gea-Aguilera *et al.* [120] and it was shown that while 1-component Fourier mode methods provide satisfactory results for thin aerofoils, a 2-component Fourier mode method or the advanced digital filter method is required to accurately predict the leading-edge noise radiated by thick aerofoils.

As the size of the problem that can be solved using the LEEs is limited, CAA simulations have been used mostly for canonical studies. These studies mostly focus on validating the assumptions used in the analytical flat-plate models. These assumptions include the fact that the aerofoil is treated as a flat-plate, the aerofoil is assumed to be unloaded (zero angle of attack) and that the mean-flow is assumed to be uniform. Atassi *et al.* [127], Gill *et al.* [123], and Lockhard *et al.* [128] have studied the effects of aerofoil geometry, aerofoil angle of attack and non-uniform mean-flow. Gill *et al.* [123] show that the analytical flat-plate predictions over-predict the noise produced by a NACA 0012 aerofoil by up to 3 dB. They also show that a non-uniform mean-flow is required to accurately predict the noise generated by thick aerofoils. Gea-Aguilera *et al.* [84] have used their advanced digital

filter method to simulate aerofoils in open jet wind tunnels, cascades, and anisotropic turbulence being ingested by wings with wavy leading-edges [129].

2.4.3 Simulations of leading-edge noise using Lattice Boltzman solvers

The Lattice Boltzman (LB) method simulates the macroscopic behaviour of the flow on a lattice. The flow is simulated by modelling the collision of individual gas molecules using kinetic theory. The LB equations can be shown to converge to the weakly compressible Navier Stokes equations [130]. Li and Shan [131] state that there are two main discrepancies in modelling acoustics with the LB method. The first being that the LB method has an error term that is cubic in the Mach number. Secondly, the inclusion of energy conservation for the macroscopic flow has been shown to cause stability problems. Thus the LB method might not be applicable for high Mach number flows. However, recent studies using PowerFLOW (which is a LB method coupled with an LES model) are overcoming these issues and delivering good acoustic predictions for various acoustic sources including turbulence/leading-edge interaction noise [132].

2.5 Conclusions

This chapter has provided an overview of the available literature on leading-edge noise. The literature review has detailed previous work that has been done in analytical modelling, experimental measurements and computational simulations of leading-edge noise of isolated aerofoils and open rotors. From the literature review it is apparent that the full scale numerical simulations of open rotor broadband noise is still not feasible. Aircraft designers must therefore rely on analytical models or experimental measurements. This thesis will focus on the development of an analytical model to predict the noise produced by a rotor ingesting a boundary layer.

The thesis will modify Amiet's [18] simplified rotor noise model by including wall-effects using the MOI. This is similar to the work done by Kucukcoskun *et al.* [72]. However, this thesis will use the far-field formulation of Amiet [18] and will also model blade-to-blade correlation. The use of the far-field formulation will enable the investigation of the physics of the noise source because the resulting formulation is simplified. The MOI will be systematically tested for the simpler case of a 2D aerofoil ingesting turbulence in proximity to a hard-wall using CAA simulations. Modelling blade-to-blade correlation is essential to accurately predict the boundary layer ingestion noise source as more than one blade can chop the same elongated structures in the boundary layer thus resulting in prominent peaks at the BPFs. Additionally, the anisotropic turbulence of the boundary

layer will be modelled using the axisymmetric anisotropic turbulence model of Kerschen and Gliebe [24].

Chapter 3

Amiet's rotor noise formulation

This chapter presents a frequency-domain rotor noise model that will be used to predict the noise radiated from a rotor due to the ingestion of a turbulent boundary layer. The rotor noise model is based on the simplified rotor noise model of Amiet [18]. The model assumes that the acceleration of the rotor blades is negligible as the rotors rotational is much smaller than the frequency of the impinging turbulence.

Amiet's model has been used by several authors to study both the leading and trailing-edge noise of axial fans [71; 133], helicopters [74; 134], pylon wake interaction noise [66], and wind turbines [70]. In order to predict turbulent boundary layer interaction noise, Amiet's [18] formulation needs to be modified. There are three modifications that need to be made to Amiet's simplified rotor model to enable it to predict the noise generated by a rotor ingesting a boundary layer. The first modification is to account for the presence of the hard-wall. The second is to introduce a turbulence model that accounts for the anisotropy of the turbulent boundary layer. The third modification is a numerical switch to account for the partial loading of the rotor since the rotor is only partially immersed in the boundary layer.

Amiet's [18] simplified rotor noise model approximates the rotation of a blade as a series of translations. The noise radiated as a consequence of each translation is computed using Amiet's [21] formulation. The noise radiated is then averaged over all the azimuthal angles to determine the sound radiated by a rotor. This averaged sound field then needs to be frequency corrected twice. The reason that the correction factor needs to be applied twice is that when the Power Spectral Density (PSD) is averaged over the azimuth, there is no relative motion between the source and the observer. This is because the source will spend the same amount of time moving away from an observer as it does moving towards an observer. Thus, there is a Doppler correction factor for the instantaneous PSD (the PSD of the translating aerofoil) and an additional factor to account for the azimuthal averaging of the instantaneous spectrum [18; 135].

This chapter will re-derive Amiet's [18] simplified rotor noise model and present a numerical switch that accounts for the partial loading of the rotor. Amiet's rotor noise formulation will be presented with blade-to-blade correlation modelled.

Using Amiet's simplified rotor noise model with the isotropic von Kármán spectrum a preliminary comparison with experimental results will be presented. Using this comparison, the additional features that need to be added to Amiet's [18] simplified rotational model to accurately predict the boundary layer ingestion noise source will be identified.

Finally, using the von Kármán spectrum a parameter study of the integral length scale of the turbulence is performed with and without blade-to-blade correlation. The results from this study will be used to show how modelling blade-to-blade correlation affects the distribution of energy in the noise spectrum.

3.1 Rotor noise model

In this section, the formulation of the acoustic PSD of a rotor ingesting arbitrary isotropic turbulence is presented. The formulation was proposed by Amiet [21]. The formulation procedure involves the computation of the PSD for a translating aerofoil. This PSD is then corrected by using an appropriate Doppler factor and the result is then averaged over all azimuthal angles. This procedure does not account for the full rotation of the rotor and in doing so neglects acceleration effects. This assumption is valid as long as the rotational frequency of the rotor is much smaller than the frequency of the turbulent structures impinging on the rotors. This lower frequency bound is $f_{low} \simeq \Omega/10$ where Ω is the rotational speed of the blades [135]. As there will be correlation peaks at the Blade Passing Frequency (BPF), this model is applicable for the frequencies of interest and can be used to predict the typical noise frequencies generated by a rotor ingesting a turbulent boundary layer.

3.1.1 Coordinate systems

The coordinate systems used in the derivation are shown in Fig. 3.1. Figure 3.1(a) shows the far-field coordinate system fixed to the engine hub. The mean flow moves in the positive x-direction and the observer is located in the $x-z$ plane at a distance r_0 from the engine hub. The coordinates of the observer ($\mathbf{O}$) in the engine-fixed frame are then given by,

$$\mathbf{O} = (r_0 \cos\theta, 0, r_0 \sin\theta)\,. \tag{3.1}$$

From Fig. 3.2 one can define the source Mach number with respect to the observer to be,

$$\mathbf{M}_{SO} = (0, -M_\phi \cos\phi, -M_\phi \sin\phi)\,, \tag{3.2}$$

and with respect to the fluid to be,

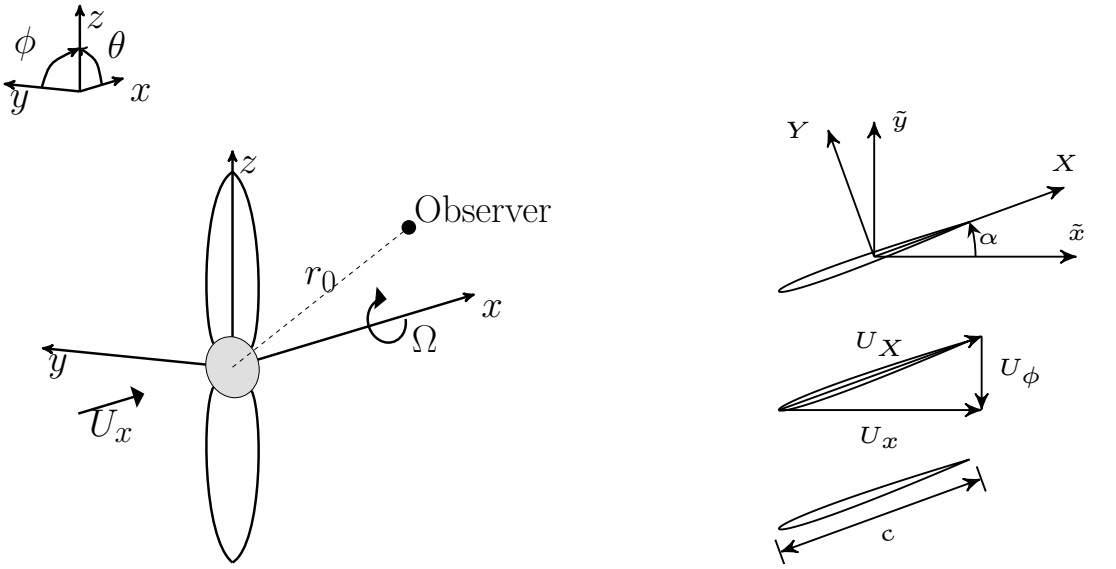

(a) The engine-fixed coordinate system.

(b) The two on-blade coordinate systems.

Figure 3.1: The coordinate systems used in the rotor noise model.

$$\mathbf{M}_{SF} = (-M_x, -M_\phi \cos\phi, -M_\phi \sin\phi)\,. \tag{3.3}$$

This would be the source position when the sound is emitted at a time $t = T_e$. The retarded source position can be determined using the fact that $c_0 T_e = r_e$ as,

$$\mathbf{S} = (r_e M_x, 0, 0)\,. \tag{3.4}$$

The retarded distance to the observer is then given by,

$$\begin{aligned} r_e =& \sqrt{(r_0 \cos\theta - M_x r_e)^2 + r_0^2 \sin^2\theta}, \\ r_e =& \frac{r_0 \left(\sqrt{1 - M_x^2 \sin^2\theta} - M_x \cos\theta\right)}{\beta^2}, \end{aligned} \tag{3.5}$$

where $\beta = \sqrt{1 - M_X^2}$ is the compressibility factor and the retarded observer vector is found as $\mathbf{O'} = \mathbf{O} - \mathbf{S} - \mathbf{M_{SF}} r_e$,

$$\mathbf{O'} = (r_0 \cos\theta, r_e M_\phi \cos\phi, r_0 \sin\theta + r_e M_\phi \sin\phi)\,. \tag{3.6}$$

Using (3.4) and (3.1) in polar coordinates one can define a unit vector in the direction from the retarded source to the observer as,

$$\widehat{\mathbf{SO}} = \frac{(x - r_e M_x, 0, z)}{r_e}, \tag{3.7}$$

where the observer is located at $(x, 0, z)$. Figure 3.1(b) shows a section of unrolled blades at a particular radius from the engine hub. Three coordinate systems have been used, one engine fixed (x, y, z) and two blade fixed coordinate systems $(\tilde{x}, \tilde{y}, \tilde{z})$ and (X, Y, Z). For a blade at azimuthal angle $\phi = \Omega t$ and for a blade segment with stagger angle α the two coordinate systems are related as,

$$\begin{pmatrix} \tilde{x} \\ \tilde{y} \\ \tilde{z} \end{pmatrix} = \begin{bmatrix} 1 & 0 & 0 \\ 0 & \cos\phi & \sin\phi \\ 0 & -\sin\phi & \cos\phi \end{bmatrix} \begin{pmatrix} x' \\ y' \\ z' \end{pmatrix}, \tag{3.8}$$

$$\begin{pmatrix} X \\ Y \\ Z \end{pmatrix} = \begin{bmatrix} \cos\alpha & \sin\alpha & 0 \\ -\sin\alpha & \cos\alpha & 0 \\ 0 & 0 & 1 \end{bmatrix} \begin{pmatrix} \tilde{x} \\ \tilde{y} \\ \tilde{z} \end{pmatrix}. \tag{3.9}$$

The location of the observer in the blade-fixed coordinate system can then be written as,

$$\begin{aligned} X &= r_e \left(\cos\theta\cos\alpha + \sin\theta\sin\phi\sin\alpha\right), \\ Y &= r_e \left(-\cos\theta\sin\alpha + \sin\theta\sin\phi\cos\alpha\right), \\ Z &= r_e \sin\theta\cos\phi. \end{aligned} \tag{3.10}$$

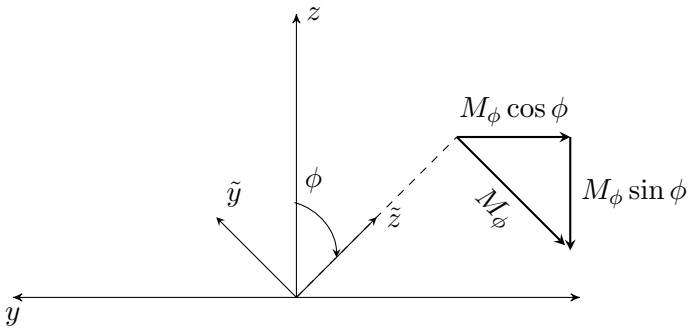

Figure 3.2: Velocity triangle for the source velocity in the engine-fixed frame.

3.1.2 Formulation for the power spectral density for the rotor

The noise produced by an unloaded flat plate encountering a turbulent gust is a well known solution given by Amiet [21]. A single frequency component of the turbulent gust

interacting with the leading edge of the aerofoil is given by,

$$\tilde{v}_g\left(X_C - U_X t, Y, Z\right) = v_R\left(k_X, k_Y, k_Z\right) e^{-\mathrm{i}[k_X(X_C - U_X t) + k_Y Y + k_Z Z]}, \tag{3.11}$$

where v_g is the gust upwash velocity, v_r is the spatial Fourier transform of the gust velocity, (k_X, k_Y, k_Z) define the wavenumber vector and U_X is the chord-wise component of the flow. The pressure jump on the flat plate due to the interaction with this gust is then given by,

$$\Delta p^{(n)}(X, Y, Z, t, k_X, k_Z) = 2\pi\rho_0 U_X v_R(k_X, k_Z) g^{LE}\left(X, k_X, k_Z, M_X\right) e^{\mathrm{i}(k_X U_X t - k_Y Y - k_Z Z)}, \tag{3.12}$$

where g is the non-dimensional gust response function for leading edge interactions. It should be noted that Eqn. (3.12) is different from Amiet's [21] regular formulation as an discrete 'Y' distance is introduced to model blade-to-blade correlation. This distance is the distance normal to the blade and is shown schematically in Fig. 3.3. Eqn. (3.12) is the pressure jump for one gust. The pressure jump for all gust is determined by integrating Eqn. (3.12) over all wavenumbers,

$$\Delta p^{(n)}(X, Y, Z) = 2\pi\rho_0 U_X \iint_{-\infty}^{\infty} v_R(K_X, k_Z) g^{LE}\left(X, K_X, k_Z, M_X\right) e^{-\mathrm{i}(k_Y Y + k_Z Z)} \mathrm{d}k_Y \mathrm{d}k_Z, \tag{3.13}$$

where $K_X = \omega / U_X$[1]. The loading of the blade due to the interaction with this gust can be modelled as a point dipole. For a dipole located at the coordinates (X_C, Z_C) and aligned with the Y-axis, the loading is given by [18],

$$p^{(n)}(X, \mathcal{C}, Z, \omega) = \frac{\mathrm{i}k_0\rho_0 Y}{2\sigma^2} e^{\mathrm{i}[\omega t + \mu(M_X X - \sigma)]} \int_{-d}^{d}\int_{-b}^{b} e^{-\mathrm{i}\mu\left(M_X X_C - \frac{X X_C + \beta^2 Z Z_C}{\sigma}\right)} \times$$
$$\iint_{-\infty}^{\infty} v_R(K_X, k_Y, k_Z) g(X, K_X, k_Z, M_X) e^{-\mathrm{i}[k_Y(n\mathcal{C}) + k_Z Z]} \mathrm{d}k_Y \mathrm{d}k_Z \mathrm{d}X_C \mathrm{d}Z_C, \tag{3.14}$$

where $k_0 = \omega / c_0$ is the acoustic wave number, $\mu = M_X K_X / \beta^2$ is the acoustic reduced frequency, $\sigma = \sqrt{X^2 + \beta^2\left(Y^2 + Z^2\right)}$ is the flow corrected distance to the observer, and d and b represent the half span and half chord of the rotor blade respectively. Additionally, in Eqn. (3.14) the discrete distance $n\mathcal{C}$ has been introduced to represent the normal distance between the 0^{th} and n^{th} blades as shown in Fig. 3.3. The above equation can be developed to obtain the far-field pressure as,

$$p^{(n)}(X, \mathcal{C}, Z, \omega) = \frac{\mathrm{i}\pi k_0\rho_0 Y b}{2\sigma^2} e^{\mathrm{i}\mu(M_X X - \sigma)} \mathcal{L}(K_X, K_Z, \kappa) \int_{-\infty}^{\infty} v_R(K_X, k_Y, K_Z) e^{-\mathrm{i}k_Y n\mathcal{C}} \mathrm{d}k_Y, \tag{3.15}$$

[1] In this thesis the convention of using an upper case wavenumber (K_i) is used when this wavenumber is selected through the sifting property of the Dirac delta function.

where $\kappa = (k_0 (M_X - X/\sigma)) / \beta^2$ is the acoustic coupling wavenumber, $K_Z = \mu_a \beta^2 Z/\sigma$, and $\mathcal{L}$ is the acoustic lift integral defined as,

$$\mathcal{L}(K_X, K_Z, \kappa) = \frac{1}{b} \int_{-b}^{b} g(X_C, K_X, K_Z, M_X) e^{-\mathrm{i}\kappa X_C} \mathrm{d}X_C. \tag{3.16}$$

The acoustic lift integral for gusts at normal incidence ($k_Z = 0$) is defined for a low-frequency regime and a high-frequency regime. The low-frequency limit acoustic lift integral for $\tilde{\mu} < \pi/4$ (quantities with a tilde, $\tilde{(.)}$, indicate quantities non-dimensionalised by the semi-chord) is defined as,

$$\mathcal{L}_{\text{low}}(\kappa, K_X, k_Z = 0) = \frac{1}{\beta} \mathrm{S}(\tilde{\mu}_h) e^{\mathrm{i}\tilde{\mu}_h f(M_X)} \left[J_0 (\tilde{\mu} M_X - \kappa b) - \mathrm{i} J_1 (\tilde{\mu} M_X - \kappa b) \right], \tag{3.17}$$

where $\mu_h = \mu / M_X$, S is the Sears function defined as,

$$\mathrm{S}(\tilde{\mu}_h) = \frac{2}{\pi \tilde{\mu}_h} \frac{1}{H_0^2(\tilde{\mu}_h) - \mathrm{i} H_1^2(\tilde{\mu}_h)}, \tag{3.18}$$

and the function f is defined as,

$$f(M_X) = (1 - \beta) \ln(M_X) + \beta \ln(1 + \beta). \tag{3.19}$$

The acoustic lift integral for the high-frequency regime ($\tilde{\mu} > \pi/4$) is split into two functions $\mathcal{L}_1$ and $\mathcal{L}_2$,

$$\mathcal{L}_{\text{high}}(\kappa, K_X, K_Z = 0) = \mathcal{L}_1(\kappa, K_X, K_Z = 0) + \mathcal{L}_2(\kappa, K_X, K_Z = 0) \tag{3.20}$$

where the function $\mathcal{L}_1$ is defined as,

$$\mathcal{L}_1(\kappa, K_X, K_Z = 0) = \frac{\sqrt{2}}{\pi \beta \sqrt{\tilde{\mu}_h (1 + M_X) \Theta_1}} E^*(2\Theta_1) e^{\mathrm{i}\Theta_2}, \tag{3.21}$$

and the function $\mathcal{L}_2$ is defined as,

$$\begin{aligned} \mathcal{L}_2(\kappa, K_X, K_Z = 0) = & \frac{e^{\mathrm{i}\Theta_2}}{\pi \Theta_1 \beta \sqrt{2\pi \tilde{\mu}_h (1 + M_X)}} \times \\ & \left[\mathrm{i} \left(1 - e^{-2\mathrm{i}\Theta_1} \right) + (1 - \mathrm{i}) \left\{ E^* \left(4\tilde{\mu}\beta^2 \right) - \sqrt{\frac{2\tilde{\mu}}{\Theta_3}} e^{-2\mathrm{i}\Theta_1} E^*(2\Theta_3) \right\} \right], \end{aligned} \tag{3.22}$$

where,

$$\begin{aligned} \Theta_1 &= \tilde{\mu} (1 - M_X) + \kappa b, \\ \Theta_2 &= \beta^2 \tilde{\mu}_h + \kappa b - \frac{\pi}{4}, \\ \Theta_3 &= \tilde{\mu} (1 + M_X) - \kappa b. \end{aligned} \tag{3.23}$$

The noise spectrum with blade-to-blade correlation is determined by computing the cross-correlation of the 0^{th} and n^{th} blade,

$$S_{pp}^{(n)}(X, \mathcal{C}, Z, \phi, \omega) = \frac{\pi U_X}{R} \mathbb{E}\left[p^{(0)}\left(r_0, \theta, \phi, \omega\right)\left(p^{(n)}\left(r_0, \theta, \phi, \omega\right)\right)^*\right]. \tag{3.24}$$

This gives the cross PSD of the acoustic pressure with blade-to-blade correlation modelled as,

$$S_{pp}^{(n)}(X, \mathcal{C}, Z, \phi, \omega) = \pi U_X d \left(\frac{k_0 \rho_0 Y b}{\sigma^2}\right)^2 |\mathcal{L}(K_X, K_Z, \kappa)|^2 \tilde{\Phi}_{vv}^{(n)}(K_X, K_Y, K_Z). \tag{3.25}$$

where,

$$\tilde{\Phi}_{vv}^{(n)}(K_X, K_Y, K_Z) = \int_{-\infty}^{+\infty} \Phi_{vv}(K_X, k_Y, K_Z) e^{-\mathrm{i}k_Y n\mathcal{C}} \mathrm{d}k_Y, \tag{3.26}$$

and the transverse velocity spectrum $\Phi_{vv}(k_x, k_y, k_z)$ is defined as,

$$\Phi_{vv}(k_X, k_Y, k_Z) = \frac{\pi^2}{Rd} \mathbb{E}\left[v_R\left(k_X, k_Y, k_Z\right) v_R^*\left(k_X, k_Y, k_Z\right)\right]. \tag{3.27}$$

Eqn. (3.25) and (3.26) represent the cross-correlation of the acoustic pressures of two blades of a rotor. The above formulation becomes Amiet's [21] classical PSD when $n = 0$. The cross-correlation between the 0^{th} and the n^{th} blade (which is at a distance $n\mathcal{C}$ from the 0^{th} blade) is modelled by the introducing a wavenumber that is perpendicular to the chord. This correlation wavenumber, K_Y, is determined from the kinematics of the eddy chopping process as explained below.

To account for multiple blade passes the cross-correlation function of the acoustic pressure of the 0^{th} blade and the n^{th} blade can be defined as [18],

$$R_{pp}(x, y, \tau) = \sum_{n=-\infty}^{+\infty} R_{pp}^{(n)}(x, y, \tau - nT), \tag{3.28}$$

where nT is the time between eddy chops as heard by the observer. This time is determined next.

Fig. 3.3 shows a schematic of two consecutive blades in a blade row. The blades are separated by the inter-blade spacing $s_b = U_\phi T_0$ where $T_0 = 2\pi/B\Omega$. In the reference frame fixed to a rotor blade, the eddy is moving parallel to the chord at a speed $\sqrt{U_x^2 + U_\phi^2}$. The time between eddy chops (T_1) by two consecutive blades is then given by,

$$T_1 = \frac{s_b \sin\alpha}{\sqrt{U_x^2 + U_\phi^2}} = \frac{U_\phi^2 T_0}{U_x^2 + U_\phi^2}, \tag{3.29}$$

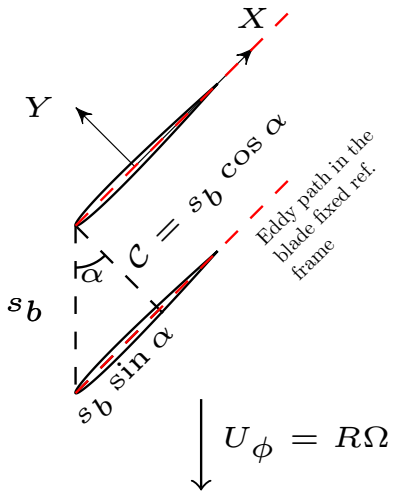

Figure 3.3: An eddy moving through the rotor disk.

where the fact that the blade is unloaded (see Fig. 3.1(b)) is used to determine $\sin\alpha = U_\phi/\sqrt{U_x^2 + U_\phi^2}$. In Eqn. (3.25) a blade-normal wavenumber K_Y has been introduced to model blade-to-blade correlation. The effective wavelength for this wavenumber is then the perpendicular distance between the consecutive blades given by,

$$\mathcal{C} = s_b \cos\alpha = \frac{U_x U_\phi T_0}{\sqrt{U_x^2 + U_\phi^2}}. \tag{3.30}$$

The time between the eddy chops, as heard by the observer, is the time T_1 plus the time difference for the acoustic wave to propagate from the second blade to the observer and from the first blade to the observer. The time taken for the acoustic wave to travel from the first blade to the observer is given by the far-field approximation of the phase radius [136] divided by the wave-speed,

$$\tau_0 = \frac{M_X X - \sigma}{c_0 \beta^2}. \tag{3.31}$$

The time taken for an acoustic wave to travel from the second blade to the observer is then obtained by replacing Y in Eqn. (3.31) with $Y + \mathcal{C}$. The time between blade chops as heard by the observer is then given by,

$$T = T_1 - \frac{\mathcal{C}Y}{c_0 \sigma}. \tag{3.32}$$

This is the time between eddy chops as heard by the observer from the real rotor.

The next step in determining the PSD for a rotating aerofoil is to apply an appropriate

Doppler correction and subsequently, average the PSD over all azimuthal angles in order to determine the noise spectrum of the rotating aerofoil. There are two frequencies to consider in the problem, ω is the angular frequency at the source with no relative motion between the blade and the observer and ω_ϕ which is the Doppler shifted frequency that takes into account the motion between the source and the observer.

To determine the correct Doppler factor consider a fixed observer feels a pressure p with perceived frequency ω and an observer moving relative to the source feels a pressure p_ϕ and a perceived frequency ω_ϕ [135],

$$p(t) = e^{-\mathrm{i}\omega t}, \quad p_\phi(t) = e^{-i\omega_\phi t}. \tag{3.33}$$

The two pressures can then be related as,

$$p_\phi(t) = e^{-\mathrm{i}(\frac{\omega_\phi}{\omega}\omega)t} = p\left(\frac{\omega_\phi}{\omega}t\right). \tag{3.34}$$

In a similar manner the auto-correlation of the fixed pressure signal (R_{pp}) and moving observers ($R_{pp}^{(\phi)}$) can be computed as [135],

$$\begin{aligned} R_{pp}^{(\phi)}(t) &= \lim_{T\to\infty}\frac{1}{2T}\int_{-T}^{T} p_\phi(\tau)p_\phi(t-\tau)\mathrm{d}\tau = \lim_{T\to\infty}\frac{1}{2T}\int_{-T}^{T} p\left(\frac{\omega_\phi}{\omega}\tau\right)p\left(\frac{\omega_\phi}{\omega}(t-\tau)\right)\mathrm{d}\tau, \\ &= \lim_{T\to\infty}\frac{1}{2T}\frac{\omega}{\omega_\phi}\int_{-aT}^{aT} p(\tau')p\left(\frac{\omega_\phi}{\omega}t-\tau'\right)\mathrm{d}\tau' = R_{pp}\left(\frac{\omega_\phi}{\omega}t\right). \end{aligned} \tag{3.35}$$

From this the spectrum can be computed by taking the Fourier transform of the auto-correlation [135],

$$\begin{aligned} S_{pp}^{\phi}(\omega_\phi) &= \int_{-\infty}^{+\infty} R_{pp}^{\phi}(t)e^{\mathrm{i}\omega_\phi t}\mathrm{d}t = \int_{-\infty}^{+\infty} R_{pp}\left(\frac{\omega_\phi}{\omega}t\right)e^{\mathrm{i}(\frac{\omega_\phi}{\omega}\omega)t}\mathrm{d}t \\ S_{pp}^{\phi}(\omega_\phi) &= \frac{\omega}{\omega_\phi}S_{pp}(\omega). \end{aligned} \tag{3.36}$$

The correction that needs to be applied is then ω/ω_ϕ, where ω is the frequency for the fixed observer and ω_ϕ is the frequency as perceived by a moving observer. However, this correction factor needs to be applied twice [18; 135]. The reason that the correction factor needs to be applied twice is that when the PSD is averaged over the azimuth, there is no relative motion between the source and the observer. This is because the source will spend the same amount of time moving away from an observer as it does moving towards an observer. Thus, there is a Doppler correction factor for the instantaneous PSD (the PSD of the translating aerofoil) and an additional factor to account for the azimuthal averaging of the instantaneous spectrum [18; 135]. The PSD for the rotor is then given

by,

$$S_{pp}(\omega) = \frac{1}{2\pi}\int_0^{2\pi}\left(\frac{\omega}{\omega_\phi}\right)^2 S_{pp}^{\phi}(\omega_\phi,\phi)\mathrm{d}\phi, \tag{3.37}$$

where,

$$\frac{\omega}{\omega_\phi} = \left(1 + \frac{\mathbf{M}_\phi^O.\widehat{SO}}{1-\mathbf{M}_\phi^F.\widehat{SO}}\right), \tag{3.38}$$

where $\mathbf{M}_\phi^O$ is the Mach number of the source relative to the observer and $\mathbf{M}_\phi^F$ is the Mach number of the source relative to the fluid. From Fig. 3.2 the unit vector of the source velocity is $(0, -\cos\phi, \sin\phi)$ and the source unit vector is $(\cos\theta, 0, \sin\theta)$. Thus, (3.38) can be written as,

$$\begin{aligned}\frac{\omega}{\omega_\phi} &= 1 + \frac{(z/r_e)M_\phi \sin\phi}{1 - M_x^2 - (xM_x + zM_\phi\sin\phi)/r_e},\\ \frac{\omega_\phi}{\omega} &= 1 + M_\phi\frac{\sin\theta\sin\phi}{\sqrt{1-M_x^2\sin^2\theta}},\end{aligned} \tag{3.39}$$

where $M_\phi = R\Omega/c_0$. The full derivation of this Doppler factor is provided in Appendix A.

The variation of the Doppler factor with azimuthal angle ϕ and axial angle θ is shown in Fig. 3.4. From this figure it can be seen that the Doppler factor is larger than one when $0° < \phi < 180°$ and $180° < \theta < 360°$ or when $180° < \phi < 360°$ and $0° < \theta < 180°$. The first case represents the observer in the bottom half of the xz plane and thus the Doppler factor is greater than one when the blade is moving towards the observer or when $0° < \phi < 180°$ as shown in Fig. 3.5(a). Similarly, the second case represents the observer in the top of the xz plane and thus the Doppler factor is larger than one when the blade is moving towards the observer or when $180° < \phi < 360°$ as shown in Fig. 3.5(b).

The acoustic spectrum can now be determined for multiple blade passages by taking the Fourier transform of Eqn. (3.28)[18],

$$S_{pp}(r_0,\theta,\phi,\omega) = \sum_{n=-\infty}^{\infty} S_{pp}^{(n)}(r_0,\theta,\phi,\omega)e^{\mathrm{i}n\omega T}. \tag{3.40}$$

Therefore, the cross PSD for a rotor with blade-to-blade correlation can be modelled as,

$$S_{pp}(r_0,\theta,\phi,\omega) = \sum_{j=1}^{l}\sum_{n=-\infty}^{\infty}\frac{2\pi}{\mathcal{C}}\frac{\pi B U_{X,j}\delta r_j}{2}(k_0\rho_0 b_j)^2\left\{\frac{(Y|\mathcal{L}|)^2}{\sigma^4}\Phi_{vv}\left(K_X, K_{Y,j,n}\right)\right\}, \tag{3.41}$$

where K_Y is given by,

$$K_{Y,n} = \frac{\omega T + 2\pi n}{\mathcal{C}}. \tag{3.42}$$

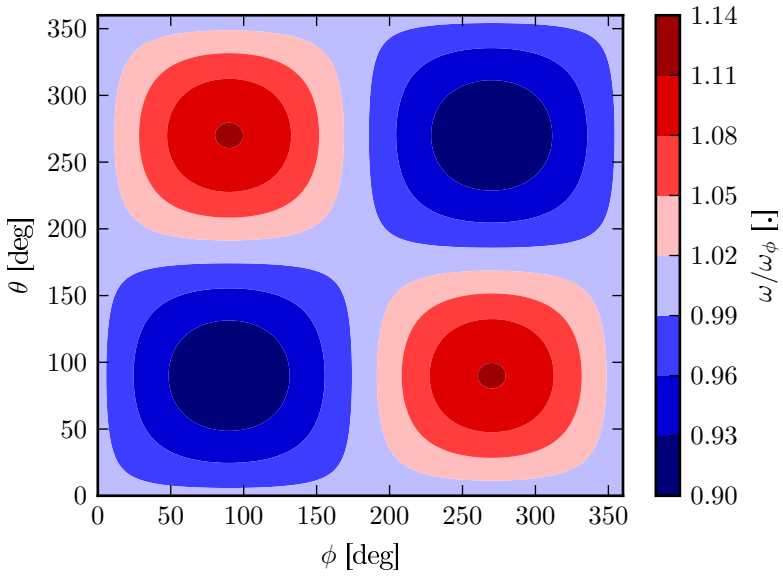

Figure 3.4: Contours of the Doppler correction factor ω/ω_ϕ that needs to be applied to account for the rotation of the aerofoil. The Doppler factor is computed for $M_\phi = M_x = 0.1$.

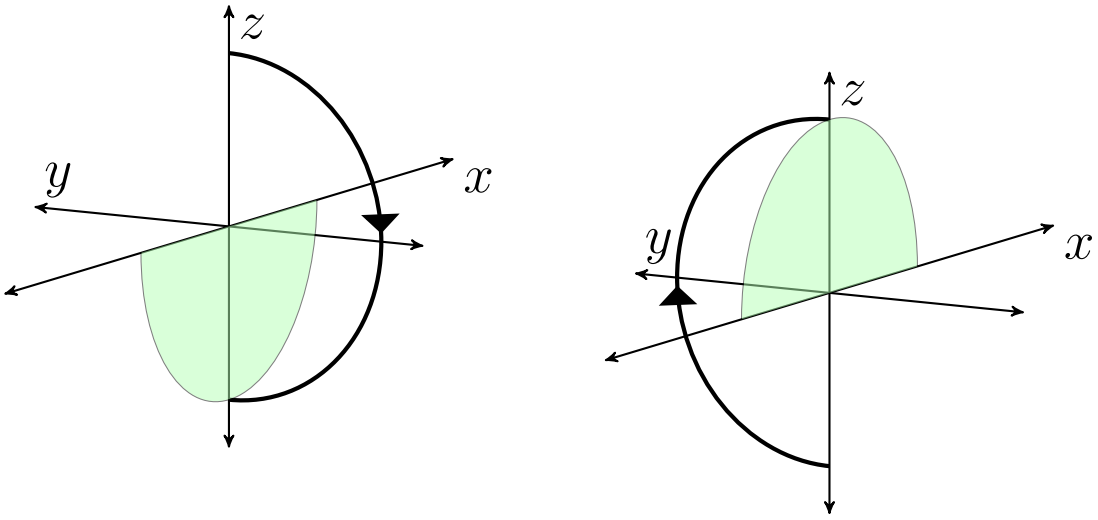

(a) The observer located between $180° < \theta < 360°$ (shaded green region) with the blade moving towards the observer for $0° < \phi < 180°$.

(b) The observer located between $0° < \theta < 180°$ (shaded green region) with the blade moving towards the observer for $180° < \phi < 360°$.

Figure 3.5: Schematic showing the relative positions of the observer and the rotor blade.

Equation (3.41) and (3.37) give the cross PSD of a rotor ingesting turbulence with blade-to-blade correlation modelled. In Eqn. (3.41) strip theory has been used to sum the sound pressure at l span-wise locations with each strip having a width δr_j. This strip theory is valid as long as the width of the span is much larger than the span-wise correlation length [137]. The effect of the skewed gusts has been neglected. This implies that in the coordinate system fixed to the blade, the span-wise wavenumber, k_Z is set to zero.

In Eqn. (3.41) any potential interaction between blades is neglected and the response of each blade is computed assuming that this response is not affected by the adjacent blades. This assumption would not be valid if the blade-normal acoustic wavelength of the impinging gust was larger than the inter-blade spacing. This is a valid assumption to make for open rotors that usually have a low solidity. However, if this model were to be used for rotors with high solidity this interaction would have to be accounted for. A cascade model would be more suitable in this case. Additionally, Blandeau *et al.* [15] have compared a rotor noise model with and without cascade effects for an open rotor. Cascade effects are shown to have a minor impact on the resulting acoustic spectra. Next the PSD of the translating aerofoil developed above will be extended to model rotational effects.

Using the above formulation, the cross PSD of a rotor fully immersed in a wake can be computed. However, for the boundary layer ingestion noise source, the rotor will encounter turbulence for only certain parts of its rotation. To account for this a numerical switch was developed. This numerical switch is described next.

3.1.3 Numerical switch to account for the presence of the boundary layer

The formulation presented above details the computation of the cross PSD for a rotor ingesting turbulence. Amiet's formulation must be modified to account for the fact that the blade will encounter the turbulence of the boundary layer only in certain parts of its rotation. To account for this, a numerical switch is implemented that switches the turbulence off when a rotor blade is not in the boundary layer. The geometry of the blade entering the boundary layer is shown in Fig. 3.6. The azimuthal angles between which the blades will encounter turbulence in the boundary layer are given by,

$$\pi - \cos^{-1}\left[\frac{d_{wall}-\delta}{R}\right] < \phi < \pi + \cos^{-1}\left[\frac{d_{wall}-\delta}{R}\right], \tag{3.43}$$

where d_{wall} is the distance from the hub centre to the wall, δ is the height of the boundary layer and R is the tip radius of the rotor. Additionally, when the blade is in the turbulence only part of its span will interact with the turbulence. Thus, the sound pressure must be computed for only a few strips. The span of the blade that is immersed in the boundary layer is given by,

$$b_I = R - \frac{d_{wall}-\delta}{\cos(\psi-\gamma)}, \tag{3.44}$$

where b_I is the length of span immersed in the boundary layer, γ is the azimuthal angle traversed by the blade in the boundary layer and $\psi = \cos^{-1}\left[(d_{wall}-\delta)/R\right]$.

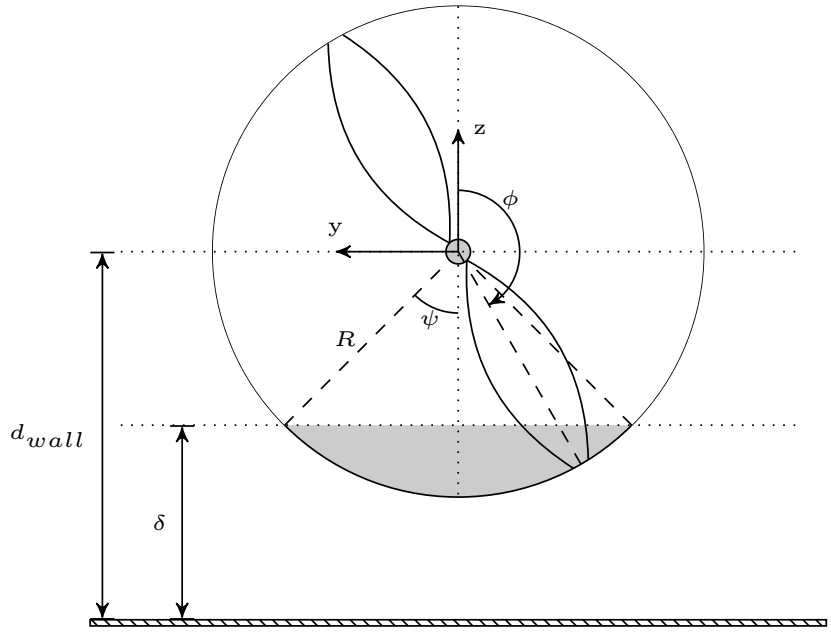

Figure 3.6: Schematic showing the region where a rotor blade is partially immersed in a turbulent boundary layer. d_{wall} is the distance from the centre of the hub to the wall, R is the distance from the hub centre to blade tip and δ is the height of the boundary layer.

3.2 Results

This section presents initial results using Amiet's [18] rotor noise model with the isotropic von Kármán spectrum. Using the isotropic von Kármán spectrum the effect of changing the integral length scale is investigated and it is shown that including blade-to-blade correlation changes the distribution of energy in the spectrum.

The results are compared to experimental measurements that were provided with the Fundamental Case 3 (FC3) of the 2015 American Institute of Aeronautics and Astronautics (AIAA) Fan Broadband Noise (FBN) workshop [138]. The inputs required to specify the PSD of the transverse velocity perturbations are taken from a 4D space and time-varying velocity correlation tensor of the undistorted boundary layer. The rotor geometry and the turbulence properties extracted from this dataset are detailed in Appendix B.

3.2.1 Comparison with experimental results

In this section initial predictions using the rotor, noise model are compared with experimental measurements. The initial predictions are computed with the isotropic von-Kármán spectrum used to model the PSD of the transverse velocity perturbations. For the predictions with blade-to-blade correlation a blade normal wavenumber is introduced

and therefore a 3D isotropic von Kármán spectrum is used,

$$\Phi_{vv}(k_X, k_Y, k_Z) = \frac{55}{36\pi^2}\frac{u^2 L}{k_e^2}\frac{\hat{k}_X^2 + \hat{k}_Z^2}{\left[1 + \hat{k}_X^2 + \hat{k}_Y^2 + \hat{k}_Z^2\right]^{17/6}}, \tag{3.45}$$

where $k_e = \frac{\sqrt{\pi}}{L}\frac{\Gamma(5/6)}{\Gamma(1/3)}$ and $\hat{k}_i = k_i/k_e$. For the predictions without blade-to-blade correlation the isotropic von Kármán spectrum is integrated over k_Y to get,

$$\Phi_{vv}(k_X, k_Z) = \frac{4}{9\pi}\frac{u^2}{k_e^2}\frac{\hat{k}_X^2 + \hat{k}_Z^2}{\left[1 + \hat{k}_X^2 + \hat{k}_Z^2\right]^{7/3}}, \tag{3.46}$$

in both cases the span-wise wavenumber k_Z is set to zero. The von Kármán spectrum requires as input an integral length scale and turbulence intensity. The integral length scale used for this study is the axial length scale ($L_{11}^{(1)}$) obtained from Eqn. (B.3). The turbulence velocity is computed as,

$$u^2 = \frac{1}{3}\left[u_e^2 + v_e^2 + w_e^2\right], \tag{3.47}$$

where the values of (u_e, v_e, w_e) are obtained from Eqn. (B.4). Values for the integral length scale and turbulence velocity are obtained as a function of wall-normal distance. This is because boundary layer turbulence is not homogeneous in the wall-normal direction and thus the properties of the turbulence change with changing wall-normal distance.

Fig. 3.7 shows the frequency-domain method prediction with blade-to-blade correlation compared to the experimental measurements of Glegg *et al.* [25] where the Sound Pressure Level (SPL) is computed as,

$$\mathrm{SPL} = 10\log_{10}\left(\frac{4\pi S_{pp}(r_0, \theta, \omega)}{p_{ref}^2}\right), \tag{3.48}$$

where $p_{ref} = 2 \times 10^{-5}$ Pa. A factor of 2π has been added to obtain results in Hz instead of rad.s^{-1} and an additional factor of 2 has been added to obtain the one sided spectrum.

The integral length scale and turbulence intensities used for these predictions are computed using Eqn. (B.3). The rotor is operating at the zero thrust condition. This corresponds to a rotor speed of 2734 RPM and a mean flow speed of 30 m s^{-1}. The observer is located at (r_0, θ)=(3.01 m, 127.3°). This operating condition is chosen as it is the zero thrust operating condition and therefore the incoming boundary layer is not distorted significantly as it is at higher thrust operating conditions. The results are compared at this particular microphone location because a majority of the published results for the FC3 case are published for this microphone location. The speed of sound and mean density used in the computations are 350 m s^{-1} and 1.05 kg m^{-3} respectively. The computations for the rotor noise model are computed using 200 azimuthal integration points and 10

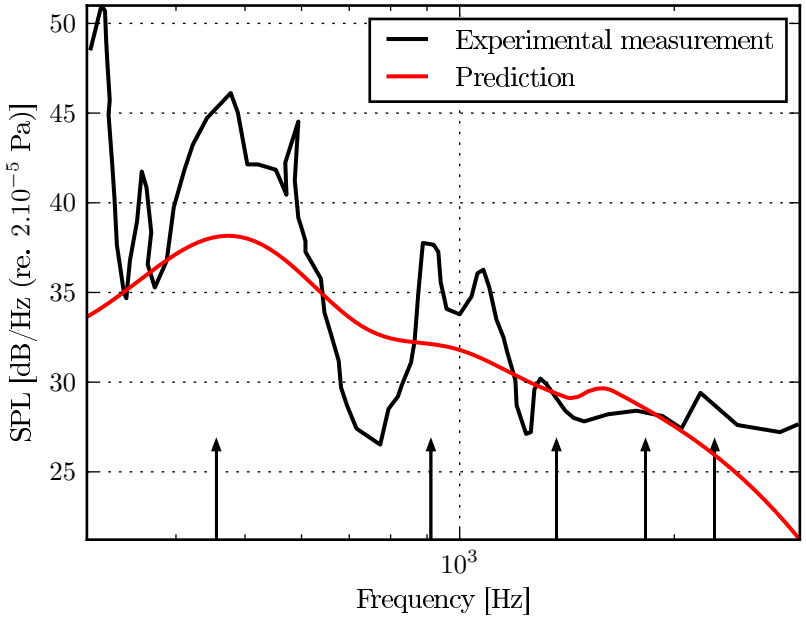

Figure 3.7: Power spectral density of the acoustic pressure compared with experimental results from Glegg *et al.* [139]. The arrows represent the BPFs of the rotor. The observer is located at (r_0, θ)=(3.01 m, 127.3°).

span-wise strips. The strips are logarithmically spaced so that the tip of the blade has a larger density of strips.

It can be seen that the frequency-domain solution predicts the experimental results of Glegg *et al.* [25; 139] poorly. One possible explanation for this is that frequency-domain model does not model a hard-wall. It has been shown that the hard-wall can increase levels by as much as 6 dB at the lower frequencies and by as much as 3 dB at the higher frequencies [25]. As the frequency domain solution presented here does not model the wall, it is expected that the spectrum under-predicts the measured values and that this under-prediction is larger at low frequencies than at high frequencies. Additionally, the peak at the second BPF is not as prominent in the frequency-domain solution. This could potentially be explained due to the fact that a simplified isotropic turbulence spectrum has been used to model the turbulence while boundary layer turbulence is significantly anisotropic. Both of these discrepancies will be addressed in Chapters 5 and 6.

Fig 3.8 shows the directivity of the rotor. From this figure, it is observed that the directivity of the rotor resembles that of a dipole. The cusp of the dipole is at $\theta = 90°$ and the maximum sound is observed along the axis of the rotor. Additionally, a prominent peak is observed at the first BPF because of the blade-to-blade correlation. It is also observed that the downstream lobe is slightly louder than the upstream lobe as has been previously observed by various authors due to convective amplification. The discontinuities observed around the 3$^{\text{rd}}$ BPF occur when the frequency-domain model switches between the high and low frequency acoustic lift formulation.

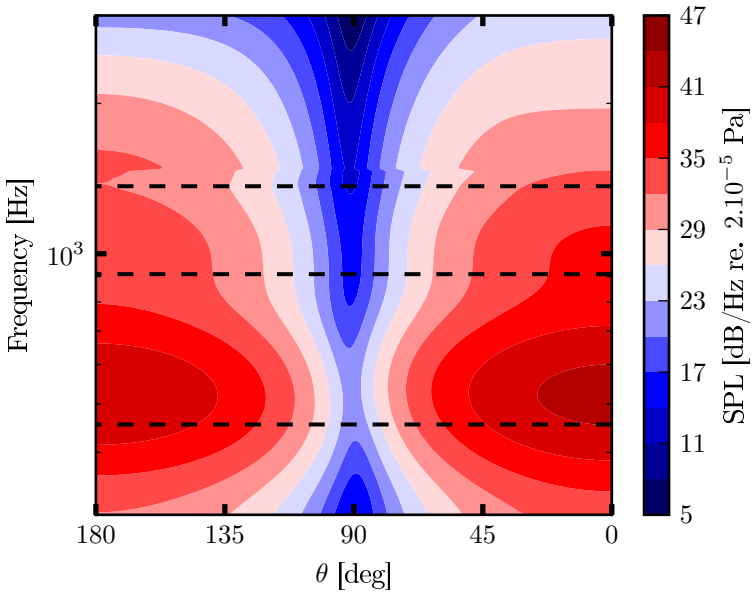

Figure 3.8: Contours of the SPL for varying observer angles (0° points downstream) and varying frequencies. The dashed lines represent the BPFs of the rotor.

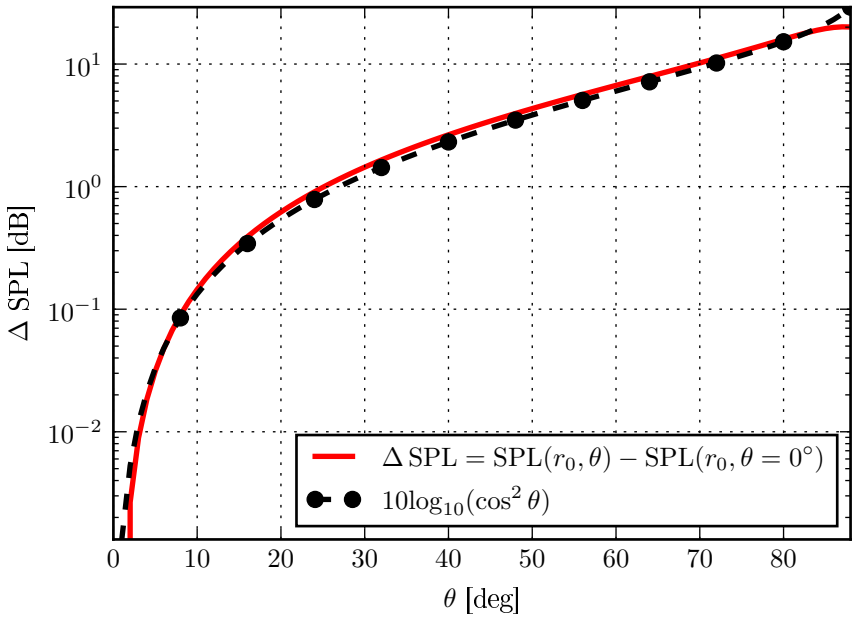

Figure 3.9: The decay of the SPL for the rotor at $f = 450$ Hz.

Fig 3.9 shows the difference of the of the SPL at a frequency of 450 Hz from the $\theta = 0°$ observer angle. The decay of the SPL follows the $\cos^2\theta$ directivity of a dipole, further showing that the directivity of the rotor is that of a dipole as has been commonly observed.

3.2.2 Parameter study of the integral length scale using an isotropic velocity spectrum

The rotor noise model described in section 3.1 requires the geometry of the rotor, the turbulence velocity and the integral length scale to be given as inputs. Of these, only the turbulence velocity and integral length scale of the turbulence can be varied because the geometry of the rotor is fixed. The variable parameters are required to define the velocity spectrum in Eqn. (3.27). The shape of the spectrum is only affected by the integral length scale L.

The von Kármán energy spectrum is given by [35],

$$E(k) = \frac{55}{9\sqrt{\pi}} \frac{\Gamma(5/6)}{\Gamma(1/3)} \frac{u^2}{k_e^5} \frac{k^4}{\left[1 + \hat{k}^2\right]^{17/6}}. \tag{2.2}$$

Using this definition of the energy spectrum, the normalised energy spectrum for various length scales can be plotted as shown in Fig. 3.10. Increasing the integral length scale moves the energy to the lower wave-numbers and reducing the integral length scale shifts the energy in the spectrum to the higher wave-numbers.

As shown in Fig. 3.10, the choice of the integral length scale is important to achieve the correct PSD from the rotor noise model presented in section 3.1. In order to understand the effect of the integral length scale on the rotor noise model, a parameter study of the integral length scale has been performed. This will determine if changing the integral length scales shift the frequency spectrum of the noise in a similar manner as it does in the energy spectrum. This parameter study has been performed considering that there is no blade-to-blade correlation and then again when assuming that there is blade-to-blade correlation. Both of these studies used the geometry from the FC3 case and a constant turbulence velocity $u^2 = 1.65\,\mathrm{m^2\,s^{-2}}$.

3.2.2.1 Results without blade-to-blade correlation

The results of varying the integral length scale on the PSD, for a rotor without blade-to-blade correlation are shown in Fig. 3.11. Changes in the energy spectra with increasing

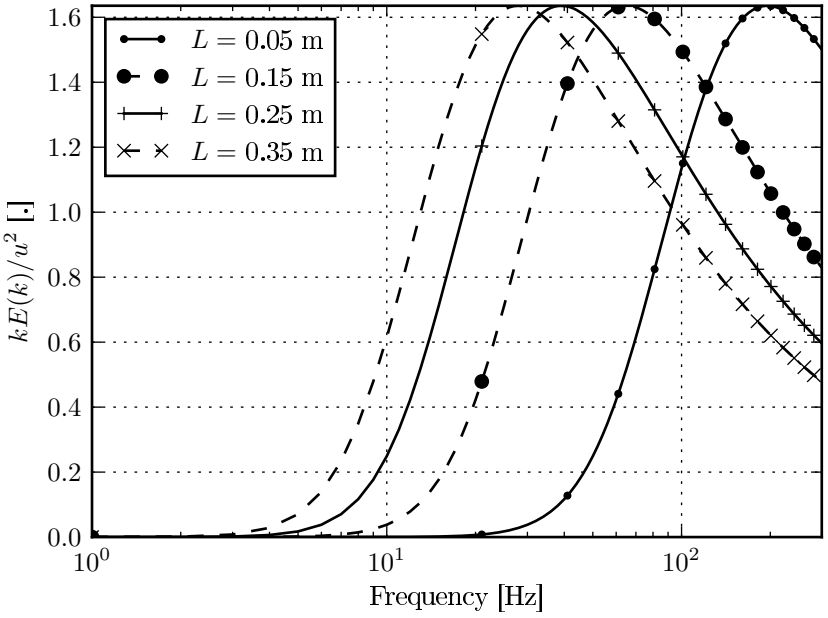

Figure 3.10: The energy spectra for different integral length scales.

length scale are mirrored in the rotor noise spectra, i.e., increasing the integral length scale shifts the energy in the spectra to lower frequencies.

It is also observed that the trend in the amplitude of the spectra is reversed at approximately 200 Hz. This can be explained by the fact that as the turbulence velocity is kept constant, the energy in the spectrum is the same across all the length scales. Thus, as the larger length scales transfer more energy to the lower frequencies, this must be compensated by having a smaller amount of energy at the higher frequencies as compared to the spectra with the smaller integral length scales, whose spectra have an equal spread of energy across the frequency range.

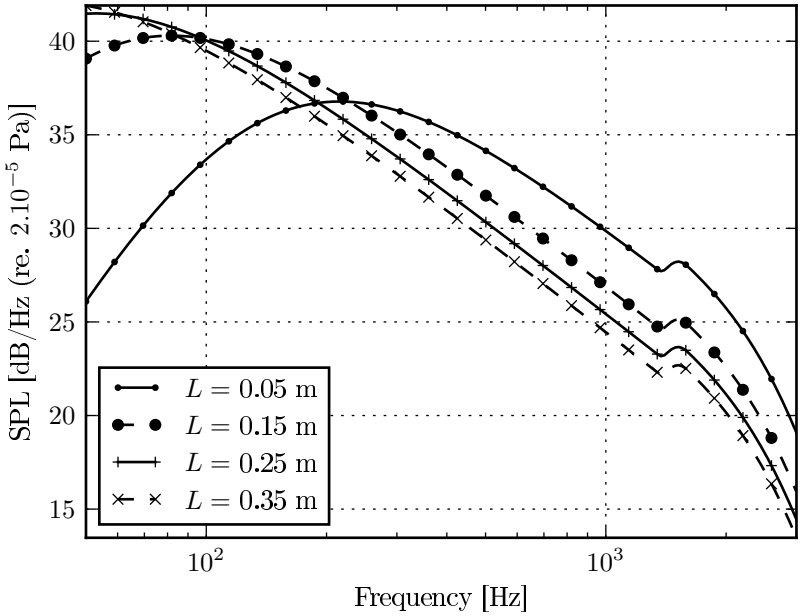

Figure 3.11: Power spectral density of the acoustic pressure at various integral length scale. The arrows are at multiples of the BPF.

3.2.2.2 Results with blade-to-blade correlation

The results of varying the integral length scale on the PSD for a rotor with blade-to-blade correlation are shown in Fig. 3.12. There is a prominent peak at the BPF, at approximately 450 Hz. The location of this peak does not vary with changes in the length scale. Additionally, unlike the case without the blade-to-blade correlation, it appears that changing the length scale for the case with blade-to-blade correlation does not shift the energy in the spectrum as much as it does in the case that ignores blade-to-blade correlation. In Fig. 3.11 the main peak for the smallest length scale is at approximately 200 Hz and the peak for the largest length scale is at approximately 50 Hz.

There are two peaks in the spectrum for the case that includes blade-to-blade correlation. This is in contrast to the case without correlation. The first peak for the smallest integral length scale is at approximately 80 Hz while the first peak for the largest integral length scale is absent. It is apparent that the spread in the frequencies at which the first peaks occur is smaller when compared to the case without blade-to-blade correlation. One possible explanation for this is that the peak at the BPF affects the way the energy would normally be distributed in the spectrum, thus minimising the distribution of energy in the lower frequency range.

However, the trend in amplitude is the same as in the case without blade-to-blade correlation. Thus to compensate for shifting a large proportion of the energy to the low-frequency region, the predictions made when using the largest integral length scale have a

lower amplitude at the BPF. Therefore, above a certain cut off frequency (approximately 100 Hz, due to the correlation peak, it is seen that the main effect of changing the correlation length scale is to change the amplitude of the spectrum.

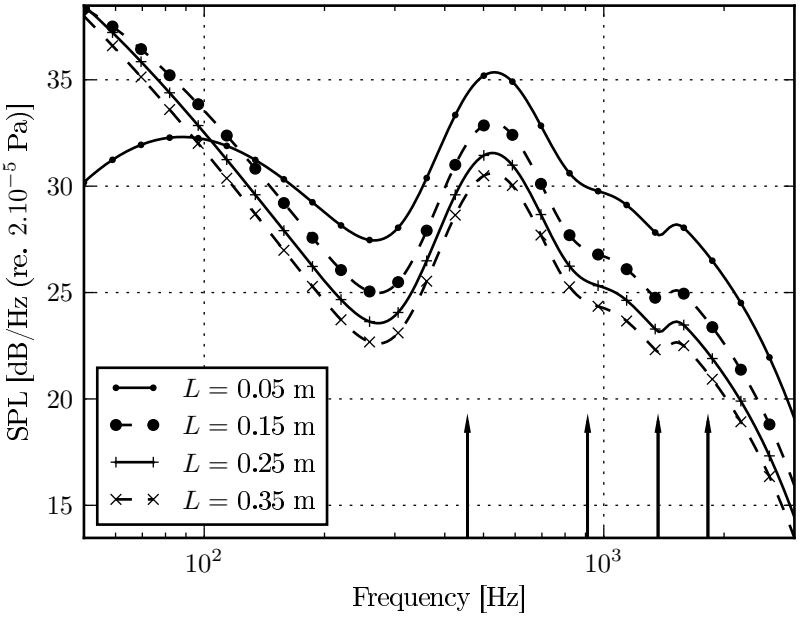

Figure 3.12: Power spectral density of the acoustic pressure at various integral length scales with the correlation between the blades modelled. The arrows are at multiples of the BPF.

3.3 Conclusions

This chapter has presented Amiet's simplified rotor noise model with blade-to-blade correlation modelled. Amiet's [18] rotor noise model approximates the rotational effects of an aerofoil by treating the rotation as a series of small translations. The PSD obtained for a translating aerofoil is then azimuthally averaged and frequency corrected to obtain the sound field of the rotor. This approach is valid at frequencies greater than $\Omega/10$. Amiet's [18] rotor noise model is an ideal tool to model the boundary layer ingestion noise source, which is the main motivation of this thesis. This is because the rotor noise model is computationally cheap and has a relatively simple formulation. The fact that it is fast to run ensures that it will be a useful tool for preliminary design studies. The fact that the formulation is relatively simple ensures that it can be extended to include wall effects and that it can be extended to include an anisotropic velocity spectrum. Additionally, the simple formulation will enable the investigation of the physics of the noise source by considering various parts of the rotor noise model individually. While the model has many advantages, it does also have some disadvantages. Amiet's [21] formulation assumes

that the rotor blade is a flat-plate, that the blade is unloaded and that the incoming mean-flow is uniform. The main conclusions that are drawn from this chapter are,

- This chapter has re-derived Amiet's rotor noise model for a coordinate system that will be used for the rest of this thesis. The Doppler factor that is used to frequency-correct the azimuthally averaged sound spectrum has been re-derived and it has been shown that the Doppler correction factor is consistent with the coordinate system considered. The blade-to-blade correlation wavenumber has also been re-derived for the present case.
- A simple numerical switch has been presented to account for the partial loading of the rotor. This is relevant for the boundary layer noise source as the rotor will only be partially loaded. Thus a switch has been developed that will compute the noise for only the strips that are immersed in the turbulence.
- Using Amiet's rotor noise model with blade-to-blade correlation and the numerical switch an initial prediction is made for a Sevik rotor as specified in the FC3 case of the 2015 AIAA FBN workshop. Major discrepancies are observed between the predictions and the measurements. The main discrepancies that are observed are that the amplitude of the spectrum is under-predicted and that no haystacks are observed at the second and third BPFs. The first discrepancy can be explained by the fact that the wall has not been modelled. The second discrepancy is because an isotropic velocity spectrum has been used. Both of these discrepancies will be addressed in the following chapters.
- Amiet's rotor noise model has been used to perform a parameter study of the integral length scale with, and without, the effects of blade-to-blade correlation. Without blade-to-blade correlation, it is shown that increasing the integral length scale transfers energy to the lower frequencies and vice-versa. With the blade-to-blade correlation modelled, it is observed that a correlation peak appears at the BPF. This affects the distribution of the energy and thus the net result of changing the integral length scale is to only change the spectrum amplitude, above a particular frequency. Therefore, the shape of the spectrum is not significantly affected by the integral length scale when blade-to-blade correlation is modelled.

Chapter 4

The noise radiated by a flat plate ingesting turbulence near a hard-wall

This chapter presents the development of an analytical method to determine the noise generated by an aerofoil ingesting turbulence near a hard-wall. The main aim of this chapter is to investigate the Method of Images (MOI) and to quantify the assumptions that are made when using the MOI. The MOI is a common analytical technique to model a reflecting surface. This is done by adding a mirror source and summing the resultant pressure at a far-field observer location. This chapter extends Amiet's [21] 2D translating aerofoil model to include wall-effects using the MOI. Amiet's 2D translating aerofoil model is used in order to make comparisons with Computational AeroAcoustic (CAA) simulations possible. While the MOI gives an approximation of the wall, it does not model all of the effects, such as diffraction from the edges of the flat plate and acoustic shielding due to the presence of the flat plate. These effects, which are ignored in the MOI are quantified using a CAA simulation that models the wall using a hard-slip-wall boundary condition. The MOI is then used with Amiet's [18] simplified rotor noise model in Chapter 5 to include wall-effects for a rotor. This chapter will therefore illustrate the accuracy of the MOI in modelling the hard-wall.

The hard-wall produces significant interaction in the sound field due to the reflected acoustic waves interacting with the acoustic waves generated by the aerofoil, which acts as a non-compact dipole. The frequency of the interference peaks is determined as a function of observer location and it is shown that the sound power approaches the sound power of a dipole near a wall at low frequencies.

The analytical solution is verified using a CAA simulation that also uses the MOI to simulate a wall. The assumptions that are made in the derivation of the analytical solution are quantified using a second CAA simulation that uses a hard-slip-wall boundary condition to simulate a wall. Finally, the effect of changing the height of the aerofoil on the resulting noise spectrum is investigated.

4.1 Analytical formulation

In this section Amiet's [21] solution for a flat-plate ingesting turbulence near a hard-wall is extended using the MOI to account for wall-effects. The model described below follows the derivation of Blandeau *et al.* [137] which uses the Kirchoff-Helmholtz formulation to determine the far-field acoustic pressure radiated from the surface of a flat plate at zero angle of attack due to a turbulent gust causing a pressure jump Δp. The assumptions made in the development of the model are:

- The flat plate is assumed to be unloaded.
- The impinging turbulence is assumed to be isotropic.
- The shielding of the reflected acoustic waves by the aerofoil is not accounted for.
- The scattering of the reflected acoustic waves around the edges of the flat plate is not accounted for.

This model is now described with the modifications required to account for a mirror source due to the presence of a wall.

4.1.1 Coordinate system

The geometry of the problem is shown in Fig. 4.1 with the coordinate system located at the centre of the flat plate as shown in Fig. 4.2. The observer is located at a position (r_0, θ) with respect to the flat plate and at a position $(r_0^{\#}, \theta^{\#})$ with respect to the image source. The two coordinates are related as,

$$r_0^{\#} = \sqrt{(r_0 \sin\theta + 2d_{wall})^2 + r_0^2 \cos^2\theta}, \tag{4.1}$$

$$\sin\theta^{\#} = \frac{r_0 \sin\theta + 2d_{wall}}{r_0^{\#}}. \tag{4.2}$$

Note that all symbols with superscript # denote quantities related to the image source. Additionally, coordinates indicated by capital letters denote quantities on the surface

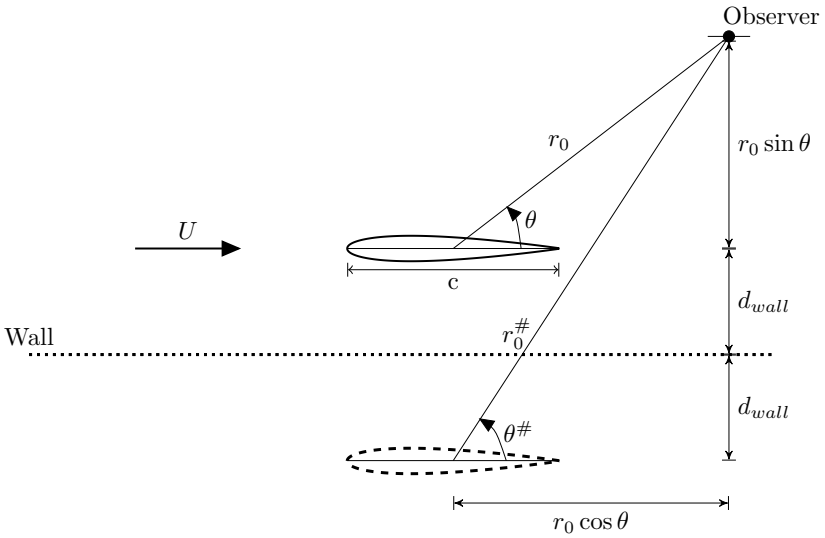

Figure 4.1: A schematic of an aerofoil (modelled as a flat plate) near a wall and its image source. The flat plate has a chord c and is at a height d_{wall} from the wall. The observer is located at (r_0, θ) from the flat plate and at $(r_0^{\#}, \theta^{\#})$ from the image source.

of the flat plate whereas quantities in lower-case letters are distances measured to the observer.

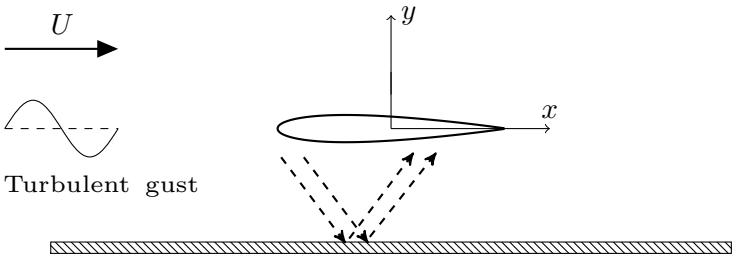

Figure 4.2: A schematic of an aerofoil (modelled as a flat plate) ingesting turbulence near a hard-wall.

4.1.2 Formulation of the power spectral density

For turbulence that is frozen, the velocity field, $v(X,t)$, is a combination of all the Fourier components in wavenumber space $\hat{v}(k_X)$. The velocity field can then be expressed as a Fourier pair [21],

$$v(X,t) = \frac{1}{2\pi}\int_{-\infty}^{\infty} \hat{v}(k_X) e^{-\mathrm{i}k_X(X-Ut)} \mathrm{d}k_X, \tag{4.3}$$

$$\hat{v}(k_X) = \int_{-\infty}^{\infty} v(X) e^{\mathrm{i}k_X X} \mathrm{d}X, \tag{4.4}$$

where k_X is the stream-wise vortical wavenumber and U is the velocity. The pressure jump caused due to a harmonic gust of the form $v_0 e^{-\mathrm{i}k_X(X-Ut)}$ is given by [21],

$$\Delta p(X,t) = 2\pi\rho_0 U v_0 g(X,k_X,M) e^{\mathrm{i}k_X Ut}, \tag{4.5}$$

where $g(X,k_X,M)$ is the leading-edge transfer function [21]and $M = U/c_0$ is the Mach number. The pressure jump in (4.5) only accounts for one gust. To determine the pressure jump due to all the wavenumber components (4.5) is integrated to get,

$$\Delta p = \rho_0 U \int_{-\infty}^{\infty} \hat{v}(k_X) g(X,k_X,M) e^{\mathrm{i}k_X Ut} \mathrm{d}k_X. \tag{4.6}$$

The pressure jump across the aerofoil can then be determined in the frequency-domain by taking the Fourier transform of (4.6) to obtain,

$$\Delta\hat{p}\,(X,\omega) = \int_{-\infty}^{\infty} \Delta p(X,t) e^{-\mathrm{i}\omega t} \mathrm{d}t = 2\pi\rho_0 \hat{v}(K_X) g(X,K_X,M), \tag{4.7}$$

where the Fourier transform has selected only the stream-wise wave-numbers $K_X = \omega/U$. This implies that a given frequency component of the pressure jump is produced by the gust with wavenumber ω/U [21].

The far-field acoustic pressure can then be computed using the Kirchoff-Helmholtz integral as [140],

$$p(x,y,t) = -\frac{1}{2\pi} \int_{-\infty}^{\infty} \int_{-b}^{b} \Delta\hat{p}(X,\omega) \frac{\partial G}{\partial y}(x,y,X,\omega) e^{\mathrm{i}\omega t} \mathrm{d}X \mathrm{d}\omega, \tag{4.8}$$

where the Green's function with the effects of mean flow is given by,

$$G(x,y,X,\omega) = -\frac{e^{\mathrm{i}k_0 M(x-X)/\beta^2}}{4\beta} H_0^{(2)}\left(\frac{k_0}{\beta^2}\sqrt{(x-X)^2+\beta^2 y^2}\right), \tag{4.9}$$

where $k_0 = \omega/c_0$ is the acoustic wavenumber, $\beta = \sqrt{1-M^2}$ is the compressibility factor and $H_0^{(2)}$ is the Hankel function of the second kind and of order zero. The derivative of (4.9) is then given by,

$$\frac{\partial G}{\partial y}(x,y,X,\omega) = \frac{\mathrm{i}y e^{\mathrm{i}k_0 M(x-X)/\beta^2}}{4\beta\sqrt{(x-X)^2+\beta^2 y^2}} H_1^{(2)}\left(\frac{k_0}{\beta^2}\sqrt{(x-X)^2+\beta^2 y^2}\right). \tag{4.10}$$

If the observer is assumed to be in the far-field, two simplifications can be made. Firstly, the Hankel function can be approximated as,

$$H_1^{(2)}(\xi) = \sqrt{\frac{2}{\pi\xi}} e^{-\mathrm{i}\xi + \mathrm{i}3\pi/4}. \tag{4.11}$$

Secondly, the flow corrected distance to the observer $\sqrt{(x-X)^2+\beta^2y^2}$ can be approximated using a Taylor series expansion as,

$$\sqrt{(x-X)^2+\beta^2y^2} \simeq \sigma - \frac{Xx}{\sigma},$$

where $\sigma = \sqrt{x^2+\beta^2y^2}$. Using these simplifications (4.10) can be written as,

$$\frac{\partial G}{\partial y}(x,y,X,\omega) = \frac{\mathrm{i}y}{4}\sqrt{\frac{2k_0}{\pi\sigma^3}}e^{-\mathrm{i}\frac{k_0}{\beta^2}[\sigma - Xx/\sigma - M(x-X)]+\mathrm{i}\frac{3\pi}{4}}. \tag{4.12}$$

To account for the wall (4.8) is modified by adding the image Green's function term [1],

$$p(x,y,t) = -\frac{1}{2\pi}\int_{-\infty}^{\infty}\int_{-b}^{b}\Delta\hat{p}(X,\omega)\left[\frac{\partial G}{\partial y}(x,y,X,\omega) - \frac{\partial G^{\#}}{\partial y}(x^{\#},y^{\#},X,\omega)\right]e^{\mathrm{i}\omega t}\mathrm{d}X\mathrm{d}\omega, \tag{4.13}$$

The Power Spectral Density (PSD) of the acoustic pressure can now be computed as the Fourier transform of the auto-correlation function,

$$S_{pp}(x,y,\omega) = \int_{-\infty}^{\infty}\mathbb{E}\left[p^*(x,y,t)p(x,y,t+\tau)\right]e^{-\mathrm{i}\omega\tau}\mathrm{d}\tau, \tag{4.14}$$

where $\mathbb{E}$ represents the ensemble average operator and the superscript $*$ indicates the complex conjugate of the quantity. Substituting (4.13) into (4.14) gives,

$$\begin{aligned}
S_{pp}(x,y,\omega) = \frac{1}{2\pi}\int\!\!\!\int_{-\infty}^{\infty}\int\!\!\!\int_{-b}^{b} S_{QQ}(X_1,X_2,\omega_1,\omega_2)\delta(\omega-\omega_2)e^{\mathrm{i}(\omega_1-\omega_2)}\times \\
\Bigg[\underbrace{\frac{\partial G}{\partial y}(x,y,X_1,\omega_1)\left(\frac{\partial G}{\partial y}(x,y,X_2,\omega_2)\right)^*}_{\text{Term 1}} - \\
\underbrace{\frac{\partial G}{\partial y}(x,y,X_1,\omega_1)\left(\frac{\partial G^{\#}}{\partial y^{\#}}(x^{\#},y^{\#},X_2,\omega_2)\right)^*}_{\text{Term 2}} - \underbrace{\frac{\partial G^{\#}}{\partial y^{\#}}(x^{\#},y^{\#},X_1,\omega_1)\left(\frac{\partial G}{\partial y}(x,y,X_2,\omega_2)\right)^*}_{\text{Term 3}} + \\
\underbrace{\left(\frac{\partial G^{\#}}{\partial y^{\#}}(x^{\#},y^{\#},X_1,\omega_1)\right)^*\frac{\partial G^{\#}}{\partial y^{\#}}(x^{\#},y^{\#},X_2,\omega_2)}_{\text{Term 4}}\Bigg]\mathrm{d}X_1\mathrm{d}X_2\mathrm{d}\omega_1\mathrm{d}\omega_2
\end{aligned} \tag{4.15}$$

[1] It should be noted that the Green's functions and the acoustic lift functions that have a superscript # are not different functions but indicate that their arguments should be evaluated for the image source.

where the cross-spectrum of the acoustic pressure S_{QQ} is given by,

$$\begin{aligned} &S_{QQ}(X_1, X_2, \omega_1, \omega_2) = \mathbb{E}\left[\Delta\hat{p}(X_1, \omega_1)\Delta\hat{p}^*(X_2, \omega_2)\right], \\ &= (2\pi\rho_0)^2 \mathbb{E}\left[v(K_{X1})v^*(K_{X2})\right] g\left(X_1, K_{X1}, M\right) g^*\left(X_2, K_{X2}, M\right), \\ &= (2\pi\rho_0)^3 \delta(K_{X1} - K_{X2})\Phi_{vv}(K_{X2}) g\left(X_1, K_{X1}, M\right) g^*\left(X_2, K_{X2}, M\right). \end{aligned} \tag{4.16}$$

The first term in (4.15) is the term one would get without the mirror source. This term results in Amiet's classic formulation for an aerofoil ingesting turbulence [21],

$$S_{pp}(r_0, \theta, \omega)|_{\text{Term1}} = \frac{\pi\rho_0^2 b^2 \sin^2\theta U k_0}{2r_0 A(\theta, M)^3}\Phi_{vv}(K_X)|\mathcal{L}(\theta, K_X)|^2. \tag{4.17}$$

Using (4.12) the second term of (4.15) is developed in radial coordinates to get,

$$\begin{aligned} &\frac{\partial G}{\partial y}(r_0, \theta, X_1, \omega_1)\left(\frac{\partial G^\#}{\partial y^\#}(r_0^\#, \theta^\#, X_2, \omega_2)\right)^* = \\ &\left[\frac{ir_0\sin\theta}{4}\sqrt{\frac{2k_0}{(r_0A)^3}}e^{-\mathrm{i}\frac{k_0}{\beta_X^2}[r_0A - X_1\cos\theta/A - M_X(r_0\cos\theta - X_1)] + \mathrm{i}\frac{3\pi}{4}}\right] \\ &\times\left[\frac{-ir_0^\#\sin\theta^\#}{4}\sqrt{\frac{2k_0}{\pi(r_0^\#A^\#)^3}}e^{+\mathrm{i}\frac{k_0}{\beta_X^2}\left[r_0^\#A^\# - X_2\cos\theta^\#/A^\# - M_X(r_0^\#\cos\theta^\# - X_2)\right] - \mathrm{i}\frac{3\pi}{4}}\right]\mathrm{d}X_1\mathrm{d}X_2\mathrm{d}\omega_1\mathrm{d}\omega_2, \\ &= \frac{k_0 r_0^\# r_0\sin\theta\sin\theta^\#}{8\pi}\sqrt{\frac{1}{(r_0^\#A^\# r_0 A)^3}}e^{-\mathrm{i}\frac{k_0}{\beta_X^2}\left[(-r_0^\#A^\# + r_0A)\right] + \mathrm{i}\kappa X_1 - \mathrm{i}\kappa^\# X_2}, \end{aligned} \tag{4.18}$$

where $A = \sqrt{1 - M_X^2\sin^2\theta}$ and $\kappa = \cos\theta/A - M_X$. The PSD can now be evaluated for only the second term of (4.15) using (4.16) and (4.18) to get,

$$\begin{aligned} &S_{pp}(r_0, r_0^\#, \theta, \theta^\#, \omega)\Big|_{\text{Term 2}} = \\ &\frac{1}{2\pi}\int_{-\infty}^{\infty}\iint_{-b}^{b} S_{QQ}\left(X_1, X_2, \omega_1, \omega_2\right)\delta(\omega - \omega_2)e^{\mathrm{i}(\omega_1 - \omega_2)} \\ &\times\frac{k_0 r_0^\# r_0\sin\theta\sin\theta^\#}{8\pi}\sqrt{\frac{1}{r_0 r_0^\#(AA^\#)^3}}e^{-\mathrm{i}\frac{k_0}{\beta_X^2}\left[(-r_0^\#A^\# + r_0A)\right] + i\kappa X_1 - i\kappa^\# X_2}\mathrm{d}X_1\mathrm{d}X_2\mathrm{d}\omega_1\mathrm{d}\omega_2, \\ &= \frac{\pi b^2\rho_0 k_0\sin\theta\sin\theta^\# U}{2}\sqrt{\frac{1}{r_0 r_0^\#(AA^\#)^3}}e^{-\mathrm{i}\frac{k_0}{\beta_X^2}\left[r_0A - r_0^\#A^\#\right]}\Phi_{vv}(K_X)\mathcal{L}(\theta, K_X)\left(\mathcal{L}^\#(\theta^\#, K_X)\right)^*. \end{aligned} \tag{4.19}$$

Terms 3 and 4 in Eqn. (4.15) can be obtained similarly. The final PSD can thus be written as,

$$
\begin{aligned}
S_{pp}\left(r_0,\theta,\omega\right) = \\
&\frac{\pi b^2\rho_0^2 k_0 \sin^2\theta U}{2r_0 A^3}|\mathcal{L}|^2\Phi_{vv}(K_X) - \\
&\frac{\pi b^2\rho_0^2 k_0 \sin\theta \sin\theta^{\#} U}{2}\sqrt{\frac{1}{r_0 r_0^{\#}(AA^{\#})^3}}\Psi|\mathcal{L}\left(\mathcal{L}^{\#}\right)^*|\Phi_{vv}(K_X) - \\
&\frac{\pi b^2\rho_0^2 k_0 \sin\theta \sin\theta^{\#} U}{2}\sqrt{\frac{1}{r_0 r_0^{\#}(AA^{\#})^3}}\Psi^*|\mathcal{L}^{\#}\left(\mathcal{L}\right)^*|\Phi_{vv}(K_X) + \\
&\frac{\pi b^2\rho_0^2 k_0 \sin^2\theta^{\#} U}{2r_0^{\#} A^{\#3}}|\mathcal{L}^{\#}|^2\Phi_{vv}(K_X),
\end{aligned}
\tag{4.20}
$$

where $\Psi = e^{-\mathrm{i}\frac{k_0}{\beta_X^2}\left[(-r_0^{\#}A^{\#}+r_0 A)\right]}$ and this is referred to as the interference term. Analysing Eqn. (4.20) it is seen that the first term is Amiet's [21] classical solution for an aerofoil ingesting turbulence. The term Ψ is expected to cause interference peaks in the frequency spectra. This is because Ψ is imaginary and thus changes the phase of the solution. This term is therefore responsible for modelling the constructive and destructive interference of acoustic waves. The fourth term modulates the amplitude producing the expected doubling of sound power in the absence of the interference terms.

Additionally, it is observed that the second and third terms are complex conjugates and thus the imaginary parts of these terms cancel. This is shown in Fig. 4.3. The real parts of the exponential of the second and third terms in Eqn. (4.20) are identical and are shown in Fig. 4.3(a). The imaginary parts of the two terms on the other hand are exactly out of phase and thus cancel out as shown in Fig. 4.3(b).

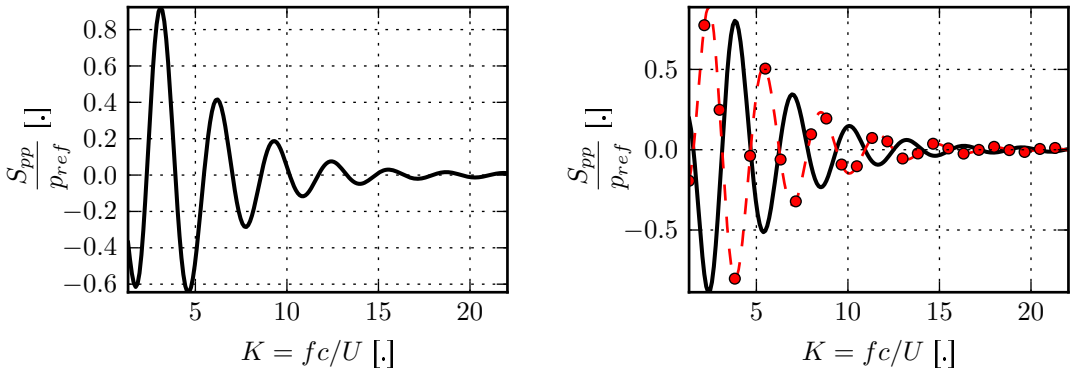

(a) The real part of the second and third terms of the PSD in (4.20).

(b) The imaginary part of the second (-) and third terms (filled circle) of the PSD in (4.20).

Figure 4.3: The real and imaginary parts of the second and third terms of the PSD in Equation (4.20). The observer is at 45° and in a free-stream at Mach number 0.1.

From this, it can be concluded that the interference peaks that will be caused due to the aerofoil placed near a wall will be due to the real parts of the second and third terms of Eqn. (4.20). This term is of the form $-2\cos\left(\frac{k_0}{\beta_X^2}\left[(-r_0^{\#}A^{\#}+r_0A)\right]\right)$. If it is assumed that,

$$A \simeq A^{\#} \simeq \beta_X \simeq 1,$$

the wave-numbers at which the amplitudes will be at a maximum can be determined by computing the minimum (due to the negative sign) of the real parts of terms 2 and 3. This is given by,

$$k_{0,max} = \frac{(2n+1)\pi}{\sqrt{r_0^2 + 4d_{wall}^2 + 4r_0 d_{wall}\sin\theta} - r_0}, \forall\, n \in \{0,1,2,...\}, \tag{4.21}$$

where n is an integer that denotes the peak number for a particular observer angle. Fig. 4.4 shows an example frequency spectra with the location of the peaks predicted using Eqn. (4.21).

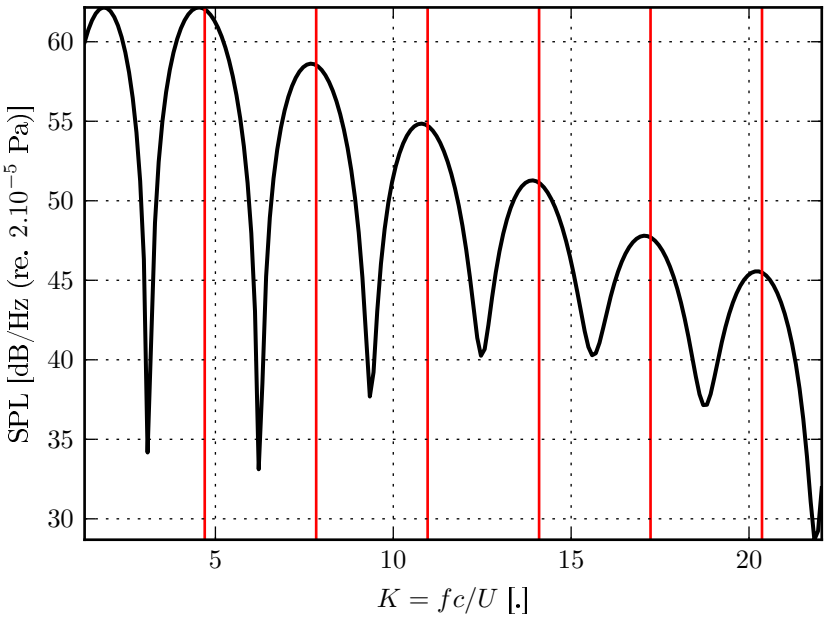

Figure 4.4: Example spectrum for a flat plate ingesting turbulence near a hard-wall. The observer is at 45° and in a free-stream at Mach number 0.1. The red lines represent the peak locations predicted using Equation (4.21).

Physically an acoustic wave travelling from the real aerofoil to the observer will arrive at the observer at a time $t_1 = r_0/c_0$ and the acoustic wave travelling from the image source to the observer will reach at time $t_2 = r_0^{\#}/c_0$. Thus, the acoustic waves from the two sources arrive at the observer separated by a time $\Delta t = t_2 - t_1$. As the frequency of the reflected acoustic waves is the same as the frequency of the acoustic waves emitted by the aerofoil, these acoustic waves would interfere constructively if the wavelength

corresponds to the time delay Δt. This implies that reflected waves arrive at intervals that are an integer multiple of the wavelength when they arrive at the observer.

From Eqn. (4.21) it can be seen that the effective wavelength at which the maximum interference occurs is, $\lambda_{max} = \left(r_0^{\#} - r_0\right)$ and this corresponds to an acoustic wave that will arrive at the observer at an integer multiple of the wavelength as discussed above.

The upwash velocity spectrum in Eqn. (4.20) is modelled as the 2D isotropic von Kármán spectrum which is defined as,

$$\Phi_{vv}^{(2D)}\left(K_X\right) = \int_{-\infty}^{+\infty} \frac{E^{(2D)}(k)}{\pi k}\left(1 - \frac{k_y^2}{k^2}\right) \mathrm{d}k_y, \tag{4.22}$$

where,

$$E^{(2D)}(k) = \frac{110\overline{u^2}L}{27\pi} \frac{\left(k/k_e\right)^4}{\left[1 + \left(k/k_e\right)^2\right]^{17/6}}, \tag{4.23}$$

$k = \sqrt{K_X^2 + k_y^2}$, $k_e = \frac{\sqrt{\pi}}{L}\frac{\Gamma(5/6)}{\Gamma(1/3)}$, and L is the integral length scale of the turbulence. It should be noted that the energy spectrum defined in Eqn. (4.22) is for purely 2D turbulence. This is a mathematical construct to generate a 2D isotropic fluctuating field without spanwise disturbances. The CAA method that will be used to verify the analytical formulation uses the same definition of the turbulence spectrum and thus the comparison between the two is valid.

4.1.3 Formulation for the radiated power of the flat plate

In this section, the expression for the power radiated from a flat plate ingesting turbulence near a hard-wall is derived. This is done in order to simplify Eqn. (4.20) and from this simplified expression for the PSD, determine the physical significance of the additional terms that are added due to the presence of the hard-wall. Examining the sound power of the flat plate in the low Mach number low frequency limit, makes it easier to understand the physical meaning of each of the terms. Another advantage of examining the sound power of the flat plate in this limit, is that it can be compared to the power radiated by a vertical dipole. As the flat plate in the low Mach number low frequency limit is expected to behave like a dipole [79], this comparison serves as an initial verification of the analytical solution.

In the low frequency and low Mach number limit, the following simplifications can be made [140],

$$\begin{aligned} \lim_{k_X L\to 0} \Phi_{vv} =& \frac{\overline{u^2} L}{2\pi}, \quad \lim_{\mu_a\to 0} |\mathcal{L}|^2 = \frac{1}{\beta^2}|S(\mu_h)|^2, \\ \lim_{M\to 0} A =& 1, \quad \lim_{M\to 0} \beta = 1, \end{aligned} \tag{4.24}$$

where the low frequency limit of the velocity spectrum is for the Liepmann spectrum, S is the Sears function, $\mu_a = \omega b/c_0\beta^2$, and $\mu_h = \mu_a/M$. Substituting the limits in Eqn. (4.24) into Eqn. (4.20), the PSD of the acoustic pressure can be written as,

$$\begin{aligned} &\lim_{\substack{f\to 0 \\ M_x\to 0}} S_{pp}\left(r_0, \theta, \omega, d_{wall}\right) = \\ &\frac{\pi b^2 \rho_0^2 k_0 U}{2} \frac{\overline{u^2} L}{2\pi} |S(\mu_h)|^2 \left[\frac{\sin^2\theta}{r_0} - 2\frac{\cos\left(k_0(r_0^{\#} - r_0)\right)\sin\theta\sin\theta^{\#}}{\sqrt{r_0 r_0^{\#}}} + \frac{\sin^2\theta^{\#}}{r_0^{\#}} \right]. \end{aligned} \tag{4.25}$$

If it is further assumed that $r_0 >> d_{wall}$, the following simplifications can be made,

$$\begin{aligned} r_0^{\#} - r_0 \simeq& 2 d_{wall}\sin\theta + \mathcal{O}\left(d_{wall}^2\right), \\ \frac{r_0^{\#}}{r_0} \simeq& 1 + \mathcal{O}\left(\frac{d_{wall}}{r_0}\right), \\ \sin\theta^{\#} \simeq& \sin\theta + \mathcal{O}\left(\frac{d_{wall}}{r_0}\right), \end{aligned} \tag{4.26}$$

and Eqn. (4.25) can be written as,

$$\lim_{\substack{f\to 0 \\ M_x\to 0}} S_{pp}\left(r_0, \theta, \omega, d_{wall}\right) = \frac{\pi b^2 \rho_0^2 k_0 U}{2 r_0} \frac{\overline{u^2} L}{2\pi} |S(\mu_h)|^2 \mathcal{D}(\xi, \theta), \tag{4.27}$$

where,

$$\mathcal{D}(\xi, \theta) = 2\sin^2\theta - 2\cos\left(\xi\sin\theta\right)\sin^2\theta, \tag{4.28}$$

and $\xi = 2k_0 d_{wall}$. The directivity function for an isolated dipole is $\sin^2\theta$. The addition of a factor of 2 to the first term on the right hand side of Eqn. (4.28) is caused by a doubling of sound pressure due to the wall. This increase in amplitude is due to the fourth term on the right hand side that is added to Amiet's original formulation in Eqn. (4.20). The second term in Eqn. (4.28) is the interference term that modifies the directivity function due to the wall. This term is the low Mach number, low frequency asymptote of the second and third terms on the right hand side that are added added to Amiet's original formulation in Eqn. (4.20). The directivity function in Eqn. (4.28) generates interference patterns as shown in Fig. 4.5. In the low frequency, low Mach number limit, the maximum noise is radiated at $\theta = 90°$ when $\cos(\xi)$ is a minimum. Therefore, the peaks occur at,

$$\xi = (2n+1)\pi, \, \forall\, n \in \{0, 1, 2, ...\}, \tag{4.29}$$

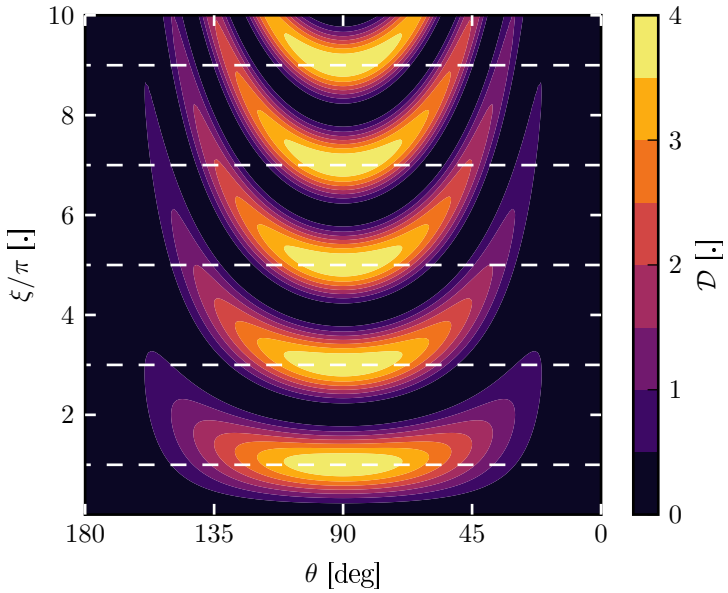

Figure 4.5: The directivity of the PSD of the noise and the power ratio in the low frequency low Mach number limit.

as shown in Fig. 4.5. Additionally, the SPL is increased by a maximum of 4 times which is consistent with the 6 dB increase in noise that is expected from classical acoustics due to the interference of coherent waves. This is due to the doubling of the PSD of the sound due to the presence of the reflecting plane. Additionally, the acoustic waves can interfere constructively or destructively. A constructive interference quadruples the PSD of the sound and a destructive interference leads to a cancellation of the acoustic wave. In the low Mach number limit, the sound power ($\mathcal{P}$), of the flat plate without mean flow effects is given by,

$$\mathcal{P}(\omega) = \frac{r_0}{2\rho_0 c_0} \int_0^{\pi} S_{pp}\left(r_0, \theta, \omega\right) \mathrm{d}\theta. \tag{4.30}$$

Substituting Eqn. (4.27) into Eqn. (4.30) the power factor, which is the ratio between the power radiated with the wall present and the power radiated in the free-field ($\mathcal{P}_0$), is then obtained as,

$$\frac{\mathcal{P}(\omega)}{\mathcal{P}_0(\omega)} = 1 - 2\left[\frac{J_1\left(\xi\right)}{\xi} - J_2\left(\xi\right)\right]. \tag{4.31}$$

where J_ν are Bessel functions of the first kind of order ν. This is identical to the power factor of a vertical dipole as shown in Appendix C. This serves as an initial verification of the analytical solution.

Fig. 4.6 shows the power factor computed using Eqn. (4.31). The power factor goes to zero as the dipole moves towards the wall and the maximum value is 1.83 for the flat plate in the low frequency limit. Additionally, as $\xi \to \infty$, the terms in the bracket in Eqn. (4.31) tend to zero and thus the free-field power is recovered.

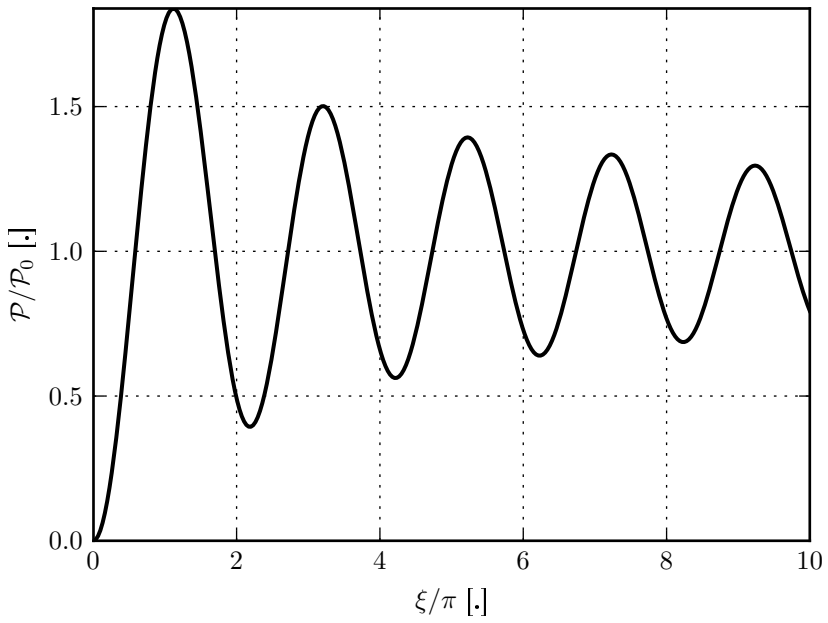

Figure 4.6: The power factor computed using Eqn. (4.31).

4.2 Computational method

To verify the analytical method and to determine its accuracy a CAA code was used. The CAA code used in this study is called SotonCAA. This code solves the Linearised Euler Equations (LEE) and has been used by various authors to study a number of noise sources. Gill *et al.* [141; 142] have used the SotonCAA code to study the effect of aerofoil geometry on leading-edge noise. They use the SotonCAA code with the spatial schemes of Hixon [115] and turbulence is synthesized using 1,2 and 3 component Fourier methods. Gea-Aguilera *et al.* [126] use the SotonCAA code with the spatial schemes of Kim [118] and an advanced digital filter method is developed to synthesize turbulence. The advanced digital filter method synthesizes turbulence by superimposing Gaussian eddies of the appropriate length scale and turbulence intensity to obtain a target turbulence velocity spectrum. This method generates divergence free turbulence that is injected at a specified plane in the computational domain. The injected turbulence is assumed to be frozen and divergence free (this ensures that the jet is not a source of noise).

This study uses the SotonCAA code with the fourth order compact finite-difference spatial schemes of Kim [118] with sixth order filtering of Kim [118]. The temporal scheme used is an explicit low-dissipation and low-dispersion Runge-Kutta fourth order accurate 4-6 scheme of Hu *et al.* [143]. In order to minimize reflections at the edges of the computational domain a non-reflective implicit buffer zone boundary condition developed by Gill *et al.* [119] is used. The PSD of the acoustic pressure was computed from the pressure time-history data using the multi-taper method of Thomson [144]. The details of the numerical simulation are summarised in Tab. 4.1.

Parameter	Value/Description
Spatial scheme	Fourth order compact finite-difference scheme of Kim [117] with sixth order filtering of Kim [118]
Temporal scheme	Explicit low-dissipation and low-dispersion Runge-Kutta fourth order accurate 4-6 scheme of Hu *et al.* [143]
Non-dimensional time step	$\Delta t_{ND} = (\Delta t c_0)/L_{ref} = 3 \times 10^{-6}$
Number of time steps	7.56×10^6 with data collected every 756 time steps
CFL_{max}	< 0.5
Spatial resolution	10 Points Per Wavelength (PPW) for the smallest vortical wavelength
Non-reflective boundary conditions	Non-reflective implicit buffer zones of Gill *et al.* [119]

Table 4.1: Computational parameters used to validate the analytical method.

Turbulence was synthesized using the advanced digital filter method of Gea-Aguilera *et al.* [126]. The chosen target spectrum was the 2D von kármán spectrum with an integral length scale of 0.008 m and a turbulence velocity of $0.015U$ for a free-stream Mach number of 0.6. Five Gaussian spectra were summed to achieve the target spectra with these properties. The integral length scale and turbulence intensities of each of these spectra are provided in Tab. 4.2. The upwash velocity spectra generated using these parameters using the advanced digital filter method is compared to the analytical von Kármán velocity spectrum computed using Eqn. (4.22) in Fig. 4.7. The comparisons show that the velocity spectra computed using the advanced digital filter method is within 2 dB of the analytical predictions at a majority of the frequencies.

Integral Length Scale [m]	Turbulence Intensity [$\text{m}^2\,\text{s}^{-2}$]
2.524×10^{-2}	1.617×10^{-1}
1.401×10^{-2}	6.708×10^{-1}
7.285×10^{-3}	9.106×10^{-1}
3.559×10^{-3}	5.735×10^{-1}
1.973×10^{-3}	5.735×10^{-1}

Table 4.2: Parameters for the Gaussian superposition used in the advanced digital filter method.

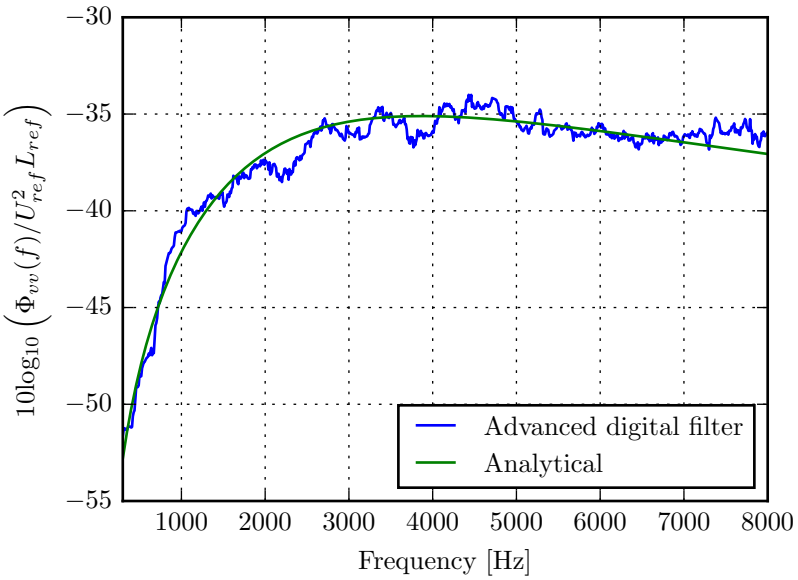

Figure 4.7: The upwash velocity spectra computed at a location $0.02c$ upstream of the aerofoil compared with the analytical upwash velocity spectra. $L_{ref} = 1\,\mathrm{m}$ and $U_{ref} = 1\,\mathrm{ms}^{-1}$.

The grid that was used for these studies is shown in Fig. 4.8. The grid extended to 9 chords in all the directions except under the aerofoil. This dimension was dictated by the required distance to the wall for the cases with the hard-wall boundary condition and for the free-field/MOI cases the grid extended to 3 chord lengths below the aerofoil. The observer arc was placed at a radius of 8 chords from the aerofoil centre. The grid metrics such as aspect ratio, grid size and grid skewness were controlled in accordance with the recommendations of Fattah *et al.* [145]. As an example of the grid quality, the mesh and the skewness in the vicinity of the aerofoil leading-edge are shown in Figs. 4.8(b) and 4.8(c). Additionally, the largest mesh cell size Δx was chosen so as to fit at least 10 grid points for the smallest acoustic vortical wave (highest frequency). The mesh used in this study can propagate waves up to frequencies of 8000 Hz. However, the highest frequency that can be resolved for this study was constrained by the temporal requirements. Pressure-time history data was collected every 756 time steps for a total of 7.56 million time steps. This corresponds to fitting 30 points per wavelength for a maximum frequency of 5000 Hz.

4.2.1 Investigating the errors introduced due to the grid

The SotonCAA code used in these studies has two distinct sources of error. The first stems from the grid and the finite difference schemes used. The second source of error is the recreation of the velocity spectrum using the digital filter method as shown in Fig. 4.7. This section will isolate the errors introduced because of the grid and the finite

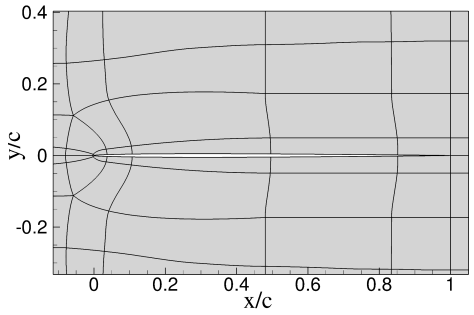

(a) Grid topology around the aerofoil.

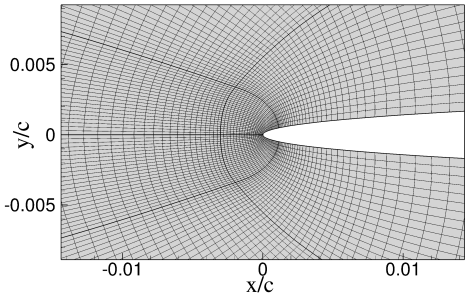

(b) 'C' shaped grid around the aerofoil.

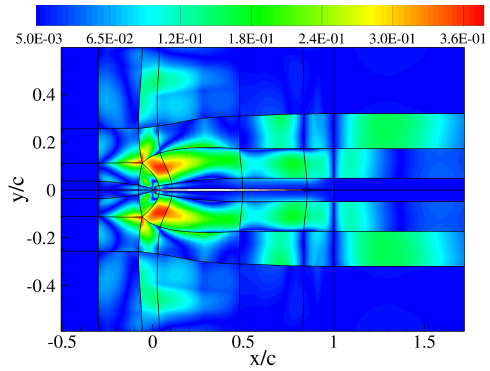

(c) Mesh skewness.

Figure 4.8: Details of the grid that was used for the CAA simulations.

difference schemes used in SotonCAA by computing the noise radiated by a flat plate in the free-field using Amiet's [21] formulation given by the first term in Eqn. (4.20).

Fig. 4.9 shows the PSD of the acoustic pressure determined in three different ways. The first two are determined using Amiet's [21] formulation (the first term of Eqn. (4.20)) with the upwash velocity spectrum computed analytically (shown in black in Fig. 4.9) and the upwash velocity spectrum computed by interpolating the upwash velocity spectrum generated by the Advanced Digital Filter method as shown in Fig. 4.7 (shown in red in Fig. 4.9). Finally, the PSD of the acoustic pressure is computed by computing the PSD from the time-history of the pressure obtained from the CAA simulation.

Comparing the results, it is observed that predictions using Amiet's [21] formulation with the upwash velocity spectrum obtained from the Advanced Digital Filter method compares well to the predictions using Amiet's [21] formulation with the upwash velocity spectrum analytically determined. The largest discrepancies are observed when the PSD of the acoustic pressure is directly obtained from the CAA simulations. This indicates that a majority of the errors that will be observed will either be due to the grid or due to inaccuracies associated with the finite difference schemes used.

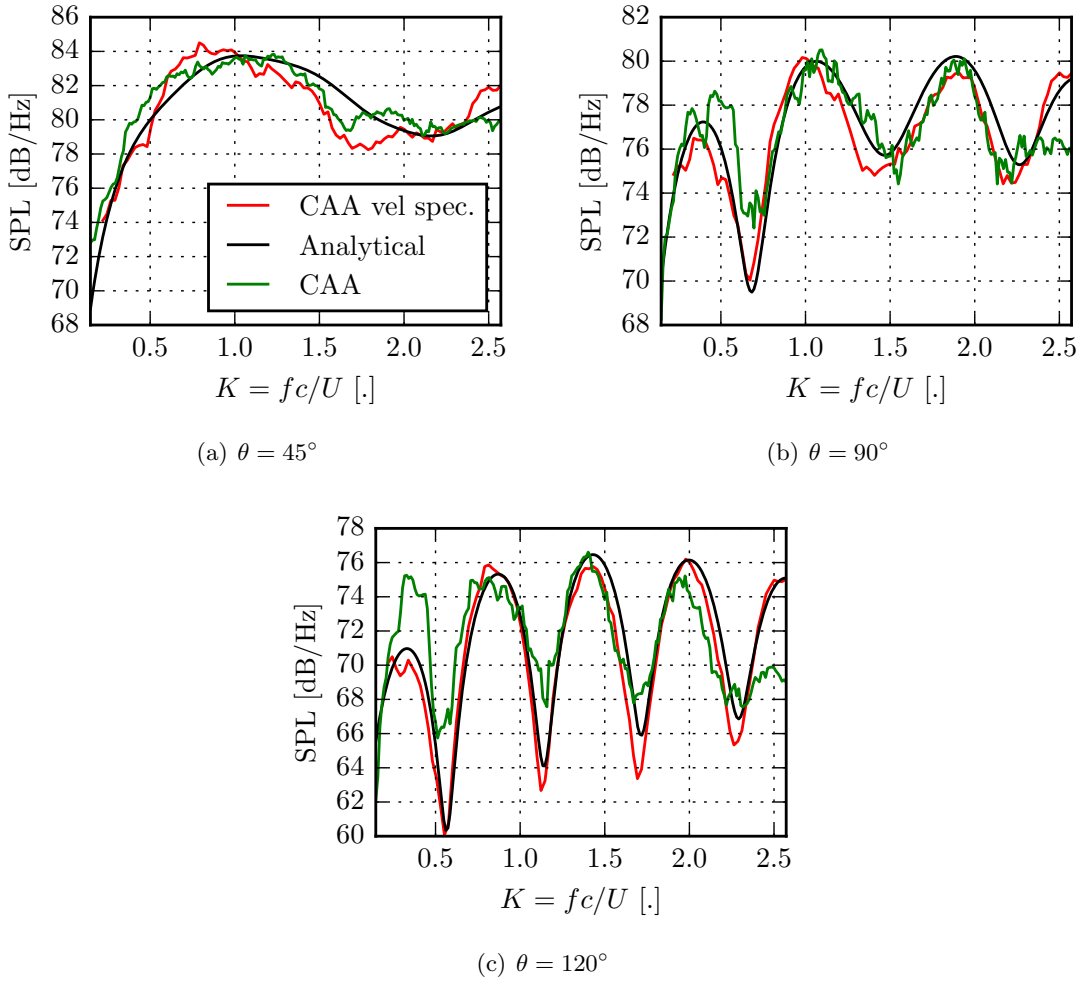

(a) $\theta = 45°$

(b) $\theta = 90°$

(c) $\theta = 120°$

Figure 4.9: The PSD of the acoustic pressure computed using Amiet's (first term of Eqn. (4.20)) formulation with the velocity spectrum determined analytically (black), determined from the Advanced Digital Filter method and the PSD of the acoustic pressure determined directly from a CAA simulation (green).

4.2.2 Computational setup for verification tests

To verify the analytical results, the computations were run so as to closely match the assumptions that were made in deriving the analytical formulation. Thus, the flat plate in Amiet's theory was approximated using a NACA 0001 aerofoil and a uniform mean-flow was used when solving the LEE. The parameters used in the simulations are tabulated in Tab. 4.3.

Additionally, the pressure time-history data was collected on two surfaces placed at the locations of the actual source and the mirror source as shown in Fig. 4.10. This was done instead of using a wall boundary condition in order to isolate the effects of acoustic waves diffracting around the edges of the aerofoil and the shielding effect of the aerofoil.

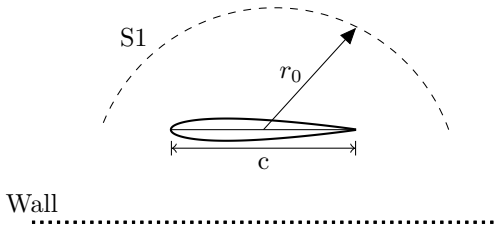

(a) The position of the data collection surface with respect to the real aerofoil.

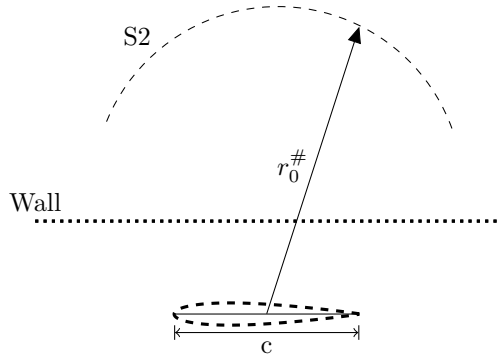

(b) The position of the data collection surface with respect to the image aerofoil.

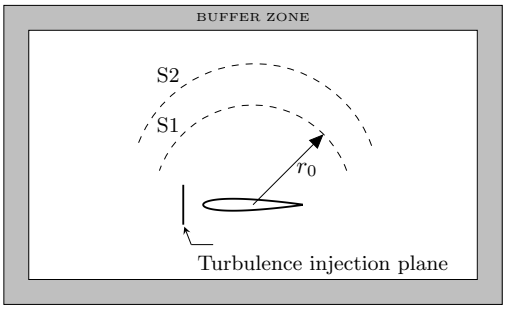

(c) The schematic of the CAA simulation used to validate the analytical model.

Figure 4.10: The schematic of the CAA simulation used to validate the analytical model. S1 and S2 represent the data collection surfaces for the real and image aerofoils. Using this data collection strategy one can model the analytical solution without using a hard slip-wall boundary condition.

Parameter	Value
Aerofoil	NACA 0001
Aerofoil chord	0.15 m
Mach number	0.6
Turbulence integral length scale	0.008 m
Turbulence intensity	$0.015U$
Distance from the aerofoil chord to the wall	0.3 m
Radius of observer arc	1.2 m

Table 4.3: Computational parameters.

4.2.3 Computational setup for the quantification of the assumptions made in the analytical solution

To quantify the assumptions that were made in deriving Eqn. (4.20) a hard slip-wall boundary condition was used in the CAA simulations to model the physical wall. Unlike the CAA simulations that use the MOI to model the wall, these simulations are physically

representative. Similar to the CAA simulations that used the MOI , the computations were run using a NACA 0001 aerofoil and a uniform mean flow. The parameters used for these simulations are the same as the parameters used in the CAA simulations using the MOI and are given in Tab. 4.3.

In simulations where the hard slip-wall boundary condition has been used, the pressure time-history data was collected on one surface (surface 'S1' in Fig. 4.11) that represents the location of the observers with respect to the real aerofoil.

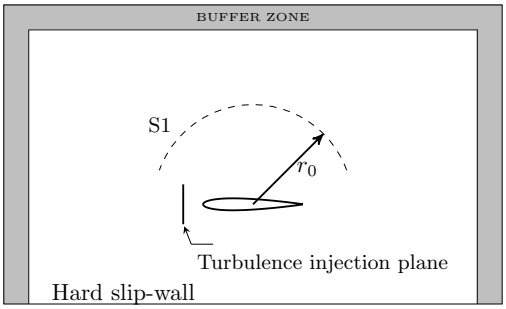

Figure 4.11: The schematic of the physically representative CAA simulation used to test the assumptions made in the analytical model for an aerofoil ingesting turbulence near a hard slip-wall.

4.3 Results

The results of the CAA simulation with and without the hard-wall boundary condition, using the computational setup described in Section 4.2.3, are shown in Fig. 4.15. These simulation results will allow the quantification of the missing diffraction and shielding effects in the analytical model. The verification of the analytical solution is made using the CAA simulation with the MOI as described in Section 4.2.2.

4.3.1 Verification of the analytical method using CAA

In this section, the analytical solution using the MOI is verified by comparing results from the analytical solution to results from a CAA simulation that uses the MOI to simulate the wall. Fig. 4.12 shows a comparison of the analytical solution for a flat plate ingesting turbulence with and without a wall, compared to the corresponding CAA simulation using the MOI. The CAA and analytical solutions match reasonably well. The levels and locations of the constructive and destructive interference peaks are well represented. There are significant destructive troughs seen in the analytical solution using the MOI in Fig. 4.12(b) and these troughs do not appear in the CAA simulation using the MOI . These troughs occur when the PSD of the sound tends to zero due to the cancellation effect of the interference term Ψ in Eqn. (4.20).

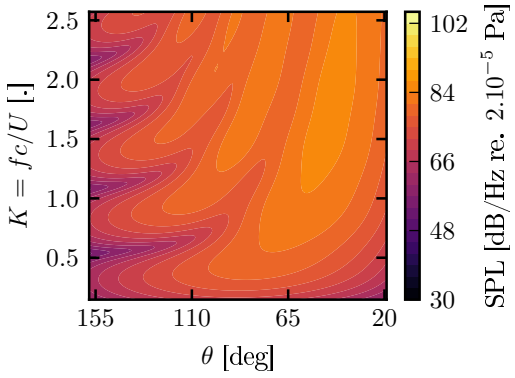

(a) Analytical solution without a wall.

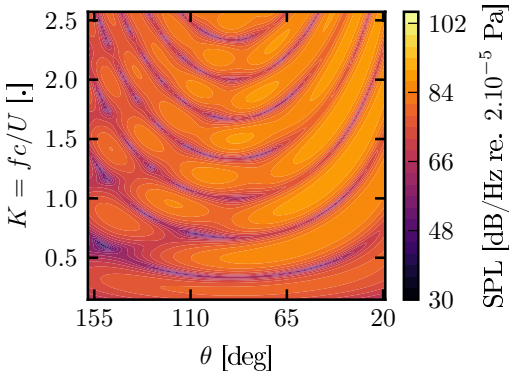

(b) Analytical solution with a wall $d_{wall} = 2c$.

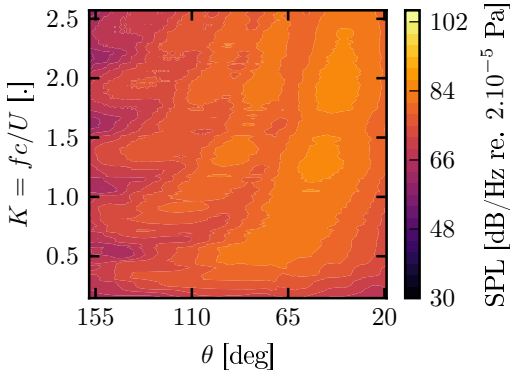

(c) Results from the CAA simulation without a wall.

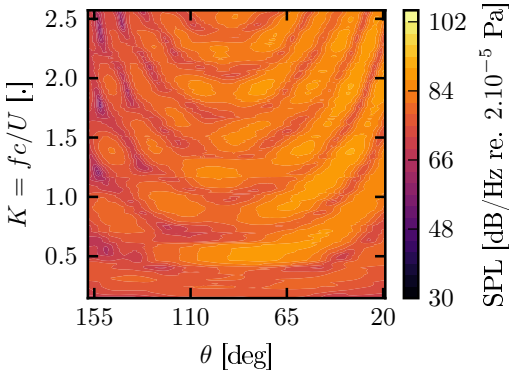

(d) Results from the CAA simulation with a wall (simulated using the MOI) at $d_{wall} = 2c$.

Figure 4.12: Contours of sound pressure level (SPL) as a function of reduced frequency $K = fc/U$ and observer angle θ for analytical (Equation 4.20) (top) and CAA (bottom) predictions.

Fig. 4.13 shows spectral plots comparing the analytical solution for a flat plate ingesting turbulence with and without a wall compared to the corresponding results from the CAA simulations at three observer locations. The figures compare the noise spectrum for the case with and without a wall. The results for the flat plate without a wall are presented to establish the efficacy of the CAA simulations to predict the noise radiated by an aerofoil in the free-field and to demonstrate the effect of the reflecting surface on the noise spectrum. From the spectral plots shown in Fig. 4.13 it can be seen that there is a reasonable agreement at all observer angles. The biggest differences are seen at the downstream observer angle $\theta = 45°$. Due to a frequency shift of the lobes at $K = 1.5$ and 2, the destructive peaks of the CAA simulation move towards the constructive peaks. The CAA simulations using the MOI, predicts the effect of a hard-wall by collecting pressure time-history data on two surfaces (one corresponding to the flat plate and one corresponding to the flat plates' mirror image) and subtracts them. From Fig. 4.13(a) it is observed that the CAA solution without a wall (which corresponds to data collected from one surface) also deviates at $K = 1.5$ and $K = 2$. This could explain the shift in

the peak locations as the minimum/maximum values of the individual solutions that are being subtracted are shifted. Additionally, the deviations in the CAA solution without the wall are within the expected accuracy of the CAA code of ±1.5 dB for most of the frequency range as reported by Gea-Aguilera *et al.* [120]. Thus adding the data collected on two surfaces could compound this error up to 3 dB. The results shown in Fig. 4.13 confirm that the analytical predictions are within 1.5 dB of the CAA simulation for a majority of the frequencies and observer angles with a maximum error of 3 dB at certain frequencies and observer angles.

Fig. 4.13(d) shows the sound power computed using Eqn. (4.32) for the analytical solution and for the CAA simulations. To compute the power radiated by the flat plate, the following equation for the power that accounts for mean flow effects is used [140],

$$\mathcal{P}(\omega) = \frac{r_0}{2\rho_0 c_0} \int_0^{\pi} \frac{\beta^4 A(M,\theta)}{\left(A(M,\theta) - M\cos\theta\right)^2} S_{pp}(r_0,\theta,\omega)\mathrm{d}\theta. \tag{4.32}$$

The sound PoWer Level (PWL) can then be computed as,

$$\mathrm{PWL} = 10\log_{10}\left(\frac{\mathcal{P}\left(r_0,\omega\right)}{\mathcal{P}_{\mathrm{ref}}}\right), \tag{4.33}$$

where $\mathcal{P}_{\mathrm{ref}} = 10^{-12}\,\mathrm{W}$. The power for the flat plate without a wall is computed by integrating the sound intensity from $\theta = 0°$ to $\theta = 180°$ and then doubling the output of this result. For the flat plate in the presence of a reflecting surface, the power is computed by integrating the sound intensity from $\theta = 0°$ to $\theta = 180°$. This value should match the total power radiated by the flat plate in the absence of a wall as the energy in the system in conserved. However, it should be noted that this is an approximation for the power radiated by the flat plate in the presence of a reflecting surface as the data-collection surface does not extend all the way to the wall. Thus, a small amount of the energy escapes. The PWLs match to within 1.5 dB for a majority of the frequency range as shown in Fig. 4.13(d). This demonstrates that the analytical solution and the CAA simulations are conserving energy and that the total power radiated by the flat plate with and without the wall is the same.

Fig. 4.14 shows directivity plots comparing the analytical solution for a flat plate ingesting turbulence with and without a wall compared with the corresponding results from the CAA simulations at two different reduced frequencies. From the directivity plots shown in Fig. 4.14, there is a reasonable agreement between the analytical solution and the CAA simulations at both reduced frequencies. The destructive peaks in the directivity plots at $K = 1.4$ are not as prominent as the analytical solution around $\theta = 90°$. Additionally, a slight shift in the lobes is seen at $K = 2.2$.

From the results shown, it can be concluded that the analytical solution using the MOI (given in Eqn. (4.20)) matches the CAA simulations using the MOI to within the accuracy

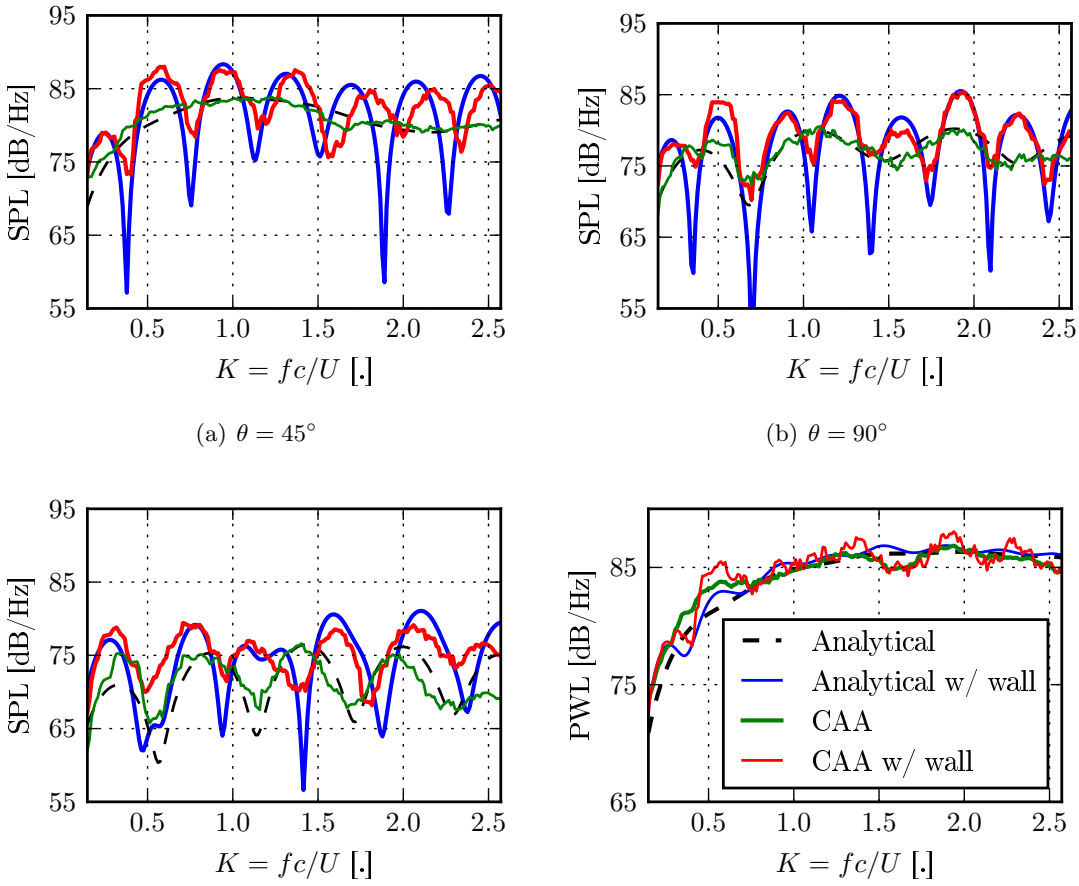

(a) $\theta = 45°$

(b) $\theta = 90°$

(c) $\theta = 120°$

(d) PWL

Figure 4.13: Spectral plots of Sound Pressure Level (SPL) and PWL. The wall is located at $d_{wall} = 2c$ and is simulated using the MOI.

of the CAA simulation.

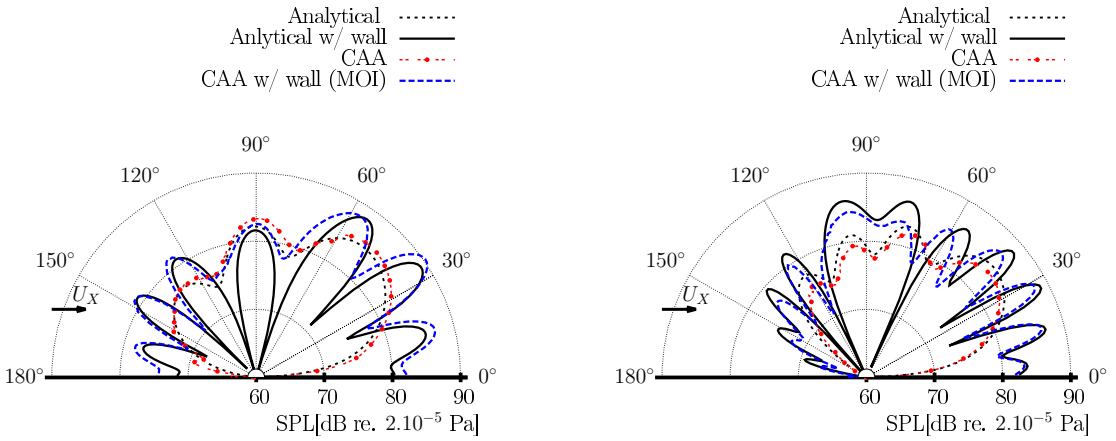

(a) $K = 1.4$ (b) $K = 2.2$

Figure 4.14: Directivity plots of sound pressure level for analytical and CAA simulations at two different reduced frequencies. The wall is located at $d_{wall} = 2c$ and is simulated using the MOI.

4.3.2 Quantification of the assumptions made in the analytical model using CAA

In this section the assumptions made in the derivation of the analytical solution are analysed by running two CAA simulations, one using the MOI and one with a physical hard-wall, as described in Section 4.2.2. The assumptions are the negation of shielding and diffraction effects.

The results of the CAA simulation with and without the hard-wall boundary condition, using the computational setup described in Section 4.2.3, are shown in Fig. 4.15. These simulation results will allow the quantification of the missing diffraction and shielding effects in the analytical model.

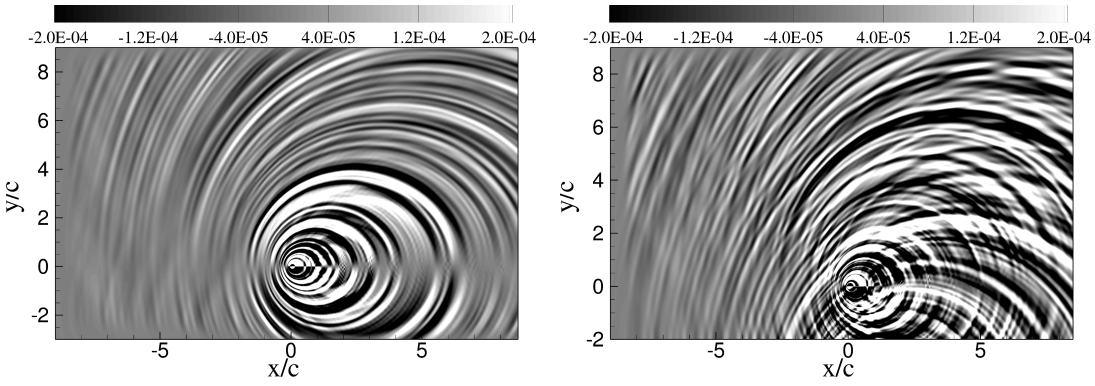

(a) CAA simulation without a wall. (b) CAA simulation with a hard slip-wall.

Figure 4.15: Contours of instantaneous non-dimensional pressure $p/(\rho_0 c_0^2)$ for CAA simulations with (right) and without (left) the hard-wall boundary condition.

Fig. 4.16 shows the PSD of the acoustic pressure computed with CAA simulations using the MOI and, using the hard-slip-wall boundary condition. Looking at the difference between the two CAA simulations in Fig. 4.16(d), the largest differences in the simulations are for the downstream observer locations. However, these differences appear in the location of the destructive peaks as can be seen from Fig. 4.16(b). A slight change in the location or amplitude of the troughs due to numerical errors could cause large differences between the CAA simulation using the MOI and the CAA simulation using the hard-slip-wall boundary condition. These errors are therefore not physical and are an artefact of the numerical implementation. The more substantial differences are located around the 90° observer angle, particularly at high reduced frequencies. This indicates that the flat plate is shielding acoustic waves.

Fig. 4.16(f) shows the difference between the CAA simulations with the hard-wall boundary condition and the analytical solution. There are once again differences observed at the location of the destructive peaks. Additional differences are seen around the $\theta = 90°$ observer angle for reduced frequencies larger than 1.8. From the above discussions it appears that the difference between the two CAA simulations and the analytical solution are minor. There are however, some larger differences around the $\theta = 90°$ observer location at high reduced frequencies that might indicate the flat-plate is shielding acoustic waves from interfering. This effect can be further analysed by looking at spectral and directivity plots.

Fig. 4.17 shows spectral plots comparing the analytical solution for a flat plate ingesting turbulence with a wall compared with the corresponding results from the CAA simulations using the MOI and the hard-slip-wall boundary condition at three observer locations. At $\theta = 45°$ and 120° the analytical prediction and the CAA simulations using the MOI match within 1.5 dB of the CAA simulation using the hard-slip-wall boundary condition for a majority of the frequencies with a maximum error in the peaks of 3 dB at certain frequencies. At $\theta = 90°$, the discrepancy between the MOI and the hard-wall boundary condition is up to 5 dB at certain frequencies. This indicates that the MOI is not capturing the effect of the flat plate shielding acoustic waves.

Fig. 4.17(d) shows the sound power levels for the analytical and CAA simulations. It should be noted that the data collection surface for the hard-wall simulations only extended from $\theta = 20°$ to $\theta = 158°$ due to numerical considerations. Thus the sound power level is computed by integrating the sound intensity only between these angles. While, this will not reflect the true sound power level of the flat plate, it will still provide a valid comparison between the three simulations. From Fig. 4.17(d) it can once again be seen that the levels match to within 1.5 dB for a majority of the frequency range for the two CAA simulations and prediction using Eqn. (4.20).

The results in this section have highlighted the fact that the MOI does not capture all the effects of noise produced by a flat plate ingesting turbulence near a hard-wall. The main discrepancies observed occur around the 90° observer angle. This indicates that the flat plate is shielding acoustic waves. This effect can be further analysed by computing the PSD of the sound at different heights from the wall.

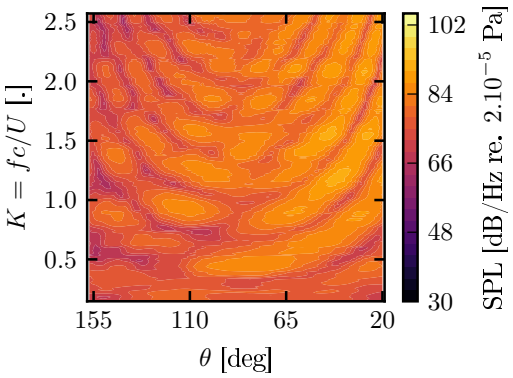

(a) Results from the CAA simulation with a wall at $d_{wall} = 2c$.

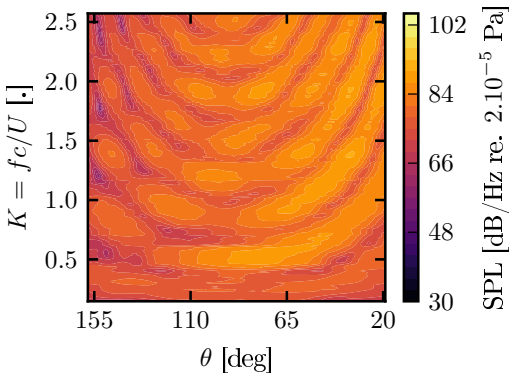

(b) Results from the CAA simulation with a wall (simulated using the MOI) at $d_{wall} = 2c$.

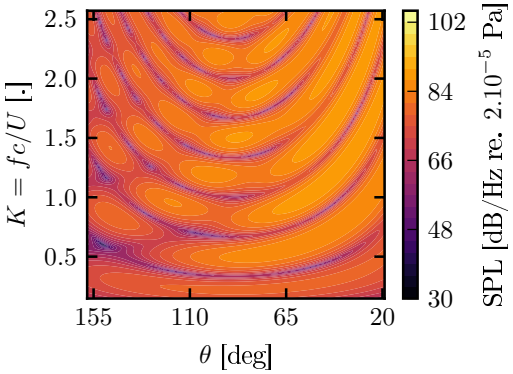

(c) Analytical solution with a wall at $d_{wall} = 2c$.

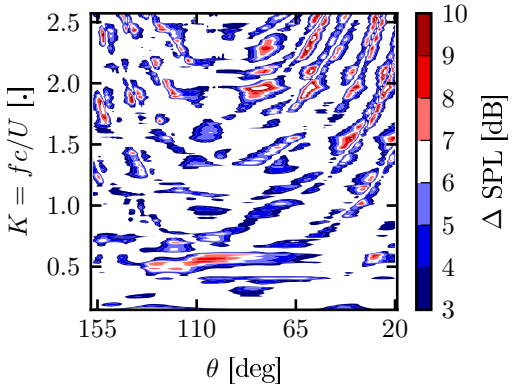

(d) The absolute difference in SPL between the CAA simulations.

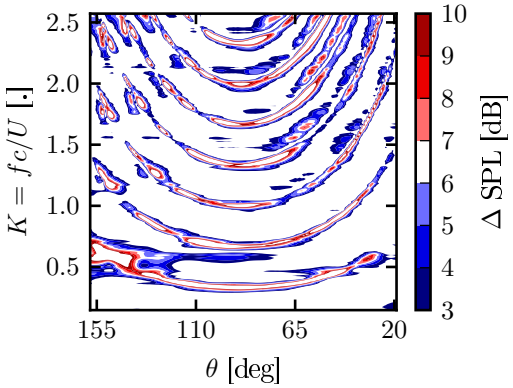

(e) The absolute difference in SPL between the CAA simulation with the MOI and the analytical solution.

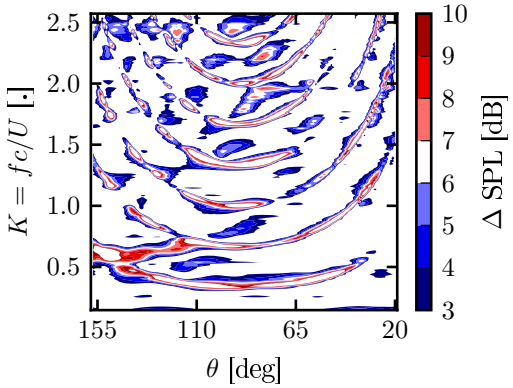

(f) The absolute difference in SPL between the CAA simulation using the hard-wall boundary condition and the analytical solution.

Figure 4.16: Contours of sound pressure level as a function of reduced frequency $K = fc/U$ and observer angle θ for analytical (Equation 4.20) (bottom) and CAA (top) predictions.

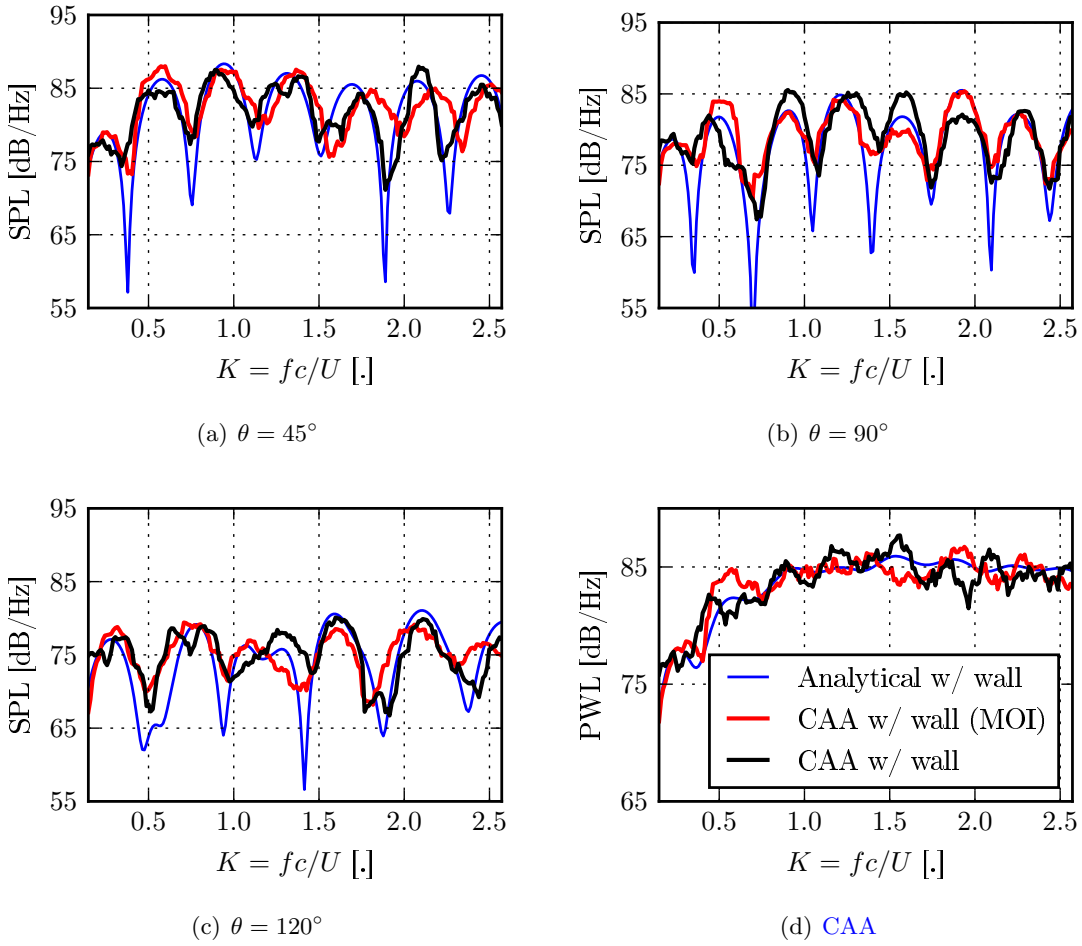

(a) $\theta = 45°$

(b) $\theta = 90°$

(c) $\theta = 120°$

(d) CAA

Figure 4.17: Spectral plots of SPL and PWL. The wall is located at $d_{wall} = 2c$ and is simulated in the CAA simulation using both the MOI and the hard-wall boundary condition.

4.3.3 The effect of changing the distance of the aerofoil to the wall.

In this section the effect of changing the height of the flat plate from the wall is investigated. As the height of the flat plate from the wall is changed, it is expected that the shadow zone created by the aerofoil will change. Analysing the directivity pattern for the flat plate at different heights to the wall will therefore help identify the extent of the shadow zone and its effect on the PSD of the radiated sound with a wall. In this section the PSD of the sound is investigated at three different heights to the wall, *viz.* $2c$, $1c$, and $0.75c$.

Fig. 4.18 shows the directivity plots for analytical predictions and CAA solutions of a flat plate ingesting turbulence at three different heights from the wall. The green lines on the plot depict the extent of the geometrical shadow-zone caused by the presence of the flat plate. This angle is computed as the solution of the following equation,

$$r_0 c \sin\theta_s - 2 r_0 d_{wall} \cos\theta_s + c\, d_{wall} = 0, \tag{4.34}$$

where $2\theta_s$ is the extent of the shadow zone. In Fig. 4.18, the CAA simulations using the hard-wall boundary condition match well with the analytical solution at all observer angles except within the shadow-zone. It is also observed that outside the shadow zone, the location of the crests and troughs for all three simulations are in approximately the same location. However, within the shadow zone, the CAA simulation with the hard-slip-wall displays crests and troughs that are at a different location than the MOI predicts. This implies that as the flat plate is shielding acoustic waves, the interference of the acoustic waves above the surface of the flat plate is modified.

Additionally, discrepancies are seen in the amplitudes at all observer angles for the high frequency directivity plots in Figs. 4.18(b), 4.18(d), and 4.18(f). This can be explained by two effects. Firstly, the smaller wavelength acoustic waves at the higher frequencies are likely to be more effectively shielded by the flat plate. Secondly, the acoustic waves at high-frequencies are more susceptible to scattering. For a flat plate the radius of the nose is small enough for the scattering object to scatter waves according to Rayleigh scattering. Thus the smallest wavelengths are scattered the most.

Another observation that can be made from examining the directivity plots in Fig. 4.18 is the effect of the distance from the flat plate to the wall. From Figs. 4.18(a), 4.18(c), and 4.18(e) it can be seen that the closer the flat plate is to the wall, the more significant the discrepancies are within the shadow zone. This is to be expected as the extent of the shadow zone increases as the flat plate moves closer to the wall and thus a larger proportion of the acoustic waves are shielded. These findings imply that the shielding of acoustic waves by the flat plate is an important factor to consider only if the flat plate is placed very close the wall.

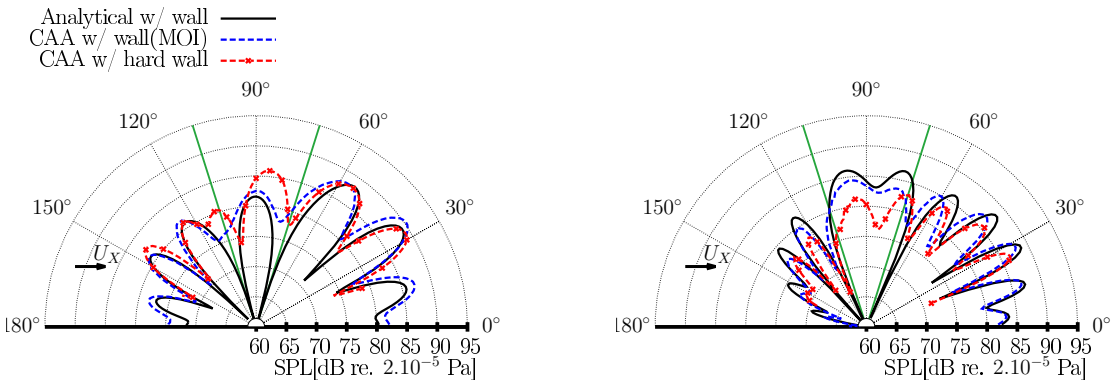

(a) $K = 1.4$, $d_{wall} = 2c$

(b) $K = 2.2$, $d_{wall} = 2c$

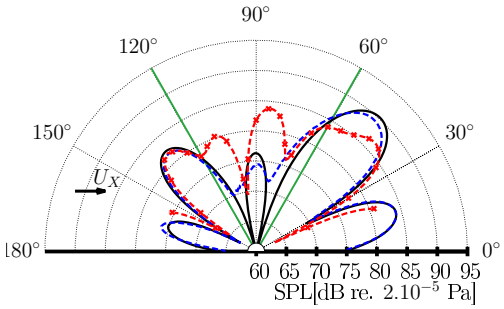

(c) $K = 1.4$, $d_{wall} = 1c$

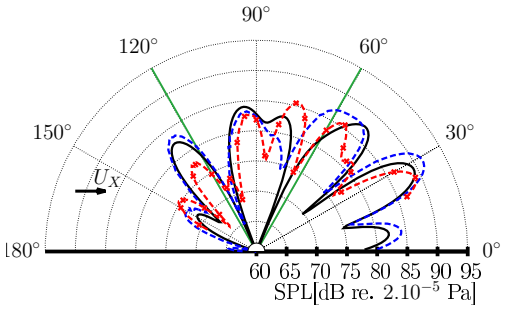

(d) $K = 2.2$, $d_{wall} = 1c$

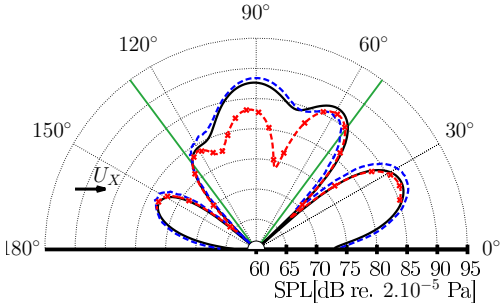

(e) $K = 1.4$, $d_{wall} = 0.75c$

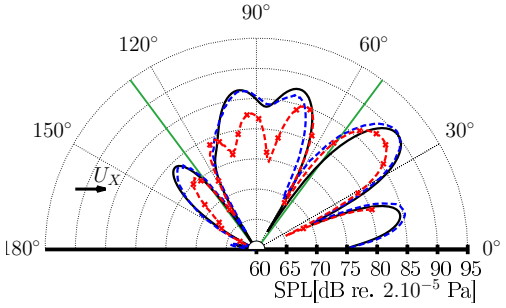

(f) $K = 2.2$, $d_{wall} = 0.75c$

Figure 4.18: Directivity plots of sound pressure level for analytical and CAA simulations at two different reduced frequencies. The green lines indicate the extent of the shadow zone.

From the results shown, it can be concluded that while the MOI predicts the noise spectrum of a flat plate ingesting turbulence in proximity to a wall at most observer angles, it does not predict the shielding effect of the flat plate. It has been shown that the MOI does not capture the shadow-zone effect and the predictions using the MOI differ significantly from the CAA simulations using a hard-slip-wall around the 90° observer angle. This effect has been shown to be more pronounced at higher frequencies than at

lower frequencies due to the smaller wavelengths being shielded more effectively. The errors seen at high frequencies might also be caused due to the scattering of acoustic waves. Finally, the shadow-zone effect diminishes as the distance from the aerofoil to the wall is increased. This is because the extent of the shadow-zone decreases as the height from the aerofoil to the wall is increased.

4.4 Conclusions

This chapter has extended Amiet's [21] 2D translating aerofoil model to include wall-effects by using the MOI. The main aim of this chapter was to quantify the assumptions that were made in developing this analytical model. This was done by conducting two different types of CAA simulations. One CAA simulation modelled the wall using the MOI and the other CAA simulation was physically representative and modelled the hard-wall using a hard-wall boundary condition. The CAA simulation using the MOI was used to verify the analytical solution. Comparing the MOI with the physically representative CAA simulation allowed the quantification of assumptions that were made in the MOI. The main conclusions that are drawn from this chapter are:

- Amiet's formulation for a 2D translating aerofoil was extended to included the effects of a hard-wall by using the MOI.
- This extension to Amiet's formulation adds three terms to Amiet's original formulation. The physical significance of these terms has been examined by computing the low frequency, low Mach number limit of the PSD. Examining the formulation in this limit, it is shown that the first two additional terms cause interference patterns and the third term modulates the amplitude. It is shown that the ratio of the power radiated by the flat plate with a hard-wall to the power radiated by the flat plate in the free-field, in the low Mach number, low frequency limit is the same as that of a compact dipole. The power ratio in this limit goes to 0 as the distance to wall is decreased and has a maximum of approximately 1.8.
- The analytical solution using the MOI is verified using a CAA simulation that also uses the MOI to model a the effect of a wall. This was done by using 2 data collection surfaces that represent the location of the observer from the real and image sources. The pressure data collected on these two surfaces was then subtracted to obtain the final result. When the analytical solution is compared to the CAA simulation using the MOI, it is shown that the analytical solution matches the results of the CAA simulation to within the accuracy levels permitted by the CAA simulation.

- The assumptions that were made in deriving the analytical solution, i.e. the negation of shielding and diffraction effects, were quantified by running a physically representative CAA simulation that models the hard-wall using a hard-slip-wall boundary condition. By comparing the CAA simulation that uses the MOI and the CAA simulation that uses the hard-slip-wall boundary condition, it is shown that the MOI does not capture the shielding effect of the flat plate. This can have a significant effect on the noise spectrum for observers located above the flat plate. By comparing the directivity of the sound at three different heights from the wall it is shown that the effect of the shadow zone decreases as the height from the flat plate to the wall is increased. This is because the extent of the shadow zone becomes narrower as the height from the flat plate to the wall is increased.

]

Chapter 5

Modelling wall-effects in Amiet's rotor noise model

The aim of this thesis is to predict the noise radiated by a rotor ingesting a turbulent boundary layer. In Chapter 3 Amiet's [18] frequency-domain rotor noise model was presented. This rotor noise model predicts the noise radiated by a rotating aerofoil by azimuthally averaging and frequency correcting the noise radiated by a translating aerofoil. This model ignores the acceleration effects of the blades. This is a valid assumption as long as the frequency of turbulence impinging on the rotor is much smaller than the frequency of the rotor. Using the isotropic von Kármán spectrum presented in that chapter it was shown that the resultant noise spectrum had several discrepancies when predictions obtained using the rotor noise model were compared with the experimental results of a rotor ingesting a turbulent boundary layer. The biggest discrepancies were the missing second correlation peak and a significant discrepancy in amplitude. This chapter extends Amiet's [18] rotor noise model by including wall-effects using the Method of Images (MOI). This is expected to improve the amplitude discrepancy that was observed.

In Chapter 4 the assumptions made in using the MOI were quantified using Computational AeroAcoustic (CAA) simulations. Using these simulations it was found that the MOI is accurate at predicting wall effects except in the shadow-zone of the aerofoil. While discrepancies were observed in the shadow-zone above the aerofoil, they were restricted to a small range of observers and the discrepancies became smaller as the aerofoil was moved away from the wall. As such the MOI provides satisfactory results and will be used in Amiet's [18] rotational model to predict wall-effects for a rotor ingesting turbulence near a hard-wall.

This chapter will first provide the formulation for the Power Spectral Density (PSD) of a rotor ingesting turbulence near a hard-wall. This is done by adding a mirror image to

the Green's functions terms of Amiet's formulation for a translating aerofoil as was done in Chapter 4. The formulation for the PSD of the translating aerofoil is then extended to account for rotational effects by azimuthally averaging and frequency correcting the PSD of the translating aerofoil. It is shown that in the low Mach number low frequency limit, the rotor behaves like a dipole. By changing the azimuthal and stagger angle of the blade, the solution is verified with analytical solutions for horizontal and vertical dipoles. The predictions using Amiet's [18] rotor noise model with wall effects are then compared against experimental measurements. Finally, the effect of the wall is examined by computing predictions without and with wall effects modelled. This study is done without and with blade-to-blade correlation modelled.

5.1 Formulation for the power spectral density of the rotor

In this section the formulation for the PSD of the acoustic pressure of a rotor ingesting turbulence near a hard-wall is developed. The effects of a hard-wall are included in the analytical rotor noise model of Amiet [18] by using the MOI. First, the coordinate system with the mirror rotor is detailed. Next, the MOI is used to add wall-effects to Amiet's [18] translating aerofoil noise model. This translating aerofoil model is then azimuthally averaged and frequency corrected to account for the rotation of the aerofoil. Finally, the low frequency low Mach number limit of the analytical solution is examined.

5.1.1 Coordinate systems

The coordinate systems used to model the mirror rotor are now described. In the engine fixed frame as shown in Fig. 5.1, the observer coordinates from the mirror rotor are given by,

$$\left(x^{\#}, y^{\#}, z^{\#}\right) = \left(r_0 \cos\theta, 0, -\left(r_0 \sin\theta + 2d_{wall}\right)\right),$$

where the superscript # indicates distances measured with respect to the mirror source and the wall is located at a distance d_{wall} from the engine hub. The conversion from the engine-fixed coordinates to blade-fixed coordinates is given by the coordinate transformation matrices in Eqns. (3.8) and (3.9).

The addition of a hard-wall only changes the wall-normal coordinate of the observer and thus the horizontal coordinate of the observer from the real and image source is identical. This fact is made use of to compute the distance of the observer from the image source

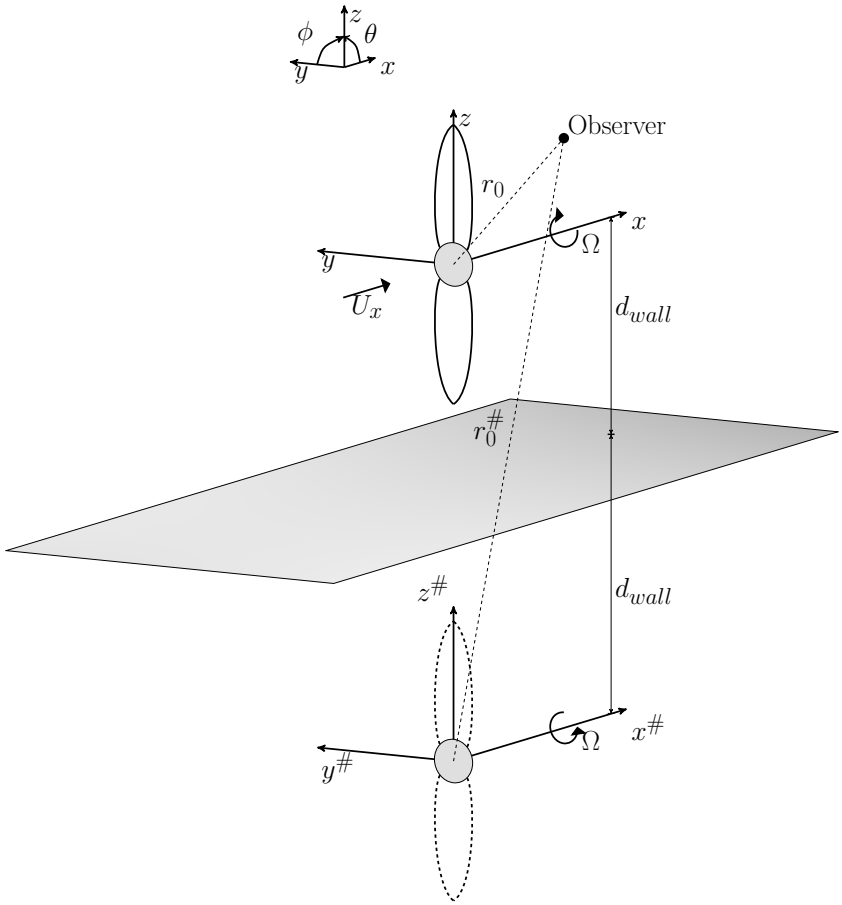

Figure 5.1: The engine-fixed coordinate system for a rotor and its mirror image.

and the angle of the observer from the axis of the image rotor,

$$\begin{aligned} r_0^{\#} &= \sqrt{\left(r_0 \sin\theta + 2d_{wall}\right)^2 + \left(r_0 \cos\theta\right)^2}, \\ \theta^{\#} &= \tan^{-1}\left(\frac{r_0 \sin\theta + 2d_{wall}}{r_0 \cos\theta}\right). \end{aligned} \tag{5.1}$$

5.1.2 Formulation for the power spectral density of a rotor near a hard-wall

In this section, the formulation of the noise produced by a rotor ingesting turbulence that was presented in Chapter 3, is extended to account for a hard-wall placed in proximity to the rotor. This is done using the MOI in a similar manner as was done in Chapter 4.

The formulation for the point dipole given by Eqn. (3.15) is modified by adding its mirror image to it in phase. This is done to ensure zero normal velocity at the wall [17],

$$p^{(n)}(X,\mathcal{C},Z,\omega) = \frac{\mathrm{i}\pi k_0\rho_0 Y b}{2\sigma^2} e^{\mathrm{i}\mu(M_X X-\sigma)}\mathcal{L}(K_X,K_Z,\kappa)\int_{-\infty}^{\infty} v_R(K_X,k_Y,K_Z)e^{-\mathrm{i}k_Y n\mathcal{C}}\mathrm{d}k_Y + \frac{\mathrm{i}\pi k_0\rho_0 Y^{\#} b}{2\sigma^2} e^{\mathrm{i}\mu(M_X X^{\#}-\sigma^{\#})}\mathcal{L}^{\#}(K_X,K_Z,\kappa^{\#})\int_{-\infty}^{\infty} v_R(K_X,k_Y,K_Z)e^{-\mathrm{i}k_Y n\mathcal{C}}\mathrm{d}k_Y, \tag{5.2}$$

where $k_0 = \omega/c_0$ is the wave number, $\beta = \sqrt{1-M_X^2}$ is the compressibility factor, $\mu = M_X k_X/\beta^2$ is the acoustic reduced frequency and $\sigma = \sqrt{X^2+\beta^2\left(Y^2+Z^2\right)}$ is the flow corrected distance to the observer.

The noise spectrum with blade-to-blade correlation is determined by computing the cross-correlation of the 0^{th} and n^{th} blade,

$$S_{pp}^{(n)}(X,\mathcal{C},Z,\phi,\omega) = \frac{\pi U_X}{R}\mathbb{E}\left[p^{(0)}\left(r_0,\theta,\phi,\omega\right)\left(p^{(n)}\left(r_0,\theta,\phi,\omega\right)\right)^*\right]. \tag{5.3}$$

Using (5.3) and (5.2) the cross-PSD of the acoustic pressure can be developed as,

$$S_{pp}^{(n)}(r_0,d_{wall},\theta,\phi,\omega) = S_{pp}^{NW} + S_{pp}^{P1} + S_{pp}^{P2} + S_{pp}^{I}, \tag{5.4}$$

where each of the terms are defined as,

$$\begin{aligned}
S_{pp}^{NW}(X,\mathcal{C},Z,\phi,\omega) &= \pi U_X d\left(\frac{k_0\rho_0 Y b}{\sigma^2}\right)^2 |\mathcal{L}(K_X,K_Z,\kappa)|^2\tilde{\Phi}_{vv}(K_X,K_Y,K_Z),\\
S_{pp}^{P1}(X,\mathcal{C},Z,d_{wall},\phi,\omega) &= \pi U_X d(\mathrm{A})(k_0\rho_0 b)^2\tilde{\Phi}_{vv}(K_X,K_Y,K_Z),\\
S_{pp}^{P2}(X,\mathcal{C},Z,d_{wall},\phi,\omega) &= \pi U_X d(\mathrm{A})^*(k_0\rho_0 b)^2\tilde{\Phi}_{vv}(K_X,K_Y,K_Z),\\
S_{pp}^{I}(X,\mathcal{C},Z,d_{wall},\phi,\omega) &= \pi U_X d\left(\frac{k_0\rho_0 Y^{\#} b}{\sigma^2}\right)^2 |\mathcal{L}^{\#}(K_X,K_Z,\kappa)|^2\tilde{\Phi}_{vv}(K_X,K_Y,K_Z),
\end{aligned} \tag{5.5}$$

where quantities with a superscript $^{\#}$ indicate values at the mirror source and [1],

$$\mathrm{A} = \left(\frac{YY^{\#}}{\sigma\sigma^{\#}}\right)^2 e^{\mathrm{i}\mu\left(M_X\left(X-X^{\#}\right)+\left(\sigma^{\#}-\sigma\right)\right)}|\mathcal{L}\left(\mathcal{L}^{\#}\right)^*|, \tag{5.6}$$

where,

$$\tilde{\Phi}_{vv}(K_X,K_Y,K_Z) = \int_{-\infty}^{+\infty}\Phi_{vv}(K_X,k_Y,K_Z)e^{-\mathrm{i}k_Y n\mathcal{C}}\mathrm{d}k_Y. \tag{3.26}$$

Eqn. (5.4) and Eqn. (5.5) show that the hard-wall has added three additional terms to Amiet's original formulation [21] for the cross-PSD of the rotor. S_{pp}^{NW} represents Amiet's

[1] It should be noted that the Green's functions and the acoustic lift functions that have a superscript # are not different functions but indicate that their arguments should be evaluated for the image source.

original formulation. The cross-terms S_{pp}^{P1} and S_{pp}^{P2} represent the interference of the rotor and image rotor sources. The third additional term S_{pp}^{I} gives the amplitude contribution of the image rotor. The interference of the acoustic waves in the cross-terms is due to the factor $e^{\pm \mathrm{i}\mu\left(M_X\left(X-X^{\#}\right)+\left(\sigma^{\#}-\sigma\right)\right)}$. This factor can be imaginary and thus changes the phase of the solution. This term is a function of the distance to the observer from the real and image sources and thus represents the phase difference in the acoustic waves that arrive at the observer from the real and image sources. This phase difference can result in either constructive or destructive interference. The S_{pp}^{I} term gives the amplitude contribution of the image rotor as it would represent the doubling of acoustic pressure in the absence of the interference terms.

Equation 5.5 represents the formulation for a translating aerofoil near a hard-wall with blade to blade correlation. As was done in Chapter 3, multiple blade passes are accounted for by computing the following cross-correlation function [18],

$$R_{pp}(x, y, \tau) = \sum_{n=-\infty}^{+\infty} R_{pp}^{(n)}(x, y, \tau - nT), \tag{3.28}$$

where nT is the time between eddy chops as heard by the observer. Each of the four terms in Eqn. 5.4 will have different times between blade chops as heard by the observer. For the first and fourth terms of Eqn. 5.4, T represents the time between the 0^{th} and n^{th} blade of the real and image rotor chopping an eddy. For the cross-terms, T represents the time between the 0^{th} blade of the real rotor chopping an eddy and the n^{th} blade of the image rotor (or vice-versa) chopping the same eddy. The next step is to determine these time differences.

The time between eddy chops by the real rotor is the same as for the case without the wall. This was defined in Chapter 3 as,

$$T = T_1 - \frac{\mathcal{C}Y}{c_0\sigma}, \tag{3.32}$$

The time between eddy chops by the image rotor is then determined by replacing the relevant distances with distances measured from the image rotor,

$$T^{\#} = T_1 - \frac{\mathcal{C}Y^{\#}}{c_0\sigma^{\#}}. \tag{5.7}$$

For the first cross-term, the time between the 0^{th} blade from the real rotor and the n^{th} blade from the image rotor chopping an eddy is given by,

$$T^{P1} = T_1 + \frac{M_X\left(X^{\#} - X\right) + \left(\sigma - \sigma^{\#}\right)}{c_0\beta^2} - \frac{\mathcal{C}Y^{\#}}{c_0\sigma^{\#}}, \tag{5.8}$$

and for the second cross-term, the time between the n^{th} blade from the real rotor and the 0^{th} blade from the image rotor chopping an eddy is given by,

$$T^{P2} = T_1 + \frac{M_X\left(X - X^{\#}\right) + \left(\sigma^{\#} - \sigma\right)}{c_0\beta^2} - \frac{\mathcal{C}Y}{c_0\sigma}. \tag{5.9}$$

The cross PSD can now be determined for multiple blade passages by taking the Fourier transform of Eqn. (3.28)[18],

$$S_{pp}(r_0, d_{wall}, \theta, \phi, \omega) = \sum_{n=-\infty}^{\infty} S_{pp}^{(n)}(r_0, \theta, \phi, \omega)e^{\mathrm{i}n\omega T}. \tag{3.40}$$

Eqn. (5.5) is the formulation for the cross-PSD of a translating aerofoil. This formulation can be extended for rotational motion by the application of the appropriate Doppler factors as is done in Chapter 3. However, for the extension to the case with a rotor placed near a hard-wall one must account for the Doppler shift and retarded time effects of both the rotor and its image source. Thus we have two Doppler factors. We denote the Doppler shifted frequency as heard by the observer from the real rotor as ω_ϕ^R and from the image rotor as ω_ϕ^I. These two frequencies can be computed using the following formulations,

$$\begin{aligned} \frac{\omega_\phi^R}{\omega} &= 1 + M_\phi \frac{\sin\theta\sin\phi}{\sqrt{1 - M_x^2\sin^2\theta}}, \\ \frac{\omega_\phi^I}{\omega} &= 1 - M_\phi \frac{(r_0 + 2d_{wall})\sin\theta\sin\phi}{r_0\sqrt{1 - M_x^2\sin^2\theta^{\#}}}. \end{aligned} \tag{5.10}$$

where it should be noted that the mirror rotor is rotating in the opposite direction of the real rotor.

However, the S_{pp}^P term in Eqn. (5.4) contains frequencies from both the image and the real rotor. Acoustic waves that are produced by the real rotor arrive at a frequency ω^R while acoustic waves from the image rotor arrive at a frequency ω^I. From Eqn. (5.10) it is observed that the Doppler factor will by approximately 1 plus a small factor for the real rotor and 1 minus a small factor for the image rotor. Thus, the two Doppler factors should negate each other. For this reason, no Doppler correction is applied to the cross terms. This approach should be valid for rotors operating at low rotational speed. The validity of this approach for faster rotational speeds will need to be investigated further.

The cross-PSD of the translating aerofoil can now be extended for the rotational case using Eqns. (5.4) and (5.10) with azimuthal averaging,

$$S_{pp} = \frac{1}{2\pi}\int_0^{2\pi}\left[\left(\frac{\omega}{\omega_\phi^R}\right)^2 S_{pp}(\omega_\phi)^{NW} + S_{pp}^{P1} + S_{pp}^{P2} + \left(\frac{\omega}{\omega_\phi^I}\right)^2 S_{pp}^{I}(\omega_\phi)\right]\mathrm{d}\phi.$$

Therefore, the cross PSD for a rotor with blade-to-blade correlation and with a hard-wall can be modelled as,

$$\begin{aligned} S_{pp}(r_0, d_{wall}, \theta, \phi, \omega) = &\sum_{j=1}^{l}\sum_{n=-\infty}^{\infty}\frac{2\pi}{\mathcal{C}}\frac{\pi B U_{X,j}\delta r_j}{2}(k_0\rho_0 b_j)^2\times \\ &\left\{\frac{(Y|\mathcal{L}|)^2}{\sigma^4}\Phi_{vv}\left(K_X, K_{Y,j,n}\right) + \frac{\left(Y^{\#}|\mathcal{L}^{\#}|\right)^2}{\left(\sigma^{\#}\right)^4}\Phi_{vv}\left(K_X, K_{Y,j,n}^{\#}\right) + \right. \\ &\left. \mathrm{A}\Phi_{vv}\left(K_X, K_{Y,j,n}^{P1}\right) + \mathrm{A}^*\Phi_{vv}\left(K_X, K_{Y,j,n}^{P2}\right)\right\}, \end{aligned} \tag{5.11}$$

where quantities with the superscript # correspond to the mirror source quantities and K_Y is given by,

$$K_{Y,n} = \frac{\omega T + 2\pi n}{\mathcal{C}}. \tag{3.42}$$

In Eqn. (5.11) strip theory has been used to sum the sound pressure at l span-wise locations with each strip having a width δr_j. This strip theory is valid as long as the width of the span is much larger than the span-wise correlation length [137]. Additionally, the effect of the skewed gusts has been neglected. This implies that in the coordinate system fixed to the blade, the span-wise wavenumber, k_Z is set to zero.

The cross PSD of the real and image rotor (the first and second terms in the curly braces that arise from the S_{pp}^{NW} and S_{pp}^{I} terms in Eqn. (5.5)) are in phase and thus are real. However, the terms that account for the interference between the real and image rotor (the third and fourth terms in the curly braces that arise from the S_{pp}^{P1} and S_{pp}^{P1} terms in Eqn. (5.5)) are not in phase and thus the individual cross PSD could be imaginary.

Eqn. (5.11) represents the extension to account for the hard-wall. This extension is important to model the boundary layer ingestion noise source. If the hard-wall was not accounted for there would be a severe discrepancy in the amplitude of the noise spectrum. The next step is to determine the noise spectra of the rotating aerofoil using the extended translating aerofoil model.

This section has determined the PSD for a rotor ingesting turbulence near a hard-wall. The MOI has been used to include wall-effects in Amiet's [18] rotor noise model. This is

similar to the approach that was used in Chapter 4. However, this section adds wall-effects to a 3D translating aerofoil model. This translating aerofoil model is then extended to determine the noise radiated by a rotor by azimuthally averaging and frequency correcting the noise spectrum. The Doppler correction that needs to be applied to the real and imaginary terms of the formulation has been determined. The cross terms that contain frequencies from both, the real and image rotor are not frequency corrected. This is because the real and image rotor are rotating in the opposite directions and thus their Doppler factor should approximately cancel out for low rotational speeds. In the next section, the low Mach number low-frequency asymptote for the rotor ingesting turbulence near a hard-wall will be determined. This will be used as an initial verification of the rotor noise model and to further analyse the additional terms that are added to the formulation due to the presence of the hard-wall.

5.1.3 Formulation for the radiated power in the low-frequency low Mach number limit

In this section the low-frequency low Mach number limit of Eqn. 5.4 is examined. This is done in order to perform an initial verification of the analytical solution. This is because in this limit a single blade of the rotor should behave like a compact dipole. By varying the blade stagger angle α and the blade azimuthal angle ϕ, the inclination of the dipole axis with respect to the wall can be varied. As analytical solutions for a compact dipole whose axis is horizontal and perpendicular to the wall have been computed by Ingard and Lamb [146], the low-frequency low Mach number limit of the rotor can be verified against these analytical solutions. Additionally, the analytical solution in this limit is simplified and it is thus easier to determine the effect of each of the individual terms that are added due to the presence of a hard-wall.

In a similar manner as was done in Sect. 4.1.3 of Chapter 4 the low Mach number low-frequency limits of the acoustic lift integral and the velocity correlation spectrum are determined using Eqn. (4.24). The PSD of one rotor blade without azimuthal averaging and blade-to-blade correlation is given by,

$$\begin{aligned} &S_{pp}\left(r_0,\theta,\omega,d_{wall}\right) = \\ &\pi U_x d\left(k_0\rho_0 b\right)^2 \frac{\overline{u^2}L}{2\pi}\left|S\left(\mu_h\right)\right|^2\left\{\mathcal{D}^{NW}+\mathcal{D}^{P}\left(e^{\mathrm{i}\mu(\sigma-\sigma^{\#})}+e^{-\mathrm{i}\mu(\sigma-\sigma^{\#})}\right)+\mathcal{D}^{I}\right\}, \end{aligned} \tag{5.12}$$

The next step in simplifying Eqn. (5.12) is to determine each of the directivity functions. To determine the directivity functions, the on-blade coordinates aligned with the blade chord for the real and mirror rotor need to be determined. The on-blade coordinates aligned with the blade chord for the real rotor are determined using Eqns. (3.8) and (3.9)

as,

$$\begin{aligned} X &= x\cos\alpha + \sin\alpha\left[y\cos\phi + z\sin\phi\right], \\ Y &= -x\sin\alpha + \cos\alpha\left[y\cos\phi + z\sin\phi\right], \\ Z &= -y\sin\phi + z\cos\phi, \end{aligned} \tag{5.13}$$

and for the mirror rotor as,

$$\begin{aligned} X^{\#} &= x\cos\alpha + \sin\alpha\left[y\cos\phi + z^{\#}\sin\phi\right], \\ Y^{\#} &= -x\sin\alpha + \cos\alpha\left[y\cos\phi + z^{\#}\sin\phi\right], \\ Z^{\#} &= -y\sin\phi + z^{\#}\cos\phi, \end{aligned} \tag{5.14}$$

where $z^{\#} = -(r_0\sin\theta + 2d_{wall})$. In the low Mach number limit the compressibility factor β is 1 and therefore the flow corrected distances to the observer for the real and mirror rotor are $\sigma = \sqrt{X^2+Y^2+Z^2} = r_0$ and $\sigma^{\#} = \sqrt{(X^{\#})^2+(Y^{\#})^2+(Z^{\#})^2} = r_0^{\#}$. Using a Taylor series approximation,

$$\begin{aligned} r_0^{\#} &= r_0(X+\delta_x, Y+\delta_y, Z+\delta_z) \simeq r_0\left(X,Y,Z\right) + \delta_x\frac{\partial\sigma}{\partial X} + \delta_y\frac{\partial\sigma}{\partial Y} + \delta_z\frac{\partial\sigma}{\partial Z}, \\ &\simeq r_0 - \frac{2d_{wall}}{r_0}\left\{\sin\phi\left(y\cos\phi + z\sin\phi\right) + \left(-y\sin\phi + z\cos\phi\right)\cos\phi\right\} + \mathcal{O}\left(d_{wall}^2\right) \\ &\simeq r_0 - 2d_{wall}\sin\theta + \mathcal{O}\left(d_{wall}^2\right), \end{aligned} \tag{5.15}$$

where $x = r_0\cos\theta$, $y = 0$, $z = r_0\sin\theta$, $\delta_x = -2d_{wall}\sin\alpha\sin\phi$, $\delta_y = -2d_{wall}\sin\phi\cos\alpha$ and $\delta_z = -2d_{wall}\cos\phi$. Additionally, from Eqn. (5.15),

$$\frac{r_0^{\#}}{r_0} = 1 - \mathcal{O}\left(\frac{d_{wall}}{r_0}\right). \tag{5.16}$$

The first directivity function, $\mathcal{D}^{NW}$, is the distance from the real source to the observer,

$$\begin{aligned} \sigma^4\mathcal{D}^{NW} &= Y^2, \\ r_0^4\mathcal{D}^{NW} &= x^2\sin^2\alpha + z^2\cos^2\alpha\sin^2\phi - xz\sin 2\alpha\sin\phi. \end{aligned} \tag{5.17}$$

The second directivity term $\mathcal{D}^P$ is given by,

$$\begin{aligned} (\sigma^2(\sigma^{\#})^2)\mathcal{D}^P &= \left[YY^{\#}e^{i\mu(\sigma-\sigma^{\#})} + YY^{\#}e^{-i\mu(\sigma-\sigma^{\#})}\right], \\ r_0^4\mathcal{D}^P &= 2\left\{x^2\sin^2\alpha - zz^{\#}\cos^2\alpha\sin^2\phi - \frac{x\sin 2\alpha\sin\phi}{2}\left(z - z^{\#}\right)\right\}\cos\left(\xi\sin\theta\right), \end{aligned} \tag{5.18}$$

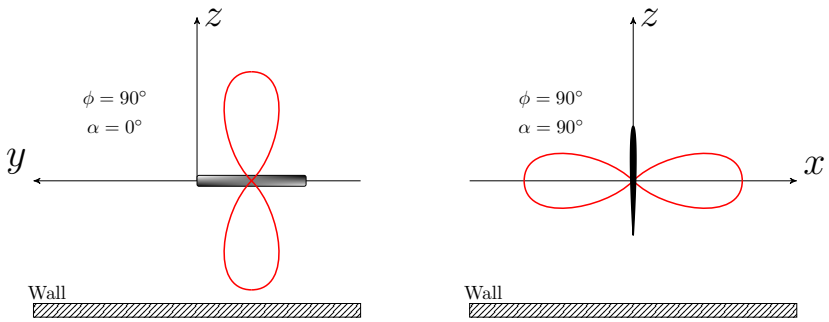

Figure 5.2: A schematic of one rotor blade at azimuthal angle (ϕ) = 90°. Setting the stagger angle (α) to 0° results in a vertical dipole and setting the stagger angle (α) to 0° results in a horizontal dipole.

where $\xi = 2k_0 d_{wall}$. The third directivity function $\mathcal{D}^I$ is the distance from the mirror source to the observer,

$$\begin{aligned}(\sigma^{\#})^4 \mathcal{D}^I &= \left(Y^{\#}\right)^2, \\ r_0^4 \mathcal{D}^I &= x^2 \sin^2\alpha + (z^{\#})^2 \cos^2\alpha \sin^2\phi + x(z^{\#}) \sin 2\alpha \sin\phi.\end{aligned} \tag{5.19}$$

The total directivity function is $\mathcal{D} = \mathcal{D}^{NW} + \mathcal{D}^P + \mathcal{D}^I$. From Fig. 5.2 for a blade at an azimuthal angle (ϕ) of 90°, setting the blade stagger angle (α) to 0° should result in a dipole whose axis is perpendicular to the wall,

$$\mathcal{D}\left(\alpha = 0, \phi = \frac{\pi}{2}\right) = \frac{1}{r_0^4}\left[z^2 + (z^{\#})^2 - 2zz^{\#}\cos(\xi \sin\theta)\right], \tag{5.20}$$

which after making the approximation $z^{\#} \simeq r_0 \sin\theta$ results in,

$$\mathcal{D}\left(\alpha = 0, \phi = \frac{\pi}{2}\right) = \frac{2}{r_0^2}\sin^2\theta\left[1 - \cos(\xi \sin\theta)\right]. \tag{5.21}$$

The ratio of the power radiated with the wall present to the free-field power is given by,

$$\begin{aligned}\frac{\mathcal{P}}{\mathcal{P}_0} &= \frac{\int_{-\pi/2}^{\pi/2} \sin^2\theta\left[1 - \cos(\xi\sin\theta)\right]\cos\theta \mathrm{d}\theta}{2\int_{-\pi/2}^{\pi/2}\sin^2\theta\cos\theta \mathrm{d}\theta} \\ &= 1 - \frac{6\cos\xi}{\xi^2} + \frac{6\sin\xi}{\xi^3} - \frac{3\sin\xi}{\xi}.\end{aligned} \tag{5.22}$$

Similarly, for a blade at an azimuthal angle (ϕ) of 90°, setting the blade stagger angle (α) to 90° should result in a dipole whose axis is parallel to the wall,

$$\mathcal{D}\left(\alpha = \frac{\pi}{2}, \phi = \frac{\pi}{2}\right) = \frac{2}{r_0^2}\cos^2\theta\left[1 + \cos(\xi \sin\theta)\right]. \tag{5.23}$$

and the power ratio is given by,

$$\frac{\mathcal{P}}{\mathcal{P}_0} = 1 - \frac{3\cos\xi}{\xi^2} + \frac{3\sin\xi}{\xi^3}. \tag{5.24}$$

As was shown in Sect. 4.1.3 of Chapter 4, the directivity without the wall is given by the $\mathcal{D}^{NW}$ directivity function. This is $\sin^2\theta$ for the vertical dipole and $\cos^2\theta$ for the horizontal dipole. The amplitude contribution due to the hard-wall is given by the $\mathcal{D}^{I}$ directivity function. This is responsible for the factor of 2 in Eqns. (5.21) and (5.23). The interference of the acoustic waves is represented by the $\cos(\xi\sin\theta)$ factor in the $\mathcal{D}^{P}$ directivity function.

The power ratios given by Eqns. (5.22) and (5.24) are identical to the theoretical power ratios derived by Ingard *et al.* [146]. The derivation of these expressions is provided in Pierce [17]. However, it should be noted that coordinate system used in the present work is rotated by 90° as compared to the one found in Pierce [17]. This serves as initial validation of the rotor noise model and the coordinate systems used.

Fig. 5.3 shows the low-frequency low Mach number power ratios and directivity functions for a vertical and a horizontal dipole. Fig. 5.3(a) shows the power ratio for a vertical dipole. It is observed that as ξ goes to 0 the power ratio goes to 0 and the peak power ratio is 1.6. Fig. 5.3(b) shows the power factor for a horizontal dipole. The peak power ratio of 2 occurs at a reduced frequency of $\xi = 2$.

Figs. 5.3(c) and 5.3(d) show the directivity functions computed using Eqns. (5.21) and (5.23). For a vertical dipole the peak noise is radiated along the axis of the rotor at $\theta = 90°$ whereas, for the horizontal dipole, the peak noise is radiated at $\theta = 0°$. Both figures also show interference fringes due to the presence of the hard-wall. These fringes are caused by the $\cos(\xi\sin\theta)$ term in the $\mathcal{D}^{P}$ directivity function. It is also observed that the maximum and minimum for both cases is 4 and 0. These are the values that are expected due to the coherent interference of acoustic waves.

The low-frequency low Mach number analysis presented above is still a function of the azimuthal angle ϕ. Amiet's rotor noise model azimuthally averages the sound field of a translating aerofoil to determine the radiated noise. This procedure is shown to reproduce the exact directivity function when compared against a rotor-wake interaction analytical model by Blandeau [28]. Thus azimuthally averaging the above directivity functions should provide directivity functions and power ratios that are indicative of the low-frequency low Mach number noise of a rotor. The azimuthally averaged directivity

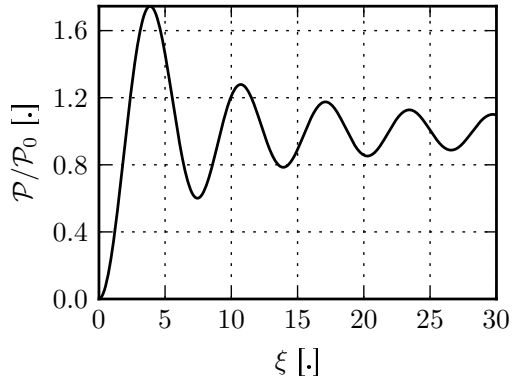

(a) Power factor for a vertical dipole.

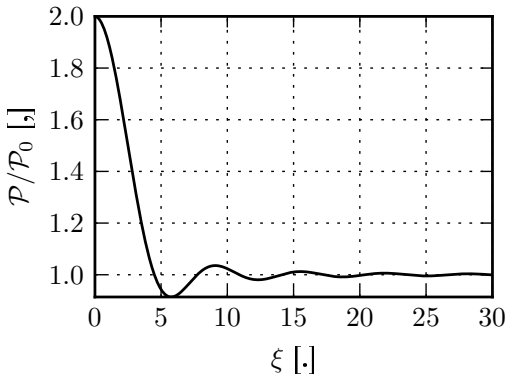

(b) Power factor for a horizontal dipole.

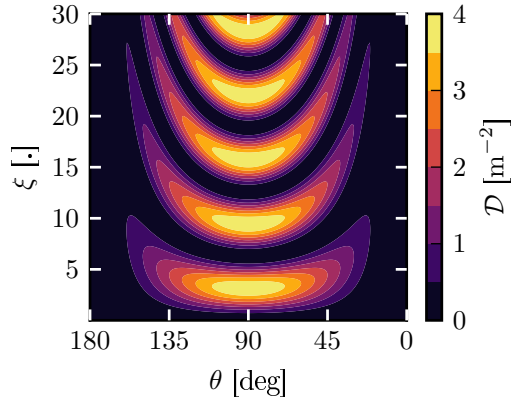

(c) Directivity of a vertical dipole.

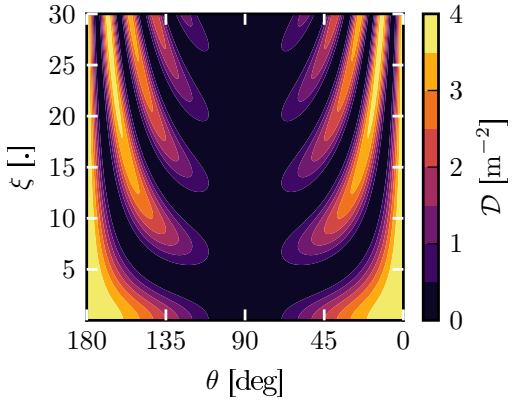

(d) Directivity of a horizontal dipole.

Figure 5.3: The low frequency low Mach number power ratio and directivity functions for a vertical and a horizontal dipole. The observer is at a radius $r_0 = 1$ m.

is given by,

$$\frac{r_0^4}{2\pi}\int_0^{2\pi}\mathcal{D}(\xi,\theta,\alpha,\phi)\mathrm{d}\phi = 2x^2\sin^2\alpha\left[1+\cos\left(\xi\sin\theta\right)\right] + z^2\cos^2\alpha\left[1-\cos\left(\xi\sin\theta\right)\right], \tag{5.25}$$

and the power ratio is,

$$\frac{\mathcal{P}}{\mathcal{P}_0} = 1 - \frac{6\xi\left(\cos^2\alpha + 2\sin^2\alpha\right)\cos\xi - \left(6\cos^2\alpha - 3\xi^2\cos^2\alpha + 12\sin^2\alpha\right)\sin\xi}{\xi^3\left(\cos^2\alpha + 4\sin^2\alpha\right)}. \tag{5.26}$$

Fig. 5.4(a) shows the azimuthally averaged directivity function for a blade at a stagger angle of 45° computed using Eqn. (5.25). It is observed that at a blade stagger angle of 0° the azimuthally averaged directivity function is the same as a vertical dipole and at a blade stagger angle of 90° the directivity function is the same as that of a horizontal dipole. Thus having the blade stagger angle at 45° results in a directivity function that

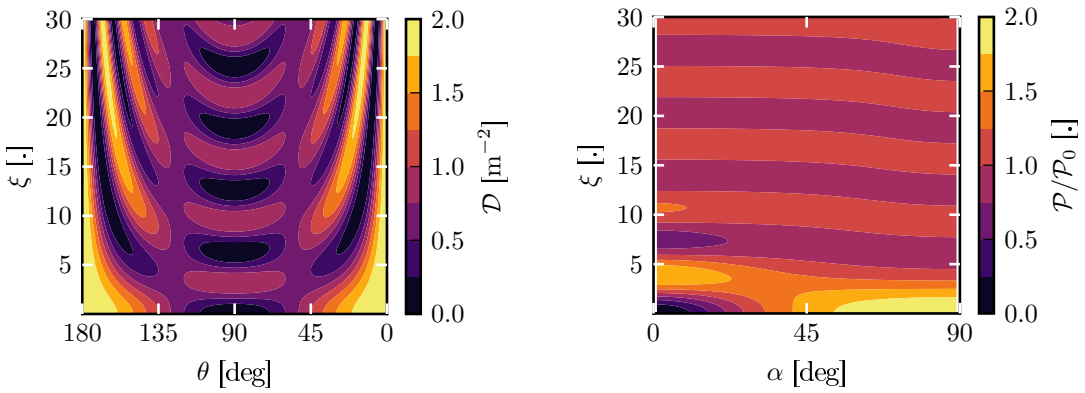

(a) Azimuthally averaged directivity at $\alpha = 45°$.

(b) Azimuthally averaged power ratio.

Figure 5.4: The azimuthally averaged directivity and power ratio.

is in between a vertical and horizontal dipole. Additionally, the maximum directivity due to constructive interference has now reduced from 4 to 2.

Fig. 5.4(b) shows the power ratio for the azimuthally averaged sound field varying with blade stagger angle and reduced frequency ($\xi = 2k_0 d_{wall}$). As expected, the power ratio resembles that of a vertical dipole at $\alpha = 0°$ and that of a horizontal dipole at $\alpha = 90°$. Because of this the power ratio increases from 0 to a global maximum of 2 as the stagger angle is increased from 0° to 90°. These results show that the blade stagger angle is an important parameter. Changing the blade stagger angle has a large impact on the resultant noise directivity and a moderate impact on the peak power ratio.

This section has analysed the noise produced by a rotor ingesting turbulence near a hard-wall in the low Mach number low frequency limit. In this limit the noise produced by a translating aerofoil reduces to that of a compact dipole. As the solution has been obtained in 3D space, the dipole axis can be oriented at any angle. An initial verification of the noise model has been made by comparing the power ratio for vertical and horizontal dipoles with available analytical solutions. As was done in Chapter 4 the contribution of each of the additional terms that were added due to the presence of the hard-wall have been analysed. The noise produced by the rotor in the low Mach number low frequency limit is estimated by azimuthally averaging the noise spectrum. Analysing the directivity function and the power ratio for the azimuthally averaged sound spectra shows that the blade stagger is an important parameter in determining the directivity and power amplification due to the presence of the reflecting plane.

5.2 Results

In this section, predictions using Amiet's [18] rotor noise model with wall-effects included will be compared with experimental measurements from the Fundamental Case 3 (FC3) case of the 2015 American Institute of Aeronautics and Astronautics (AIAA) Fan Broadband Noise (FBN) [138] workshop. Predictions made with and without wall effects modelled will be compared to determine the effect of the wall on the noise spectrum.

5.2.1 Comparison with experimental results

In this section predictions made using Amiet's [18] rotor noise model with wall-effects included are compared with experimental measurements. The predictions are made using Eqn. (5.11) to obtain the PSD of the acoustic pressure and the von Kármán spectrum, given by Eqn. (3.45), is used to specify the PSD of the upwash velocity. The geometry of the rotor and the parameters of the incoming turbulence that are used for these simulations are given in Appendix B.1. The computations for the rotor noise model are computed using 200 azimuthal integration points and 10 span-wise strips. The strips are logarithmically spaced so that the tip of the blade has a larger density of strips.

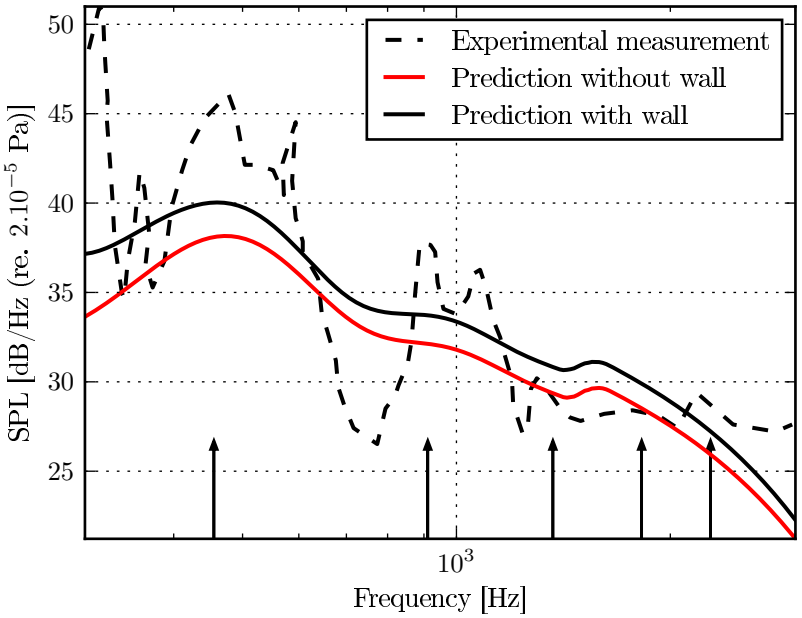

Figure 5.5: Power spectral density of the acoustic pressure,for a rotor in the free-field and in the presence of a hard-wall ($d_{wall} = 0.2486$ m), compared with an experimental results from Glegg *et al.* [139]. The arrows represent the Blade Passing Frequencies of the rotor. The observer is located at (r_0, θ)=(3.01 m, 127.3°).

Fig. 5.5 shows the predictions using the rotor noise model with and without wall-effects compared with experimental measurements. From this figure, it is observed that including wall-effects has increased the amplitude by approximately 3 dB at the lower frequencies and by approximately 1.5 dB at the higher frequencies. The noise spectra still show several discrepancies when compared with the experimental measurements. While the amplitude of the spectrum has increased, there is still a severe under-prediction at most frequencies, and while the high frequency drop off still remains, it has been shifted to higher frequencies in the predictions that are made with the hard-wall included. The second peak is still absent in the predictions. These discrepancies will be addressed in Chapter 6 with the introduction of an anisotropic velocity spectrum.

5.2.2 The effect of the hard-wall

In this section, the effect of the reflecting plane on the radiated noise is investigated. These investigations will be performed without the switch that was introduced in Sect. 3.1.3 of Chapter 3 to account for the partial loading of the rotor. The effect of the hard-wall on the noise spectrum will be investigated without and with blade-to-blade correlation modelled.

The effect of the wall is investigated without blade-to-blade correlation modelled in order to investigate wall effects without the additional complexity of modelling a separate velocity correlation tensor for each of the terms in Eqn. (5.11). In doing so, only the directivity functions $(Y, Y^{\#})$ determine the effect of the wall.

Next, the effect of the wall is investigated with blade-to-blade correlation modelled. The effect of the wall is investigated for varying rotor RPMs and for varying distances to the wall. All the results shown below are computed using the von Kármán spectrum with an integral length scale of 0.1 m and a turbulence velocity of $2\,\mathrm{m^2\,s^{-2}}$

5.2.2.1 Without blade-to-blade correlation

Fig. 5.6 shows the Sound Pressure Level (SPL) for a rotor operating at 2734 RPM in a mean flow of the $30\,\mathrm{m\,s^{-1}}$. The noise spectra is computed by replacing the velocity correlation tensors of all the terms in Eqn. (5.11) with $\Phi_{vv}(k_X, k_Z = 0)$. This velocity correlation tensor is modelled using Eqn. (3.46). The predictions with the wall (Fig. 5.6(a)) and without the wall (Fig. 5.6(b)) show a dipole like directivity with a cusp at $\theta = 90°$.

Fig. 5.6(c) shows the difference in the noise spectrum computed with and without a wall. The difference in SPL shows the wall has increased the noise by 3 dB at most

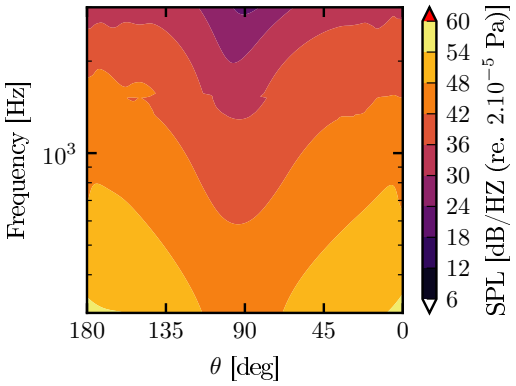

(a) SPL directivity with the hard-wall.

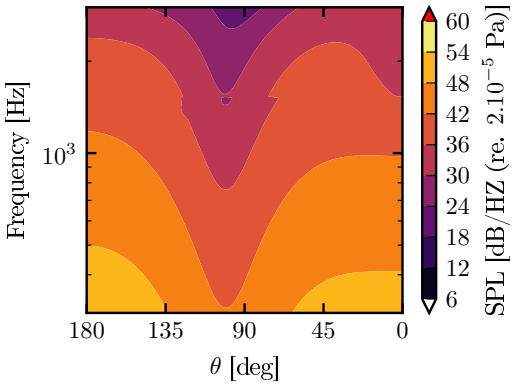

(b) SPL directivity without the hard-wall.

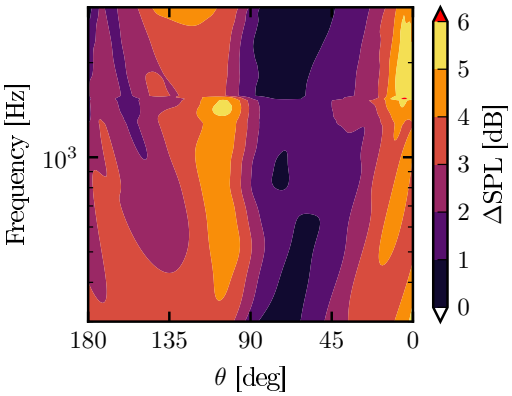

(c) SPL directivity without the hard-wall.

Figure 5.6: SPL directivity computed for a rotor in the presence of a hard-wall and in the free-field. The rotor is operation at 2734 RPM in a mean flow of $30\,\mathrm{m\,s^{-1}}$. The wall is at $d_{wall} = 0.2486$ m and the observer is at $r_0 = 3.01$ m.

observers with some observers showing an increase of between 4 to 5 dB at the low frequencies. Some upstream observers around $\theta = 0°$ show an increase of 6 dB at the higher frequencies. This could be because of the un-physical peak seen in the noise spectrum when switching from the low-frequency lift function to the high-frequency lift function. Additionally, interference patterns are seen for the upstream observer angles. These interference patterns are a result of the term,

$$\frac{1}{2\pi}\int_0^{2\pi} \frac{YY^{\#}}{(\sigma\sigma^{\#})^2}\left[2\cos\left(\mu\left[M_X\left(X^{\#}-X\right)+(\sigma-\sigma^{\#})\right]\right)\right]\mathrm{d}\phi.$$

However, these interference patterns are obtained for multiple strips at varying stagger angles and varying blade relative Mach numbers. This is, therefore, the cumulative effect of a number of dipoles that are inclined at varying angles to the hard-wall.

Fig. 5.7 shows the sound PoWer Level (PWL) spectra and the OverAll Sound Pressure Level (OASPL) directivity. The PWL spectra is computed as,

$$\mathcal{P}(r_0, \omega) = \frac{r_0^2}{\rho_0 c_0} \int_0^{\pi} S_{pp}\left(r_0, \theta, \omega\right) F(\theta, M) \mathrm{d}\theta. \tag{5.27}$$

Fig. 5.7 shows the un-physical peak at 1500 Hz where Amiet's [18] lift function switches from the low-frequency function to the high-frequency function. From Fig. 5.7(b) it is observed that the hard-wall increases the sound power by 2.8 dB at the higher frequencies and by 2 dB at the lower frequencies.

Fig. 5.7(c) shows the OASPL computed as,

$$\mathrm{OASPL} = 10 \log_{10} \left(\frac{4\pi \int_{f=300\mathrm{Hz}}^{f=3000\mathrm{Hz}} S_{pp}\left(r_0, \theta, \omega\right) \mathrm{d}f}{p_{\mathrm{ref}}^2} \right). \tag{5.28}$$

The OASPL directivities shows that both the predictions, with and without the wall, show increased sound levels for the downstream observers due to convective amplification. Fig. 5.7(d) shows that the wall has increased the sound by slightly more than 4 dB. There is a peak in the OASPL at $\theta = 112.5°$ of approximately 4.2 dB and a peak of 4.1 dB at the downstream observer angles.

The OASPL directivities without blade-to-blade correlation are a function of the directivity functions (Y, $YY^{\#}$, and $(Y^{\#})^2$). This, in turn, implies that the directivity of the rotor is primarily a function of the blade stagger angle. Additionally, as emission coordinates have been used, the real and image rotor are moving in opposite directions. Thus when the real rotor is moving towards an observer, the image rotor is moving away from it or vice-versa. Because of this, the directivity lobes will be amplified for the downstream observers for the real rotor due to convective amplification and for the upstream lobes of the image rotor. The peak at $\theta = 112.5°$ is due to a combination of these two effects.

5.2.2.2 With blade-to-blade correlation

In this section, the effect of the hard-wall on the noise spectrum is examined with blade-to-blade correlation modelled using Eqn. (5.11). Fig. 5.8 shows the individual components, i.e., the total contribution (S_{pp}), the contribution without the wall (S_{pp}^{NW}), the real and imaginary parts of the interference terms (S_{pp}^{P1}, S_{pp}^{P2}), and the amplitude contribution because of the presence of the hard-wall (S_{pp}^{I}). From Fig. 5.8 it is observed that the amplitude terms contribute to increasing the amplitude of the spectrum and the peak is at the first BPF. The amplitude term has lower sound pressure levels than the terms without the wall as the image rotor is farther away from the observer than the real rotor.

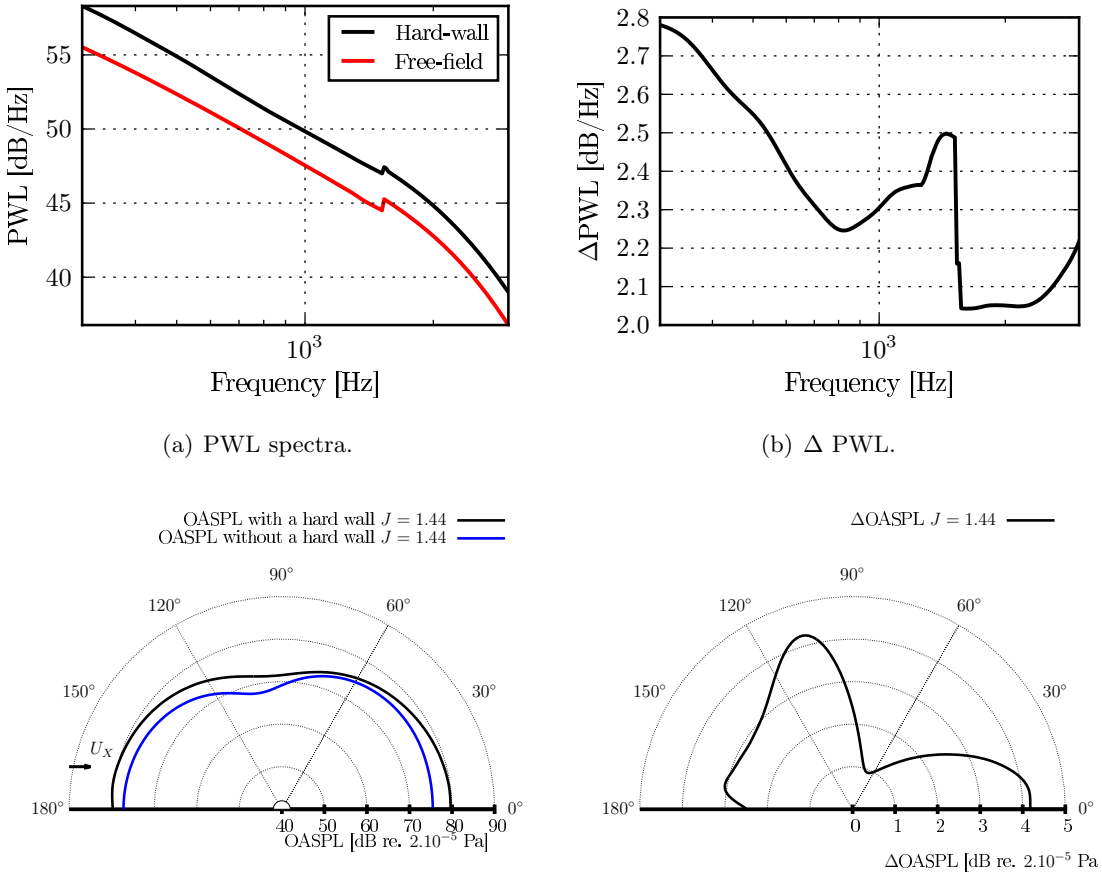

(a) PWL spectra.

(b) Δ PWL.

(c) OASPL.

(d) Δ OASPL.

Figure 5.7: The PWL spectra and OASPL for the rotor with and without a hard-wall. The rotor is operation at 2734 RPM in a mean flow of $30\,\mathrm{m\,s^{-1}}$. The wall is at $d_{wall} = 0.2486$ m and the observer is at $r_0 = 3.01$ m.

The interference terms resemble Bessel functions as would be expected from Sect. 5.1.3. It is also interesting to note that the hard-wall is affecting the blade-to-blade correlation. The hard-wall changes the propagation time of the acoustic waves (and consequently the wavenumber K_Y) to the observer, and this subsequently determines how correlated the source is as perceived by the observer.

Fig. 5.9 shows the SPL with and without a wall with blade-to-blade correlation modelled at varying observer locations. Both the predictions with and without the wall show a peak at the first BPF. The directivities with and without the wall resemble that of a dipole with a cusp at $\theta = 90°$. The difference in SPL shows that a majority of the observers see an increase in sound of approximately 2 to 3 dB. The observers at approximately 112.5° show an increase of approximately 5 dB. The reasons for this increase have been discussed in the previous section. The upstream observers show an increase in the SPL of approximately 5 to 6 dB at all frequencies.

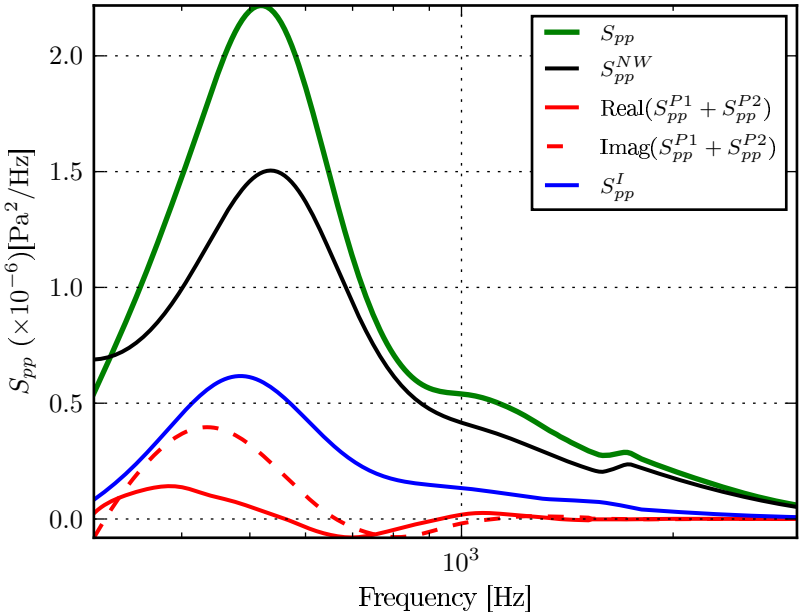

Figure 5.8: Individual components of Eqn. (5.11) for PSD of the acoustic pressure with a hard-wall. The observer is at (r_0, θ)=(3.01 m, 45°).

Fig. 5.10 shows the individual terms of Eqn. (5.11) at varying observer angles. It is once again observed that the amplitude terms contributes to increasing the sound pressure levels. It is also seen that the amplitude term has narrower peaks around the BPF. The interference terms have the expected interference fringes that are a result of the exponential terms, $e^{\pm i\mu((X-X^{\#})+(\sigma^{\#}-\sigma))}$. Additionally, due to blade-to-blade correlation, the acoustic waves have different propagation times for the two interference terms. This implies that the velocity correlation tensor for the cross-terms are not identical and the imaginary terms do not cancel as they would for the case without blade-to-blade correlation.

Fig. 5.11 shows the PWL and OASPL computed for a rotor in the presence of a hard-wall with blade-to-blade correlation modelled. The figures show that the presence of the hard-wall has increased the PWL spectra by 3 dB around the 1st BPF and by approximately 2.25 dB at the higher frequencies. The OASPL directivities show that the observers at $\theta = 0°$ and $\theta = 180°$ show an increase of OASPL of 5 dB. Additionally, there is constructive interference at approximately $\theta = 112.5°$ where the OASPL is increased by 6 dB. The reason for this peak has been discussed in the previous section.

Fig. 5.12 shows the PWL spectra computed at various heights to the wall. From Fig. 5.12(b) it is seen that as the rotor is moved farther away from the wall, the Δ PWL spectra goes to 0. This is to be expected as the influence of the hard-wall is minimized as the rotor moves away from it.

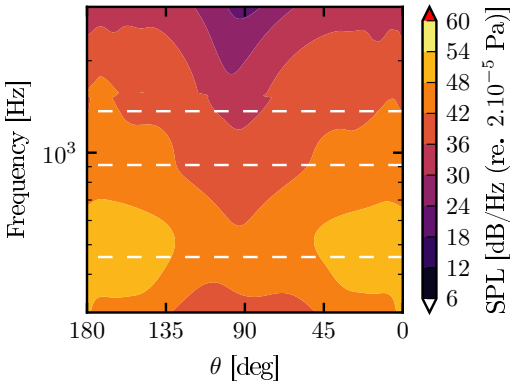

(a) SPL directivity with the hard-wall.

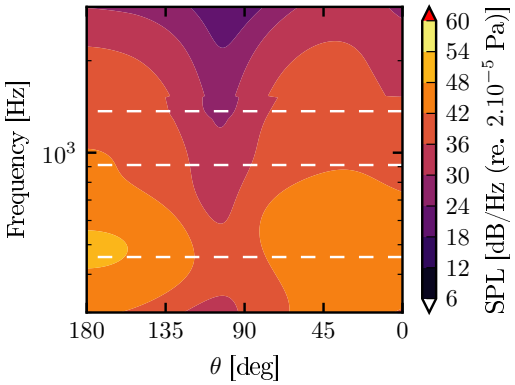

(b) SPL directivity without the hard-wall.

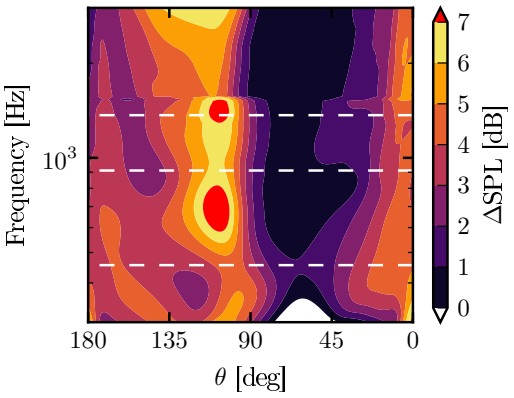

(c) SPL directivity without the hard-wall.

Figure 5.9: SPL directivity computed for a rotor with blade-to-blade correlation modelled in the presence of a hard-wall and in the free-field. The rotor is operation at 2734 RPM in a mean flow of $30\,\mathrm{m\,s^{-1}}$. The wall is at $d_{wall} = 0.2486$ m and the observer is at $r_0 = 3.01$ m.

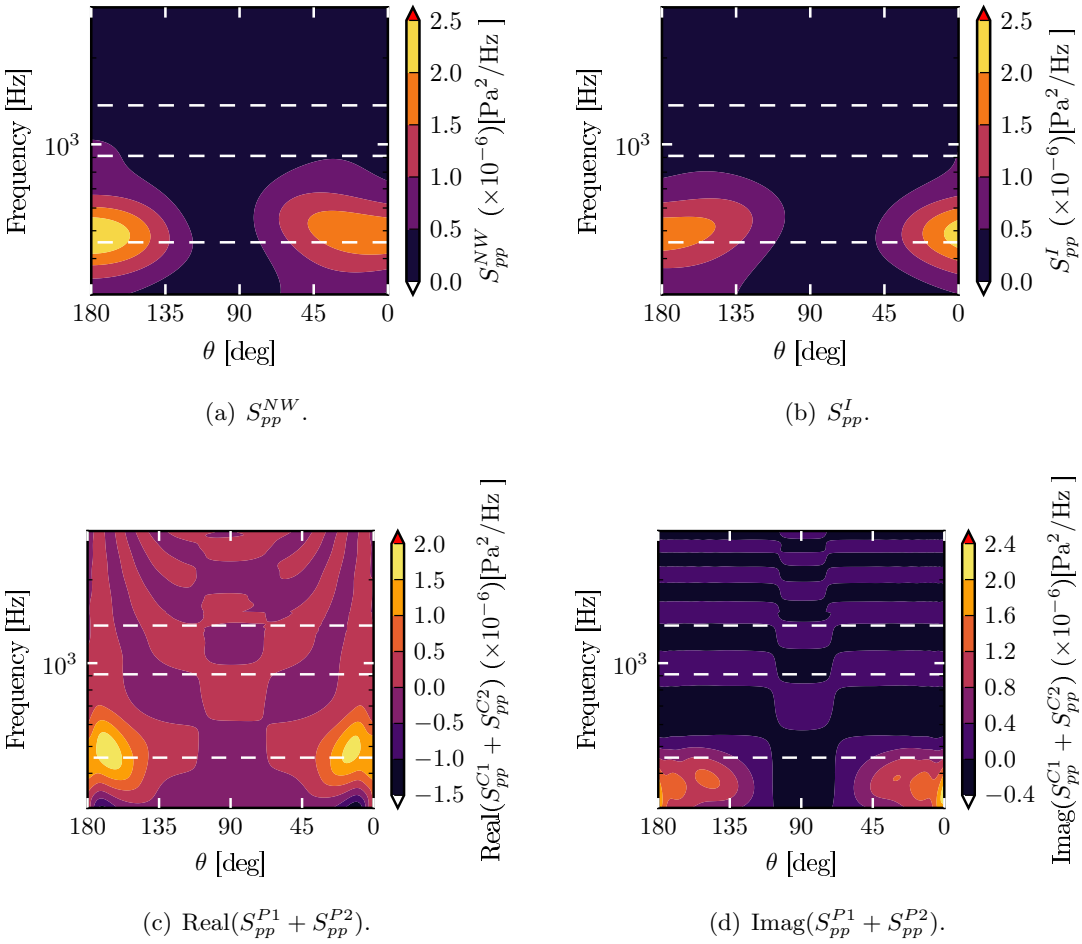

(a) S_{pp}^{NW}.

(b) S_{pp}^{I}.

(c) Real($S_{pp}^{P1} + S_{pp}^{P2}$).

(d) Imag($S_{pp}^{P1} + S_{pp}^{P2}$).

Figure 5.10: SPL directivity computed for a rotor with blade-to-blade correlation modelled in the presence of a hard-wall and in the free-field. The rotor is operation at 2734 RPM in a mean flow of 30 m s^{-1}. The wall is at $d_{wall} = 0.2486$ m and the observer is at $r_0 = 3.01$ m.

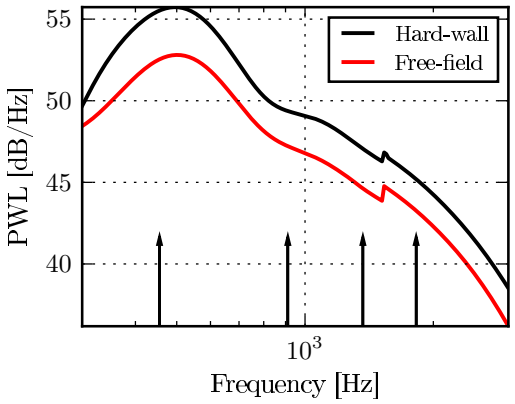

(a) PWL spectra.

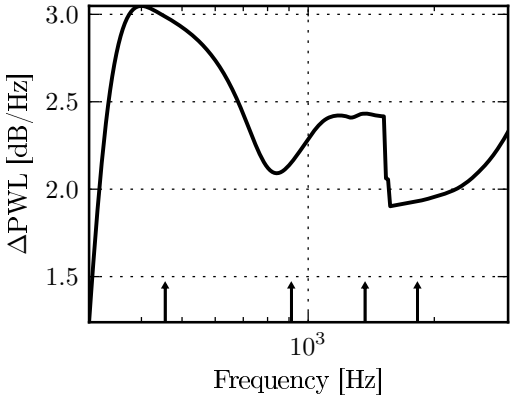

(b) Δ PWL spectra.

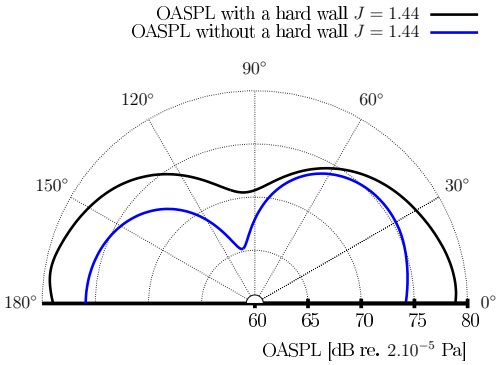

(c) OASPL.

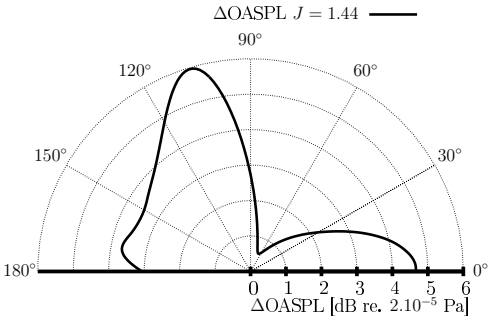

(d) Δ OASPL.

Figure 5.11: The PWL spectra and OASPL for the rotor with blade-to-blade correlation modelled with and without a hard-wall. The rotor is operation at 2734 RPM in a mean flow of $30\,\mathrm{m\,s^{-1}}$. The wall is at $d_{wall} = 0.2486$ m and the observer is at $r_0 = 3.01$ m.

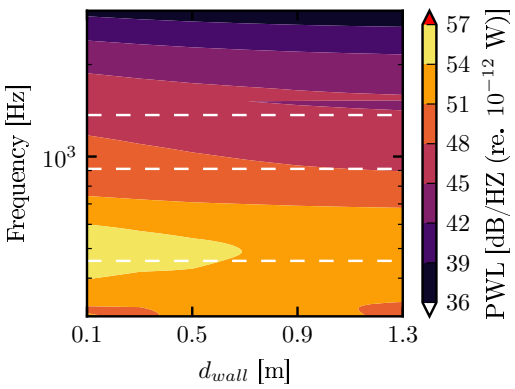

(a) PWL spectra for a rotor at varying distances to the hard-wall.

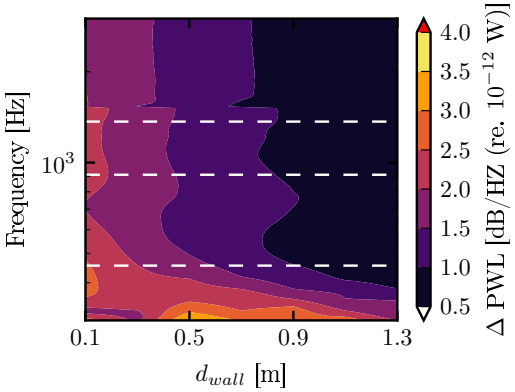

(b) ΔPWL spectra for a rotor at varying distances to the hard-wall.

Figure 5.12: PWL spectra for a rotor at varying distances to the hard-wall. The observer is at $r_0 = 3.01$ m.

5.3 Conclusions

This chapter has extended Amiet's [18] simplified rotor noise model to include wall effects. Wall effects were added in a similar manner as was done in Chapter 4. Additionally, the effect of blade-to-blade correlation was included in the velocity correlation tensor by accounting for the various propagation times for the acoustic waves to travel to the observer. It is shown that adding wall-effects can significantly alter the resulting noise spectrum. The amplitude of the spectrum is increased, especially at low-frequencies, and the interference terms can alter the directivity of the rotor. The main conclusions that are drawn from this chapter are:

- Amiet's [18] simplified rotor noise model has been extended to include wall-effects using the MOI. This is done by adding a mirror source to Amiet's [18] 3D formulation for the pressure. This is subsequently frequency corrected and azimuthally averaged to determine the noise produced by a rotor.
- The effects of blade-to-blade correlation have been considered by considering the cross-correlation of the pressure of the 0^{th} and n^{th} blades. Including wall-effects using the MOI adds three additional terms to Amiet's [18] original formulation. These include two interference terms and one amplitude term. To model blade-to-blade correlation, the various times it takes for an acoustic wave to travel to the observer have been taken into account.
- An initial verification of the model has been made by examining the low-frequency low-Mach number limit. In this limit, the solution reduces to that of a point dipole. By changing the azimuthal angle and blade stagger angle, the orientation of the dipole can be altered. Using this, it is shown that for appropriate azimuthal and stagger angles the noise produced by a rotor reduces to that of a vertical or horizontal dipole. It is shown that for these two cases the ratio of the power radiated in the presence of reflecting plane to the power radiated in the free-field matches available analytical expressions for these. It is also shown that the blade stagger angle can change the noise spectra significantly as it changes the axis of the dipole.
- Comparing the predictions made using Amiet's [18] extended rotor noise model to experimental measurements, it is shown that including the hard-wall has improved the amplitude of the spectrum. However, the predictions still do not capture the peak at the 2^{nd} BPF. This will be addressed in the next chapter by including an anisotropic velocity spectrum.
- The effect of the hard-wall on the noise spectrum has been studied without and with blade-to-blade correlation modelled. Without blade-to-blade correlation modelled, only the directivity terms $(Y, Y^{\#})$ and the additional imaginary phase term affect

the solution. It is observed that the sound directivity has a peak at approximately $\theta = 112.5°$. This is because of the stagger angle of the blades and the fact that the real and image rotor are rotating in opposite directions.

- With blade-to-blade correlation modelled, the peak that is observed in the predictions without blade-to-blade correlation is still present.
- The effect of the individual terms that are added to Amiet's [18] original solution because of the presence of the hard-wall have been examined. Due to the acoustic waves taking different times to propagate to the observer, the imaginary parts of the cross-terms do not cancel. These terms act like sinusoids around zero and contribute to increasing or decreasing the amplitude of the spectrum depending on the frequency and the observer location. It is shown that the amplitude terms contributes to increasing the overall noise levels.
- The PWL spectra and the OASPL directivities with blade-to-blade correlation modelled show similar trends as the predictions without blade-to-blade correlation modelled. An increase of 3 dB in the PWL spectra is observed at the 1^{st} BPF and an increase of 2.2 dB is observed at higher frequencies. As the distance from the rotor to the wall is increased, the effect of the reflecting surface diminishes and the radiated power returns to that of the rotor in the free-field.

Chapter 6

Modelling anisotropy

In this chapter Amiet's [18] rotor noise model, which was described in Chapter 3 is used with an anisotropic model spectrum in order to account for the anisotropy in the boundary layer that is being ingested by the rotor. In Chapter 5 Amiet's [18] rotor noise model was extended to include wall effects. When predictions using this model were compared with experimental results, several discrepancies were observed. One of the main discrepancies that was observed, was the absence of the second correlation peak. In this chapter this discrepancy is addressed by using the axisymmetric anisotropic velocity spectrum of Kerschen and Gliebe [147] in Amiet's [18] rotor noise model.

The turbulence spectrum of Kerschen *et al.* [147] makes the assumption that the turbulent structures are homogeneous and axisymmetric. Thus, two integral length scales and the turbulence intensities in the corresponding directions are required to specify the Power Spectral Density (PSD) of the turbulent velocity fluctuations. It is assumed that the integral length scale in the mean flow direction is larger than in the other directions. This chapter will first investigate anisotropy in Amiet's [18] translating aerofoil model. Using the translating aerofoil model, the effect of changing the axial and transverse length scale is examined. This is done to examine the effect of anisotropy for a simplified case in order to better isolate the effects of anisotropy. As Amiet's [18] rotor noise model azimuthally averages and frequency corrects the translating aerofoil model, the insight gained will be relevant in understanding how anisotropy affects the noise produced by the rotor.

Next, the anisotropic turbulence model is coupled to Amiet's [18] rotor noise model to model the anisotropy in the boundary layer. The suitability of using the anisotropic spectrum of Kerschen and Gliebe [20] to model boundary layer turbulence is investigated next. The assumption of axisymmetry that is made by the turbulence model is a good approximation of the turbulence in a boundary layer as the turbulent structures in the log-layer are known to be long cylindrical structures [37; 29; 148]. While boundary layer turbulence is axisymmetric, it is not homogeneous in the wall-normal direction. The

rotor noise model presented will take into account the varying turbulence parameters at varying wall-normal locations, thus partially accounting for the inhomogeneity of the flow. However, the homogeneous axisymmetric turbulence model is an approximation of the turbulence in the boundary layer and a degree of empiricism is introduced into the rotor noise model in order to approximate this turbulence. The anisotropic turbulence spectrum of Kerschen and Gliebe [20] has been used in cascade models by several authors [58; 61].

Predictions using the anisotropic spectrum coupled with Amiet's [18] rotor noise model are compared with experimental measurements. Next, the effect of changing the axial and transverse length scale on the resultant noise spectrum is investigated. Finally, the effect of the stagger angle, rotor speed, and eddy speed on the anisotropic spectrum is examined.

6.1 Formulation of the 3D axisymmetric anisotropic velocity spectrum

In this section the formulation for the velocity correlations based on the axisymmetric turbulence model of Kerschen *et al.* [147] are presented. The Kerschen and Gliebe [24] model spectrum is a modified Liepmann spectrum. The model is derived based on the work of Chandrashekar [38] whose work is based on the work of Batchelor [39]. The axisymmetric velocity correlation tensor derived by Chandrashekhar [38] is given by,

$$R_{ij}(x) = \epsilon_{jlm} \frac{\partial q_{im}}{\partial x_l}, \tag{6.1}$$

where R_{ij} is the velocity correlation tensor, ϵ_{jlm} is the alternating tensor, and

$$q_{ij} = Q_1 \epsilon_{ijk} x_k + Q_2 \epsilon_{ilm} \lambda_l x_m + \frac{1}{r} \frac{\partial Q_1}{\partial \mu} x_j \epsilon_{ilm} \lambda_l x_m, \tag{6.2}$$

where λ is the preferred direction of turbulence and $\lambda.x = \mu$. Additionally Batchelor [39] showed that the axisymmetric velocity correlation tensor must have the form,

$$R_{ij} = C_1 x_i x_j + C_2 \delta_{ij} + C_3 \lambda_i \lambda_j + C_4 \left(\lambda_i x_j + \lambda_j x_i \right), \tag{6.3}$$

where C_i are constants that are functions of r and $x.\lambda$. Kerschen and Gliebe [24] used the Fourier transform of this equation along with the continuity equation to specify constraints on the model constants. The velocity correlation tensor in spectral space is

given by,

$$\begin{aligned}\Phi_{ij}(\mathbf{k}) = &\left[|\mathbf{k}|^2\delta_{ij} - k_i k_j\right]\mathcal{F} + \\ &\left[\left(|\mathbf{k}|^2 - (k_m\lambda_m)^2\right)\delta_{ij} - k_i k_j - |\mathbf{k}|^2\lambda_i\lambda_j + k_m\lambda_m\left(\lambda_i k_j + k_i\lambda_j\right)\right]\mathcal{G},\end{aligned} \tag{6.4}$$

where $\mathbf{k}$ is the wave number vector, $\mathcal{F}$ and $\mathcal{G}$ are functions that are determined from Q_1 and Q_2.

Kerschen and Gliebe [24] determined constraints for the constants Q_1 and Q_2. This was done by equating the the constants in physical space (Q_1 and Q_2) with the constants in spectral space ($\mathcal{F}$ and $\mathcal{G}$) after taking the Fourier transform of Eqn. (6.4). With these constraints in mind and using the fact that most turbulence decays as $e^{-x/L}$ in a direction x for turbulence with an integral length scale L, they proposed two models. Both the models use the same function Q_1,

$$Q_1 = -\frac{u_a^2}{2}e^{-y}, \tag{6.5}$$

where,

$$y = \left(\frac{x_1^2}{l_a^2} + \frac{\sqrt{x_2^2 + x_3^2}}{l_t^2}\right)^{1/2}. \tag{6.6}$$

They then proposed two models for Q_2,

$$\begin{aligned}Q_2^A &= \left(u_a^2 - u_t^2\right)e^{-y}, \\ Q_2^B &= -u_a^2\left[\frac{u_t^2}{u_a^2} - 1 + \frac{1}{2y}\left(\frac{x_1}{l_a}\right)^2\left(2 - \frac{l_t^2}{l_a^2} - \frac{l_a^2}{l_t^2}\right)\right]e^{-y},\end{aligned} \tag{6.7}$$

where $l_a = L_{11}^{(1)}$ is the integral length scale in the axial direction, u_a is the axial turbulence velocity, $l_t = L_{22}^{(2)} = L_{33}^{(3)}$ is the integral length scale in the transverse direction, and u_t is the turbulence velocity in the transverse direction.

Both the models A and B produce the desired 1D correlations, $R_{11}(x_1) = u_a^2 e^{-|x_1|/l_a}$ and $R_{22}(x_2) = u_a^2 e^{-|x_1|/l_t}$. For typical fan noise applications the axial length scale is larger than the transverse length scale ($l_a/l_t > 1$). Kerschen and Gliebe [24] have shown that when $l_a/l_t >> 1$ model A produces incorrect results and in some cases predicts a negative PSD. Therefore model B is shown to be correct and it is the model used for the remainder of the thesis.

The constants $\mathcal{F}$ and $\mathcal{G}$ can be determined by taking the Fourier transform of Q_1 and Q_2^B,

$$\mathcal{F} = \frac{2l_a l_t^4 u_a^2}{\pi^2 z^3}, \quad \mathcal{G} = \left[2\frac{u_t^2}{u_a^2} - \frac{l_t^2}{l_a^2} - 1\right]\mathcal{F}, \tag{6.8}$$

where,

$$z = 1 + l_a^2 k_x^2 + l_t^2 \left(k_y^2 + k_z^2\right)^2, \tag{6.9}$$

Using the above definitions the velocity correlations in the three principal directions in the engine-fixed reference are given by,

$$\begin{aligned} \Phi_{11}(\mathbf{k}) = \Phi_{uu}(\mathbf{k}) &= \left[k_y^2 + k_z^2\right] \mathcal{F}, \\ \Phi_{22}(\mathbf{k}) = \Phi_{vv}(\mathbf{k}) &= \left[k_x^2 + k_z^2\right] \mathcal{F} + k_z^2 \mathcal{G}, \\ \Phi_{33}(\mathbf{k}) = \Phi_{ww}(\mathbf{k}) &= \left[k_x^2 + k_y^2\right] \mathcal{F} + k_y^2 \mathcal{G}. \end{aligned} \tag{6.10}$$

These equations describe 3D anisotropic turbulence. In the next section, the anisotropic turbulence spectra described above is compared against experimental data.

6.2 Investigating the effects of anisotropy in a translating aerofoil ingesting anisotropic turbulence

In this section the anisotropic velocity spectrum defined in Sect. 6.1 will be used in the translating aerofoil model of Amiet [21] to determine the noise radiated by a flat-plate ingesting homogeneous anisotropic turbulence. This noise model is then used to investigate the effect of changing the length scales on the noise spectra.

6.2.1 The PSD of the sound radiated by a translating aerofoil ingesting turbulence

The coordinate system that is used is shown in Fig. 6.1. The PSD of the acoustic pressure is given by [21],

$$S_{pp}(r_0, \theta, \omega) = \pi U d \left(\frac{k_0 \rho_0 Y b}{\sigma^2}\right)^2 |\mathcal{L}(\theta, k_x)|^2 \Phi_{vv}(k_x, k_z = 0), \tag{6.11}$$

where ρ_0 is the mean density, b is the semi-chord, d is the semi-span, $Y = r_0 \sin\theta$, θ is the angle to the observer, U is the mean flow speed, $k_0 = \omega/c_0$ is the acoustic wavenumber, $\sigma = r_0 A$, r_0 is the distance to the observer, $A = \sqrt{1 - M^2 \sin^2\theta}$, and $\mathcal{L}$ is the acoustic lift integral as defined by Amiet [21].

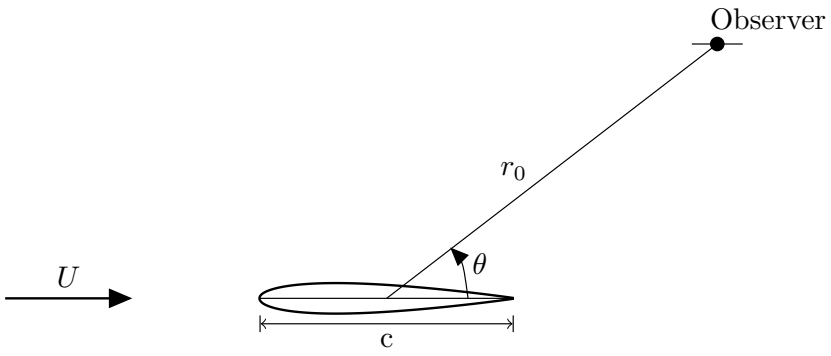

Figure 6.1: A schematic of a flat plate ingesting turbulence.

The velocity spectrum to be used in Eqn. (6.11) is the PSD of the transverse velocity perturbations integrated over the k_y wavenumbers. This is given by,

$$\int_{-\infty}^{+\infty} \Phi_{vv}(k_x, k_y, k_z)\mathrm{d}k_y = \frac{3\pi\alpha k_x^2}{8l_t\left(1 + l_a^2k_x^2 + l_t^2k_z^2\right)^{5/2}} + \frac{3\pi\alpha\xi k_z^2}{8l_t\left(1 + l_a^2k_x^2 + l_t^2k_z^2\right)^{5/2}}, \tag{6.12}$$

where,

$$\begin{aligned} \alpha &= \frac{2l_a l_t^4 u_a^2}{\pi^2}, \\ \xi &= \left(2\frac{u_t^2}{u_a^2} - \frac{l_t^2}{l_a^2}\right). \end{aligned} \tag{6.13}$$

6.2.2 The effect of changing the transverse and axial length scales

In this section, the PSD of the acoustic pressure given by Eqn. (6.11) is computed using the PSD of the transverse velocity perturbations given by Eqn. (6.12). The PSD is computed for an aerofoil with a chord $c = 0.15$ m, a semi-span $d = 0.225$ m in a stream at Mach number $M = 0.6$ and mean density $\rho_0 = 1.2\,\mathrm{kg.m^{-3}}$. The observer is at a distance $10d$ away from the aerofoil. For all the computations listed below the axial turbulence velocity is $u_a^2 = \sqrt{2}/3\ \mathrm{m^2\,s^{-2}}$ and the transverse turbulence velocity is $u_t^2 = 2\sqrt{2}/3\ \mathrm{m^2\,s^{-2}}$.

Fig. 6.2 shows the PSD of the transverse velocity perturbations and the sound sound PoWer Level (PWL) spectra varying with changing axial and transverse length scales. The sound power ($\mathcal{P}$) is computed as,

$$\mathcal{P}(r_0, \omega) = \frac{r_0 d}{\rho_0 c_0}\int_0^{\pi} S_{pp}\left(r_0, \theta, \omega\right) F(\theta, M)\mathrm{d}\theta. \tag{6.14}$$

From Fig. 6.2 it is observed that the PWL spectra match the trends in the velocity spectra. From Fig. 6.2(a) and Fig. 6.2(c) it is observed that changing the axial integral

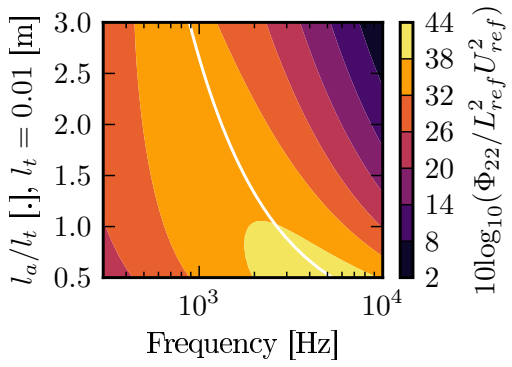

(a) PSD of the transverse velocity perturbations with l_a varying.

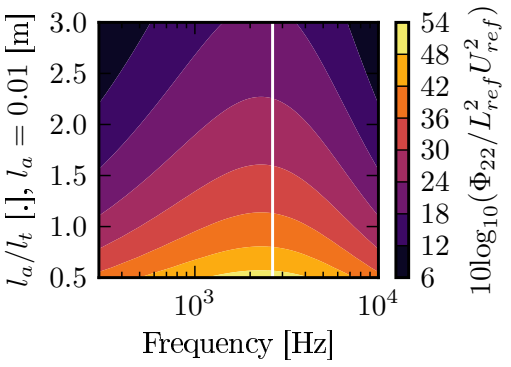

(b) PSD of the transverse velocity perturbations with l_t varying.

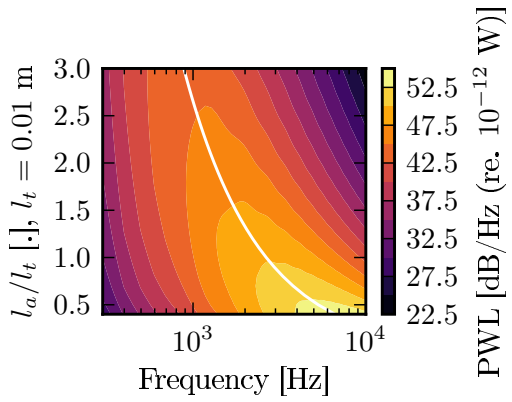

(c) PWL of the acoustic pressure for varying l_a.

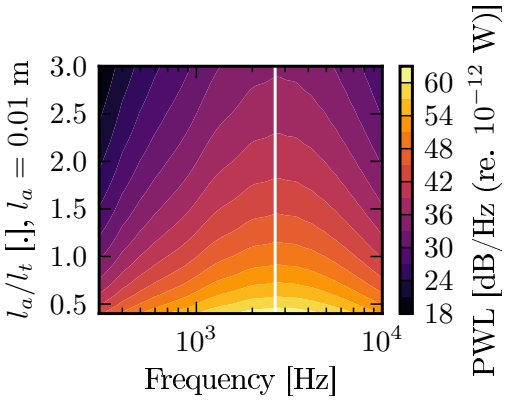

(d) PWL of the acoustic pressure for varying l_t.

Figure 6.2: The PSD of the transverse velocity perturbations for varying axial and transverse length scales with $L_{ref} = 1$ m and $U_{ref} = 10^{-6}\,\mathrm{m\,s^{-1}}$ and the PWL spectra for varying axial and transverse length scales. The white lines on the contours of the PSD shows the frequency at which the PSD is a maximum.

length scale has two effects. Firstly, the frequency at which the PSD is at a maximum decreases as the axial integral length (l_a) scale is increased. Secondly, as l_a is increased more energy is shifted to lower frequencies. The first result can be explained by computing the frequency at which the PSD is at a maximum by taking the derivative of Eqn. (6.12) with k_x and setting this to zero (N.B. k_z is already 0). The maximum frequency is then given by,

$$f_{max} = \sqrt{\frac{2}{3}}\frac{U}{2\pi l_a}, \tag{6.15}$$

These maximum frequencies are shown by the white lines in Fig. 6.2(a) and Fig. 6.2(b). Equation (6.15) implies that the PSD maxima will only change if the axial length scale is changed.

This is confirmed by observing that the maximum frequency at which the PSD or PWL occur does not change in Fig. 6.2(b) and Fig. 6.2(d). From Fig. 6.2(d) it is seen that

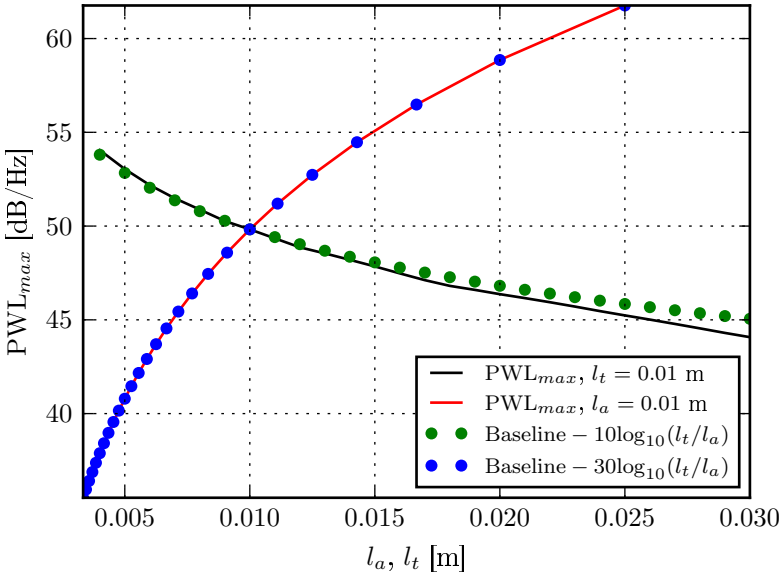

Figure 6.3: The maximum power at various axial and transverse length scales.

as l_t is made larger (a smaller l_a/l_t for a fixed l_a) more energy is shifted to the lower frequencies.

From Fig. 6.2(c) and Fig. 6.2(d) it is also observed that increasing the axial length scale does not change the maximum power as much as changing the transverse length scale. The maximum power at each integral length scale is shown in Fig. 6.3. From Fig. 6.3 it can be seen that the maximum PWL increases by almost 25 dB as the transverse length scale is increased from 0.005 m to 0.02 m and decreases by approximately 10 dB as the axial length scale is increased from 0.005 m to 0.03 m. From Fig. 6.3, it is also observed that the maximum power deviates from $1/l_a$ trend for the larger integral length scales. This is because of the factor , F, in Eqn. (6.14) that is used to account for flow effects.

The reason for the increase in the PWL can be understood by using the Fourier pair relationship of the transverse velocity spectrum and the velocity correlation tensor. Consider the relationship between two velocity spectra, one of which has a wavenumber component multiplied by a factor γ [37; 74],

$$\Phi'_{vv}(k_x, k_z) = \Phi_{vv}(\gamma k_x, k_z). \tag{6.16}$$

Then,

$$\begin{aligned} R'_{vv}(x, k_z) &= \int_{-\infty}^{+\infty} \Phi'_{vv}(k_x, k_z) e^{\mathrm{i}k_x x} \mathrm{d}k_x, \\ R'_{vv}(x, k_z) &= \int_{-\infty}^{+\infty} \Phi_{vv}(\gamma k_x, k_z) e^{\mathrm{i}\gamma k_x (x/\gamma)} \mathrm{d}k_x, \\ R'_{vv}(x, k_z) &= R_{vv}(x/\gamma, k_z) = \gamma R_{vv}(x, k_z). \end{aligned} \tag{6.17}$$

If an integral length scale is defined as,

$$L = \frac{1}{R_{vv}(0, k_z)} \int_0^{+\infty} R_{vv}(x, k_z) \mathrm{d}x, \tag{6.18}$$

it implies that $L' = \gamma L$. From Eqn. (6.12),

$$\int_{-\infty}^{+\infty} \Phi_{vv}(k_x, k_y, k_z = 0) \mathrm{d}k_y = \frac{3 l_t^3 u_a^2}{4\pi l_a} \frac{l_a^2 k_x^2}{(1 + l_a^2 k_x^2)^{5/2}}. \tag{6.19}$$

In Eqn. (6.19) $l_a k_x$ can be thought of as a modified wavenumber and therefore l_a corresponds to the multiplication factor γ in Eqn. (6.17). Therefore changing l_a can be thought of as elongating the eddies in the streamwise direction in an isotropic spectrum resulting in a subsequent redistribution of energy. On the other hand, the transverse length scale is only acting as a multiplicative constant and thus changing it does not contribute to the redistribution of energy in the spectra but only an increase in its amplitude. This is a consequence of setting the spanwise wavenumber k_z to zero.

This section has implemented an anisotropic velocity spectrum in the analytical leading-edge noise model of Amiet [21]. Using this model it is shown that changing the axial length scale significantly redistributes the energy but does not change the amplitude of the PWL spectra. Changing the transverse length scale does not redistribute energy in the spectrum but increases the amplitude.

6.3 Investigating the effect of anisotropy in a rotor ingesting anisotropic turbulence

In this section Amiet's [18] simplified rotor noise model described in Chapter 3 is coupled with the anisotropic turbulence model of Kerschen and Gliebe [20] to study the effect of anisotropy on the noise radiated by a rotor. First, the anisotropic turbulence model is compared to boundary layer turbulence and its suitability in modelling boundary layer turbulence is assessed. Next the turbulence model is coupled to the rotor noise model. This rotor noise model is then used to investigate the effect anisotropy has on the noise radiated by the rotor. Finally, the effect of changing the blade eddy convection speed, blade stagger angle, and rotor RPM are investigated.

6.3.1 Comparison with experimental measurements

In this section, the anisotropic model spectrum of Kerschen and Gliebe [20] is compared against experimental data. First, the model spectrum is compared against boundary layer

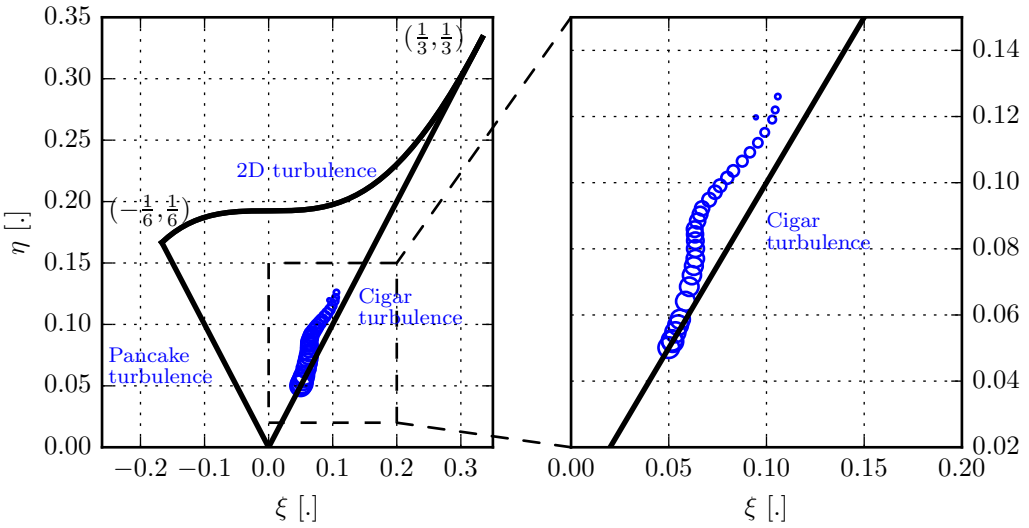

Figure 6.4: The Lumley triangle. The dots represent boundary layer turbulence data obtained from the FC3 dataset at zero spanwise separation and zero time lag. The larger dots represent values obtained farther from the wall.

turbulence. Finally, the predictions made using the frequency-domain rotor noise model are compared against experimental measurements obtained from the Fundamental Case 3 (FC3) dataset.

6.3.1.1 Comparison of the axisymmetric model spectrum with boundary layer turbulence

In this section the anisotropic velocity spectra of Kerschen and Gliebe [147] is compared against experimental boundary layer data. This is done in order to assess how accurately boundary layer turbulence can be modelled by the homogeneous axisymmetric turbulence model of Kerschen and Gliebe [147]. The model spectra of Kerschen and Gliebe [147] makes two key assumptions. Namely, that the turbulence is axisymmetric and that the turbulence is homogeneous. It is known that boundary layer turbulence is not homogeneous in the wall-normal direction. The integral length scale and turbulence velocities are different at varying wall-normal-locations. The turbulence in the free-stream and cross-stream directions is homogeneous. Thus, when the Kerschen and Gliebe [147] model is used with the frequency-domain rotor noise model the integral length scale and turbulence velocities are treated as functions of the wall-normal distance. Doing this accounts for the inhomogeneity of the boundary layer.

The type of turbulence that is present in the flow can be studied by computing the anisotropy tensor (b_{ij}) given by [37],

$$b_{ij} = \frac{\overline{u_i u_j}}{\overline{u_k u_k}} - \frac{1}{3}\delta_{ij}. \tag{6.20}$$

The anisotropy tensor has two invariants (II_b, III_b) from which two variables can be defined,

$$\eta = \sqrt{-\frac{1}{3}\mathrm{II}_b}, \quad \xi = \left(\frac{\mathrm{III}_b}{2}\right)^{1/3}. \tag{6.21}$$

Choi and Lumley [149] used these two invariants to define various turbulence states. These are graphically represented by the Lumley triangle as shown in Fig. 6.4. The origin of the graph represents isotropic turbulence with all three turbulence velocities being exactly equal. The top right vertex at (1/3,1/3) represents one-component turbulence. The top left vertex at (-1/6,1/6) represents two-component axisymmetric turbulence ($u = v, \quad w = 0$). The line joining the top vertices represents two-component turbulence. The line joining the origin to (-1/6,1/6) represents axisymmetric turbulence with $v = w = u_t$ and $u < u_t$. This turbulence is referred to as pancake like turbulence. The line joining the origin to (1/3,1/3) represents axisymmetric turbulence with $v = w = u_t$ and $u > u_t$. This turbulence is referred to as cigar like turbulence.

The boundary layer data obtained from the FC3 dataset in Fig. 6.4 is represented in the triangle as dots. The data is obtained at various wall-normal positions at zero spanwise separation and zero time lag. The larger dots represent values farther away from the wall. It is observed that the turbulence obtained away from the wall is exactly axisymmetric while turbulence closer to the wall is slightly less axisymmetric. This trend can also be observed by examining the turbulence intensities.

Fig. 6.5 shows the turbulence intensities in all three directions at varying wall-normal locations. It is observed that for $r/R_{tip} > 0.8$ the cross-stream and wall-normal velocities are not identical. From Figs. 6.4 and 6.5 it can be concluded that while boundary layer is almost axisymmetric it is not strictly axisymmetric. Therefore using an axisymmetric turbulence model is a valid modelling assumption. However, this is still an approximation as the turbulence is not strictly axisymmetric and it is not homogeneous in the wall-normal direction. The homogeneity in the wall normal direction can partly be accounted for as the data is sampled at various strip positions.

Next, the one-dimensional energy spectra is compared against experimental one-dimensional energy spectra. The theoretical energy spectra are defined as,

$$\mathrm{E}_{11}(k_x) = 2\iint_{-\infty}^{+\infty} \Phi_{11}\mathrm{d}k_y\mathrm{d}k_z = \frac{\pi\alpha}{2l_t^4\left(1 + l_a^2k_x^2\right)}, \tag{6.22}$$

$$\mathrm{E}_{22}(k_x) = 2\iint_{-\infty}^{+\infty} \Phi_{22}\mathrm{d}k_y\mathrm{d}k_z = \frac{\pi\alpha k_x^2}{2l_t^2}\frac{1}{\left(1 + l_a^2k_x^2\right)^2} + \frac{\pi\alpha\xi}{4l_t^4}\frac{1}{\left(1 + l_a^2k_x^2\right)}. \tag{6.23}$$

The experimental energy spectra are computed from the velocity correlation tensor (R_{ij}) as [37],

$$\mathrm{E}_{ij}(k_x) = \frac{1}{\pi}\int_{-\infty}^{\infty} R_{ij}(r_1e_1)\, e^{-\mathrm{i}k_xr_1}\mathrm{d}r_1, \tag{6.24}$$

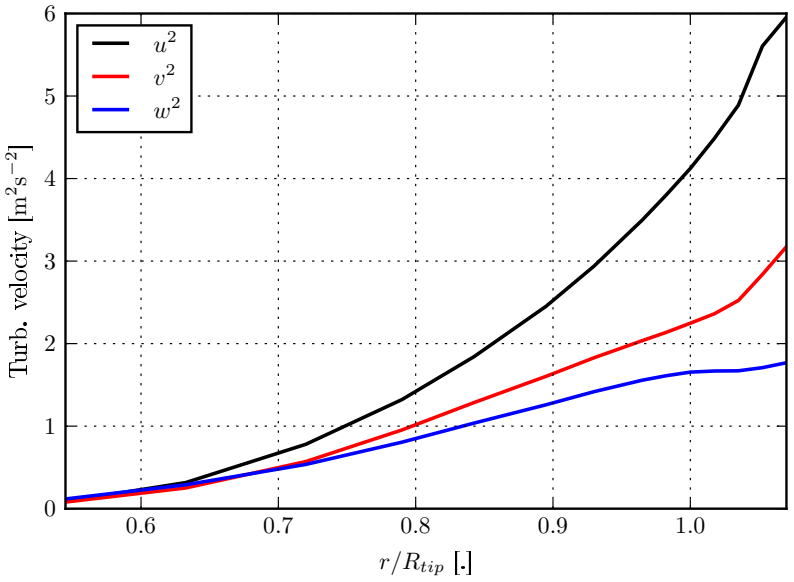

Figure 6.5: RMS velocities.

where $r_1 e_1$ is the separation in the x direction. This separation is computed for the FC3 data set by using the frozen turbulence assumption.

Fig. 6.6 shows the 1D energy spectra computed from the experimental velocity correlation tensor compared with the theoretical 1D energy spectra computed using Eqn. (6.23) at varying wall-normal locations. The integral length scales and turbulence velocities that are used to compute the theoretical energy spectra are taken from experimental data. While the axial energy spectra compares favourably with the theoretical predictions, the cross-stream and wall-normal energy spectra are significantly different. This shows that the boundary layer turbulence is not well modelled by the axisymmetric turbulence model of Kerschen and Gliebe [147]. Fig. 6.6 shows that the cross-stream and wall-normal energy spectra are over-predicted at the low wavenumbers by the theoretical equations of Kerschen and Gliebe [147].

The one-dimensional longitudinal (f) and normal (g) normalised correlation functions can be computed from Eqn. (6.23) as [37],

$$f(r) = \frac{R_{11}}{u_a^2} = \frac{1}{u_a^2}\int_{-\infty}^{+\infty} \Phi_{11}(k_x)\, e^{\mathrm{i}k_x r}\mathrm{d}k_x = e^{-r/l_a}, \tag{6.25}$$

$$g(r) = \frac{R_{22}}{u_t^2} = \frac{1}{u_t^2}\int_{-\infty}^{+\infty} \Phi_{22}(k_x)\, e^{\mathrm{i}k_x r}\mathrm{d}k_x = e^{-r/l_a}\left\{1 - \frac{u_a^2 l_t^2}{u_t^2 l_a^2}\frac{r}{2l_a}\right\}. \tag{6.26}$$

The longitudinal one-dimensional correlation function is the same as that for the isotropic case. The normal velocity correlation differs from the isotropic case for the Liepmann [36] spectrum by the factor $u_a^2 l_t^2 / u_t^2 l_a^2$.

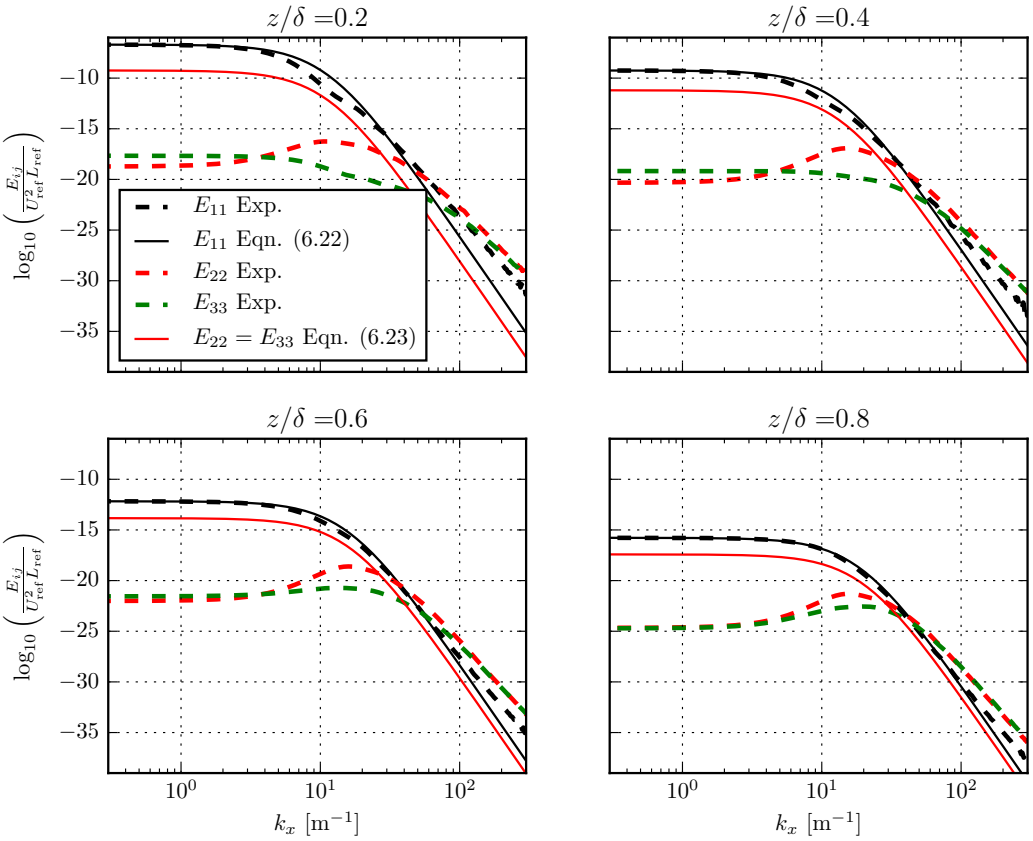

Figure 6.6: One dimensional energy spectra at varying wall-normal locations. Experimental data is extracted from the FC3 dataset. The theoretical 1D spectra are computed using Eqn. (6.23). $L_{ref} = 1\,\mathrm{m}$ and $U_{ref} = 1\,\mathrm{ms}^{-1}$.

A further check can be made by determining a relationship between three length scales, the axial ($l_a = L_{11}^{(1)}$), the transverse ($l_t = L_{22}^{(2)}$), and the length scale for which the vertical turbulence velocities are correlated in the axial direction ($L_{22}^{(1)}$).

The integral length scale can be computed as [37],

$$L_{ij}^{(l)} = \frac{\pi E_{ij}\left(k_l = 0\right)}{2 u_i u_j}, \tag{6.27}$$

where,

$$E_{ij}\left(k_i\right) = 2 \iint_{-\infty}^{+\infty} \Phi_{ij}(k_i, k_j, k_l) \mathrm{d}k_j \mathrm{d}k_l. \tag{6.28}$$

Using Eqns. (6.27) and (6.10) it can be verified that,

$$\begin{aligned} l_a &= \frac{\pi}{u^2} \iint_{-\infty}^{+\infty} \Phi_{11}(k_x = 0, k_y, k_z) \mathrm{d}k_y \mathrm{d}k_z, \\ l_t &= \frac{\pi}{v^2} \iint_{-\infty}^{+\infty} \Phi_{22}(k_x, k_y = 0, k_z) \mathrm{d}k_x \mathrm{d}k_z. \end{aligned} \tag{6.29}$$

It can additionally be shown that by using,

$$L_{22}^{(1)} = \frac{\pi}{v^2} \iint_{-\infty}^{+\infty} \Phi_{22}(k_x = 0, k_y, k_z) \mathrm{d}k_y \mathrm{d}k_z, \tag{6.30}$$

the following relationship for the length scales is obtained,

$$l_t = \frac{\sqrt{2} l_a u_t}{u_a} \left[1 - \frac{L_{22}^{(1)}}{l_a} \right]^{1/2}. \tag{6.31}$$

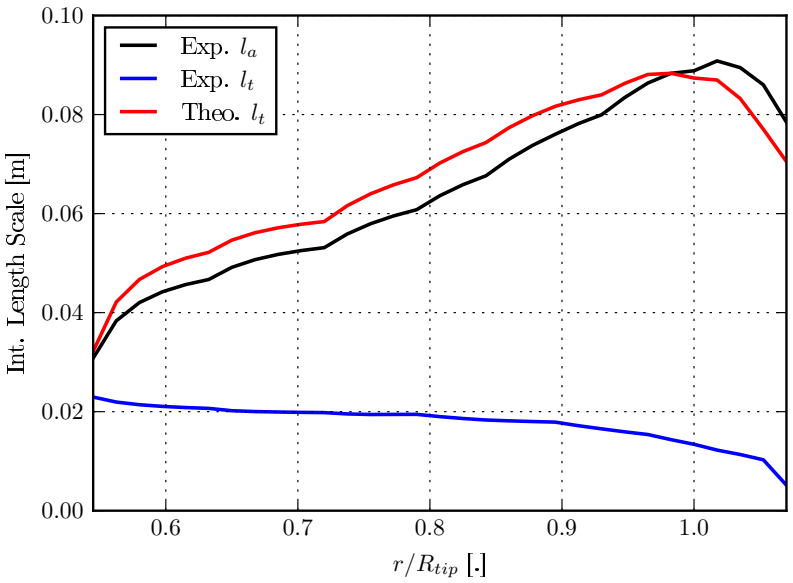

Figure 6.7: The integral length scales computed from experimental data by integrating the normalized correlation curves and using Eqn. (6.31).

Replacing the appropriate values for isotropic turbulence ($u_a = u_t$, $l_a = 2L_{22}^{(1)}$) it can be shown that Eqn. (6.31) reduces to $l_a = l_t$. Fig. 6.7 shows the axial and transverse integral length scales computed from experimental data and using Eqn. (6.31). The integral length scale computed using Eqn. (6.31) is significantly larger than the transverse integral length scale determined from experimental measurements. This is a consequence of the model spectrum over-predicting the energy.

This section has shown that the Kerschen and Gliebe [147] model spectrum has significant discrepancies when compared to experimental measurements. The main discrepancies are that the transverse energy is over-predicted and consequently the theoretical transverse integral length scales are larger than the one determined from experimental measurements. These are most likely because boundary layer turbulence is not axisymmetric and is not homogeneous in the wall-normal directions.

Because of the above mentioned reasons the transverse integral length scale will be chosen empirically. All other quantities will be extracted from the FC3 dataset. The rotor noise model that will use this turbulence model will therefore be semi-empirical.

6.3.2 Coupling the Kerschen and Gliebe turbulence model to Amiet's simplified rotor noise model

As the axisymmetric model of Kerschen *et al.* [20] is derived in the engine fixed reference frame, the above velocity spectra need to be transformed to the blade-fixed coordinate system using the following transformation,

$$\begin{pmatrix} \tilde{\Phi}_{uu} \\ \tilde{\Phi}_{vv} \\ \tilde{\Phi}_{ww} \end{pmatrix} = \begin{bmatrix} \cos\alpha & \sin\alpha\cos\phi & \sin\alpha\sin\phi \\ -\sin\alpha & \cos\alpha\cos\phi & \cos\alpha\sin\phi \\ 0 & -\sin\phi & \cos\phi \end{bmatrix} \begin{pmatrix} \Phi_{uu} \\ \Phi_{vv} \\ \Phi_{ww} \end{pmatrix}, \tag{6.32}$$

where $(\tilde{\Phi}_{uu}, \tilde{\Phi}_{vv}, \tilde{\Phi}_{ww})$ are the velocity correlations in the blade fixed coordinate system. Thus the PSD of the velocity perturbations perpendicular to the blade chord is given by,

$$\tilde{\Phi}_{vv}\left(k_X, k_Y, k_Z\right) = -\Phi_{uu}\sin\alpha + \Phi_{vv}\cos\alpha\cos\phi + \Phi_{ww}\cos\alpha\sin\phi. \tag{6.33}$$

In Eqn. (6.33), the wavenumbers on the blade can be computed from the wavenumbers computed in the engine-fixed reference frame using the following transformation,

$$\begin{pmatrix} k_x \\ k_y \\ k_z \end{pmatrix} = \begin{bmatrix} \cos\alpha & -\sin\alpha & 0 \\ \sin\alpha\cos\phi & \cos\alpha\cos\phi & -\sin\phi \\ \sin\alpha\sin\phi & \cos\alpha\sin\phi & \cos\phi \end{bmatrix} \begin{pmatrix} k_X \\ k_Y \\ k_Z \end{pmatrix}. \tag{6.34}$$

Thus using Eqn. (6.33) along with Eqn. (6.34) in Eqn. (3.41) or (5.11) allows one to compute the noise radiated by a rotor ingesting anisotropic turbulence.

6.3.2.1 Comparison of the PSD of the acoustic pressure with experimental measurements

In this section predictions made using the rotor noise model coupled with the turbulence model of Kerschen and Gliebe [20] are compared to experimental measurements from the FC3 dataset.The predictions are made using the frequency-domain rotor noise model presented in Chapter 3 (Eqn. (3.41)). First, predictions are made using variables that are directly extracted from the experimental dataset as described in Appendix B. However, it is observed that using these values the predictions over-predict the 3^{rd} and 4^{th} Blade Passing Frequency (BPF). Therefore, predictions are next made using an empirical value

of the transverse length scale. Finally, predictions are made by artificially slowing the speed of an eddy as it moves through the rotor disk using an isotropic velocity spectrum.

Fig. 6.8 shows the predicted PSD computed with the anisotropic rotor noise model with the hard-wall included. All variables that are used as input for the turbulence model (l_a, l_t, u_a and u_t) are taken from experimental measurements as described in Appendix B. It is observed that there is an under-prediction at the first peak and that there are peaks at the 3$^{\text{rd}}$ and 4$^{\text{th}}$ BPFs in the predictions that do not appear in the experimental measurements.

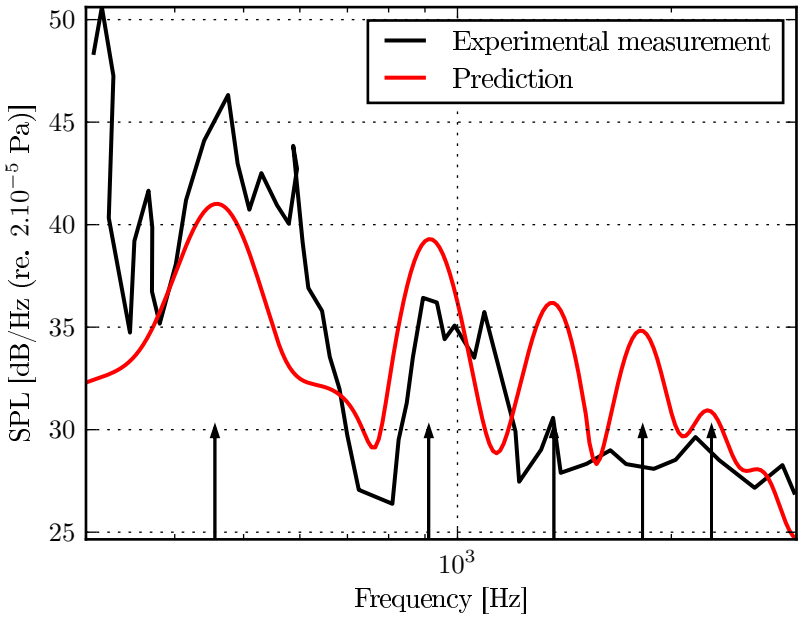

Figure 6.8: The PSD of the acoustic pressure for a rotor operating at the zero thrust operating condition. Predictions are made using the transverse integral length scale obtained from experimental data. The arrows represent the BPFs of the rotor. The observer is located at $r_0 = 3.01$ m and $\theta = 127.3°$ (upstream).

The discrepancies that are observed are most likely due to an incorrect value of the transverse length scale. This is because as shown in Section 6.3.1.1 the turbulence model does not capture the one-dimensional transverse energy spectra. This is due to boundary layer turbulence not being strictly axisymmetric and because of the inhomogeneity of the turbulence in the wall-normal direction. Because of these reasons the transverse integral length scale must be chosen empirically. The value for the transverse integral length scale used is 0.03 m. This is close to the value of the transverse length scale at the rotor hub as shown in Fig. 6.7. The assumptions required to use the anisotropic turbulence model of Kerschen and Gliebe [147] get better further away from the wall. Additionally, the transverse length scale does not vary significantly at various wall normal positions. Thus, the transverse length scale used seems a reasonable choice for this study. All other parameters are taken directly from the experimental measurements.

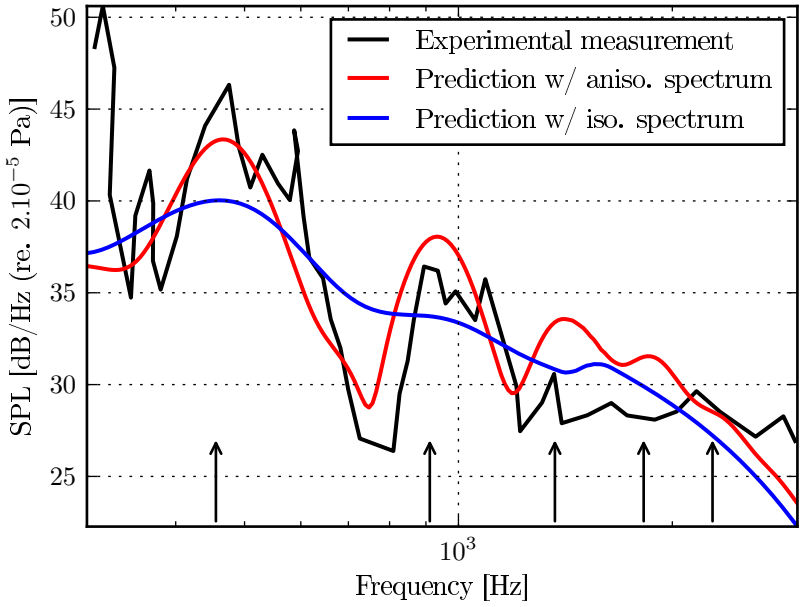

Figure 6.9: The PSD of the acoustic pressure for a rotor operating at the zero thrust operating condition. The transverse integral length scale is chosen to be $l_t = 0.3$ m. All other variables are extracted from experimental data. The arrows represent the BPFs of the rotor. The observer is located at $r_0 = 3.01$ m and $\theta = 127.3°$ (upstream).

Fig. 6.9 shows the predicted PSD of the acoustic pressure computed with the empirical length scale ($l_t = 0.03$ m). Also shown is the prediction with the isotropic model spectrum. It is seen that using the empirical length scale improves the result and a good match is seen between the predictions with the anisotropic spectrum and the experimental measurements. There is a moderate over-prediction at the 2$^{\text{nd}}$ BPF and a moderate over-prediction around the 3$^{\text{rd}}$ and 4$^{\text{th}}$ BPFs. It is additionally observed that using the anisotropic spectrum results in the characteristic haystacks around the BPFs. Therefore, while the hard-wall increases the amplitude of the spectra, especially at low frequencies, the anisotropic spectrum results in the characteristics haystacks. Including these two features in addition to modelling blade-to-blade correlation is crucial to accurately predicting boundary layer ingestion noise. A thorough investigation of the predictions at various microphone locations and operating conditions will be conducted in Chapter 7.

Fig. 6.10 shows the predictions made using the anisotropic velocity spectrum along with predictions made using the isotropic von Kármán velocity spectrum with the eddy speed artificially slowed down by 1/3 as it moves through the rotor disk. This simulates a stretching of the eddy in the streamwise direction. This is the same approach that Paterson and Amiet [79] used to model anisotropy in a helicopter ingesting turbulence. The eddy speed was chosen empirically to fit the experimental measurements. The predictions using the isotropic velocity spectrum match well with predictions made using the anisotropic velocity spectrum. The main differences that are observed are the presence

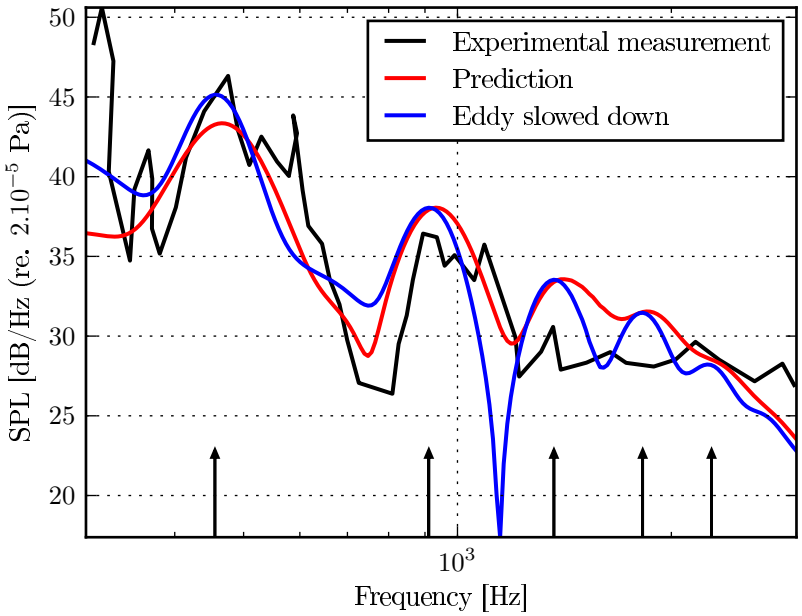

Figure 6.10: The PSD of the acoustic pressure for a rotor operating at the zero thrust advance ratio. Predictions are computed using the anisotropic velocity spectrum and the isotropic von Kármán spectrum with the eddy speed artificially slowed down. The arrows represent the BPFs of the rotor. The observer is located at $r_0 = 3.01$ m and $\theta = 127.3°$ (upstream).

of a strong destructive peak between the 2$^{\text{nd}}$ and 3$^{\text{rd}}$ BPFs and additional correlation peaks at the 3$^{\text{rd}}$ and 4$^{\text{th}}$ BPFs. While the predictions made using the isotropic spectrum match the predictions made using the anisotropic spectrum, the amount that the eddy had to be slowed down was chosen arbitrarily. While the transverse length scale is also chosen empirically, the choice of transverse length scale is informed by values extracted from experimental data, i.e. it is close to the value of the transverse length scale extracted in Appendix B at the edge of the boundary layer. Additionally, the anisotropic spectra is also changing the distribution of energy in the spectra in a more representative manner when the axial and integral length scales are changed. Predictions will therefore be made using the anisotropic velocity spectrum for the remainder of this thesis.

6.3.3 The effect of anisotropy on the noise radiated by a rotor ingesting anisotropic turbulence

In this section the anisotropic turbulence model of Kerschen and Gliebe [20] is used to study the effect of a rotor ingesting anisotropic turbulence. The rotor geometry that is used for this study is a scaled Sevik rotor that is taken from the data provided with the FC3 of the Fan Broadband Noise (FBN) workshop. The rotor is operating at the zero thrust condition ($\Omega = 2734$ RPM, $U = 30\ \text{m}\,\text{s}^{-1}$) and the turbulence intensities are $u_a^2 = 1\ \text{m}^2\,\text{s}^{-2}$ and $u_t^2 = 4\ \text{m}^2\,\text{s}^{-2}$ respectively. Additionally, the entire rotor is ingesting

turbulence. Using Amiet's [18] rotor noise model (without wall effects) the effect of changing the axial and transverse length scale on the power radiated by the rotor is investigated.

Fig. 6.11 shows the PWL spectra of the rotor computed using Eqn. (5.27) for varying axial and transverse length scales. Fig. 6.11(a) shows the PWL spectra of the rotor computed at varying axial length scales while keeping the transverse length scale constant. From this figure it is observed that the power in the spectra increases as the axial length scale increases, the haystacks at the higher BPFs increases as the axial length scale increases, and the width of the first BPF decreases as the ratio of the axial to transverse length scale is increased.

Fig. 6.11(b) shows the PWL spectra of the rotor computed at varying transverse length scales while keeping the axial length scale constant. From this figure it is observed that there is a slight increase in the power as the transverse length scale is increased. The number of haystacks at the higher BPFs decreases as the transverse length scale increases (ratio of length scales increases).

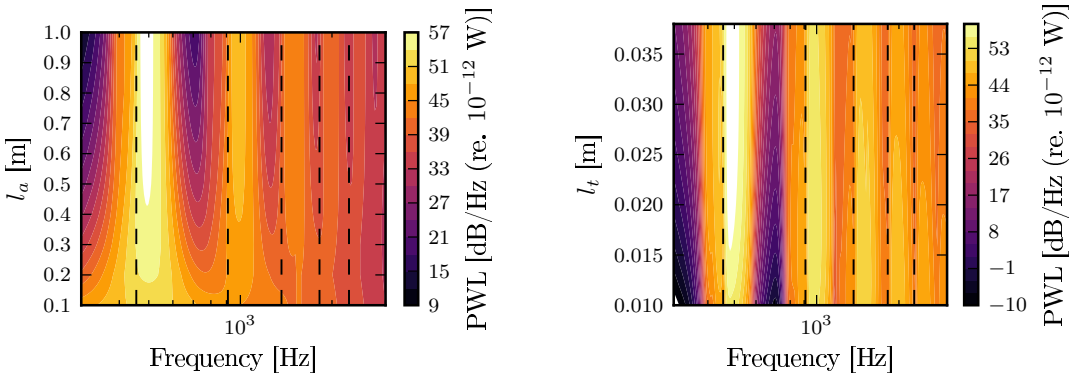

(a) PWL spectra for l_a varying.

(b) PWL spectra for l_t varying.

Figure 6.11: The PWL spectra for varying length scales and frequencies. The dashed lines indicate the BPFs of the rotor.

The maximum power in the spectra at the various length scales is shown in Fig. 6.12. From Fig. 6.12(a) it is observed that the maximum power increases as the axial length scale and consequently the ratio of the axial to transverse length scale increases. Fig. 6.12(b) shows that the maximum power increases as the transverse length scale increases to $l_t = 0.03$ m. It then subsequently begins decreasing.

The behaviour in Fig. 6.11 and Fig. 6.12 can be understood by looking at Eqn. (6.33). From this it is observed the transverse velocity spectrum in the blade-fixed coordinate system has contributions from all three fluctuating velocity components in the engine-fixed coordinate system. This is unlike the case for the translating aerofoil where only the transverse velocity spectrum contributes to the noise radiated by the blade. In that

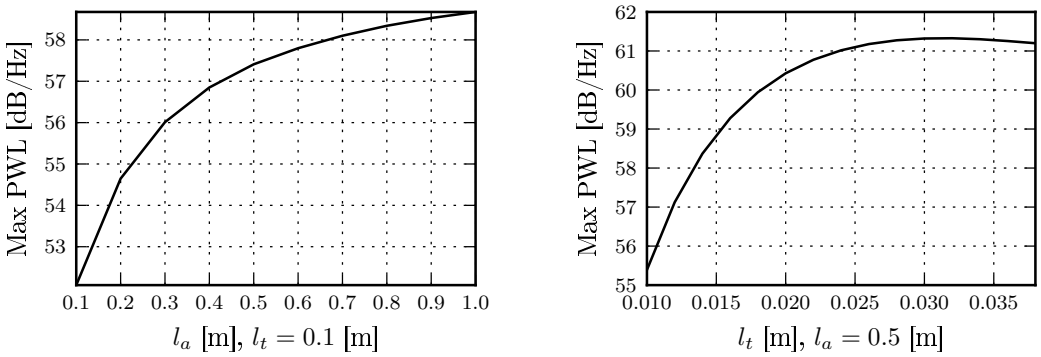

(a) Maximum PWL for l_a varying.

(b) Maximum PWL for l_t varying.

Figure 6.12: The maximum PWL for varying axial and transverse length scales.

case increasing the transverse length scale implies more of the energy in the spectrum is being distributed to the transverse spectrum and this resulted in an increase in noise. For the case of the rotor all the velocity components contribute to the transverse velocity spectrum in the blade-fixed reference frame.

Fig. 6.14 shows the bandwidth of the 1st haystack at 3 dB below the maximum amplitude. A schematic of the definition of the bandwidth is shown in Fig. 6.13. The bandwidth of the peaks is known to scale as l_a/U [20] where U is the speed of the eddy as it moves through the rotor disk. For the case of varying axial length scales in Fig. 6.14(a) the bandwidth follows this scaling law closely. For the case of varying transverse length scales with the axial length scale fixed, the bandwidth should be a constant of 60 Hz for an axial length scale of 0.5 m and an eddy speed of 30 m s^{-1}. The bandwidth is close to this value in Fig. 6.14(a) and is relatively constant. It should be noted that transverse integral length scale should be smaller than the inter-blade spacing as the rotor noise model that is used does not account for potential effects between blades.

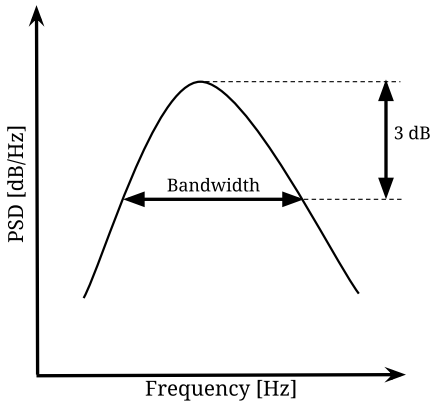

Figure 6.13: A schematic showing the definition of the bandwidth.

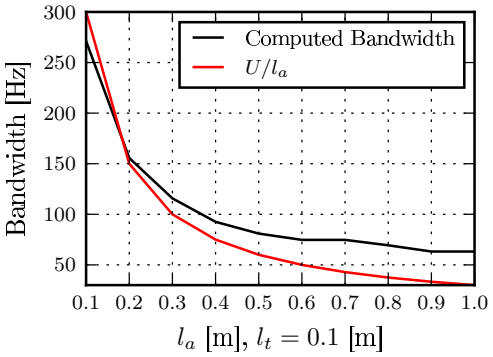

(a) The width of the first haystack for varying l_a.

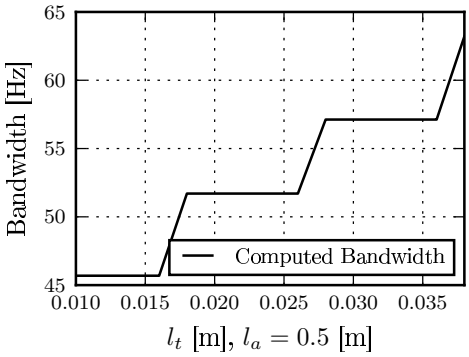

(b) The width of the first haystack for varying l_t.

Figure 6.14: The width of the first haystack for varying axial and transverse length scales. The bandwidth is computed at 3 dB below the peak value of the 1st haystack.

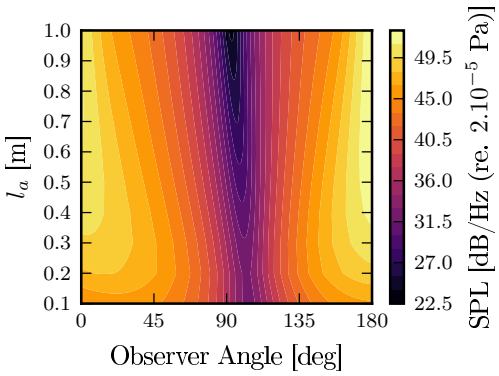

(a) Directivity for l_a varying.

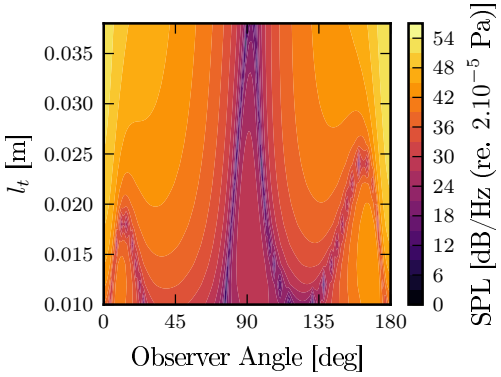

(b) Directivity for l_t varying.

Figure 6.15: The directivity of the rotor for varying axial and transverse length scales. The directivity plots are obtained at a frequency of 455 Hz.

Fig. 6.15 shows the directivity of the rotor with varying axial and transverse length scales. It is noticed that the directivity increases by 5 dB at certain observer angles for the case of the axial length scale varying. Changing the transverse integral length scale on the other hand has a minimal impact on the directivity at particular observer angle. Additionally, it is observed that constructive and destructive interference peaks are observed. These constructive and destructive interference peaks are a result of the wavenumbers changing as the length scale is changed.

This section has shown that the maximum power in the spectrum is a function primarily of the ratio of the axial to transverse length scales. Increasing the ratio of the axial to transverse length scale increases the power at the haystacks and also the number of haystacks seen at the higher frequencies. It is shown that the width of the haystacks

scales as the ratio of the axial length to the eddy convection speed as has been previously reported.

6.3.4 Investigating the parameters that affect the blade-to-blade correlation for a rotor ingesting anisotropic turbulence

In this section the effects of varying the blade stagger angle, rotor RPM, and eddy convection speed are investigated. This is done by examining the azimuthally averaged PSD of the velocity spectrum. This is done in order to isolate the other effects in Amiet's simplified model and is expected to be representative of the radiated sound as has been shown in Sect. 6.2. From Eqn. (6.35), the azimuthally averaged velocity spectrum is given by,

$$\int_0^{2\pi} \sum_{n=-\infty}^{\infty} \frac{2\pi}{\mathcal{C}} \Phi_{vv}\left(k_X, K_{Y,n}, k_Z = 0\right) \mathrm{d}\phi. \tag{6.35}$$

The velocity correlation with blade-to-blade correlation is modelled for a rotor blade with only one strip at a radius of 0.1 m. The mean flow speed (which is assumed to be the same as the eddy convection speed), the rotor speed, and the blade stagger angle were varied by ensuring that they always satisfy the zero loading assumption,

$$\tan\alpha = \frac{R\Omega}{U_x}. \tag{6.36}$$

Therefore, when one variable was varied, one variable was kept constant and the other variable was computed from Eqn. (6.36).

Fig. 6.16(a) shows the velocity spectra varying as the blade stagger angle is varied. The rotor speed is kept constant at 2734 RPM. From Fig. 6.16(b) it is seen that increasing the blade stagger angle reduces the eddy convection speed. This implies that more blades chop the same eddy and haystacks appear at the higher BPFs as is seen in Fig. 6.16(a). From 6.16(a) it is also observed that changing the blade stagger angle shifts the peaks at which the haystacks appear away from the BPF. From Eqn. (3.32) this shift is approximately $1/\sin^2\alpha$ (assuming that $c_0\sigma >> \mathcal{C}Y$). This implies that the predicted BPF will deviate the most for the smaller stagger angles as is shown in Fig. 6.16(b). This feature has also been found by Martinez [150].

Fig. 6.16(c) shows the velocity spectra varying as the rotor speed is varied. The blade stagger angle is kept constant at 45°. From Fig. 6.16(d) it is seen that increasing the rotor speed increases the eddy convection speed. Therefore the lowest RPM will have the most haystacks as is seen in Fig. 6.16(c). Additionally, the BPFs in Fig. 6.16(c) are also shifted to higher frequencies as the rotor RPM is increased.

Fig. 6.16(e) shows the velocity spectra varying as the eddy convection speed is varied. The rotor speed is kept constant at 2734 RPM. As was observed in the previous cases a slower eddy speed once again corresponds to more haystacks appearing at the higher frequencies due to eddies moving more slowly through the plane of rotation.

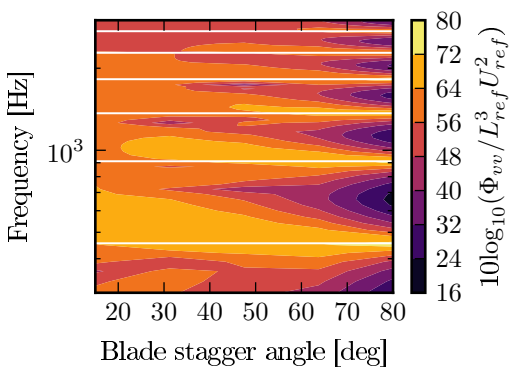

(a) The velocity sectrum for a varying blade stagger angle.

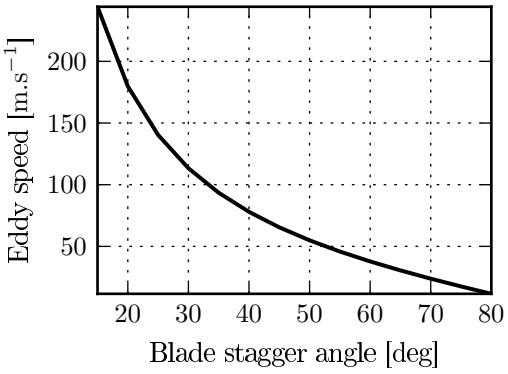

(b) The eddy convection speed computed for a varying blade stagger angle.

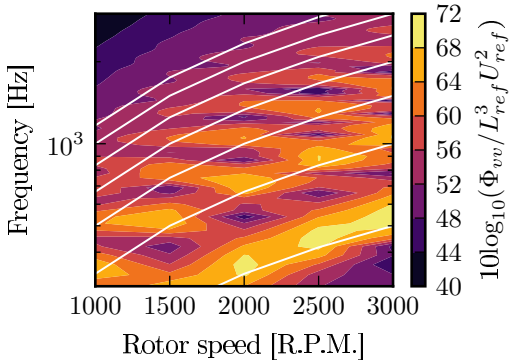

(c) The velocity sectrum for a varying rotor speed.

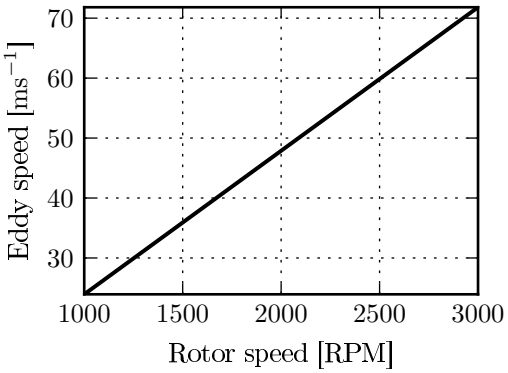

(d) The eddy convection speed computed for a varying rotor speed.

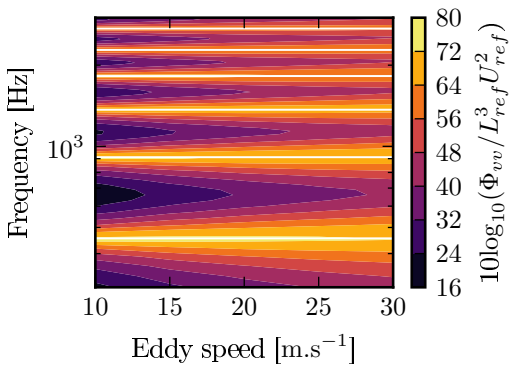

(e) The velocity sectrum for a varying eddy convection seed.

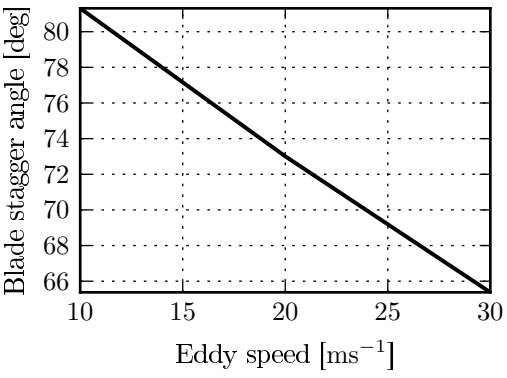

(f) The blade stagger angle computed for a varying eddy convection speed.

Figure 6.16: The PWL spectra for varying length scales and frequencies. The dashed lines indicate the BPFs of the rotor.

This section has shown how the blade stagger angle, rotor speed, and eddy convection speed affect the velocity spectra. It has been shown that the eddy convection speed is an important parameter and this affects the number of haystacks seen. Additionally, it has been observed that changing the blade stagger angle can shift the frequencies at which the haystacks appear away from the BPFs of the rotor.

6.4 Conclusions

This chapter has introduced an axisymmetric anisotropic velocity spectrum. The velocity spectrum that is derived by Kerschen and Gliebe [20] is a modified Liepmann spectrum that is based on the works of Chandrashekhar [38] and Batchelor [39]. This chapter has first investigated the effects of anisotropy for a translating aerofoil ingesting turbulence. Then the anisotropic model is compared to experimental boundary layer turbulence. Finally, the anisotropic turbulence model is coupled to Amiet's [18] frequency-domain rotor noise model. The main conclusions that are drawn from this chapter are as follows,

- For the case of a translating aerofoil ingesting turbulence, anisotropy can have a significant impact on the radiated noise. Increasing the transverse integral length scale results in a significant increase in noise and increasing the axial length scale reduces the radiated noise. This is because increasing the transverse integral length scale distributes more energy to the transverse velocity spectra, and this is the main generator of noise.
- When the axisymmetric turbulence model is compared to realistic boundary layer turbulence several discrepancies are found. It is shown that the 1D energy spectra do not match and consequently the integral length scales computed from the theoretical autocorrelations differ significantly from the integral length scales computed from the experimental data. These discrepancies are most likely because boundary layer turbulence does not fit the axisymmetric assumption and because boundary layer turbulence is not homogeneous in the wall-normal direction.
- Predictions using the anisotropic turbulence coupled with Amiet's [18] extended frequency-domain model show a good match to experimental measurements. The addition of an anisotropic turbulence model results in the a peak at the 2^{nd} BPF. Due to the limitations of the anisotropic turbulence model in capturing boundary layer turbulence, the transverse length scale from these predictions is chosen empirically.
- The effect of anisotropy is studied by computing the PWL spectra for varying axial length scales with the transverse length scale fixed and the for varying transverse length scales while keeping the axial length scale fixed. It is seen that the power increase as the axial length scale is increased and as the transverse length scale is increased up to a certain length scale. The bandwidth of the haystacks is shown to scale as l_a/U. The effect of the eddy speed, blade stagger angle, and rotation speed of the rotor are determined by examining how the velocity correlation tensor changes when these parameters are varied.

Chapter 7

Validation of the rotor noise model

The previous chapters have extended Amiet's [18] rotor noise model to include wall-effects and to model anisotropy. In this chapter the frequency-domain rotor noise model that has been developed in the previous chapters will be compared against the time-domain rotor noise model results of Glegg *et al.* [25] and against experimental measurements.

The time-domain method of Glegg *et al.* [25] uses a time-domain formulation of the Ffowcs Williams and Hawkingss (FWHs) equations along with Amiet's [77] two-dimensional time-domain compressible response function to compute the Power Spectral Density (PSD) of the noise. The method does not rely on a model of the velocity statistics and instead, takes as input a four-dimensional time and space varying velocity correlation tensor. This makes the method very accurate, and the power spectral density computed using this method is very close to the noise spectra measured in experiments. The inputs required for the model are the undistorted velocity correlation tensor that was measured in the absence of the rotor. Thus this methods accuracy reduces as the rotor thrust increases and correspondingly, the distortion of the boundary layer, is increased. This could be fixed by using rapid distortion theory to account for the distortion.

Comparing the frequency-domain method and the time-domain method to experimental measurements will determine the accuracy of the method. Comparisons between Amiet's [18] extended frequency-domain method and the time-domain method of Glegg *et al.* [25] will also determine how successful the axisymmetric anisotropic turbulence model is at capturing the statistics of boundary layer turbulence.

The predictions made in this chapter using Amiet's [18] extended frequency-domain method are made using a semi-empirical length scale of 0.03 m. This is because boundary

layer turbulence is not strictly axisymmetric and is not homogeneous in the wall-normal direction. In order to determine how sensitive the model is to the transverse length scale a sensitivity study is performed to determine the effect that varying the length scale has on the PSD of the noise.

7.1 Results

In this section, the results obtained from the developed rotor noise model are compared against experimental data and predictions from the time-domain model of Glegg *et al.* [25]. The details of the time-domain model are presented in Appendix D. The results for the time-domain predictions are taken from the results presented at the 2017 American Institute of Aeronautics and Astronautics (AIAA) Fan Broadband Noise (FBN) workshop.

The rotor geometry is based on a scaled Sevik rotor. The Sevik rotor has a tip diameter of 457.2 mm and a hub diameter of 127 mm. The rotor has 10 blades with a constant chord of 57.2 mm and the stagger angle of the blades varies from 34.4° at the hub to 68.8° at the tip. Further details of the test case are provided in Appendix B.1.

The FC3 benchmark case tests the rotor at 4 different advance ratios given in Tab. 7.1. However, at an advance ratio of $J = 0.50$, a large tip vortex forms between the blade tip and the wind tunnel wall [151]. This tip vortex subsequently interacts with the rotor resulting in a large increase in the noise and large tonal peaks at the Blade Passing Frequencies due to multiple blades passing through the same vortical structure. As the rotor noise model does not include the noise due to the ingestion of a tip vortex, predictions at this advance ratio were not performed.

Name	Advance Ratio	Rotor speed [RPM]	Mean flow speed [$\mathrm{m\,s^{-1}}$]
OpA	1.44	2734	30
OpB	1.05	2500	20
OpC	0.87	4500	30
OpD	0.50	2500	10

Table 7.1: The different advance ratios of the Fundamental Case 3 (FC3).

The computations for the rotor noise model are computed using 200 azimuthal integration points and 10 span-wise strips. The strips are logarithmically spaced so that the tip of the blade has a larger density of strips. The mean density and speed of sound for all computations are 1.08 $\mathrm{kgm^{-3}}$ and 350 $\mathrm{ms^{-1}}$ respectively. The predictions were compared to experimental measurements at 3 microphone locations. The microphone locations are given in Tab. 7.2 and a schematic of their position relative to the rotor are shown in Fig.

7.1. Microphones 1 and 4 are located in an anechoic chamber that is connected to the wind-tunnel via a Kevlar lined window. Microphone 5 is placed in the wind tunnel.

Position	θ [deg]	r_0 [m]
1	90	3.591
4	127.3	3.036
5	165.6	2.309

Table 7.2: Microphone positions at which experimental measurements were taken.

The turbulence properties that are used to specify the axisymmetric turbulence model of Kerschen and Gliebe [24] are extracted from the Fundamental Case 3 (FC3) dataset, the details of which are provided in Appendix B.1. The transverse integral length scale is chosen empirically to be 0.03 m as explained in Chapter 6 .

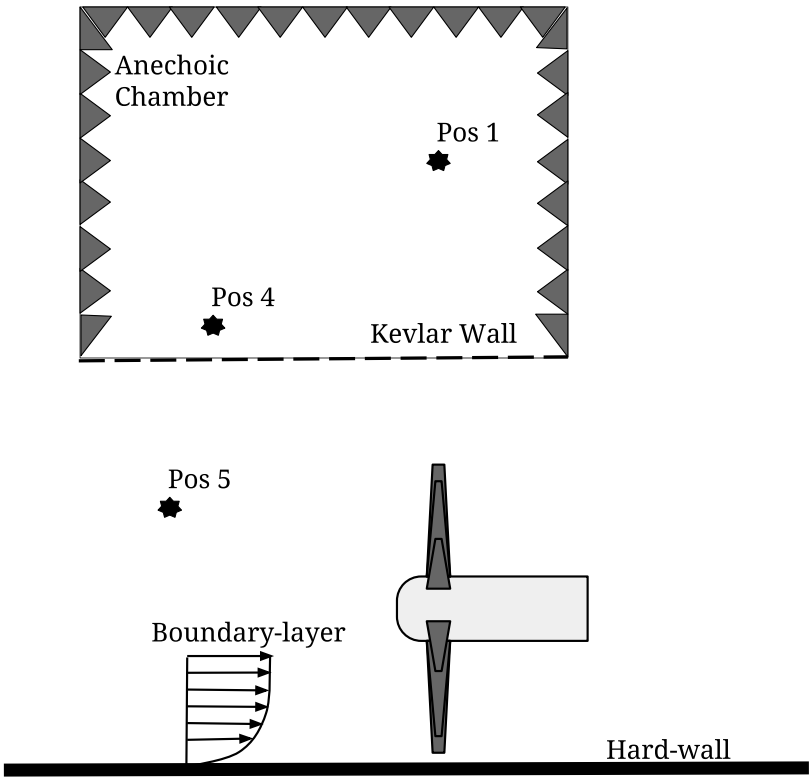

Figure 7.1: Schematic of the different microphone locations.

Fig. 7.2 shows the results for the rotor operating at the zero thrust (Op A) condition. Both the frequency-domain predictions using Amiet's [18] extended model and time-domain predictions show under-predictions at Pos. 1. The frequency-domain predictions show under-predictions at all frequencies while the time-domain predictions only show under-predictions at the higher frequencies. Analytical predictions usually show bad

agreements in the cusp of the dipole ($\theta = 90°$) because the PSD of the acoustic pressure becomes very close to 0 at this observer location. Additionally, due to the low sound pressure radiated by the rotor at this observer location, the experimental measurements are more susceptible to background noise.

At Pos. 4, the frequency-domain predictions and the time-domain predictions show a good match with the experimental measurements. The frequency-domain predictions show additional peaks at the 3rd and 4th BPFs that are absent from the experimental measurements and there is a steep drop-off at the higher frequencies. The additional peaks could be due to the rotor affecting the turbulence that it is ingesting. Even though this is the zero thrust operating condition, it is possible that the rotor is changing the pressure gradient through which the boundary layer must traverse. The time-domain rotor noise model on the other hand, does not capture the 2nd BPF accurately and the haystack is almost absent from the predictions.

At Pos. 5, there is an under-prediction of approximately 5 dB of the amplitude of the 1st BPF by the frequency-domain method. This is most likely because this microphone is in the wind-tunnel, and therefore there is additional background noise at this measurement location. Alternatively, there might be some refractions through the mean-flow gradients of the boundary layer that are affecting the noise at this microphone location. The frequency-domain predictions at Pos. 5 compare favourably with the time-domain predictions at this observer location with the exception of an approximately 2 dB under-prediction at the 1st BPF. While the high frequency drop off remains, it is not as prominent as at Pos. 4.

Table 7.3 shows the OverAll Sound Pressure Level (OASPL) for all three positions. As confirmed by the qualitative analysis, the predictions at Pos. 4 are the best and the predictions at Pos. 1 are the worst. The OASPL is mostly determined by how well the predictions capture the 1st BPF peak. As this is an important level to capture correctly, this is a valid quantitative comparison at this stage.

Figures 7.3 and 7.4 show the results for the rotor operating at operating condition B (2500 RPM, 20 m s^{-1}) and C (4500 RPM, 30 m s^{-1}) respectively. The overall trends that are observed for the rotor operating at operating condition A are once again seen in these comparisons. There is a severe under-prediction at Pos. 1, a good match at Pos. 4, and an approximately 5 dB under-prediction in the amplitude of the 1st peak at Pos. 5 when the frequency-domain predictions are compared to experimental measurements and an approximately 3 dB under-prediction when the time-domain predictions are compared to experiential measurements. At operating condition B and at Pos. 4 it is observed that the location of the 2nd BPF is incorrectly predicted. The location of 2nd peak of the experimental measurements is not at the 2nd BPF. Wisda *et al.* [98] have reported that the cause of this peak not being at the BPF could be because of the vortical structures

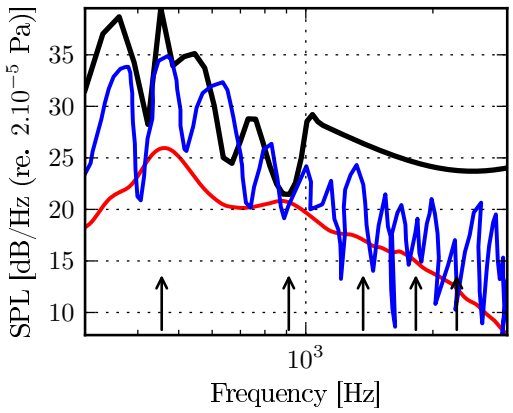

(a) Pos. 1.

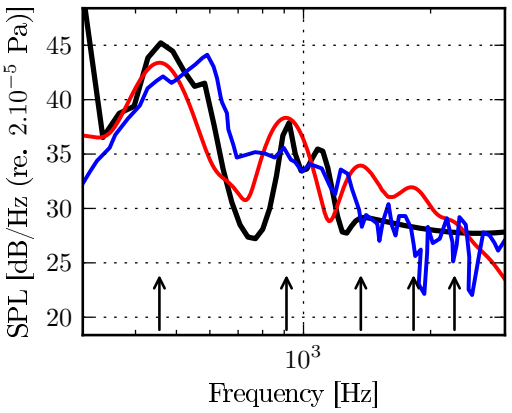

(b) Pos. 4.

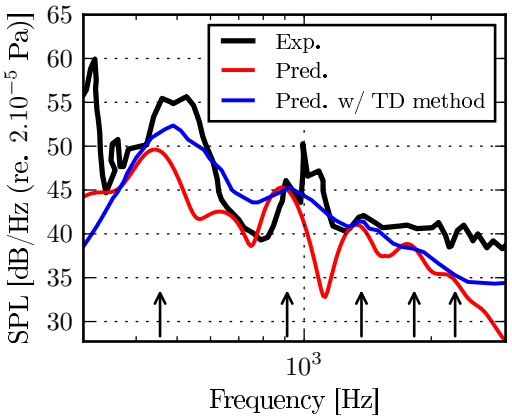

(c) Pos. 5.

Figure 7.2: Predictions using Amiet's extended frequency domain rotor noise model and Glegg's time-domain model compared to experimental measurements for the rotor operating at 2734 RPM with a mean-flow speed of 30 m s^{-1} (OpA).

in the boundary layer being inclined. This in turn implies that the time between blade chops is altered and this causes the frequency shift that is observed.

Another interesting comparison that can be made is the comparison between the predictions using Amiet's [18] extended frequency-domain model and the time-domain predictions of Glegg *et al.* [25]. The predictions using the two different methods match well. From Tabs. 7.3 and 7.4 it can be seen that the largest differences between the predictions are at Pos. 1, where the OASPL is under-predicted by 7 dB by the frequency-domain method at all microphone locations. At Pos. 4 there is almost no difference between the predictions and at Pos. 5 there is an approximately 2.5 dB difference at all operating conditions. The main difference between the frequency-domain and time-domain method is the method in which the turbulence is modelled. The frequency-domain model uses the axisymmetric homogeneous model of Kerschen and Gliebe [20] while the time-domain model computes the velocity correlation tensor directly from experimental measurements.

Op Cond./Mic	OASPL(Exp) [dB]	OASPL(FD) [dB]	Δ OASPL [dB]
OpA P1	67.5	52.4	15.1
OpA P4	72.5	68.5	4.0
OpA P5	83.1	74.7	8.1
OpB P1	63.5	46.6	16.6
OpB P4	68.5	62.7	5.8
OpB P5	77.4	69.3	8.1
OpC P1	70.8	60.0	10.8
OpC P4	75.5	76.1	0.6
OpC P5	87.2	82.4	4.8

Table 7.3: The OASPL from the experimental measurements and Amiet's extended frequency-domain rotor noise model.

As the predictions using these different models match reasonably, it can be concluded that the Kerschen and Gliebe [20] turbulence model can be used to make a good approximation of boundary layer turbulence. However, this is dependant on determining an accurate length scale and this can be difficult. The major advantage of the frequency-domain model is the fact that it is much cheaper to run.

Op Cond./Mic	OASPL(Exp) [dB]	OASPL(TD) [dB]	Δ OASPL [dB]
OpA P1	67.5	58.8	8.7
OpA P4	72.5	68.9	3.6
OpA P5	83.1	77.5	5.6
OpB P1	63.5	54.1	9.4
OpB P4	68.5	62.7	5.8
OpB P5	77.4	71.7	5.7
OpC P1	70.8	68.1	2.7
OpC P4	75.5	77.5	-2.0
OpC P5	87.2	84.0	3.2

Table 7.4: The OASPL from the experimental measurements and Glegg's time-domain rotor noise model.

Computationally, the frequency domain model takes approximately 5 minutes to run for predictions at one observer location and one operating condition while the time-domain model takes 6 hours [1]. Additionally, the experimental data required as input for the time-domain model is a 4D time and space varying velocity correlation tensor. This

[1]For one operating condition and one microphone location. The simulations are run on a workstation with 16 GB of RAM and a 4 core Intel(R) Core(TM) i7-3770 CPU @ 3.40GHz with hyper-threading. The frequency-domain code is written in MATLAB using parallel for loops while the time-domain code was reproduced written in Fortran90 using the OpenMP library to make it run in parallel.

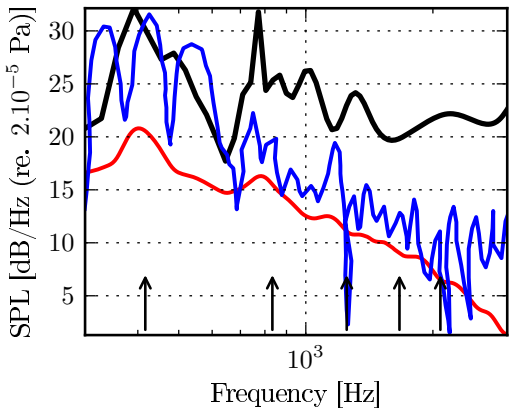

(a) Pos. 1.

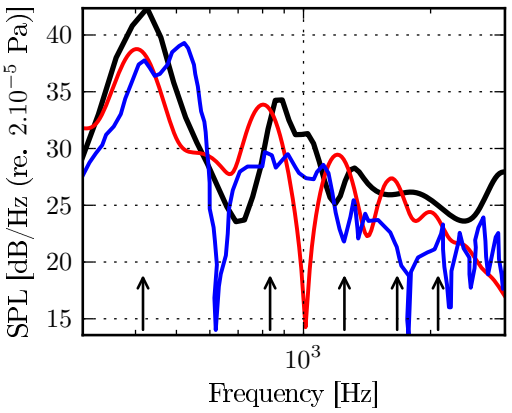

(b) Pos. 4.

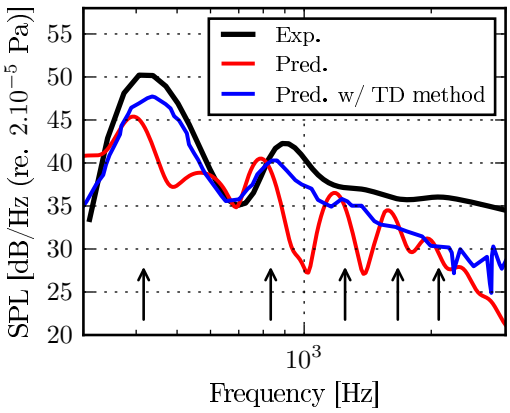

(c) Pos. 5.

Figure 7.3: Predictions using Amiet's extended frequency domain rotor noise model and Glegg's time-domain model compared to experimental measurements for the rotor operating at 2500 RPM with a mean-flow speed of 20 m s^{-1} (OpB).

tensor is very time-consuming to measure and prohibitively expensive to make use of in preliminary design studies.

This section has shown that the frequency-domain and time-domain predictions show a representative match when compared to experimental data. There are amplitude discrepancies that are observed at certain observer angles. This could be because of additional noise sources that are not modelled or because of the background noise not being accounted for. The time-domain results of Glegg [25] that are presented in the section have been corrected for background noise. Comparing the frequency-domain and time-domain predictions shows that the Kerschen and Gliebe [20] turbulence model can be used to make a good approximation of boundary layer turbulence. As the extended frequency-domain model is much cheaper to use, it is the most appropriate tool to use for preliminary design studies.

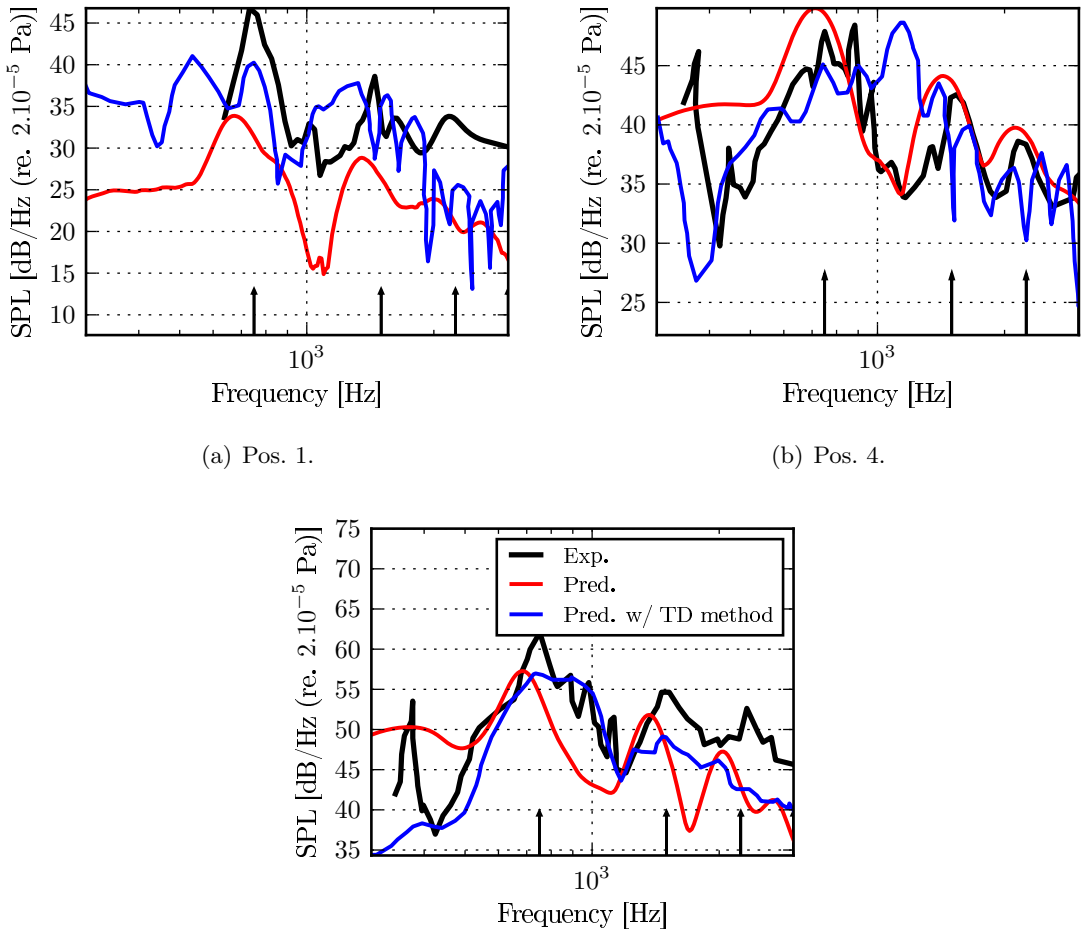

(a) Pos. 1.

(b) Pos. 4.

(c) Pos. 5.

Figure 7.4: Predictions using Amiet's extended frequency domain rotor noise model and Glegg's time-domain model compared to experimental measurements for the rotor operating at 4500 RPM with a mean-flow speed of 30 m s^{-1} (OpC).

7.2 Sensitivity study

The results in the previous section were computed by specifying the inputs required for the Kerschen and Gliebe [24] anisotropic turbulence model. These inputs are the axial and transverse length scales and turbulent velocities (l_a, l_t, u_a, u_t). However, due to the inhomogeneity of the boundary layer in the wall normal direction a transverse length scale could not be accurately computed from experimental data. Instead, an empirical transverse integral length scale was used. In this section, the effect of changing the transverse integral length scale on the computed PSD of noise is quantified.

This is done by running the noise model for a number of transverse integral length scales that are randomly sampled. This assumes that the transverse length scale is uniformly distributed. This study has used 100 different predictions for a transverse length randomly chosen between $0.01\,\text{m} < l_t < 0.05\,\text{m}$.

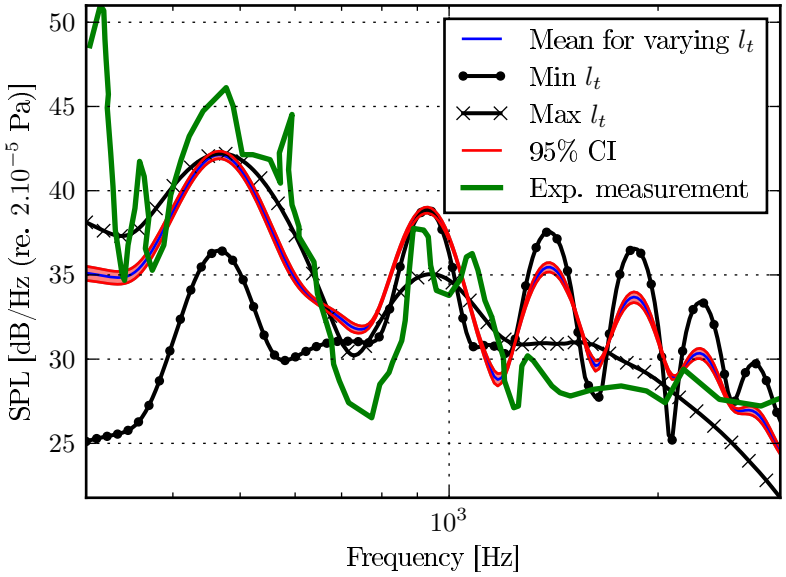

Figure 7.5: The variation of the PSD of the acoustic pressure at one observer location ($r_0 = 3.01$ m, $\theta = 127.3°$).

Fig. 7.5 shows the variation of the PSD of the acoustic pressure compared to the experimental measurements. Looking at the difference in the predictions made using the maximum and minimum transverse length scale, it is clear that the choice of transverse length scale has a significant impact on the noise spectrum. This fact has been observed by various authors for different analytical models. Having said that, the mean noise spectra matches the predictions well and is comparable to the predictions made using $l_t = 0.03$ m. The 95 % confidence interval (which is computed as $\pm 1.96\sigma$, where σ is the standard deviation) has a relatively small spread.

Therefore from the results presented above one can conclude that the transverse length scale can have a significant impact on the radiated noise. However, in the absence of *a priori* information, predictions can be made by determining the likely range of transverse length scales and computing the mean of the PSD predicted at each of the integral length scales.

7.3 Conclusions

This section has compared the extended frequency-domain method against experimental measurements and a time-domain method developed by Glegg *et al.* [25]. The time-domain analytical method is very accurate as it does not model the turbulence in the boundary layer. Instead, it takes as input a 4D time and space varying velocity correlation tensor. This velocity correlation tensor is then convolved with a response function to

determine the blade loading. The far-field radiated noise is then determined using the FWH acoustic analogy, The conclusions that are drawn from this chapter are,

- The frequency-domain method produces a good match when compared to experimental measurements at Pos 4. There is a severe under-prediction at Pos 1 and moderate under-prediction at Pos 5. The under-prediction at Pos 5 is also observed in the time-domain predictions. The under-predictions could be due to the background noise. The microphone at Pos 5 is not in the anechoic chamber and the sound levels are low at Pos 1. This makes the microphones at these positions particularly susceptible to background noise. At all the measurement positions the frequency-domain method predicts an extra peak at the 3^{rd} BPF and there is a sharp-drop off at high frequencies. The additional peak that is observed could be due to a slightly incorrect transverse length scale. This value had to be chose empirically because boundary layer turbulence is not homogeneous in the wall-normal direction and not strictly axisymmetric. The sharp drop-off that is observed at high-frequencies could be because the experiments are measuring noise sources that are not modelled.

- Comparing Amiet's [18] extended frequency-domain and time-domain methods provides insight into how well the axisymmetric anisotropic turbulence spectrum of Kerschen and Gliebe [20] is capturing boundary layer turbulence. This is because the time-domain method takes a velocity correlation tensor from experiments as input. At most of the microphone locations a good match is observed between the frequency-domain and time-domain methods. This indicates that the turbulence model is good approximation of boundary layer turbulence. However, this is dependant on choosing the correct transverse length scale and this value is difficult to determine *a priori*.

- Amiet's [18] extended frequency-domain method is significantly cheaper to run than the time-domain method. The frequency-domain method is significantly faster to run computationally. Additionally, the 4D time and space varying velocity correlation tensor is prohibitively expensive to obtain for preliminary design studies.

- As the transverse length is chosen empirically a sensitivity study is performed on this parameter. It is observed that the transverse length scale can have a significant impact on the radiated noise. However, the mean PSD shows a good match to the experimental measurement and the 95 % confidence interval has a narrow spread.

Chapter 8

Conclusions and future work

In this chapter the conclusions of the thesis are presented. Counter Rotating Open Rotors (CRORs) are an engine technology that could present step changes of fuel efficiency for future aircraft generations. The literature review has shown that the leading-edge noise produced by a translating aerofoil is a well understood problem. Analytical models, experimental measurements, and numerical simulations have been undertaken to understand this mechanism in detail. This understanding has subsequently been applied to develop analytical models for uninstalled open rotors ingesting turbulence. However, there are not as many analytical models for installed open rotor noise. Analytical models that have been implemented to study installed open rotor noise have focused on studying broadband pylon-wake interaction noise and tonal scattering by fuselage centre bodies. This thesis aims to develop a fast to run analytical model that predicts the noise radiated by a rotor ingesting a turbulent boundary layer.

This thesis has extended the simplified frequency-domain rotor noise model of Amiet [18] to predict this noise source. The simplified frequency-domain rotor noise model of Amiet [18] extends Amiet's [21] translating aerofoil noise model to account for rotation. This is done by treating the rotation of a blade as a series of small translations. Thus the noise radiated by a translating aerofoil is azimuthally averaged and frequency corrected to determine the noise at an observer location. This modelling approach neglects acceleration effects of the rotor blade. This is a valid simplifying assumption as long as the frequency of the impinging turbulence is significantly larger than the frequency of the rotor. This rotor noise model has been re-derived in Chapter 3. Initial predictions using Amiet's [18] simplified rotor noise model with blade-to-blade correlation modelled showed several discrepancies when compared with experimental measurements. Namely, there was a severe under-prediction in the amplitude of the spectrum and the peak at the 2^{nd} Blade Passing Frequency (BPF) was missing. The discrepancy in amplitude was the result of neglecting wall-effects. The absence of the 2^{nd} correlation peak was because the

turbulence model used was the isotropic von Kármán spectrum. However, boundary layer turbulence is known to be highly anisotropic consisting of elongated eddies in the axial direction. The remainder of the thesis focused on addressing these issues. The effect of the hard-wall was added to the model using the Method of Images (MOI). The effects of anisotropy were added using the axisymmetric homogeneous anisotropic velocity spectrum of Kerschen and Gliebe [24].

The MOI was first added to Amiet's [21] 2D translating aerofoil noise model in Chapter 4. This was done to study how accurate the MOI is and to assess what impact the assumptions that are used in implementing the MOI have when compared to a physically representative solution. This was done by comparing the analytical predictions against results from 2 Computational AeroAcoustic (CAA) simulations. One set of CAA simulations used the MOI to model the hard-wall. This was done by adding pressure data collected on two surfaces, one that represents the location of the real observer and one that represents the location of the image observer. The other set of CAA simulations used a physically representative hard-wall boundary condition to model the hard-wall. The main conclusions that are drawn from this chapter are,

- It is shown that the MOI adds three additional terms to Amiet's [18] original solution. There are two interference terms and one amplitude term.
- Using the analytical solution it is shown that the solution for an aerofoil ingesting turbulence in proximity to a hard-wall reduces to that of a vertical dipole near a hard-wall in the low Mach number, low frequency limit.
- When the analytical solution is compared to the CAA simulation using the MOI a good match is observed at most frequencies and most observer angles.
- When the analytical solution and the CAA simulations using the MOI are compared to the CAA simulation using the hard-wall boundary condition a good match is observed at most frequencies at some observer angles. However, discrepancies are observed in the shadow-zone of the aerofoil.
- These discrepancies indicate that the MOI is not capturing shadow-zone effects. However, as the shadow-zones extent decreases as the aerofoil is moved away from the wall, the MOI can still give a good indication of the noise produced by aerofoil ingesting turbulence in proximity to a wall at most observer angles and frequencies.

The MOI that was implemented in Chapter 4 is then extended to use in Amiet's [18] simplified rotor noise model. To include the effects of blade-to-blade correlation in the cross-spectrum of the acoustic pressure, the time of propagation for an acoustic wave to travel from the real and image observer had to be taken into account. The main conclusions that are drawn from this chapter are,

- In a similar manner as was done for the translating aerofoil case, it is shown that in the low Mach number low frequency limit the analytical solution reduces to that of a point dipole. Additionally, by changing the azimuthal angle of the blade and the blade stagger angle, the axis of the dipole to the wall can be changed arbitrarily. Using this simplified analytical solution it is shown that the blade stagger angle can have a significant impact on the radiated noise.
- When predictions using Amiet's [18] simplified rotor noise model are compared to experimental measurements, it is observed that the hard-wall increases the amplitude of the spectrum. However, the peak at the 2^{nd} BPF is still absent.
- When predictions are made using the model without blade-to-blade correlation, it is observed that there is a peak in the noise directivity that occurs due to the stagger angle of the blade.
- When predictions are made using the model with blade-to-blade correlation modelled it is observed that the peak in noise directivity is still present. However, the noise directivity is also affected by the interference terms.

Next, the effects of anisotropy are added in Chapter 6. This is done by replacing the isotropic von Kármán spectrum with the axisymmetric homogeneous anisotropic turbulence model of Kerschen and Gliebe [24]. First, the anisotropic turbulence model is used to make predictions for the simplified case of a 2D translating aerofoil ingesting anisotropic turbulence. Next, the anisotropic turbulence model of Kerschen and Gliebe [20] is compared to boundary layer turbulence. Finally, the turbulence model is coupled to Amiet's [18] simplified rotor noise model. Using this model the effects of anisotropy on the radiated noise are investigated. The main conclusions that are drawn from this chapter are,

- For the case of a 2D translating aerofoil it is observed that the changing the axial and transverse length scale redistributes the energy in the spectrum. It is observed that increasing the transverse length scale significantly increases the radiated noise. This is because a majority of leading-edge noise results from the transverse spectrum and increasing the transverse integral length scale add distributes more energy to the transverse spectrum.
- When the Kerschen and Gliebe [20] turbulence model is used to boundary layer turbulence several discrepancies are found. It is observed that the transverse 1D energy spectra do not match the experimental measurements. Additionally, the transverse integral length scales determined from the analytical spectra differ significantly from the transverse integral length scales computed from experimental measurements. This is most likely because boundary layer turbulence is not strictly

axisymmetric and it is not homogeneous in the wall-normal direction. Due to these reasons, the transverse integral length scale is chosen empirically.

- Using the extended rotor noise model with anisotropy modelled the effect of varying the axial and transverse length scale is examined. It is observed that increasing the axial or the transverse length scale increases she power radiated by the aerofoil. It is also observed the bandwidth of peaks at the BPF scale with the axial length scale and the eddy speed.

- When changing the stagger angle, rotational speed of the rotor, or the eddy speed the main parameter that effects the radiated noise is the speed at which the eddy moves through the rotor disk.

Finally, the extended rotor noise model is compared to experimental measurements and predictions made using the time-domain rotor noise model of Glegg *et al.* [25] in Chapter 7. the time-domain model of Glegg *et al.* is accurate as it does not model boundary layer turbulence. The required velocity statistics are instead determined from a 4D time and space varying velocity correlation tensor obtained from experimental measurements. The main conclusions that are drawn from this chapter are,

- The extended frequency domain method produces representative predictions when compared to experimental measurements. There is a good match between the predictions and the measurements obtained from the microphone located in the anechoic chamber. There is a fair match with a slight under-prediction in sound levels when the predictions are compared to measurements taken at eh microphone in the wind-tunnel. There is a severe under-prediction at the 90° observer angle. Additionally, the predictions obtained using the extended frequency-domain method show an additional peak at the higher BPFs that are absent from the experimental measurements and there is a sharp drop off at high frequencies. The additional peak at the BPF could be due to the empirical choice of transverse length scale and the high-frequency drop off could be due to the blade response function used or because the experiment is measuring additional noise sources that are not modelled.

- The extended frequency-domain method shows a good match when compared to the predictions from the time-domain method at most frequencies and observer angles. The major difference between the two models is the manner in which the turbulence statistics are determined. The extended frequency-domain method models the statistics while the time-domain method determines them from experimental measurements. The good match between the two models, therefore, indicates that the turbulence model is accurately capturing boundary layer turbulence. this is however dependant on choosing a correct transverse length scale, which can be difficult.

- As the transverse length scale is chosen empirically a sensitivity study is performed on this parameter. While the transverse length scale can have a significant impact on the radiated noise, there is a relatively small 90% confidence interval.

8.1 Future work

This thesis has developed an analytical model for a rotor ingesting boundary layer turbulence. The following extensions could be made to make this model more general,

- The rotor noise model assumes that the observer lies in the $y-z$ plane and that the rotor blades have no lean or sweep. While this does not detract from the generality of the model these features can be added to make the model applicable to a wider variety of cases.
- This thesis has assumed the hard-wall to be an infinite flat-plate. This can be changed to account for curved surfaces by using an appropriate tailored Green's function.
- It would be interesting to experimentally verify that the MOI does not capture shadow-zone effects.
- It is apparent that the anisotropic turbulence model of Kerschen and Gliebe has some deficiencies when compared to boundary layer turbulence. This can be improved by determining a new model spectra for boundary layer turbulence.
- A larger experimental dataset is required to test the rotor noise model at various different conditions.

Appendix A

Derivation of the emission distance and the Doppler factor used in the rotor noise model

In this Appendix the emission distance and Doppler factor that are used in Chapter 3 are derived.

A.1 Derivation of the emission distance

The retarded distance to the observer is the distance between the source at the present time and the observer. The emission distance can be calculated using Eqns. (3.1) and (3.4) as,

$$\begin{aligned} r_e^2 = |\mathbf{SO}| &= (r_0 \cos\theta - r_e M_x)^2 + r_0^2 \sin^2\theta, \\ r_e &= \frac{-r_0 M_x \cos\theta \pm \sqrt{r_0^2 M_x^2 (\cos^2\theta - 1) + r_0^2}}{(1 - M_x^2)}, \\ r_e &= r_0 \frac{-M_x \cos\theta + \sqrt{1 - M_x^2 \sin^2\theta}}{(1 - M_x^2)}. \end{aligned}$$

A.2 Derivation of the Doppler factor

The Doppler factor (DF) is required to compute the noise radiated by a rotating aerofoil. Using Eqns. (3.1), (3.4), (3.2), and (3.3),

$$\begin{aligned}
\widehat{\mathbf{SO}} =& \frac{1}{r_e}\left(x - r_e M_x, 0, z\right), \\
DF = \frac{\omega}{\omega_\phi} =& 1 + \frac{M_\phi^O . \widehat{\mathbf{SO}}}{1 - M_\phi^F . \widehat{\mathbf{SO}}}, \\
DF =& 1 - \frac{M_\phi z \sin\phi / r_e}{1 - \left(M_x^2 + 1/r_e\left[-xM_x - zM_\phi \sin\phi\right]\right)}, \\
DF =& \frac{1 - M_x^2 + xM_x/r_e}{1 - M_x^2 + xM_x/r_e + zM_\phi \sin\phi/r_e}, \\
1/DF =& \frac{1 - M_x^2 + xM_x/r_e + zM_\phi \sin\phi/r_e}{1 - M_x^2 + xM_x/r_e}, \\
1/DF =& 1 + M_\phi \frac{\sin\theta \sin\phi}{\sqrt{1 - M_x^2 \sin^2\theta}}.
\end{aligned}$$

It is important to note that the Doppler factor derived above is $1/DF$.

Appendix B

Description of the benchmark case

The test case that was used to compare predictions of the extended-frequency domain method was the Fundamental Case 3 (FC3) of 2015 AIAA Fan Broadband Noise (FBN) workshop [138]. The setup of the test case is shown in Fig. B.1. The rotor has a tip diameter of 457.2 mm and a hub diameter of 127 mm. The rotor has 10 blades with a constant chord of 57.2 mm and the stagger angle of the blades varies from 55.6° at the hub to 21.2° at the tip.

B.1 Extraction of turbulence data from the test case to input into the rotor noise model

The predictions of the rotor noise model are computed for the Fundamental Case 3 (FC3) of the 2015 AIAA Fan Broadband Noise (FBN) workshop [138]. The predictions obtained using the rotor noise model are compared with experimental measurements from Glegg *et al.* [25]. The experimental results are obtained from a test-campaign in the stability wind tunnel at the Virginia Polytechnic Institute [19].

The extended frequency-domain rotor noise model requires as input, the geometry of the rotor, the rotor advance ratio and information that characterises the turbulence. The information required to characterise the turbulence are the turbulence intensities and integral length scales in the axial and transverse directions.

The turbulence data provided with the FC3 dataset, is provided as a four-dimensional space and time varying velocity correlation tensor: $R_{ij}\left(\Delta\tau, \Delta y, z, z'\right)$. Here (i, j) are the

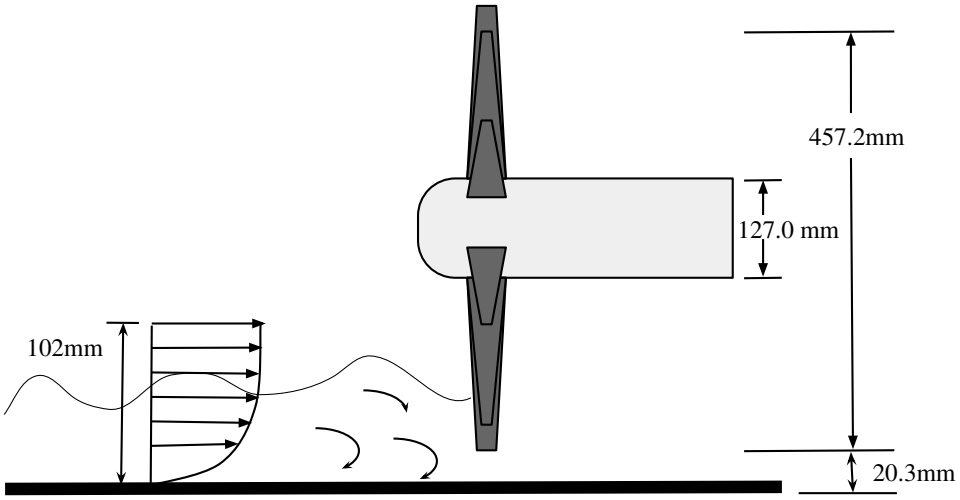

Figure B.1: Configuration of fundamental case three.

velocity component being considered, $\Delta\tau$ is the time lag, Δy is the spanwise separation at which the velocity correlation is considered and z, z' are the wall normal coordinates at which the velocity correlation is considered. It should be noted that this dataset contains space and time varying velocity correlations for an undistorted boundary layer (without a rotor)

The turbulence intensities in the longitudinal and transverse directions at each wall normal location are computed by obtaining the velocity correlation at zero time and zero spanwise separation,

$$\left(\frac{u_i'(z)}{U}\right)^2 = R_{ii}(0,0,z,z). \tag{B.1}$$

To obtain the integral length scales in the longitudinal and transverse directions, normalised velocity correlation functions were computed from the experimental data. The integral length scales were determined by integrating these velocity correlations. The results obtained were validated by comparing the experimentally determined velocity correlations with analytical velocity correlations. Two longitudinal velocity correlations f_x and f_y can be defined for the Liepmann spectrum as [35; 36],

$$\begin{aligned} f_x(r) =& e^{-|r|/L_{11}^{(1)}}, \\ f_y(r) =& e^{-|r|/L_{22}^{(2)}}, \end{aligned} \tag{B.2}$$

where r is the separation between the two points at which the correlation is considered, $L_{11}^{(1)}$ is the integral length scale computed from the correlation function of the u velocity separated in the x direction, and $L_{22}^{(2)}$ is the integral length scale computed from the correlation of the v velocity separated in the y direction. As these velocity correlations take the integral length scale computed from experimental data as an input, comparing these velocity correlations with experimental data will indicate the accuracy of the determined length scales. A similar method cannot be used to extract the integral length scales in the wall-normal direction as the turbulence is not homogeneous in this direction.

The computed normalised velocity correlations in the streamwise (x) and the cross-stream (y) directions are shown in Fig. B.2(c) and Fig. B.2(d) respectively. It can be seen that the velocity correlations extracted from the experimental data compare well against those computed using Eqn. B.2.

The computed integral length scales are shown in Fig. B.2(a) as a function of the radial location from the hub centre. The ratio of the integral length scales near the rotor hub is approximately 6 and approximately 2 near the rotor tip. Fig. B.2(b) shows the variation of the turbulence intensity as a function of radial location from the rotor hub centre. As expected, the streamwise turbulence intensities are considerably larger than in the other directions. Additionally, the turbulence intensities decrease monotonically away from the wall. To facilitate the use of this data in the rotor noise model, least square fits were computed for the integral length scales as,

$$\begin{aligned} L_{11}^{(1)} &= -0.4681z + 0.0947, \\ L_{22}^{(2)} &= \quad 0.0958z + 0.0116, \end{aligned} \tag{B.3}$$

and the turbulence intensities as,

$$\begin{aligned} u^2 &= 417.2z^2 - 98.83z + 6.070, \\ w^2 &= 131.7z^2 - 40.96z + 3.115, \\ v^2 &= 16.23z^2 - 17.35z + 1.944, \end{aligned} \tag{B.4}$$

where z is the distance from the wall in meters. In the rotor noise model presented, $L_{11}^{(1)} = l_a$, $L_{22}^{(2)} = l_t$, $u = u_a$, and $\sqrt{(v^2 + w^2)/2} = u_t$. Additionally, all the turbulence data is scaled by the free-stream velocity.

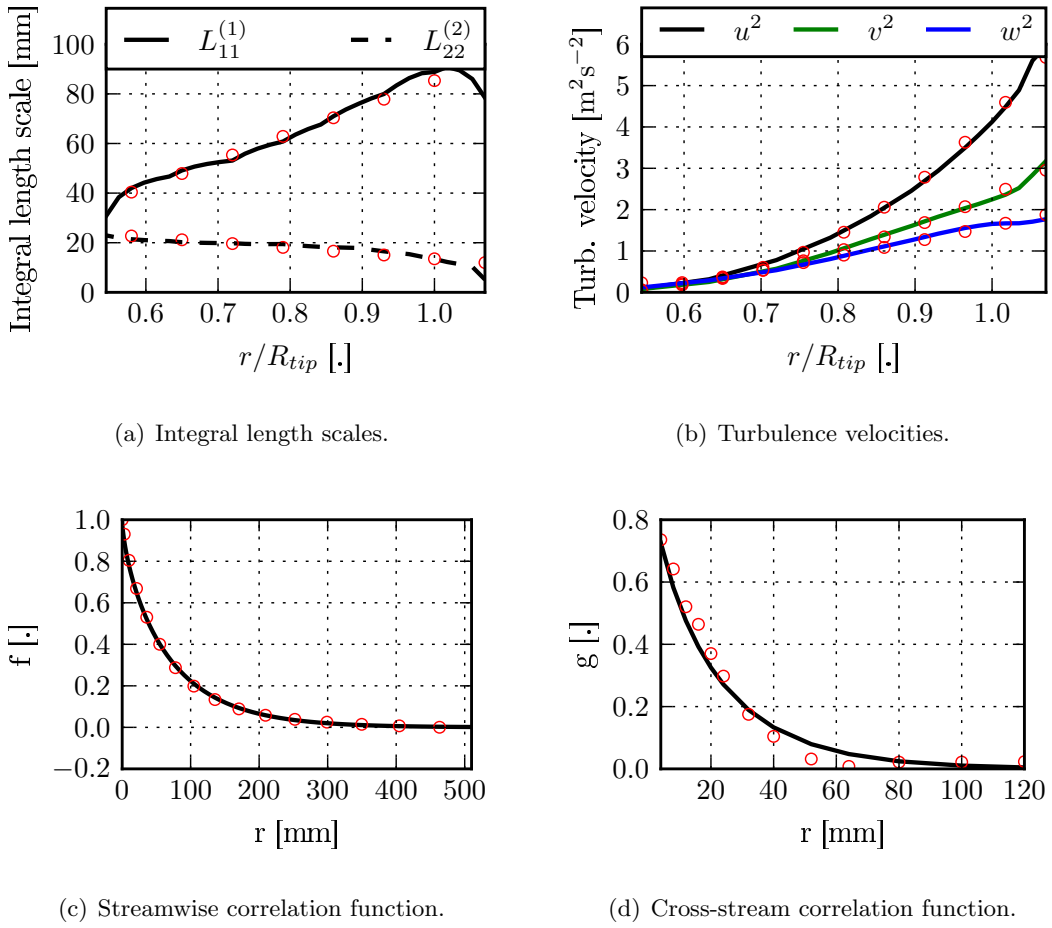

(a) Integral length scales.

(b) Turbulence velocities.

(c) Streamwise correlation function.

(d) Cross-stream correlation function.

Figure B.2: The integral length scales, RMS velocities, and normalised correlation functions. The points show the least square fits for each of the variables computed using Eqns. (B.3) and (B.4). The normalised correlation functions are computed at $r/R_{tip} = 0.825$.

Appendix C

The power factor of a two-dimensional vertical dipole

In this appendix, the power factor (the ratio of radiated power with and without a hard-wall) for a 2D dipole is considered. The derivation that follows is from Pierce [17]. However, it has been modified to determine the power factor in 2D and the coordinate system has been changed to be consistent with the coordinate system used in this paper. The pressure in the far field due to a 2D point source can be written as [152],

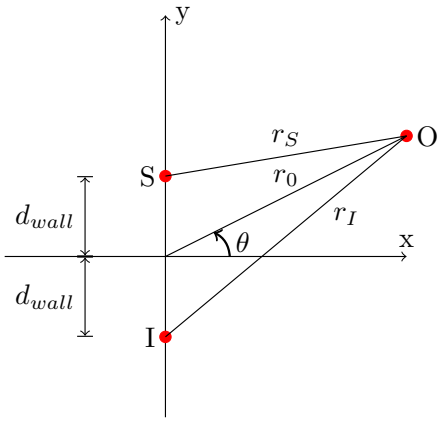

Figure C.1: A schematic of a point source (S), its image (I), and an observer (O).

$$p(r_0, \theta, \omega) = h(\theta) \frac{e^{-ik_0 r_0}}{\sqrt{r_0}},$$

where h is a function that depends on the point source being considered. Then, by superposition the pressure field at the observer O can be written as,

$$p(r_0, \theta, \omega) = \left[h(\theta) \frac{e^{-ik_0 r_S}}{\sqrt{r_S}} + h(2\pi - \theta) \frac{e^{-ik_0 r_I}}{\sqrt{r_I}} \right], \tag{C.1}$$

From Fig. C.1 the distances to the observer, from the real and image source, are given by,

$$\begin{aligned} r_S &\simeq r_0 - d_{wall}\sin\theta, \\ r_I &\simeq r_0 + d_{wall}\sin\theta. \end{aligned} \tag{C.2}$$

Using Eqn. (C.2) in Eqn. (C.1) gives the pressure at the observer as,

$$p(r_0,\theta,\omega) \simeq \frac{e^{-\mathrm{i}k_0 r_0}}{\sqrt{r_0}}\left(e^{-\mathrm{i}k_0 d_{wall}\sin\theta}h(\theta) + e^{\mathrm{i}k_0 d_{wall}\sin\theta}h(2\pi-\theta)\right). \tag{C.3}$$

The power radiated can then be computed as,

$$\mathcal{P}(r_0,\theta,\omega) = \frac{r_0}{2\rho_0 c_0}\int_0^{\pi} |p(r_0,\theta,\omega)|^2 \mathrm{d}\theta. \tag{C.4}$$

The power radiated by a point source near a hard-wall is then found by using Eqn. (C.3) in Eqn. (C.4),

$$\mathcal{P} = \mathcal{P}_0 + \mathrm{Re}\left\{\frac{r_0}{2\rho_0 c_0}\int_0^{2\pi} h^*(\theta)h(2\pi-\theta)e^{2\mathrm{i}k_0 d_{wall}\sin\theta}\mathrm{d}\theta\right\}, \tag{C.5}$$

where Re is the real operator and,

$$\mathcal{P}_0 = \frac{r_0}{2\rho_0 c_0}\int_0^{2\pi} |h(\theta)|^2 \mathrm{d}\theta.$$

For a 2D dipole point source,

$$h(\theta) = -\mathrm{i}k_0\tilde{\mathrm{D}}\sin\theta,$$

where $\tilde{\mathrm{D}}$ is the complex dipole moment. Thus, the power factor of a vertical dipole near a hard-wall is given by,

$$\frac{\mathcal{P}}{\mathcal{P}_0} = 1 - \frac{1}{\pi}\int_0^{2\pi}\cos\left(2k_0 d_{wall}\sin\theta\right)\sin^2\theta\mathrm{d}\theta = 1 - 2\left[\frac{J_1\left(2k_0 d_{wall}\right)}{2k_0 d_{wall}} - J_2\left(2k_0 d_{wall}\right)\right]. \tag{C.6}$$

This is identical to the power factor of a flat-plate ingesting turbulence near a hard-wall in the low Mach number, low frequency limit as given in Eqn. (4.31).

Appendix D

Glegg's time-domain formulation for the noise radiated by a rotor ingesting a turbulent boundary layer

In this Appendix a derivation of Glegg's [25] time-domain formulation for the noise radiated by a rotor ingesting a turbulent boundary layer is re-derived. Glegg's [25] time-domain formulation uses Amiet's [77] time-domain compressible response function to compute the loading of a blade. This is used in the Ffowcs Williams and Hawkings (FWH) equation to determine the noise radiated to the far-field. The coordinate system used in this derivation is shown in Fig. D.1.

D.1 Formulation of the PSD of the acoustic pressure

The observer coordinates are denoted as $(\mathbf{x}, t)$ and the source coordinates as $(\mathbf{y}, \tau)$. The FWH equation is then used to compute the loading noise due to a surface loading per unit area of $f_i(\mathbf{y}, \tau)$ as,

$$p(\mathbf{x}, t) = -\frac{\partial}{\partial x_i} \sum_{n=1}^{B} \int_{\Sigma_n} \left[\frac{f_i(\mathbf{y}, \tau)}{4\pi \mathbf{r} |1 - M_r|} \right]_{\tau=\tau^*} \mathrm{d}\Sigma_n(\mathbf{y}), \tag{D.1}$$

where Σ_n represents the surface of blade n, r is the distance from source to observer, $\mathbf{x} - \mathbf{y}$ and $\tau^* = t - r(\tau)/c_o$ is the retarded time.

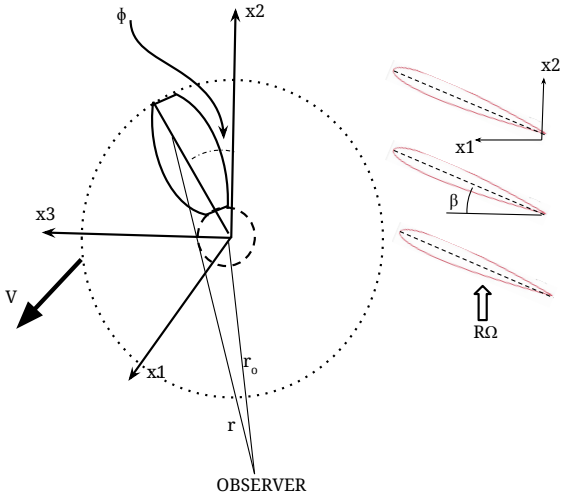

Figure D.1: Coordinate system for the rotor.

The power spectrum of the acoustic pressure is defined as,

$$S(\mathbf{x},\omega) = \frac{1}{2T}\int_{-T}^{T}\frac{1}{2\pi}\int_{-T}^{T}\overline{[p(\mathbf{x},t),p(\mathbf{x},t')]}e^{\mathrm{i}\omega(t-t')}\mathrm{d}t\mathrm{d}t', \tag{D.2}$$

where an average over multiple revolutions has been performed. This is done due to the fact that the rotor noise is not stationary. The assumption is now made that the wavelength is much larger than the chord, $c >> \lambda$. Using this assumption the surface loading per unit area can be replaced as a force per unit span, $f_i(\mathbf{y},\tau) = \mathbf{n}(R,\tau)F(R,\tau)$ that is only dependant on the radial location. Here $\mathbf{n}$ is the normal to the blade surface and R represents the radial location of the force and is given by $R = \sqrt{y_2^2 + y_3^2}$. This indicates that the surface of the blade can be divided into a number of strips and the loading at each individual strip can be computed. Equation (D.1) then becomes,

$$p(\mathbf{x},t) = -\sum_{n=1}^{B}\int_{R_{min}}^{R_{max}}\left[\frac{\partial}{\partial x_i}\frac{\mathbf{n}_i^{(n)}(R,\tau)F^{(n)}(R,\tau)}{4\pi\mathbf{r}^{(n)}(\tau)|1-M_r|}\right]_{\tau=\tau^*}\mathrm{d}R(\mathbf{y}). \tag{D.3}$$

The expected value of the acoustic pressure at two slightly different times is computed as,

$$\overline{[p(\mathbf{x},t),p(\mathbf{x},t')]} = \sum_{n=1}^{B}\sum_{m=1}^{B}\int_{R_{min}}^{R_{max}}\int_{R_{min}}^{R_{max}} \left[\left\{\frac{\partial}{\partial x_i}\frac{\mathbf{n}_i^{(n)}(R,\tau)}{4\pi\mathbf{r}^{(n)}|1-M_r|}\right\}\left\{\frac{\partial}{\partial x_j}\frac{\mathbf{n}_j^{(m)}(R',\tau)}{4\pi\mathbf{r}^{(m)}|1-M_r|}\right\}\overline{\left[F^{(n)}(R,\tau)F^{(m)}(R',\tau')\right]}\right]_{\substack{\tau=\tau^*\\ \tau'=(\tau^*)'}} \mathrm{d}R\mathrm{d}R'. \tag{D.4}$$

To compute the acoustic power spectrum, we change the integral in Eqn. (D.2) so that it is computed in source time instead of observer time. This can be accomplished by using the substitution $\mathrm{d}t = |1-M_r|\mathrm{d}\tau$,

$$S_{pp}(\mathbf{x},\omega) = \frac{1}{4\pi T}\sum_{n=1}^{B}\sum_{m=1}^{B}\int_{R_{min}}^{R_{max}}\int_{R_{min}}^{R_{max}}\int_{-T}^{T}\int_{-T}^{T} \left\{\frac{\partial}{\partial x_i}\frac{\mathbf{n}_i^{(n)}(R,\tau)e^{i\omega r^{(n)}(\tau)/c_o}}{4\pi\mathbf{r}^{(n)}(\tau)}\right\}\left\{\frac{\partial}{\partial x_j}\frac{\mathbf{n}_j^{(m)}(R',\tau)e^{-i\omega r^{(m)}(\tau)/c_o}}{4\pi\mathbf{r}^{(m)}(\tau')}\right\} R_{FF}(R,R',\tau,\tau')\mathrm{d}\tau\mathrm{d}\tau'\mathrm{d}R\mathrm{d}R', \tag{D.5}$$

where $R_{FF}(R,R',\tau,\tau') = \overline{\left[F^{(n)}(R,\tau)F^{(m)}(R',\tau')\right]}$. The normal to blade chord is given by,

$$\mathbf{n}_i^{(n)} = (\cos\beta, \sin\beta\sin(\Omega\tau+\phi_n), -\sin\beta\cos(\Omega\tau+\phi_n)),$$

the location of the blade leading edge is,

$$\mathbf{y}^{(n)}(R,\tau) = (V\tau, R\cos(\Omega\tau+\phi_n), R\sin(\Omega\tau+\phi_n)),$$

and the location of the observer is,

$$\mathbf{x} = (r_o\cos\theta_o + Vt, r_o\sin\theta_o\cos\phi_o, r_o\sin\theta_o\sin\phi_o).$$

D.2 Greens functions terms

The terms that are within the curly braces in Eqn. (D.4) are referred to as the Green's functions terms. In this section the analytical derivation of these terms is presented. To do this the fact that $\partial\mathbf{r}/\partial x_i = \hat{\mathbf{r}}$ is used.

The derivative can then be evaluated as,

$$\frac{\partial}{\partial x_i}\frac{\mathbf{n}_i(R,\tau)e^{\mathrm{i}\omega r(\tau)/c_o}}{4\pi\mathbf{r}(\tau)} = \frac{e^{\mathrm{i}\omega r(\tau)/c_o}}{4\pi}\left[\frac{1}{\mathbf{r}}\frac{\partial \mathbf{n}_i}{\partial x_i} + \frac{i\omega}{c_o}\frac{\mathbf{n}_i}{\mathbf{r}}\frac{\partial \mathbf{r}_i}{\partial x_i} - \frac{\mathbf{n}_i}{\mathbf{r}^2}\frac{\partial \mathbf{r}_i}{\partial x_i}\right], \tag{D.6}$$

$$= \frac{e^{\mathrm{i}\omega r(\tau)/c_o}}{4\pi\mathbf{r}}\left[\frac{\partial \mathbf{n}_i}{\partial \tau}\frac{\partial \tau}{\partial x_i} + \frac{i\omega\mathbf{n}_i}{c_o}\frac{\partial \mathbf{r}_i}{\partial x_i} - \frac{\mathbf{n}_i}{\mathbf{r}}\frac{\partial \mathbf{r}_i}{\partial x_i}\right], \tag{D.7}$$

$$= \frac{e^{\mathrm{i}\omega r(\tau)/c_o}}{4\pi\mathbf{r}}\left[-\frac{1}{c_o}\frac{\partial \mathbf{n}_i}{\partial \tau}\cdot\hat{\mathbf{r}}_i + \left(\frac{i\omega}{c_o} - \frac{1}{\mathbf{r}}\right)\mathbf{n}_i\cdot\hat{\mathbf{r}}_i\right]. \tag{D.8}$$

Here it is seen that the second term in Eqn. (D.8) represents a dipole with direction $\mathbf{n}.\hat{\mathbf{r}}$. There is also an additional term which is a function of the source time derivative of the normal to the blade surface. This indicates the directivity pattern that should be observed should closely resemble that of a dipole as expected.

D.3 Computation of the unsteady loading

Having determined the Green's function terms for the acoustic propagation, the unsteady loading on the blade needs to be computed. The two dimensional loading at each strip is given by,

$$F^{(n)}(\omega_o, R) = \{\pi\rho c U(R) S(\sigma)\}\, w^{(n)}(R,\omega_o), \tag{D.9}$$

where c the chord of the blade, ρ is the density, U is the speed of the blade, S is Sears function referenced at the leading edge , $w(R,\omega)$ is the Fourier transform of the gust velocity and σ is the non-dimensional frequency defined as $\sigma = \omega_o c/2U(R)$. The Sears function is defined as,

$$S(\sigma) = \frac{2e^{\mathrm{i}\sigma}}{\pi\sigma(H_o^{(1)}(\sigma) + \mathrm{i}H_1^{(1)}(\sigma))},$$

where $H_o^{(1)}$ and $H_o^{(2)}$ are Hankel functions of the first kind.

The unsteady loading on the blade is given by the convolution integral,

$$F^{(n)}(R,\tau) = \int_{-\infty}^{\tau} s(\tau-\tau_o) w^{(n)}(R,\tau_o)\mathrm{d}\tau_o, \tag{D.10}$$

where s is given by,

$$s(R,\tau) = \frac{1}{2\pi}\int_{-\infty}^{\infty}\{\pi\rho c U(R) S(\sigma)\}\, e^{-\mathrm{i}\omega\tau}\mathrm{d}\omega. \tag{D.11}$$

An approximate form of the Sears function is given by,

$$s(\sigma) \sim \sqrt{\frac{\mathrm{i}}{1+2\pi\sigma}}.$$

Using this and non-dimensionalisng the time by the half chord as $\bar{\tau} = 2U\tau/c$ the asymptotic solution for Eqn. (D.11) is obtained as,

$$s(R,\tau) = 2\rho U^2(R)\mathrm{Re}\left\{\int_0^\infty \sqrt{\frac{\mathrm{i}}{1+2\pi\sigma}}e^{-\mathrm{i}\sigma\tau}\mathrm{d}\sigma\right\} \approx \begin{cases} \frac{\sqrt{2}\rho U^2(R)}{\sqrt{\bar{\tau}}} & \bar{\tau} << 1 \\ \frac{\sqrt{2}\rho U^2(R)}{\bar{\tau}} & \bar{\tau} >> 1 \end{cases}, \tag{D.12}$$

based on these approximate solutions, the approximate form of the Sears solution can be defined as,

$$s(R,\tau) \approx \frac{\sqrt{2}\rho U^2(R)}{\sqrt{\bar{\tau}+\bar{\tau}^2}}.$$

Sears' solution is not the only solution to the problem of a gust impinging on an aerofoil. Other time domain response functions exist, such as that of Amiet and Kussener.

The response of a flat plate due to a step gust was given by Kuessener as,

$$s(R,\tau) = \rho U^2 \frac{\partial}{\partial\bar{\tau}}\left(\frac{2\pi(\bar{\tau}^2+\bar{\tau})}{\bar{\tau}^2+2.82\bar{\tau}+0.8}\right).$$

Both Sears and Kussener's functions are valid for incompressible flows. A compressible solution was defined by Amiet for a delta gust of the for $(w_o c/2U)\delta(\gamma/U-t)$. Here γ is the parallel distance along the chord. A response function can then be defined as,

$$s(R,\tau) = \rho U^2 A(2U\tau/c),$$

where $A(2U\tau/c)$ is defined as:

$$A(\bar{\tau}) = \begin{cases} \frac{2}{\sqrt{M}} & \bar{\tau} < \tau_a \\ \frac{4\sin^{-1}(\sqrt{\tau_a/\bar{\tau}})}{\pi\sqrt{M}} & \bar{\tau} > \tau_a \end{cases}, \tag{D.13}$$

where $\tau_a = 2M/(1+M)$ and $M = U/c_o$. Each of the above defined functions is shown in Fig. D.2.

It is clear from Fig. D.2 that Amiet's function is vastly different from Sears' or Kussener's function. As Amiet's function is a compressible one it allows for the acoustic wave to travel at the speed of sound unlike the incompressible ones in which the acoustic waves travel infinitely fast.

As there are a choice of different response functions, it must be determined which response function is best suited for the present problem. Consider Amiet's solution as defined in Eqn. (D.12). If a point x is defined on an aerofoil of chord c, referenced from the leading edge, it's distance from the trailing edge will be $r = x - c$. Additionally the time taken for an acoustic pulse to reach the trailing edge of the aerofoil will be $c/c_o\,(1+M)$. Then

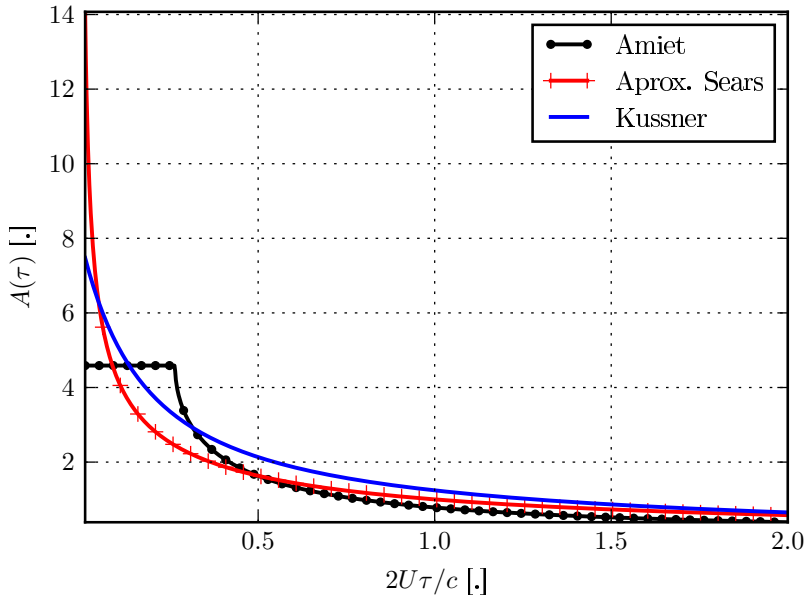

Figure D.2: The approximate Sears, Kussener, and Amiet response functions at $M = 0.19$.

the time since the acoustic wave has reached the trailing edge is $t_1 = t - c/c_o\,(1 + M)$. This implies that at $t_1 = r/c_o\,(1 + M)$ the acoustic wave has reached the trailing edge and returned to the point x. Amiets theory is exact as long as this time is not exceeded. If this time is exceeded second order correction terms must be added [77]. Thus Amiets solution is suitable when lag times are not very large. For a rotor that is subsonic this is generally the case [25]. Additionally as seen from Fig. D.2 it is seen that Amiet's response function is well defined for small lag times and thus can be numerically integrated easily.

As both Sears' and Kussener's functions are incompressible solutions they allow for the acoustic pulse to travel with an infinite velocity. They thus allow for reflections and scattering at the trailing edge. However, as they are not well defined for small lag times they require a larger number of points than Amiet's solution does to be numerically integrated.

Due to the reasons stated above we will use Amiet's function for the calculations that are presented.

D.4 The blade loading correlation function

The value of $R_{FF}(R, R', \tau, \tau')$ required in Eqn. (D.5) can now be determined. Using Eqn. (D.10),

$$R_{FF}(R, R', \tau, \tau') = \int_{-\infty}^{\tau} \int_{-\infty}^{\tau} s(R, \tau - \tau_o) s(R', \tau' - \tau_o') R_{ww}^{(n,m)}(R, R', \tau_o, \tau_o') \mathrm{d}\tau_o \mathrm{d}\tau_o', \quad \text{(D.14)}$$

where s is the chosen impulse function and R_{ww} is the velocity correlation function. The up-wash that the blade sees, w, is the perturbation, v_i, in the direction of the normal to the blade, i.e.,

$$w^{(n)}(R_o, \tau_o) = \mathbf{n}_i^{(n)} v_i \left(\mathbf{y}^{(n)}(\tau_o, R_o), \tau_o \right). \quad \text{(D.15)}$$

The velocity correlation function in Eqn. (D.14) can then be defined as,

$$R_{ww}^{(n,m)}(R, R', \tau_o, \tau_o') = \mathbf{n}_i^{(n)}(R, \tau_o) \mathbf{n}_j^{(m)}(R', \tau_o') R_{ij} \left(\mathbf{y}^{(n)}, \mathbf{y}^{(m)}, \tau_o - \tau_o' \right), \quad \text{(D.16)}$$

where R_{ij} is the velocity correlation tensor that is obtained from experiments [25].

A simplification can be made to the above results by recognizing that when the blades are in the turbulence, the correlation tensor between the first and the second blade will be the same as that between the ninth tenth blades. In other words only the difference of the blade numbers matter and not the blade numbers themselves.

The time arguments can thus be modified in the normal and source location vectors to,

$$n_i^{(n)}(R, \tau) = n_i^{(0)}(R, \tau + \phi_n), \quad y_i^{(n)}(R, \tau) = y_i^{(0)}(R, \tau + \phi_n). \quad \text{(D.17)}$$

The final velocity correlation term then becomes [25],

$$R_{ww}^{(n,m)}(R, R', \tau_o, \tau_o') = \mathbf{n}_i^0(R, \tau_m) \mathbf{n}_j^0(R', \tau_m' - s\Delta\tau) R_{ij} \left(\mathbf{y}^0(R, \tau_m), \mathbf{y}^0(R', \tau_m' - s\Delta\tau) \right), \quad \text{(D.18)}$$

where $\tau_m = \tau_o + m\Delta\tau$, $\Delta\tau = 2\pi/B\Omega$ and $s = m - n$.

This appendix has provided a detailed derivation of Glegg's [25] time-domain rotor noise model. As can be seen from the above derivation, the main difference between the time-domain solution and the extended frequency-domain solution is the manner in which the turbulence is modelled. Both the time-domain and frequency-domain methods use the same response function and thus the blade loading predicted by the models should be the same. Therefore, when the frequency-domain method is compared to the time-domain method the main differentiator will be the turbulence model used.

Bibliography

[1] "Annual Analyses of the EU Air Transport Market 2016," European Comission, Tech. Rep. 376608/ITD/Aviation/1/F, 2017.

[2] "Strategic Research Agenda, Volume 1," Advisory Council for Aeronautics Research in Europe, Tech. Rep., 2002. [Online]. Available: http://www.acare4europe.org/sites/acare4europe.org/files/document/volume1.pdf

[3] "Flightpath 2050 Europe's Vision for Aviation," European Commission, Tech. Rep., 2011. [Online]. Available: https://publications.europa.eu/en/publication-detail/-/publication/296a9bd7-fef9-4ae8-82c4-a21ff48be673

[4] W. Strack, G. Knip, A. Weisbrich, J. Godston, and E. Bradley, "Technology and Benefits of Aircraft Counter Rotation Propellers," NASA, Tech. Rep. 82983, 1982.

[5] "Aeroacoustics of Flight Vehicles: Theory and Practice. Volume 1: Noise Sources," NASA, Tech. Rep. 90-3052, 1991.

[6] F. Farassat, M. Dunn, A. Tinetti, and D. Nark, "Open Rotor Noise Prediction Methods at NASA Langley: A Technology Review," in *15th AIAA/CEAS Aeroacoustics Conference*, AIAA 2009-3133, Montreal, Canada, may 2009.

[7] D. E. V. Zante, "Progress in Open Rotor Research: A U.S. perspective," in *ASME Turbo Expo 2015: Turbine Technical Conference and Exposition*, GT2015-42203, Montreal, Canada, jun 2015.

[8] R. Hager and D. Vrabel, "Advanced Turboprop Project," NASA Lewis Research Center, Tech. Rep. SP-495, 1988.

[9] E. Hendricks and M. Tong, "Performance and Weight Estimates for an Advanced Open Rotor Engine," *48th Joint Propulsion Conference and Exhibit*, no. August, pp. 1–12, 2012.

[10] "Vought F4-U Corsair." [Online]. Available: http://www.warbirdinformationexchange.org/phpBB3/viewtopic.php?f=3{&}t=56991

[11] "R3Y1 Tradewind." [Online]. Available: http://aircraft.wikia.com/wiki/Convair{_}R3Y{_}Tradewind{%}0A

[12] "Tupolev 114." [Online]. Available: https://abpic.co.uk/pictures/model/TupolevTu-114

[13] "Northrop YB-25." [Online]. Available: https://www.cgtrader.com/3d-models/aircraft/military/northrop-b-25-flying-wing{%}0A

[14] V. Blandeau, P. F. Joseph, and G. Gabard, "Sound Power Radiation Due to an Isolated Airfoil in a Turbulent Stream," in *International Congress on Acoustics*, Paper 849, Sydney, Australia, 2010. [Online]. Available: https://www.acoustics.asn.au/conference{_}proceedings/ICA2010/cdrom-ICA2010/papers/p849.pdf

[15] V. P. Blandeau, P. F. Joseph, M. J. Kingan, and A. B. Parry, "Broadband noise predictions from uninstalled contra-rotating open rotors," *International Journal of Aeroacoustics*, vol. 12, no. 3, pp. 245–282, 2013. [Online]. Available: http://multi-science.metapress.com/index/HG0377V2658G7V8K.pdf

[16] M. J. Czech and R. H. Thomas, "Open Rotor Aeroacoustic Installation Effects for Conventional and Unconventional Airframes," in *9th AIAA/CEAS Aeroacoustics Conference*, AIAA 2013-2185, Berlin, Germany, 2013.

[17] A. D. Pierce, *Acoustics. An Introduction to its Physical Principles and Applications*. Acoustical Society of America, 1981.

[18] R. K. Amiet, "Noise Produced by Turbulent Flow Into a Rotor: Theory Manual for Noise Calculation," United Technologies Research Center, Tech. Rep. CR-181788, 1989.

[19] W. N. Alexander, W. J. Devenport, D. Wisda, M. A. Morton, and S. A. Glegg, "Sound Radiated from a Rotor and Its Relation to Rotating Frame Measurements of Ingested Turbulence," in *20th AIAA/CEAS Aeroacoustics Conference*, AIAA 2014-2746, Atlanta, Georgia, jun 2014. [Online]. Available: http://arc.aiaa.org/doi/abs/10.2514/6.2014-2746

[20] E. J. Kerschen and P. R. Gliebe, "Noise Caused by the Interaction of a Rotor with Anisotropic Turbulence," *AIAA Journal*, vol. 19, no. 6, pp. 717–723, 1981. [Online]. Available: http://arc.aiaa.org/doi/abs/10.2514/3.50995

[21] R. Amiet, "Acoustic Radiation From an Airfoil in a Turbulent Stream," *Journal of Sound and Vibration*, vol. 41, no. 4, pp. 407–420, 1975. [Online]. Available: http://www.sciencedirect.com/science/article/pii/S0022460X75801052

[22] R. Karve, D. Angland, and J. Gill, "An analytical model for predicting rotor broadband noise due to turbulent boundary layer ingestion ." in *Applied Aerodynamics Conference*, Bristol, jul 2016.

[23] R. Karve, J. R. Gill, F. Gea Aguilera, D. Angland, and T. Node-Langlois, "Including Wall Effects in Analytical Leading Edge Noise Predictions," in *23rd*

AIAA/CEAS Aeroacoustics Conference, AIAA 2017-3198, Denver, jun 2017. [Online]. Available: https://arc.aiaa.org/doi/10.2514/6.2017-3198

[24] E. J. Kerschen, "Constraints on the invariant functions of axisymmetric turbulence," *AIAA Journal*, vol. 21, no. 7, pp. 978–985, 1983.

[25] S. A. Glegg, W. Devenport, and N. Alexander, "Broadband rotor noise predictions using a time domain approach," *Journal of Sound and Vibration*, vol. 335, pp. 115–124, 2015. [Online]. Available: http://linkinghub.elsevier.com/retrieve/pii/S0022460X14007202

[26] A. Parry, M. Kingan, and B. Tester, "Relative importance of open rotor tone and broadband noise sources," in *17th AIAA/CEAS Aeroacoustics Conference*, AIAA 2011-2763, Portland, USA, jun 2011. [Online]. Available: http://arc.aiaa.org/doi/10.2514/6.2011-2763

[27] A. Carazo, M. Roger, and M. Omais, "Analytical Prediction of Wake-Interaction Noise in Counter-Rotation Open Rotors," in *17th AIAA/CEAS Aeroacoustics ConferencePortland*, AIAA 2011-2758, Portland, Oregon, jun 2011.

[28] V. P. Blandeau, "Aerodynamic broadband noise from contra-rotating open rotors," Ph.D. dissertation, University of Southampton, 2011. [Online]. Available: http://eprints.soton.ac.uk/179853/

[29] I. Marusic, B. J. McKeon, P. A. Monkewitz, H. M. Nagib, A. J. Smits, and K. R. Sreenivasan, "Wall-bounded turbulent flows at high Reynolds numbers: Recent advances and key issues," *Physics of Fluids*, vol. 22, no. 6, pp. 1–24, 2010.

[30] J. Osterlund, "Experimental Studies of Zero Pressure-Gradient Turbulent Boundary-Layer Flow," PhD Thesis, Royal Institute of Technology, 1999.

[31] R. J. Adrian, "Hairpin vortex organization in wall turbulencea," *Physics of Fluids*, vol. 19, no. 4, 2007.

[32] S. Robinson, "Coherent Motions In The Turbulent Boundary Layer," *Annual Review of Fluid Mechanics*, vol. 23, no. 1, pp. 601–639, 1991. [Online]. Available: http://fluid.annualreviews.org/cgi/doi/10.1146/annurev.fluid.23.1.601

[33] M. R. Head and P. Bandyopadhyay, "New Aspects of Turbulent Boundary Layer Structure," vol. 107, no. 1981, pp. 297–338, 1981.

[34] N. Hutchins, W. T. Hambleton, and I. Marusic, "Inclined cross-stream stereo particle image velocimetry measurements in turbulent boundary layers," *Journal of Fluid Mechanics*, vol. 541, no. 2005, pp. 21–54, 2005. [Online]. Available: http://dx.doi.org/10.1017/S0022112005005872{%}5Cnhttp://journals.cambridge.org/download.php?file=/FLM/FLM541/S0022112005005872a.pdf{&}code=f3ac05220a42b82ebb451e4f5abcf862

[35] D. K. Wilson, "Turbulence models and the synthesis of random fields for acoustic wave propagation calculations," Army Research Laboratory, Tech. Rep. ARL-TR-1677, 1998.

[36] H. W. Liepmann, J. Laufer, and K. Liepmann, "On the spectrum of isotropic turbulence," NACA, Tech. Rep. TN-2473, 1951.

[37] S. B. Pope, *Turbulent Flows*. Cambridge University Press, nov 2001.

[38] S. Chandrasekhar, "The Theory of Axisymmetric Turbulence," *Philosophical Transactions of the Royal Society A: Mathematical, Physical and Engineering Sciences*, vol. 242, no. 855, pp. 557–577, 1950.

[39] G. K. Batchelor, "The Theory of Axisymmetric Turbulence," *Proceedings of the Royal Society A: Mathematical, Physical and Engineering Sciences*, vol. 186, no. 1007, pp. 480–502, sep 1946. [Online]. Available: http://rspa.royalsocietypublishing.org/cgi/doi/10.1098/rspa.1946.0060

[40] T. von Karman and W. R. Sears, "Airfoil Theory for Non-Uniform Motion," *Journal of the Aeronautical Sciences*, vol. 5, no. 10, 1938.

[41] W. R. Sears, "Some aspects of non-stationary airfoil theory and its applications," *Journal of the Aeronautical Sciences*, vol. 8, no. 3, pp. 104–108, 1941.

[42] H. W. Liepmann, "Extension of the Statistical Approach to Buffeting and Gust Response of Wings of Finite Span," *Journal of the aeronautical sciences*, no. 3, pp. 197–200, 1955.

[43] L. T. Filotas, "Theory of airfoil response in a gusty atmosphere (Part I)," UTIAS, Tech. Rep. 139, 1969.

[44] J. M. R. Graham, "Lifting Surface Theory for the Problem of an Arbitrarily Yawed Sinusoidal Gust Incident on a Thin Airfoil in Incompressible Flow," *The Aeronautical Quarterly*, vol. 21, no. 2, pp. 182–198, 1970.

[45] J. Graham, "Similarity rules for thin aerofoils in non-stationary subsonic flows," *Journal of Fluid Mechanics*, vol. 43, no. 4, pp. 753–766, 1970.

[46] R. K. Amiet, "Compressibility Effects in Unsteady Thin-Airfoil Theory," *AIAA Journal*, vol. 12, no. 2, pp. 252–255, 1974. [Online]. Available: http://arc.aiaa.org/doi/abs/10.2514/3.49212

[47] ——, "High Frequency Thin-Airfoil Theory for Subsonic Flow," *AIAA Journal*, vol. 14, no. 8, pp. 1076–1082, 1976. [Online]. Available: http://arc.aiaa.org/doi/abs/10.2514/3.7187

[48] M. J. Lighthill, "On Sound Generated Aerodynamically. I. General Theory," *Proceedings of the Royal Society A: Mathematical, Physical and Engineering Sciences*, vol. 211, no. 1107, pp. 564–587, mar 1952. [Online]. Available: http://rspa.royalsocietypublishing.org/cgi/doi/10.1098/rspa.1983.0054http://rspa.royalsocietypublishing.org/cgi/doi/10.1098/rspa.1952.0060

[49] N. Curle, "The Influence of Solid Boundaries upon Aerodynamic Sound," *Proceedings of the Royal Society A: Mathematical, Physical and Engineering Sciences*, vol. 231, no. 1187, pp. 505–514, sep 1955. [Online]. Available: http://rspa.royalsocietypublishing.org/cgi/doi/10.1098/rspa.1955.0191

[50] J. E. F. Williams and D. L. Hawkings, "Sound Generation by Turbulence and Surfaces in Arbitrary Motion," *Philosophical Transactions of the Royal Society A: Mathematical, Physical and Engineering Sciences*, vol. 264, no. 1151, pp. 321–342, may 1969. [Online]. Available: http://rsta.royalsocietypublishing.org/cgi/doi/10.1098/rsta.1969.0031

[51] M. V. Lowson, "The sound field for singularities in motion." *Philosophical Transactions of the Royal Society A: Mathematical, Physical and Engineering Sciences*, vol. 286, no. 1407, pp. 559–572, 1965.

[52] J. E. Ffowcs Williams and D. L. Hawkings, "Theory relating to the noise of rotating machinery," *Journal of Sound and Vibration*, vol. 10, pp. 10–21, 1969. [Online]. Available: http://www.sciencedirect.com/science/article/pii/0022460X69901254

[53] L. Gutin, "On the sound field of a rotating propeller," NACA Langley Aeronautical Laboratory, Tech. Rep. 1195, 1948.

[54] D. B. Hanson, "Influence of Propeller Design Parameters on Far-Field Harmonic Noise in Forward Flight," *AIAA Journal*, vol. 18, no. 11, pp. 1313–1319, 1980. [Online]. Available: http://arc.aiaa.org/doi/10.2514/3.50887

[55] D. J. K. Hanson, "Helicoidal Surface Theory for Harmonic Noise of Propellers in the Far Field," *AIAA Journal*, vol. 18, no. 10, pp. 1213–1220, oct 1980. [Online]. Available: http://arc.aiaa.org/doi/10.2514/3.50873

[56] R. J. Astley, "Propulsion System Noise: Turbomachinery," *Encyclopedia of Aerospace Engineering*, pp. 1–12, 2010. [Online]. Available: http://doi.wiley.com/10.1002/9780470686652.eae336

[57] U. W. Ganz, P. D. Joppa, T. J. Patten, D. F. Scharpf, B. Commercial, and A. Group, "Boeing 18-Inch Fan Rig Broadband Noise Test," NASA, Tech. Rep. CR-1998-208704, 1998.

[58] S. A. Glegg, "The Response of a Swept Blade Row to a Three-Dimensional Gust," *Journal of Sound and Vibration*, vol. 227, no. 1, pp. 29–64, 1999. [Online]. Available: http://www.sciencedirect.com/science/article/pii/S0022460X99923271

[59] H. Posson, M. Roger, and S. Moreau, "On a uniformly valid analytical rectilinear cascade response function," *Journal of Fluid Mechanics*, vol. 663, pp. 22–52, 2010. [Online]. Available: http://www.journals.cambridge.org/abstract{_}S0022112010003368

[60] H. Posson, S. Moreau, and M. Roger, "On the use of a uniformly valid analytical cascade response function for fan broadband noise predictions," *Journal of Sound and Vibration*, vol. 329, no. 18, pp. 3721–3743, 2010. [Online]. Available: http://dx.doi.org/10.1016/j.jsv.2010.03.009

[61] ——, "Broadband noise prediction of fan outlet guide vane using a cascade response function," *Journal of Sound and Vibration*, vol. 330, no. 25, pp. 6153–6183, 2011. [Online]. Available: http://dx.doi.org/10.1016/j.jsv.2011.07.040

[62] D. B. Hanson, "Theory for broadband Noise of Rotor and Stator Cascades with Inhomogeneous Inflow Turbulence Including Effects of Lean and Sweep," Tech. Rep. CR-2001-210762, 2001.

[63] I. Wygnanski, F. Champagne, and B. Marasli, "On the large-scale structures in two-dimensional, small-deficit, turbulent wakes," *Journal of Fluid Mechanics*, vol. 168, no. 1986, pp. 31–71, 1986.

[64] V. Jurdic, P. Joseph, and J. Antoni, "Investigation of Rotor Wake Turbulence Through Cyclostationary Spectral Analysis," *AIAA Journal*, vol. 47, no. 9, pp. 2022–2030, sep 2009. [Online]. Available: http://arc.aiaa.org/doi/abs/10.2514/1.36728

[65] M. J. Kingan, "Open Rotor Broadband Interaction Noise," *Journal of Sound and Vibration*, vol. 332, no. 17, pp. 3956–3970, 2013. [Online]. Available: http://linkinghub.elsevier.com/retrieve/pii/S0022460X13002460

[66] T. Nodé-Langlois, F. Wlassow, V. Languille, Y. Colin, B. Caruelle, J. R. Gill, X. Chen, X. Zhang, and A. B. Parry, "Prediction of Contra-Rotating Open Rotor broadband noise in isolated and installed configurations," in *20th AIAA/CEAS Aeroacoustics Conference*, AIAA 2014-2610, Atlanta, Georgia, 2014. [Online]. Available: http://arc.aiaa.org/doi/abs/10.2514/6.2014-2610

[67] S. Sinayoko, "Broadband noise for rotating blades : analysis of acceleration effects in the time and frequency domains," in *21st AIAA/CEAS Aeroacoustics Conference*, AIAA 2015-2983, Dallas, Texas, 2015.

[68] V. P. Blandeau, P. F. Joseph, G. Jenkins, and C. J. Powles, "Comparison of sound power radiation from isolated airfoils and cascades in a turbulent flow," *The Journal of the Acoustical Society of America*, vol. 129, no. 6, pp. 3521–3530, 2011. [Online]. Available: http://asa.scitation.org/doi/10.1121/1.3569706

[69] Y. Rozenberg, M. Roger, and S. Moreau, "Rotating Blade Trailing-Edge Noise: Experimental Validation of Analytical Model," *AIAA Journal*, vol. 48, no. 5, pp. 951–962, 2010. [Online]. Available: http://arc.aiaa.org/doi/pdf/10.2514/1.43840

[70] S. Glegg, S. Baxter, and A. Glendinning, "The prediction of broadband noise from wind turbines," *Journal of Sound and Vibration*, vol. 118, no. 2, pp. 217–239, oct 1987. [Online]. Available: http://linkinghub.elsevier.com/retrieve/pii/0022460X87905220

[71] A. Pagano, M. Barbarino, D. Casalino, and L. Federico, "Tonal and Broadband Noise Calculations for Aeroacoustic Optimization of a Pusher Propeller," *Journal of Aircraft*, vol. 47, no. 3, pp. 835–848, may 2010. [Online]. Available: http://arc.aiaa.org/doi/10.2514/1.45315

[72] K. Kucukcoskun, J. Christophe, C. Schram, and M. Tournour, "A Semi-Analytical Approach on the Turbulence Interaction Noise of A Low-Speed Axial Fan Including Broadband Scattering," in *17th AIAA/CEAS Aeroacoustics Conference*, AIAA 2011-2714, Portland, Oregon, 2011. [Online]. Available: http://arc.aiaa.org/doi/abs/10.2514/6.2011-2714

[73] K. Kucukcoskun, "Prediction of free and scattered acoustic fields of low-speed fans," Ph.D. dissertation, Ecole Centrale De Lyon, 2012. [Online]. Available: https://tel.archives-ouvertes.fr/tel-00758274

[74] R. W. Paterson and R. K. Amiet, "Noise of a model helicopter rotor due to ingestion of turbulence," NASA Langley Research Center, Tech. Rep. NASA CR 3213, 1979.

[75] M. J. Kingan and R. H. Self, "Open Rotor Tone Scattering," *Journal of Sound and Vibration*, vol. 331, no. 8, pp. 1806–1828, 2012.

[76] S. A. L. Glegg, "Effect of centerbody scattering on propeller noise," *AIAA Journal*, vol. 29, no. 4, pp. 572–576, apr 1991. [Online]. Available: http://arc.aiaa.org/doi/abs/10.2514/1.44659http://arc.aiaa.org/doi/10.2514/3.10622

[77] R. K. Amiet, "Gust response of a flat-plate aerofoil in the time-domain," *The Quarterly Jounral of Applied Mathematics*, vol. 39, no. 4, pp. 485–505, 1986.

[78] D. B. Stephens and S. C. Morris, "Sound Generation by a Rotor Interacting with a Casing Turbulent Boundary Layer," *AIAA Journal*, vol. 47, no. 11, pp. 2698–2708, 2009. [Online]. Available: http://arc.aiaa.org/doi/10.2514/1.43271

[79] R. W. Paterson and R. K. Amiet, "Acoustic Radiation and Surface Pressure Characteristics of an Airfoil due to Incident Turbulence," NASA Langley Research Center, Tech. Rep. NASA CR-2733, 1976.

[80] R. W. Paterson and R. K. Amiett, "Noise and Surface Pressure Response of an Airfoil to Incident Turbulence," vol. 14, no. 8, pp. 729–736, 1977.

[81] S. Moreau and M. Roger, "Effect of Angle of Attack and Airfoil Shape on Turbulence-Interaction Noise," in *11th AIAA/CEAS Aeroacoustics Conference*, AIAA 2005-2973, Montrey, USA, may 2005. [Online]. Available: http://arc.aiaa.org/doi/10.2514/6.2005-2973

[82] W. J. Devenport, J. K. Staubs, and S. A. Glegg, "Sound radiation from real airfoils in turbulence," *Journal of Sound and Vibration*, vol. 329, no. 17, pp. 3470–3483, 2010. [Online]. Available: http://dx.doi.org/10.1016/j.jsv.2010.02.022

[83] S. A. L. Glegg and W. J. Devenport, "Panel methods for airfoils in turbulent flow," *Journal of Sound and Vibration*, vol. 329, no. 18, pp. 3709–3720, 2010. [Online]. Available: http://dx.doi.org/10.1016/j.jsv.2010.03.007

[84] F. Gea-Aguilera, "Aerodynamic and Aeroacoustic Modelling of Engine Fan Broadband Noise PhD Transfer Report," Ph.D. dissertation, University of Southampton, 2017. [Online]. Available: https://eprints.soton.ac.uk/412640/

[85] J. K. Staubs, "Real Airfoil Effects on Leading Edge Noise," Ph.D. dissertation, Virginia Polytechnic Institute and State University, 2008. [Online]. Available: https://theses.lib.vt.edu/theses/available/etd-05282008-002246/unrestricted/JKS{_}Dissertation.pdf

[86] C. Paruchuri, J. R. Gill, N. Subramanian, P. Joseph, C. Vanderwel, X. Zhang, and B. Ganapathisubramani, "Aerofoil geometry effects on turbulence interaction noise," in *21st AIAA/CEAS Aeroacoustics Conference*, no. June, Dallas, USA, jun 2015. [Online]. Available: http://arc.aiaa.org/doi/10.2514/6.2015-2830

[87] H. H. Hubbard, "Sound from dual-rotating and multiple single-rotating propellers," NACA Langley Aeronautical Laboratory, Tech. Rep. 1654, 1948.

[88] G. P. Succi, D. H. Munro, and J. A. Zimmer, "Experimental Verification of Propeller Noise Prediction," *AIAA Journal*, vol. 20, no. 11, pp. 1483–1491, 1982. [Online]. Available: http://doi.aiaa.org/10.2514/3.51211

[89] P. Block, "Noise radiation patterns of counter-rotation and unsteadily loaded single-rotation propellers," *Journal of Aircraft*, vol. 22, no. 9, pp. 776–783, 1985. [Online]. Available: http://arc.aiaa.org/doi/abs/10.2514/3.45201

[90] P. Block and G. L. J. Gentry, "Directivity and Trends of Noise Generated by a Propeller in a Wake," NASA, Tech. Rep. 2609, 1986.

[91] P. Block, "Experimental Study of the Effects of the effects of installation on Single and Counter Rotation Propeller noise," NASA Langley Research Cneter, Tech. Rep. 2541, 1986.

[92] ——, "Counter-rotating propeller noise directivity and trends," in *AIAA 10th Aeroacoustics Conference*, AIAA 86-1927, Seattle, USA, jul 1986.

[93] C. Horváth, E. Envia, and G. G. Podboy, "Limitations of Phased Array Beamforming in Open Rotor Noise Source Imaging," in *19th AIAA/CEAS Aeroacoustics Conference*, AIAA 2013-217902, Berlin, Germany, may 2013.

[94] C. Horváth, "Beamforming Investigation of Dominant Counter-Rotating Open Rotor Tonal and Broadband Noise Sources," *AIAA Journal*, vol. 53, no. 6, pp. 1–10, 2015.

[95] A. B. Parry, K. Britchford, P. Sureshkumar, M. M. J. Kingan, and P. Sureshkumar, "Aeroacoustic tests of isolated open rotors at high speed," in *18th AIAA/CEAS Aeroacoustics Conference*, AIAA 2012-2220, Colorado, USA, jun 2012. [Online]. Available: http://arc.aiaa.org/doi/pdf/10.2514/6.2012-2220http://eprints.soton.ac.uk/340555/

[96] J. Ricouard, E. Julliard, M. Omais, V. Regnier, A. Parry, and S. Baralon, "Installation Effects on Contra-Rotating Open Rotor Noise," in *16th AIAA/CEAS Aeroacoustics Conference*, AIAA 2010-3795, Stockholm, Sweeden, jun 2010. [Online]. Available: http://arc.aiaa.org/doi/pdf/10.2514/6.2010-3795

[97] W. N. Alexander, W. Devenport, M. Morton, and S. Glegg, "Noise from a Rotor Ingesting a Planar Turbulent Boundary Layer," in *19th AIAA/CEAS Aeroacoustics Conference*. American Institute of Aeronautics and Astronautics, may 2013. [Online]. Available: http://arc.aiaa.org/doi/abs/10.2514/6.2013-2285

[98] D. Wisda, W. N. Alexander, W. J. Devenport, and S. A. Glegg, "Boundary Layer Ingestion Noise and Turbulence Scale Analysis at High and Low Advance Ratios," in *20th AIAA/CEAS Aeroacoustics Conference*, AIAA 2014-2608, Atlanta, Georgia, jun 2014. [Online]. Available: http://arc.aiaa.org/doi/abs/10.2514/6.2014-2608

[99] M. A. Morton, W. J. Devenport, S. A. L. Glegg, and K. T. Lowe, "Rotor Inflow Noise Caused by a Boundary Layer: Inflow Measurements and Noise Predictions," Masters Dissertation, Virginia Polytechnic Institute and State University, 2012.

[100] S. A. L. Glegg, E. Kawashima, F. Lachowski, V. Tech, and B. Va, "Inflow Distortion Noise In a Non Axisymmetric Flow," in *19th AIAA/CEAS Aeroacoustics Conference*, AIAA 2013-2286, Berlin, Germany, may 2013.

[101] X. Zhang, "Aircraft noise and its nearfield propagation computations," *Acta Mechanica Sinica*, vol. 28, no. 4, pp. 960–977, 2012.

[102] S. Redonnet, "Aircraft Noise Prediction via Aeroacoustic Hybrid Methods - Development and Application of Onera Tools over the Last Decade : Some Examples," *Journal Aerospace Lab*, vol. 1, no. 7, pp. 1–16, 2014.

[103] E. Envia, D. L. Tweedt, R. P. Woodward, D. M. Elliott, E. B. Fite, C. E. Hughes, G. G. Podboy, and D. L. Sutliff, "An Assessment of Current Fan Noise Prediction Capability," NASA, Tech. Rep. 2008-215415, 2008.

[104] A. Stuermer and J. Yin, "Low-Speed Aerodynamics and Aeroacoustics of CROR Propulsion Systems," in *15th AIAA/CEAS Aeroacoustics Conference*, AIAA 2009-3134, Miami, Fl, may 2009.

[105] P. R. Spalart, "Initial Noise Predictions for Open Rotors Using First Principles," in *16th AIAA/CEAS Aeroacoustics Conference*, AIAA 2010-3793, Stockholm, Sweden, jun 2010.

[106] T. Deconinck, P. A. Hoffer, C. Hirsch, A. D. Meulenaere, J. C. Bonaccorsi, and G. Ghorbaniasl, "Prediction of Near- and Far-Field Noise Generated by Contra-Rotating Open Rotors," in *16th AIAA/CEAS Aeroacoustics Conference*, AIAA 2010-3794, Stockholm, Sweden, jun 2010.

[107] R. Schnell, J. Yin, S. Funke, and H. Siller, "Aerodynamic and Basic Acoustic Optimization of a Contra-Rotating Open Rotor with Experimental Verification," in *18th AIAA/CEAS Aeroacoustics Conference*, AIAA 2012-2127, Colorado, Co, jun 2012. [Online]. Available: http://arc.aiaa.org/doi/pdf/10.2514/6.2012-2127

[108] F. Falissard, R. Boisard, and G. Delattre, "Aeroacoustic Computation of a Contra Rotating Open Rotor Model with Test Rig Installation Effects," in *18th AIAA/CEAS Aeroacoustics ...*, no. June, 2012, pp. 4–6. [Online]. Available: http://arc.aiaa.org/doi/pdf/10.2514/6.2012-2218

[109] Y. Colin, A. Carazo, B. Caruelle, T. Node-Langlois, and A. Parry, "Computational strategy for predicting CROR noise at low-speed Part I: review of the numerical methods," in *18th AIAA/CEAS Aeroacoustics Conference (33rd AIAA Aeroacoustics Conference)*, no. June. Reston, Virigina: American Institute of Aeronautics and Astronautics, jun 2012, pp. 4–6. [Online]. Available: http://arc.aiaa.org/doi/10.2514/6.2012-2221

[110] R. Akkermans, A. Stuermer, and J. Delfs, "Assessment of Front-Rotor Trailing-Edge-Blowing for the Reduction of Open Rotor Noise Emissions," in *19th AIAA/CEAS Aeroacoustics Conference*, AIAA 2013-2200, may 2013. [Online]. Available: http://arc.aiaa.org/doi/abs/10.2514/6.2013-2200

[111] C. Brehm, M. F. Barad, and C. C. Kiris, "Open Rotor Computational Aeroacoustic Analysis with an Immersed Boundary Method," in *AIAA SciTech Forum*, San Diego, CA, 2016. [Online]. Available: http://arc.aiaa.org/doi/10.2514/6.2016-0815

[112] A. Stuermer, "Validation of uRANS-Simulations of Contra-Rotating Open Rotor-Powered Aircraft at Take-Off Conditions," in *AIAA SciTech Forum*, no. January, Kissimmee, Florida, 2018, pp. 1–18.

[113] M. L. Shur, P. R. Spalart, and M. K. Strelets, "Noise prediction for increasing complex jets. Part II : Applications," *International Journal of Aeroacoustics*, vol. 4, no. 3, pp. 247–266, 2005.

[114] R. A. D. Akkermans, J. W. Delfs, M. Lummer, M. Siefert, B. Caruelle, and C. Tiedemann, "Handling of Non-Periodic Contra Rotating Open Rotor Data," *AIAA Journal*, no. June, pp. 4–6, 2012.

[115] R. Hixon, "Prefactored Small-Stencil Compact Schemes," *Journal of Computational Physics*, vol. 165, no. 2, pp. 522–541, 2000. [Online]. Available: http://linkinghub.elsevier.com/retrieve/pii/S0021999100966312

[116] G. Ashcroft and X. Zhang, "Optimized prefactored compact schemes," *Journal of Computational Physics*, vol. 190, no. 2, pp. 459–477, 2003.

[117] J. W. Kim, "Optimised Boundary Compact Finite Difference Schemes for Computational Aeroacoustics," *Journal of Computational Physics*, vol. 225, no. 1, pp. 995–1019, 2007.

[118] ——, "High-Order Compact Filters with Variable Cut-Off Wavenumber and Stable Boundary Treatment," *Computers and Fluids*, vol. 39, no. 7, pp. 1168–1182, 2010.

[119] J. R. Gill, R. J. Fattah, and X. Zhang, "Evaluation and Development of Non-Reflective Boundary Conditions for Aeroacoustic Simulations," in *21st AIAA/CEAS Aeroacoustics Conference*, AIAA 2015-2677, Dallas, Texas, jun 2015. [Online]. Available: http://arc.aiaa.org/doi/10.2514/6.2015-2677

[120] F. Gea-Aguilera, X. Zhang, X. Chen, J. Gill, and T. Nodé-Langlois, "Synthetic Turbulence Methods for Leading Edge Noise Predictions," in *21st AIAA/CEAS Aeroacoustics Conference*, AIAA 2015-2670, Dallas, Texas, jun 2015. [Online]. Available: http://arc.aiaa.org/doi/10.2514/6.2015-2670

[121] J. Gill, X. Zhang, and P. Joseph, "Reduced Dimension Modeling of Leading Edge Turbulent Interaction Noise," in *20th AIAA/CEAS Aeroacoustics Conference*, AIAA 2014-2321, Atlanta, Georgia, jun 2014.

[122] V. Clair, C. Polacsek, T. L. Garrec, and G. Reboul, "CAA methodology to simulate turbulence-airfoil noise," in *18th AIAA/CEAS Aeroacoustics Conference*, AIAA 2012-2189, no. June, 2012, pp. 4–6.

[123] J. Gill, X. Zhang, and P. Joseph, "Symmetric airfoil geometry effects on leading edge noise." *The Journal of the Acoustical Society of America*, vol. 134, no. 4, pp. 2669–80, oct 2013. [Online]. Available: http://www.ncbi.nlm.nih.gov/pubmed/24116405

[124] R. Ewert, "Broadband slat noise prediction based on CAA and stochastic sound sources from a fast random particle-mesh (RPM) method," *Computers and Fluids*, vol. 37, no. 4, pp. 369–387, 2008.

[125] M. Dieste and G. Gabard, "Random particle methods applied to broadband fan interaction noise," *Journal of Computational Physics*, vol. 231, no. 24, pp. 8133–8151, 2012.

[126] F. Gea-Aguilera, J. Gill, and X. Zhang, "Synthetic turbulence methods for computational aeroacoustic simulations of leading edge noise," *Computers and Fluids*, vol. 157, pp. 240–252, 2017. [Online]. Available: http://dx.doi.org/10.1016/j.compfluid.2017.08.039

[127] H. M. Atassi, M. Dusey, and C. M. Davis, "Acoustic radiation from a thin airfoil in nonuniform subsonic flows," *AIAA Journal*, vol. 31, no. 1, pp. 12–19, 1993. [Online]. Available: http://arc.aiaa.org/doi/abs/10.2514/3.11312

[128] D. P. Lockard and P. J. Morris, "Radiated Noise from Airfoils in Realistic Mean Flows," *AIAA Journal*, vol. 36, no. 6, pp. 907–914, 1998.

[129] F. Gea Aguilera, J. R. Gill, D. Angland, and X. Zhang, "Wavy Leading Edge Airfoils Interacting with Anisotropic Turbulence," in *23rd AIAA/CEAS Aeroacoustics Conference*, AIAA 2017-3370. Denver: American Institute of Aeronautics and Astronautics, jun 2017. [Online]. Available: https://arc.aiaa.org/doi/10.2514/6.2017-3370

[130] L. Jahanshaloo, E. Pouryazdanpanah, and N. A. Che Sidik, "A Review on the Application of the Lattice Boltzmann Method for Turbulent Flow Simulation," *Numerical Heat Transfer, Part A: Applications*, vol. 64, no. 11, pp. 938–953, dec 2013. [Online]. Available: http://www.tandfonline.com/doi/abs/10.1080/10407782.2013.807690

[131] Y. Li and X. Shan, "Lattice Boltzmann method for adiabatic acoustics," *Philosophical Transactions of the Royal Society A: Mathematical, Physical and Engineering Sciences*, vol. 369, no. 1944, pp. 2371–2380, 2011. [Online]. Available: http://rsta.royalsocietypublishing.org/cgi/doi/10.1098/rsta.2011.0109

[132] D. Casalino, A. Hazir, and A. Mann, "Turbofan Broadband Noise Prediction using the Lattice Boltzmann Method," *AIAA Journal*, vol. 56, no. 2, pp. 609–628, 2017. [Online]. Available: http://arc.aiaa.org/doi/10.2514/6.2016-2945

[133] S. Moreau and M. Roger, "Competing Broadband Noise Mechanisms in Low-Speed Axial Fans," *AIAA Journal*, vol. 45, no. 1, pp. 48–57, jan 2007. [Online]. Available: http://arc.aiaa.org/doi/10.2514/1.14583

[134] R. H. Schlinker and R. K. Amiet, "Helicopter Rotor Trailing Edge Noise," NASA Langley Research Center, Tech. Rep. 3470, 1981.

[135] S. Sinayoko, M. Kingan, and A. Agarwal, "Trailing edge noise theory for rotating blades in uniform flow," *Proceedings of the Royal Society A: Mathematical, Physical and Engineering Sciences*, vol. 469, no. 2157, pp. 1–21, 2013. [Online]. Available: http://rspa.royalsocietypublishing.org/cgi/doi/10.1098/rspa.2013.0065

[136] I. Garrick and C. Watkins, "A Theoretical Study of the Effect of Forward Speed on the Free-Space Sound Pressure Field Around Propellers," National Advisory Committee for Aeronautics Langley Aeronautical Laboratory, Tech. Rep. TN-3018, 1953.

[137] V. P. Blandeau and P. F. Joseph, "Broadband Noise Due to Rotor-Wake/Rotor Interaction in Contra-Rotating Open Rotors," *AIAA Journal*, vol. 48, no. 11, pp. 2674–2686, 2010. [Online]. Available: http://arc.aiaa.org/doi/abs/10.2514/1.J050566

[138] "Fan Broadband Noise Prediction Panel Session at 21st AIAA/CEAS Aeroacoustics Conference." [Online]. Available: http://web1.oai.org/FBNWorkshop.nsf/Indexaccessedon01/06/2015

[139] S. A. Glegg, J. Grant, D. Wisda, H. Murray, W. Alexander, and W. J. Devenport, "Broadband Noise from a Rotor at an Angle to the Mean Flow," in *54th AIAA Aerospace Sciences Meeting*, Reston, Virginia, jan 2016. [Online]. Available: http://arc.aiaa.org/doi/10.2514/6.2016-1269

[140] V. P. Blandeau and P. F. Joseph, "On the Validity of Amiet's Model for Propeller Trailing-Edge Noise," in *16th AIAA/CEAS Aeroacoustics Conference*, AIAA 2010-3797, Stockholm, Sweden, 2010. [Online]. Available: http://arc.aiaa.org/doi/abs/10.2514/6.2010-3797

[141] J. Gill, X. Zhang, and P. Joseph, "Symmetric airfoil geometry effects on leading edge noise." *The Journal of the Acoustical Society of America*, vol. 134, no. 4, pp. 2669–2680, 2013. [Online]. Available: http://www.ncbi.nlm.nih.gov/pubmed/24116405

[142] ——, "Single Velocity-Component Modeling of Leading Edge Turbulence Interaction Noise." *The Journal of the Acoustical Society of America*, vol. 137, no. 6, pp. 3209–3220, 2015. [Online]. Available: http://dx.doi.org/10.1121/1.4921547

[143] F. Hu, "Low-Dissipation and Low-Dispersion Runge-Kutta Schemes for Computational Acoustics," *Journal of Computational Physics*, vol. 124, no. 1, pp. 177–191, 1996.

[144] D. J. Thomson, "Spectrum Estimation and Harmonic Analysis," *Proc. IEEE*, vol. 70, pp. 1055–1096, 1982.

[145] R. Fattah, D. Angland, and X. Zhang, "A priori grid quality estimation for high-order finite differencing," *Journal of Computational Physics*, vol. 315, pp. 629–643, 2016. [Online]. Available: http://dx.doi.org/10.1016/j.jcp.2016.03.063

[146] U. Ingard and G. L. Lamb, "Effect of a Reflecting Plane on the Power Output of Sound Sources," *The Journal of the Acoustical Society of America*, vol. 29, no. 6, pp. 743–744, 1957. [Online]. Available: http://asa.scitation.org/doi/10.1121/1.1909034

[147] E. Kerschen and P. Gliebe, "Fan noise caused by the ingestion of anisotropic turbulence - A model based on axisymmetric turbulence theory," in *6th Aeroacoustics Conference*, AIAA-80-1021, Hartford, Connecticut, jun 1980. [Online]. Available: http://dx.doi.org/10.2514/6.1980-1021

[148] M. Gad-el Hak and P. R. Bandyopadhyay, "Reynolds Number Effects in Wall-Bounded Turbulent Flows," *Applied Mechanics Reviews*, vol. 47, no. 8, pp. 307–365, 1994. [Online]. Available: http://appliedmechanicsreviews.asmedigitalcollection.asme.org/article.aspx?articleid=1395357

[149] K. S. Choi and J. L. Lumley, "The return to isotropy of homogeneous turbulence," *Journal of Fluid Mechanics*, vol. 436, pp. 59–84, 2001.

[150] R. Martinez, "Asymptotic Theory of Broadband Rotor Thrust , Part I1 : Analysis of the right frequency shift of the maximum response," vol. 63, no. March, pp. 143–148, 1996.

[151] S. A. Glegg, J. Grant, H. Murray, W. J. Devenport, and W. N. Alexander, "Sound Radiation from a Rotor Operating at High Thrust Near a Wall," in *22nd AIAA/CEAS Aeroacoustics Conference*, AIAA 2016-2995, Lyon, France, 2016. [Online]. Available: http://arc.aiaa.org/doi/10.2514/6.2016-2995

[152] A. P. Dowling and J. E. F. Williams, *Sound and Sources of Sound*, Ellis Horwood Series in Engineering Science. Ellis Horwood Limited, 1983. [Online]. Available: https://books.google.co.uk/books?id=VhNRAAAAMAAJ